



University of Kentucky  
UKnowledge

---

University of Kentucky Doctoral Dissertations

Graduate School

---

2011

## STUDIES ON SILICON NMR CHARACTERIZATION AND KINETIC MODELING OF THE STRUCTURAL EVOLUTION OF SILOXANE-BASED MATERIALS AND THEIR APPLICATIONS IN DRUG DELIVERY AND ADSORPTION

Jyotrhirmai Ambati

University of Kentucky, j\_ambati@yahoo.com

[Right click to open a feedback form in a new tab to let us know how this document benefits you.](#)

---

### Recommended Citation

Ambati, Jyotrhirmai, "STUDIES ON SILICON NMR CHARACTERIZATION AND KINETIC MODELING OF THE STRUCTURAL EVOLUTION OF SILOXANE-BASED MATERIALS AND THEIR APPLICATIONS IN DRUG DELIVERY AND ADSORPTION" (2011). *University of Kentucky Doctoral Dissertations*. 203.

[https://uknowledge.uky.edu/gradschool\\_diss/203](https://uknowledge.uky.edu/gradschool_diss/203)

This Dissertation is brought to you for free and open access by the Graduate School at UKnowledge. It has been accepted for inclusion in University of Kentucky Doctoral Dissertations by an authorized administrator of UKnowledge. For more information, please contact [UKnowledge@lsv.uky.edu](mailto:UKnowledge@lsv.uky.edu).

ABSTRACT OF DISSERTATION

Jyothirmai Ambati

The Graduate School  
University of Kentucky

2011

STUDIES ON SILICON NMR CHARACTERIZATION AND KINETIC MODELING OF  
THE STRUCTURAL EVOLUTION OF SILOXANE-BASED MATERIALS AND THEIR APPLICATIONS IN  
DRUG DELIVERY AND ADSORPTION

---

ABSTRACT OF DISSERTATION

---

A dissertation submitted in partial fulfillment of the  
requirements for the degree of Doctor of Philosophy in the  
College of Engineering  
at the University of Kentucky

By  
Jyotrhirmai Ambati

Lexington, Kentucky

Director: Dr. Stephen E. Rankin, Professor of Chemical Engineering

Lexington, Kentucky

2011

Copyright © Jyotrhirmai Ambati 2011

## ABSTRACT OF DISSERTATION

### STUDIES ON SILICON NMR CHARACTERIZATION AND KINETIC MODELING OF THE STRUCTURAL EVOLUTION OF SILOXANE-BASED MATERIALS AND THEIR APPLICATIONS IN DRUG DELIVERY AND ADSORPTION

This dissertation presents studies of the synthetic processes and applications of siloxane-based materials. Kinetic investigations of bridged organoalkoxysilanes that are precursors to organic-inorganic hybrid polysilsesquioxanes are a primary focus. Quick gelation despite extensive cyclization is found during the polymerization of bridged silane precursors except for silanes with certain short bridges. This work is an attempt to characterize and understand some of the distinct features of bridged silanes using experimental characterization, kinetic modeling and simulation. In addition to this, the dissertation shows how the properties of siloxane-materials can be engineered for drug delivery and adsorption.

The phase behavior of polymerizing mixtures is first investigated to identify the solutions that favor kinetic characterization. Microphase separation is found to cause gradual loss of NMR signal for certain initial compositions. Distortionless Enhancement by Polarization Transfer  $^{29}\text{Si}$  NMR is employed to identify the products of polymerization of some short-bridged silanes under no signal loss conditions. This technique requires knowing indirect  $^{29}\text{Si}$ - $^1\text{H}$  scalar coupling constants which sometimes cannot be measured due to second-order effects. However, the B3LYP density functional method with 6-31G basis set is found to predict accurate  $^{29}\text{Si}$ - $^1\text{H}$  coupling constants of organoalkoxysilanes and siloxanes. The scalar coupling constants thus estimated are employed to resolve non-trivial coupled NMR spectra and quantitative kinetic modeling is performed using the DEPT Si NMR transients. In order to investigate the role of the organic bridging group, the structural evolution of bridged and non-bridged silanes are compared using Monte Carlo simulations. Kinetic and simulation models suggest that cyclization plays a key role right from the onset of polymerization for bridged silanes even more than in non-bridged silanes. The simulations indicate that the carbosiloxane rings formed from short-bridged precursors slow down but do not prevent gelation.

The tuning of siloxane-based materials for adsorption technologies are also discussed here. In the first example, antioxidant enzyme loading is investigated as a means to reduce oxidative stress generated by silica nanoparticle drug carriers. Materials are engineered for promising enzyme loading and protection from proteolysis. Second, the potential of copper sulfate impregnation to enhance adsorption of ammonia by silica is explored by molecular simulation.

KEYWORDS: Sol-gel Polymerization, Kinetic Investigation, Si NMR, Bridged Silanes, DFT Calculations

Jyothirmai Ambati

---

June 30<sup>th</sup>, 2011

---

STUDIES ON SILICON NMR CHARACTERIZATION AND KINETIC MODELING OF  
THE STRUCTURAL EVOLUTION OF SILOXANE-BASED MATERIALS AND THEIR APPLICATIONS IN  
DRUG DELIVERY AND ADSORPTION

By

Jyothirmai Ambati

Dr. Stephen E. Rankin

---

Director of Dissertation

Dr. Stephen E. Rankin

---

Director of Graduate Studies

June 30<sup>th</sup>, 2011

---

Date



DISSERTATION

Jyothirmai Ambati

The Graduate School  
University of Kentucky

2011



STUDIES ON SILICON NMR CHARACTERIZATION AND KINETIC MODELING OF  
THE STRUCTURAL EVOLUTION OF SILOXANE-BASED MATERIALS AND THEIR APPLICATIONS IN  
DRUG DELIVERY AND ADSORPTION

---

DISSERTATION

---

A dissertation submitted in partial fulfillment of the  
requirements for the degree of Doctor of Philosophy in the  
College of Engineering  
at the University of Kentucky

By  
Jyothirmai Ambati

Lexington, Kentucky

Director: Dr. Stephen E. Rankin, Professor of Chemical Engineering

Lexington, Kentucky

2011

Copyright © Jyothirmai Ambati 2011

## ACKNOWLEDGEMENTS

The successful completion of this dissertation involved contribution from several sources to whom I am very thankful to. First and foremost, I am greatly indebted to my advisor, Prof. Stephen Rankin for his resourcefulness and unprecedented support on a personal and professional level during the course of my PhD. He has provided me with opportunities to explore diverse areas of research and has been very patient and flexible with my work schedule. Words are not enough to express my deep felt gratitude for his invaluable guidance and friendship.

Thanks are also due to Dr. Thomas Dzuibla for his supervision in enzyme studies (Chapter 7). He is a very pleasant person to work with and I sincerely appreciate his suggestions and encouragement in the progress of this project. My special thanks go to Dr. Hans-Joachim Lehmler. Collaboration with him on quantum chemical investigation of PCB quinones has indirectly helped me shape up my work on ammonia adsorption (Chapter 8). I am very thankful to Mr. John Layton for training and helpful discussions regarding NMR experiments. I thank my committee members, Professors Douglas Kalika, Dibakar Bhattacharyya, Folami Ladipo and Constance Wood for their time and consideration in completing this dissertation.

I acknowledge the graduate students, David Cochran and Paritosh Wattamwar (Chapter 7) and the undergraduate students, Kala Bean, Phalak Patel, Alex Lopex (Chapter 7) and Hamzah Syed (Chapter 8) that I worked with. I also thank Dr. Bing Tan for helping me get oriented in the lab when I first started my research work, Dr. Rong Xing for developing the hollow core particle synthesis protocols employed in Chapter 7 and Dr. Xin Li for providing the Monte Carlo Simulations program code developed by her for tetrafunctional silanes that I built upon to construct models of tri-functional and bridged silane systems.

Next, I thank National Science Foundation and U.S Department of Energy for financially supporting my research work. I acknowledge the University of Kentucky Facilities: High Performance Computing, NMR Center in the Department of Chemistry and Electron Microscopy Center for using their facilities.

Finally, I would like to thank my family for their continued support. Certainly, my parents Sudershan Ambati and Anjali Ambati and, my brother Sunada Venu Ambati have been the primary driving force behind my academic career. They have devoted their lives to me and have

always respected my educational endeavors. I dedicate this dissertation to them. I am very thankful to my uncles, Dr. Narayana Memula and Late Mr. Vijaya Rao and my friend, Ms. Ellen Kiser and her family for their support and encouragement in accomplishing this dissertation.

## TABLE OF CONTENTS

|  |           |
|--|-----------|
| Acknowledgements .....   | iii       |
| List of Tables.....  | xi        |
| List of Figures.....   | xiii      |
| 1. Introduction and Background .....   | 1         |
| 1.1. Sol-gel Materials and Chemistry.....  | 1         |
| 1.1.1. Organic-Inorganic Hybrid Materials .....  | 1         |
| 1.1.2. Bridged vs. Non-bridged.....  | 2         |
| 1.1.3. Sol-gel Polymerization.....   | 3         |
| 1.2. Material Synthesis and Engineering .....  | 4         |
| 1.2.1. Mesoporous Material Synthesis.....  | 4         |
| 1.2.2. Kinetic Investigation .....   | 5         |
| 1.2.2.1. Significance of Kinetic Studies .....   | 5         |
| 1.2.2.2. Mechanistic Modeling .....  | 7         |
| 1.2.2.3. Dynamic Monte Carlo Simulation .....  | 8         |
| 1.3. NMR Spectroscopy .....  | 9         |
| 1.3.1. $^{29}\text{Si}$ NMR .....  | 10        |
| 1.3.2. DEPT $^{29}\text{Si}$ NMR .....   | 11        |
| 1.3.3. Selective Decoupling .....  | 12        |
| 1.4. Dissertation Scope .....  | 12        |
| 1.5. Dissertation Outline.....   | 13        |
| <b>I DFT Calculations to Assist <math>^{29}\text{Si}</math> NMR Investigation of Alkoxysilane Polymerization .....</b>   | <b>24</b> |
| 2. DFT Calculations of Indirect $^{29}\text{Si}$ - $^1\text{H}$ Spin-Spin Coupling Constants in Organoalkoxysilanes..... | 25        |
| 2.1. Summary.....  | 25        |
| 2.2. Introduction.....   | 25        |
| 2.3. Computational Details.....  | 28        |
| 2.3.1. Geometry Optimization .....   | 28        |
| 2.3.2. NMR Calculations.....   | 28        |
| 2.4. Experimental Section.....   | 29        |
| 2.4.1. Methods .....   | 29        |

|  |           |
|--|-----------|
| 2.4.2. Materials .....   | 30        |
| 2.5. Results and Discussion.....   | 30        |
| 2.5.1. Selection of Appropriate Basis Set .....  | 31        |
| 2.5.2. Analysis of Contributions to Spin-Spin Coupling .....   | 32        |
| 2.5.3. Calculation of Heteronuclear Coupling Constants .....   | 32        |
| 2.5.4. Dihedral Angle Dependence in Ethoxysilanes.....   | 33        |
| 2.5.5. Effect of Alkyl and Alkoxy groups.....  | 35        |
| 2.5.6. Effect of Degree of Hydrolysis.....   | 36        |
| 2.6. Conclusions.....  | 37        |
| 3. Determination of $^{29}\text{Si}$ - $^1\text{H}$ Spin-Spin Coupling Constants in Organoalkoxysilanes with Nontrivial Scalar Coupling Patterns ..... | 48        |
| 3.1. Summary.....  | 48        |
| 3.2. Introduction.....   | 48        |
| 3.3. Materials and Methods .....   | 51        |
| 3.3.1. Experimental Details .....  | 51        |
| 3.3.2. Materials .....   | 51        |
| 3.3.3. Computational Details.....  | 51        |
| 3.4. Results and Discussion.....   | 52        |
| 3.4.1. Silicon Coupling to Alkoxy Group Protons.....   | 52        |
| 3.4.2. Silicon Coupling to Bridging Group Protons.....   | 52        |
| 3.4.3. Resolving Non-trivial Coupling Patterns.....  | 53        |
| 3.4.4. Ruling out Incomplete Decoupling to Alkoxy Protons .....  | 53        |
| 3.4.5. Ruling Out Hindered Rotation.....   | 54        |
| 3.4.6. Simulation of the Non-trivial Coupling Pattern.....   | 54        |
| 3.4.7. DFT Method Validation .....   | 55        |
| 3.4.8. DFT Estimation of Coupling Constants.....   | 56        |
| 3.4.9. Calculating Non-trivial Spectra from DFT Estimates .....  | 57        |
| 3.4.10. $J(\text{Si-H})$ Trends.....   | 59        |
| 3.5. Conclusions.....  | 60        |
| <b>II Investigation of Kinetic, Structure and Phase Evolution of Bridged Alkoxysilane Polymerization.....</b>  | <b>72</b> |
| 4. Reaction-Induced Phase Separation of Bis(triethoxysilyl)ethane upon Sol-gel Polymerization in Acidic Conditions.....                                | 73        |

|   |     |
|---|-----|
| 4.1. Summary.....   | 73  |
| 4.2. Introduction.....  | 73  |
| 4.3. Experimental.....  | 76  |
| 4.3.1. Materials .....  | 76  |
| 4.3.2. Phase Behavior Characterization .....  | 76  |
| 4.3.3. Gel Time Characterization.....   | 77  |
| 4.3.4. NMR Characterization .....   | 77  |
| 4.3.5. FTIR Characterization .....  | 78  |
| 4.4. Results and Discussion.....  | 78  |
| 4.4.1. Phase Behavior in Acidic Ethanol-Water Solutions.....  | 78  |
| 4.4.2. Characterization under NMR-Favorable Conditions .....  | 80  |
| 4.4.3. Characterization under Signal Loss Conditions .....  | 81  |
| 4.4.3.1. Characterization using FTIR .....  | 81  |
| 4.4.3.2. DEPT <sup>29</sup> Si NMR vs. Single Pulse <sup>29</sup> Si NMR .....                              | 82  |
| 4.4.3.3. <sup>29</sup> Si NMR vs <sup>1</sup> H NMR.....  | 82  |
| 4.4.3.4. Effect of Water Content on Signal Loss .....   | 84  |
| 4.4.3.5. Effect of pH on Signal Loss.....   | 84  |
| 4.4.4. Correlation between Signal Loss and T <sub>2</sub> .....   | 85  |
| 4.4.5. Explanation by Microphase Separation .....   | 86  |
| 4.5. Conclusions.....   | 88  |
| 5. Kinetic Modeling of Sol gel Polymerization of Bis(triethoxysilyl)methane using DEPT <sup>29</sup> Si NMR |     |
| .....   | 98  |
| 5.1. Summary.....   | 98  |
| 5.2. Introduction.....  | 98  |
| 5.3. Application of DEPT for BTESM Polymerization .....   | 100 |
| 5.4. Kinetic Model.....   | 101 |
| 5.5. Experimental Section.....  | 104 |
| 5.5.1. Source of Materials .....  | 104 |
| 5.5.2. Sample Preparation.....  | 104 |
| 5.5.3. NMR Experiments .....  | 104 |
| 5.6. Computational Details .....  | 104 |
| 5.6.1. Solution Procedure.....  | 104 |
| 5.6.2. Density Functional Theory Calculations .....   | 105 |
| 5.7. Results and Discussion.....  | 105 |

|  |            |
|--|------------|
| 5.7.1. Optimal Sensitivity .....   | 105        |
| 5.7.2. Experimental Verification of DEPT Theoretical Intensities .....   | 106        |
| 5.7.3. Peak Assignments.....   | 106        |
| 5.7.4. Chemical Shift Trends .....   | 108        |
| 5.7.5. Reaction Pathways .....   | 108        |
| 5.7.6. Hydrolysis Pseudo-equilibrium .....   | 109        |
| 5.7.7. Condensation Kinetics.....  | 109        |
| 5.8. Conclusions.....  | 110        |
| <b>6. Dynamic Monte Carlo Investigation of the Effects of Organic Bridges on the Gelation Behavior of Alkoxysilanes.....</b> | <b>120</b> |
| 6.1. Summary.....  | 120        |
| 6.2. Introduction.....   | 120        |
| 6.3. Modeling Approach .....   | 123        |
| 6.3.1. Kinetic Model .....   | 123        |
| 6.3.2. Dynamic Monte Carlo Algorithm .....   | 124        |
| 6.3.3. Accounting for Organic Components .....   | 124        |
| 6.3.4. Accounting for Cyclization Phenomena .....  | 125        |
| 6.3.5. Accounting for First Shell Substitution Effects .....   | 126        |
| 6.3.6. Reaction Rates.....   | 127        |
| 6.3.7. Model Parameters.....   | 127        |
| 6.4. Results and Discussion.....   | 128        |
| 6.4.1. Model Validation.....   | 128        |
| 6.4.2. Effect of Cyclization.....  | 129        |
| 6.4.3. Molecular Growth vs Cyclization.....  | 130        |
| 6.4.4. Implications of Unlimited Cyclization.....  | 131        |
| 6.4.5. Role of Carbosiloxane Rings .....   | 131        |
| 6.5. Conclusions.....  | 131        |
| <b>III Application of Siloxane Based Materials in Adsorption Technologies .....</b>  | <b>141</b> |
| <b>7. Loading and Protection of Antioxidant Enzyme on Engineered Silica .....</b>  | <b>142</b> |
| 7.1. Summary.....  | 142        |
| 7.2. Introduction.....   | 142        |
| 7.3. Experimental Details.....   | 144        |
| 7.3.1. Source of Materials .....   | 144        |

|   |     |
|---|-----|
| 7.3.2. Nanoparticle Synthesis.....  | 144 |
| 7.3.3. Nanoparticle Characterization .....  | 145 |
| 7.3.4. Enzyme Loading and Analysis.....   | 145 |
| 7.3.5. Statistical Analysis .....   | 146 |
| 7.4. Results and Discussion.....  | 146 |
| 7.4.1. Nanoparticle Design Attributes.....  | 146 |
| 7.4.2. Nanoparticle Properties .....  | 147 |
| 7.4.3. Loading Analysis .....   | 148 |
| 7.4.4. Activity Analysis.....   | 148 |
| 7.4.5. Protection from Pronase .....  | 149 |
| 7.4.6. Stability of Catalase .....  | 150 |
| 7.5. Conclusions.....   | 150 |
| 8. DFT Investigation of NH <sub>3</sub> Physisorption on CuSO <sub>4</sub> Impregnated SiO <sub>2</sub> ..... | 163 |
| 8.1. Summary.....   | 163 |
| 8.2. Introduction.....  | 163 |
| 8.3. Modeling Approach .....  | 165 |
| 8.4. Computational Details.....   | 166 |
| 8.5. Results .....  | 167 |
| 8.5.1. SiO <sub>2</sub> /CuSO <sub>4</sub> Model .....  | 167 |
| 8.5.2. Hydration Models.....  | 167 |
| 8.5.2.1. SiO <sub>2</sub> .....   | 167 |
| 8.5.2.2. CuSO <sub>4</sub> .....  | 168 |
| 8.5.2.3. SiO <sub>2</sub> /CuSO <sub>4</sub> .....  | 168 |
| 8.5.3. Physisorption on Dry Adsorbents.....   | 169 |
| 8.5.4. Physisorption on Hydrated Adsorbents .....   | 169 |
| 8.5.4.1. SiO <sub>2</sub> .....   | 170 |
| 8.5.4.2. CuSO <sub>4</sub> .....  | 170 |
| 8.5.4.3. SiO <sub>2</sub> /CuSO <sub>4</sub> .....  | 170 |
| 8.5.5. Physisorption Mechanism and Stability Analysis .....   | 171 |
| 8.6. Discussion .....   | 171 |
| 8.6.1. Role of CuSO <sub>4</sub> Impregnation.....  | 171 |
| 8.6.2. CuSO <sub>4</sub> Dispersion in SiO <sub>2</sub> Matrix.....   | 172 |
| 8.6.3. Modeling Hydration .....   | 173 |
| 8.6.4. Cu <sup>2+</sup> Coordination.....   | 174 |



|  |            |
|--|------------|
| 8.6.5. Effects of Hydration.....                                 | 175        |
| 8.6.6. Adsorption Mechanism .....                                | 176        |
| 8.6.7. Comparison with Literature Reports.....                   | 177        |
| 8.7. Conclusions.....  | 177        |
| <b>IV Closing Notes .....</b>                                    | <b>190</b> |
| 9. Dissertation Outcomes, Implications and Future Prospects..... | 191        |
| 9.1. Research Challenges and Outcomes.....                       | 191        |
| 9.1.1. Kinetic Investigation .....                               | 191        |
| 9.1.1.1. Phase Separation .....                                  | 191        |
| 9.1.1.2. Characterization and Modeling .....                     | 191        |
| 9.1.1.3. Kinetic Trends .....                                    | 192        |
| 9.1.1.4. NMR Coupling Constants .....                            | 193        |
| 9.1.2. End-use Investigation.....                                | 194        |
| 9.1.2.1. Biomaterial Application .....                           | 194        |
| 9.1.2.2. Adsorption Application .....                            | 194        |
| 9.2. Implications .....  | 194        |
| 9.2.1. Fundamental Research.....                                 | 195        |
| 9.2.2. Applied Research.....                                     | 195        |
| 9.3. Prospective Future Research.....                            | 196        |
| 9.3.1. NMR Characterization .....                                | 196        |
| 9.3.2. Kinetic Modeling .....                                    | 196        |
| 9.3.3. Structural Modeling .....                                 | 196        |
| 9.3.4. Therapeutic Applications .....                            | 196        |
| 9.3.5. Siliceous Adsorbents .....                                | 197        |
| 10. References .....   | 198        |
| Vita.....  | 210        |

## LIST OF TABLES

|   |     |
|---|-----|
| <b>Table 2.1.</b> Comparison with experimental values of $^{29}\text{Si}$ - $^1\text{H}$ coupling constants (in Hz) and chemical shifts relative to tetramethylsilane (in ppm) of methyltriethoxysilane calculated at the B3LYP level employing various basis sets. ....    | 39  |
| <b>Table 2.2.</b> Percent deviations from experiment for $J(\text{Si-H})$ calculated using various basis sets in methoxysilanes. ....   | 40  |
| <b>Table 2.3.</b> Individual contributions (in Hz) to $^2J(\text{Si-H})$ and $^3J(\text{Si-H})$ spin-spin coupling constants in methyltriethoxysilane. ....   | 41  |
| <b>Table 2.4.</b> Comparison with experiment of $^{29}\text{Si}$ - $^1\text{H}$ spin-spin coupling constants calculated at the B3LYP/6-31G level. ....  | 42  |
| <b>Table 2.5.</b> Effect of hydrolysis of alkoxysilanes on calculated $^{29}\text{Si}$ - $^1\text{H}$ coupling constants. ....  | 43  |
| <b>Table 3.1.</b> $^{29}\text{Si}$ - $^1\text{H}$ coupling constants of various bridged silanes. ....   | 62  |
| <b>Table 3.2.</b> Thermal averages of homo- and heteronuclear coupling constants calculated at the B3LYP/6-31G level of theory in the bridging group of fully hydrolyzed BTMSE using BTMSE AM1 energy estimates. Please refer to the adjoining structure for notation. .... | 63  |
| <b>Table 3.3.</b> Comparison of measured $^{29}\text{Si}$ - $^1\text{H}$ coupling constants with computations at B3LYP/6-31G level of theory in vinyl group of vinyltrimethoxysilane. Please refer to the adjoining structure for notation. ....                            | 64  |
| <b>Table 5.1.</b> $^{29}\text{Si}$ NMR chemical shifts and peak assignments of species formed during early time sol-gel polymerization of BTESM. ....   | 111 |
| <b>Table 5.2.</b> Average SiCSi and SiOSi bond angles and chemical shifts calculated at B3LYP/6-311+G(2d,p) level of theory for the optimized structures in Figure 5.5. ....  | 112 |
| <b>Table 7.1.</b> Structural properties of the particles used for enzyme studies. ....  | 152 |
| <b>Table 8.1.</b> Total energies of optimized $\text{SiO}_2/\text{CuSO}_4$ complexes with variable final position of the $\text{Cu}^{2+}$ and $\text{SO}_4^{2-}$ ions. See Figure 8.2 for the corresponding geometries. ....  | 179 |

**Table 8.2.** NH<sub>3</sub> adsorption energies ( $\Delta E_{\text{ads}}$ , kJ/mol) for different adsorbents at varying degrees of hydration. Except when marked with a superscript, all adsorption energies are for NH<sub>3</sub> directly interacting with the active adsorption site..... 180

**Table 8.3.** Wiberg Bond Indices of O-H and H-N in adsorbents and NH<sub>3</sub> adsorbed complexes. O-H represents the bond between oxygen and hydrogen in the silanol and H-N represents the bond between hydrogen of silanol and the nitrogen of NH<sub>3</sub>..... 181

## LIST OF FIGURES

|  |    |
|--|----|
| <b>Figure 1.1.</b> Classification of organoalkoxysilanes. ....   | 17 |
| <b>Figure 1.2.</b> Synthesis of silica via surfactant templating. ....   | 18 |
| <b>Figure 1.3.</b> Significance of kinetic studies of sol-gel polymerization. ....   | 19 |
| <b>Figure 1.4.</b> Limitations of experiments and mechanistic models in kinetic investigation.....   | 20 |
| <b>Figure 1.5.</b> DEPT $^{29}\text{Si}$ NMR pulse sequence.....   | 21 |
| <b>Figure 1.6.</b> Pulse scheme for $^1\text{H}$ single frequency decoupling of $^{29}\text{Si}$ NMR. ....   | 22 |
| <b>Figure 1.7.</b> Dissertation research pathway.....  | 23 |
| <b>Figure 2.1.</b> Optimized geometries of the unhydrolyzed form of the molecules studied here: (a) tetramethoxysilane, (b) methyltrimethoxysilane, (c) dimethyldimethoxysilane, (d) trimethylmethoxysilane, (e) trimethoxysilane, (f) vinyltrimethoxysilane, (g) phenyltrimethoxysilane, (h) tetraethoxysilane, (i) methyltriethoxysilane, (j) dimethyldiethoxysilane, (k) trimethylethoxysilane, (l) tetramethylsilane, and (m) hexamethyldisiloxane. .... | 44 |
| <b>Figure 2.2.</b> Correlation between calculated and experimental magnitudes of $^2J(\text{Si-H})$ and $^3J(\text{Si-H})$ coupling constants. Coupling constants of ethoxy (OEt) and methoxy (OMe) protons are plotted separately.....  | 45 |
| <b>Figure 2.3.</b> Variation of $^3J(\text{Si-H})$ in ethoxysilanes with dihedral angle between silicon and the proton in the ethoxy group along the O-C bond. Points are values calculated by DFT; the solid curve is the best-fit Karplus relationship for $\text{Me}_3\text{SiOEt}$ and the dashed line is the variation of relative energy with dihedral angle in $\text{Me}_3\text{SiOEt}$ . ....   | 46 |
| <b>Figure 2.4.</b> Variation of magnitude of hetero-nuclear coupling constants with degree of hydrolysis of organoalkoxysilanes: (a) $^2J(\text{Si-H})$ and (b) $^3J(\text{Si-H})$ . ....  | 47 |
| <b>Figure 3.1.</b> Optimized 3D geometries of bis(triethoxysilyl)ethane (BTESE), bis(trimethoxysilyl)ethane (BTMSE), bis(trichlorosilyl)ethane (BTCSE), bis(triethoxysilyl)ethene (BTES=E), bis(triethoxysilyl)methane (BTESM) and bis(trihydroxysilyl)methane (BTHSM) .....   | 65 |

**Figure 3.2.** Selectively decoupled experimental  $^{29}\text{Si}$  NMR spectra displaying silicon coupling to protons in various bridged silanes. Spectra (a), (c) and (g) are the result of selectively decoupling alkoxy groups in (a) BTESE (c) BTMSE and (g) BTESM. Spectrum (b) is the result of selectively decoupling the bridging group protons in BTMSE. (e) and (f) are spectra obtained from selectively decoupling BTES=E bridging groups and ethoxy group respectively. The inset in spectrum (e) is the expanded form of coupling pattern in trans-form of BTES=E. Spectrum (d) is the coupled spectrum of BTCSE..... 66

**Figure 3.3.** (a) Experimental  $^1\text{H}$  NMR spectrum of BTMSE referenced to tetramethylsilane. (b) Expanded form of the singlet in the experimental  $^1\text{H}$  NMR spectrum shown in (a); (c)  $^1\text{H}$  NMR spectrum of the singlet simulated using iterated  $J(\text{H-H})$  reported in Table 3.2 and experimental values of  $^1J(\text{C-H})=120$  Hz and  $^2J(\text{C-H})=-4.2$  Hz; (d)  $^1\text{H}$  NMR spectrum of the singlet simulated using iterated  $J(\text{H-H})$  and  $J(\text{Si-H})$  reported in Table 3.2..... 67

**Figure 3.4.** Variation of  $^3J(\text{Si-H})$  and  $^3J(\text{H-H})$  in the bridging group of bis(trihydroxysilalyethane) with the corresponding Si-C-C-H and H-C-C-H dihedral angles, respectively. Points represent the values obtained from DFT calculations and curves represent the Karplus fits. Karplus constants for these fits are provided in the text..... 68

**Figure 3.5.** Variation of splitting in the quintet [=average of ( $^2J(\text{Si-H})$  and  $^3J(\text{Si-H})$ )] of BTMSE spectrum with Si-C-C-Si dihedral angle in the bridging group plotted on primary axis. Relative energies of BTMSE and BTESE obtained from DFT and semi-empirical AM1 methods are compared on the secondary axis..... 69

**Figure 3.6.** Simulated  $^{29}\text{Si}$  NMR spectra of the ethylene bridge in BTMSE (a-c) compared with experimental spectrum (d). Coupling constants for the theoretically derived spectra (a and b) are obtained from B3LYP/6-31G, and energies for calculating thermal averages from either B3LYP/6-31G\* (a) or the semi-empirical AM1 method (b). Spectrum (c) is obtained by using regression to better fit the simulated spectrum (b) to the experimental spectrum (d). ..... 70

**Figure 3.7.** Deviation from experimental values of chemical shifts and normalized intensities of the spectrum calculated using BTMSE DFT or AM1 energies and homo- and heteronuclear coupling constants obtained by DFT from fully hydrolyzed version of BTMSE. The “Best Fit-AM1” values are the difference between experiment and the best-fit spectrum found by regression using the AM1 coupling constants as initial guesses..... 71

**Figure 4.1.** Ternary pseudo-phase diagram of BTESE, ethanol and water (pH=3) mixtures. The axes are mole fractions of the labeled components. The line  $\ell$  represents the compositions used for developing the gelation power law (Figure 4.2). The regions correspond to (A) 2-phase systems that formed a cloudy gel, (B) 2-phase systems that formed a clear gel, (C) 2-phase systems that formed precipitates, (D) 1-phase systems that remained clear but lost NMR signal at some rate, and (E) 1-phase systems that were clear and preserved NMR signal intensity. .... 90

**Figure 4.2.** Variation of gel time ( $t_g$ ) as a function of initial concentration of BTESE for solutions (pH=2) prepared with a H<sub>2</sub>O: BTESE ratio of 12. Points are measured gel time values and the curve is a power law fit giving the equation shown on the plot. .... 91

**Figure 4.3.** DEPT <sup>29</sup>Si NMR spectra of sample **a** (pH=1) processed with line broadening parameter lb=1. From bottom to top, the spectra were collected 0.1, 0.8, 3.6, 8, and 15.3 h after mixing all ingredients together. The total integrated intensity of the NMR signal was preserved over the course of observation. Peak assignments marked with an \* have been adapted from reference.<sup>91</sup> ..... 92

**Figure 4.4.** Single-pulse <sup>29</sup>Si NMR spectra collected for (a) sample **b** (pH=2.1) after 20 min. of reaction with lb=5 and averaging of 64 scans over a spectral width of 3000 Hz; (b) sample **b** (pH=2.1) after 2 months of reaction with a spectral width of 50000 Hz, an average of 64 scans and lb=10; (c) sample **a** (pH=2.2) after (i) 1.5 min, (ii) 2.7 h and (iii) 2 months of reaction. Spectra in (c) are averages of 16 scans over a spectral width of 5000 Hz and lb=5 is applied. The insets are the FIDs of the spectra adjacent to them or as indicated by arrows. .... 93

**Figure 4.5.** (a) FTIR spectra of sample **b** (pH=2.1) collected for a period of 1 hour. The arrows indicate the direction of evolution (increase or decrease) of the corresponding species with time. The legend indicates the time at which each spectrum was collected. .... 94

**Figure 4.6.** (a) DEPT <sup>29</sup>Si NMR (lb=5) spectra of (i) 1.4 M BTESE in ethanol, and sample **c** (pH=2.4) collected after (ii) 6 min., (iii) 19 min. and (iv) 36 min. of reaction. (b) Single-pulse <sup>29</sup>Si NMR (lb=10) spectra of (i) 1.4 M BTESE in ethanol, and sample **c** (pH=2.4) collected after (ii) 6 min., (iii) 4 h and (iv) 10 h of reaction and (c) <sup>1</sup>H NMR spectra of (i) 1.4 M BTESE in ethanol, and sample **c** (pH=2.4) collected after (ii) 6 min., (iii) 4 h and (iv) 10 h of reaction. .... 95

**Figure 4.7.** Normalized total integrated NMR intensities measured with time for sample **a** (pH=2.2) using single-pulse <sup>29</sup>Si NMR of the spectra ( $\Delta$ ) shown in Figure 4.4c, for sample **c**

(pH=2.4) using single-pulse  $^{29}\text{Si}$  NMR in spectra (x) shown in Figure 4.6b and  $^1\text{H}$  NMR spectra (o) shown in Figure 4.6c. The plotted intensities are the total integrated intensities of all the peaks in each spectrum except the  $^1\text{H}$  NMR intensities which are the total integrated intensities of the bridging group protons peak at  $\sim 0.5$  ppm (labeled in Figure 4.6c). ..... 96

**Figure 4.8.** Single-pulse  $^{29}\text{Si}$  NMR spectra collected for sample **d** prepared using water with (a) pH=3.6 (lb=5) and (b) pH=1.3 (lb=10). Both the samples were probed over a spectral width of 5000 Hz and pw=11.8  $\mu\text{s}$ . First spectrum (close to the chemical shift axis) in Figure (a) was collected after 14 minutes of reaction, second spectrum 45 minutes after the first, and the rest at intervals of 100 minutes. Spectra in Figure (b) were collected at regular intervals of 30 minutes after 1.5 minutes of reaction from bottom to top. .... 97

**Figure 5.1.** Structures of (a) BTESM (b) Linear dimer and (c) cyclic dimer. .... 113

**Figure 5.2.** Polarization transfer efficiency as a function of pulse angle for varying m at transfer time,  $\Delta = 45$  ms. m is the total number of protons in the ethoxy groups attached to a silicon site. .... 114

**Figure 5.3.** Comparison of theoretical and experimental intensities of unhydrolyzed BTESM for varying pulse angle at transfer time,  $\Delta = 45$  ms. .... 115

**Figure 5.4.** (a) DEPT  $^{29}\text{Si}$  NMR spectra of BTESM polymerization sample collected with  $\Delta = 45$  ms &  $\theta = 40^\circ$  after 2 minutes of reaction every 20 minutes and (b) an expanded view of part of the first spectrum of the series spectra in (a) to indicate low intensities peaks. .... 116

**Figure 5.5.** 3D-Optimized geometric structures of (a) BTESM (b) linear dimer (c) cyclic dimer. 117

**Figure 5.6.** Fraction of ( $\diamond$ )  $T_{O^0}$ , ( $\triangle$ )  $T_{O^1}$  and ( $\ominus$ )  $T_{O^2}$  sites derived from experimental data (dots) compared with those calculated using equations, 5.9-5.12 (lines). .... 118

**Figure 5.7.** Experimental (dots) concentration profiles of (o) unhydrolyzed monomer, ( $\diamond$ ) singly hydrolyzed monomer, ( $\bullet$ ) unhydrolyzed linear dimer and ( $\Delta$ ) unhydrolyzed cyclic dimer compared with model predictions (lines) (a)  $W = 0.09$  and (b)  $W = 0.1$ . .... 119

**Figure 6.1.** General structure of (a) Bridged silanes (b) Non-bridged silanes. Notation:  $R_o$  – organic group; OR – alkoxy group. .... 133

**Figure 6.2.** Formation of a four-member ring from a three bond block. Circles are silicon sites and lines represent the siloxane bonds or bridges wherever applicable. .... 134

|   |     |
|---|-----|
| <b>Figure 6.3.</b> Bridged and non-bridged random branching theoretical profiles compared with simulations of ideal polycondensation until gelation (a) site distributions (b) degree of polymerization.....  | 135 |
| <b>Figure 6.4.</b> Site distributions of bridged case compared with non-bridged for non-ideal polycondensation (a) $K=0.5$ (b) $K=10$ .....   | 136 |
| <b>Figure 6.5.</b> Variation of Degree of Polymerization with gel conversion for various cyclization tendencies for (a) Non-bridged (b) Bridged.....  | 137 |
| <b>Figure 6.6.</b> Variation of (a) gel conversion and (b) gel time with cyclization rate in non-bridged and bridged silanes.....   | 138 |
| <b>Figure 6.7.</b> Variation of Ring Involvement with gel conversion for (a) Non-bridged (b) Bridged.....   | 139 |
| <b>Figure 6.8.</b> Variation of (a) gel conversion and (b) gel time with cyclization rate short and long bridged silanes.....   | 140 |
| <b>Figure 7.1.</b> Mechanism of generation and elimination of free radicals through the action of anti-oxidant enzymes.....   | 153 |
| <b>Figure 7.2.</b> Idealized representations of mesoporous silica types: (a) nonporous silica (NPSP) (b) silica particles with radially oriented pores (SP-R) (c) hollow spherical silica particles with pores oriented parallel to the hollow core (HSSP-P) (d) hollow spherical silica particles with expanded, interconnected bimodal pores (HSSP-I).....  | 154 |
| <b>Figure 7.3.</b> SEM micrographs of (a) NPSP (b) SP-R (c) HSSP-P (d) HSSP-I1 and (e) HSSP-I2 particles, and (f) particle size distribution of SP-R derived from SEM.....  | 155 |
| <b>Figure 7.4.</b> Nitrogen adsorption-desorption isotherms of (a) NPSP, SP-R, and HSSP-P; and (b) HSSP-I1 and HSSP-I2.....   | 156 |
| <b>Figure 7.5.</b> BJH adsorption pore size distributions calculated using the adsorption branch of the nitrogen adsorption isotherm of the silica particles.....   | 157 |
| <b>Figure 7.6.</b> Amount of catalase loaded per mg silica nano particles obtained from $I^{125}$ labeled catalase studies before and after 1 h of proteolysis. One way ANOVA showed that all the silica types before proteolysis are significantly different from each other with $p < 0.05$ . All pairs except those indicated by ● are statistically significant within 95% confidence interval..... | 158 |



|  |     |
|--|-----|
| <b>Figure 7.7.</b> Activity of catalase loaded per mg silica nano particles obtained from H <sub>2</sub> O <sub>2</sub> degradation studies before and after 1 h of proteolysis. One way ANOVA showed that all the silica types before proteolysis are significantly different from each other with p<0.05. All pairs except those indicated by ● are statistically significant within 95% confidence interval. ....   | 159 |
| <b>Figure 7.8.</b> Activity per mg of catalase before and after 1 h of proteolysis. ....   | 160 |
| <b>Figure 7.9.</b> Percentage protection after 1 h of proteolysis measured by (a) mass loading and (b) H <sub>2</sub> O <sub>2</sub> elimination activity. One way ANOVA showed that all the silica types are significantly different from each other with p<0.05. All pairs except those indicated by ● are statistically significant within 95% confidence interval. ....  | 161 |
| <b>Figure 7.10.</b> Activity of catalase with time. One way ANOVA showed that all the silica types are significantly different from each other with p<0.05. HSSP-I2, HSSP-P; Free Catalase, NPSP and HSSP-I2, HSSP-P pairs are statistically insignificant within 95% confidence interval at time=24h. ....  | 162 |
| <b>Figure 8.1.</b> 3D optimized structures of the dehydrated adsorbents (1) SiO <sub>2</sub> , (2) CuSO <sub>4</sub> (5) SiO <sub>2</sub> /CuSO <sub>4</sub> , (8) SiO <sub>2</sub> /SO <sub>4</sub> <sup>2-</sup> and NH <sub>3</sub> adsorbed on (3) SiO <sub>2</sub> , (4) CuSO <sub>4</sub> (6/7) SiO <sub>2</sub> /CuSO <sub>4</sub> and (9) SiO <sub>2</sub> /SO <sub>4</sub> <sup>2-</sup> . The numbers indicate charges on the ammonia molecule. .... | 182 |
| <b>Figure 8.2.</b> 3D Optimized geometries of various configurations of SiO <sub>2</sub> /CuSO <sub>4</sub> . ....   | 183 |
| <b>Figure 8.3.</b> 3D optimized structures of SiO <sub>2</sub> ·xH <sub>2</sub> O (x= 1 or 2) and the corresponding complexes after NH <sub>3</sub> adsorption by displacement of one H <sub>2</sub> O. The numbers indicate the charge on the adjacent ammonia molecule. ....   | 184 |
| <b>Figure 8.4.</b> 3D optimized structures of CuSO <sub>4</sub> ·xH <sub>2</sub> O (x=1,2,3) and the corresponding complexes after NH <sub>3</sub> adsorption. Symmetry constraints were imposed to obtain structures <b>18</b> and <b>20</b> . The numbers indicate the charge on the adjacent ammonia molecule. ....   | 185 |
| <b>Figure 8.5.</b> Structures demonstrating the influence of hydrogen bonding in hydrated CuSO <sub>4</sub> . ( <b>22</b> ) CuSO <sub>4</sub> ·3H <sub>2</sub> O ( <b>23</b> ) CuSO <sub>4</sub> ·4NH <sub>3</sub> and ( <b>24</b> ) CuSO <sub>4</sub> ·5H <sub>2</sub> O. ....  | 186 |
| <b>Figure 8.6.</b> 3D optimized structures of SiO <sub>2</sub> /CuSO <sub>4</sub> ·H <sub>2</sub> O and the corresponding complexes after NH <sub>3</sub> adsorption. Numbers indicate charges on the adjacent ammonia molecules. ....   | 187 |
| <b>Figure 8.7.</b> 3D optimized structures of SiO <sub>2</sub> /CuSO <sub>4</sub> ·2H <sub>2</sub> O and the corresponding complexes after NH <sub>3</sub> adsorption. Numbers indicate charges on the adjacent ammonia molecules. ....  | 188 |

**Figure 8.8.** 3D optimized structures of  $\text{SiO}_2/\text{CuSO}_4 \cdot 3\text{H}_2\text{O}$  and the corresponding complexes after  $\text{NH}_3$  adsorption. Numbers indicate charges on the adjacent ammonia molecules..... 189

## **1. Introduction and Background**

### **1.1. Sol-gel Materials and Chemistry**

Sol-gel processing<sup>1,2</sup> of inorganic ceramic and glass materials has been an active area of research over the past century. It involves polymerization of metal or non-metal alkoxides resulting in the transformation of a monomer solution to colloidal (sol or gel) and eventually three dimensional solid network. The potential high purity, homogeneity and lower processing temperatures involved in sol-gel processing in comparison with traditional hydrothermal and melt processing methods form the basis behind the interest in sol-gel materials. These materials can be synthesized with various morphologies<sup>3</sup> including thin films, monoliths, fibers, particles and gels. Early investigations in this field began with the observation of the hydrolysis and condensation of tetraethylorthosilicate.<sup>4</sup> With the developments made over time, many new and improved materials offering a wide range of unique and useful properties are continually being synthesized using the sol-gel method. Being able to control the conditions of polymerization of the silica precursors to produce well-ordered porous structures and to introduce organic components into these materials has expanded the span of their applications limitlessly. In the present day, these porous materials are easily designed and engineered to form products with application-specific properties. Either directly or indirectly, silica based materials have potential uses in almost every field known to mankind. Researchers have established a wide variety of their applications in the areas of separations,<sup>5</sup> environmental remediation,<sup>6-8</sup> controlled drug release,<sup>9,10</sup> bioactive materials,<sup>11-13</sup> chromatography,<sup>14,15</sup> catalysis,<sup>16,17</sup> photonics,<sup>18,19</sup> chemical and biological sensors,<sup>20,21</sup> corrosion resistance and mechanical protection,<sup>22</sup> and coating of metal surfaces.<sup>23</sup>

#### **1.1.1. Organic-Inorganic Hybrid Materials**

Owing to their potential applications, production of nano-structured materials that are hybrids of organic and inorganic components is of growing interest in the present day. The incorporation of organics into nano- or molecular-scale hybrids is enabled by the room temperature conditions of the sol-gel method. The organic group is distributed throughout the network and becomes an integral component of the framework. By varying the organic group, density of the framework can be varied as well as functional properties such as the chemical

nature of the surface, optical characteristics (clarity, nonlinear optical, etc.), electrical properties, and catalytic activity. Thus, the organic component imparts unique physical and mechanical characteristics to the network.

Organically modified silicon alkoxides are the usual precursors to these organic-inorganic hybrid materials. Classification of organoalkoxysilanes based on the location of the organic group is illustrated in Figure 1.1. Silanes with organic groups attached to the silicon sites are termed as non-bridged silanes. This could be either mono-, di- or tri-functional silanes. They are represented as  $(R_0)_n\text{Si}(\text{OR})_{4-n}$  ( $n = 1$  or  $2$ ) where  $R_0$  is an organic group. Among the various non-bridged silanes, tri-functional alkoxy silanes  $R_0\text{Si}(\text{OR})_3$  are the most common precursors used to introduce organic groups within an inorganic network. These silanes undergo concurrent hydrolysis and condensation reactions in the presence of water to form polymeric networks and gels with inbuilt organic-inorganic components. The hybrid materials thus formed can be engineered to possess a wide range of macroscopic properties when compared to the inorganic polymers. The fully-condensed products of tri-functional silane polymerization are called “silsesquioxanes”<sup>24</sup> and have the formula  $R_0\text{SiO}_{1.5}$ . Precursors are also available with bridging organic groups (an organic group sandwiched between two silicon sites) with formula  $(\text{RO})_3\text{Si}-R_0-\text{Si}(\text{OR})_3$  and are referred to as bridged silanes. The bridging organic group in these silanes can be directly incorporated into the network structure of an organic-inorganic hybrid, to provide more structural and functional possibilities than can be achieved simply by changing  $R_0$  groups. The hybrids formed by hydrolytic-polycondensation of these precursors are called “bridged silsesquioxanes.”<sup>25-28</sup>

### 1.1.2. Bridged vs. Non-bridged

Owing to the presence of the bridging group, bridged silane precursors differ from their non-bridged counterparts in the following ways. Most of these differences serve as advantages of bridged silanes over the non-bridged silanes.

1) *Structural Flexibility*: The presence of the bridging group imparts structural flexibility to the bridged silanes which leads to an added control over the properties of the materials formed from them. The organic component in the bridged silane may include alkylene, arylene, alkenylene and alkynylene groups. Bridges can also be functionalized to contain not only hydrocarbons but also metals and organometallic components. This kind of flexibility is more limited in non-bridged silane precursors.

2) *Pore Size Control*: The organic bridges in the bridged silsesquioxanes can be burnt out for structure refinement and porosity enhancement whereas removing the organic groups does not affect the framework in non-bridged silsesquioxanes.

3) *Pore Blockage*: The bridges are built into the polymeric network of a bridged silsesquioxane while organic groups from non-bridged silanes remain dangling in the polymeric network, thus potentially blocking the pores.

4) *Gelation Time*: When compared with tri- and tetra-functional silanes, bridged silanes produce gels at lower concentrations.<sup>28</sup> Bridged precursors have also been observed to gel relatively quickly. For example, a reported study has illustrated failure at achieving gel formation using a tri-functional non-bridged methyltriethoxysilane,<sup>29</sup> while the gelation times of bridged alkoxyalkyl alkanes were observed to be in the order of hours.<sup>28</sup> Because bridged silanes have more functional groups per monomer, gelation would be anticipated at a lower siloxane bond conversion than for a non-bridged precursor.

5) *Extensive Intra-molecular Cyclization in Silanes with Short Bridges*: While tetra and tri-functional silanes form six and eight atom siloxane rings leading to the formation of silsesquioxane cages, bridged silanes with short organic bridges are prone to intra-molecular cyclization in addition to siloxane rings. Cages formed from non-bridged silanes are known to delay or inhibit gelation. However, the role of intra-molecular cyclization leading to the formation of carbosiloxane rings in gelation of bridged silanes has not been clearly established before this study.

### 1.1.3. Sol-gel Polymerization

Sol-gel polymerization<sup>1</sup> involves hydrolysis and condensation reactions starting from a silicon monomer and water. To provide homogeneity, a co-solvent is added to water and alkoxide mixture. These reactions are usually acid or base catalyzed. In both cases, hydrolysis is followed by condensation leading to gelation or phase separation. The key steps involved in a silicon alkoxide polymerization are summarized below. Equations 1.1-1.3 show the functional group-level reactions that may occur at each alkoxy group attached to a silicon site, and Equation 1.4 shows the overall stoichiometry of the reactions.

Hydrolysis:



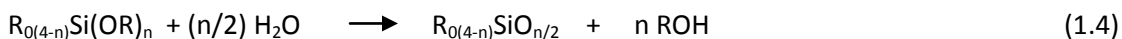
Water-producing condensation:



Alcohol-producing condensation:



Overall reaction for an n-functional non-bridged monomer:



In the hydrolysis reaction (eqn. 1.1), alkoxide group (OR) is replaced by a nucleophilic attack of oxygen present in water on a silicon site to form a silanol (Si-OH). The condensation of these silanol groups produces a siloxane bond (Si-O-Si) and water (eqn. 1.2) or alcohol (eqn. 1.3). In equations (1.1-1.3), the reaction of only one alkoxy ligand (-OR) is shown. However, the alkoxide precursors have more than one ligand and they undergo the sequence of reactions listed above to form linear, cyclic and branched polymers according to the overall reaction in equation 1.4. Three dimensional networks ultimately react to form particles or gels with a highly crosslinked structure. Cyclization leads to the formation of small rings consisting of several silicon sites (3 to 6 is most common) which can be significant structure components of alkoxy silane gels.<sup>30</sup>

These hydrolysis and condensation reactions are reversible but based on the reactants (type of alkoxide, H<sub>2</sub>O/Si ratio) and reaction conditions (pH, temperature), some of these reactions progress and some do not. However, a minimum amount of hydrolysis followed by some sort of condensation results in the formation of a siloxane-based oligomer. Under acidic conditions, hydrolysis is fast and reversible, and condensation is rate limiting. In basic conditions, hydrolysis is rate limiting and condensation is fast. pH not only has an effect on the reaction rates but it also affects the morphology of the final product formed either by altering solubility of precursors or by promoting aggregation and phase separation.

## 1.2. Material Synthesis and Engineering

### 1.2.1. Mesoporous Material Synthesis

The increasing importance of the applications<sup>31</sup> of porous solids with controlled pore sizes and shapes as catalysts, enzyme supports and adsorbents has encouraged the synthesis of a wide variety of such materials. Porous materials are classified as microporous (<2 nm), mesoporous (2-50 nm) and macroporous (>50 nm) based on their pore sizes. Zeolites are the

most widely used types of microporous materials and have excellent catalytic properties because of their uniform crystal structure and composition. However, their application is limited only to the treatment of small molecules because of their relatively small pore openings (<1.4 nm). Therefore, synthesis of materials which could mimic zeolites in their properties but with larger pores was the main concern leading to the development of ordered mesoporous ceramics.<sup>32-36</sup> MCM-41<sup>37,38</sup> marks the first report of the class of mesoporous materials that possess ordered structures and narrow pore size distributions. Ever since the discovery of MCM-41, many new silica and non-silica based mesoporous ordered materials have been synthesized.

The established route to the formation of mesoporous silica materials (Figure 1.2) is through the co-assembly of surfactants (structure directing agents) and silica precursors.<sup>31,37,38</sup> The surfactant molecules have a polar head group and a non-polar tail. In the presence of a solvent, these surfactant molecules self-assemble to form micelles having varied structures. Silica precursor is allowed to condense around these aggregates and then the surfactant is extracted out from this network resulting in a porous material. Well-ordered mesoporous silica have been prepared by electrostatic charge-matching pathways using cationic<sup>39,40</sup> and anionic<sup>41-43</sup> surfactants, and by hydrogen bonding interaction pathways using non-ionic<sup>44,45</sup> surfactants. Many reviews<sup>31,36,46</sup> have discussed advances in the synthesis procedures, mechanisms and characterization of these materials.

## **1.2.2. Kinetic Investigation**

### **1.2.2.1. Significance of Kinetic Studies**

To allow rational design of organic-inorganic hybrid materials synthesized from organoalkoxysilanes<sup>24-28</sup> and to control their organization, composition and properties, an understanding of the underlying chemistry and kinetics of their formation is very important. Kinetic investigation deals with identification of the species formed during the reaction and their rate of formation. Prior knowledge of the reaction kinetics of the precursors to these materials would give an idea about the distribution of components in the final product and the structure of the final product. The information obtained from early time kinetic studies can further be used as an input to statistical simulations (e.g. Monte Carlo simulations) to map the evolution of the polymeric system from monomers until gelation. Predicting the properties of these hybrid materials before their synthesis is advantageous because there is little scope for refining them

after they are made into solids (the final product). The insights obtained from kinetic investigations are very useful for process design and product development and in scale up.

Figure 1.3 presents a graphic illustration of the significance of the kinetic studies. “Learn while you build” is the traditional way to synthesize application specific materials, i.e., the properties of the materials are developed and tailored by repetitive synthesis and characterization which assumes a cyclic path, consuming time and effort. On the other hand, kinetic investigation follows a “build after you learn” scheme. Predicting the properties *a priori* avoids repetitive material synthesis and characterization, economizing time and cost of research by speeding up the process of tailoring the properties for applications at the same time.

While the kinetics of non-bridged silanes have been widely investigated,<sup>47-76</sup> there is very little information available about the kinetic behavior of bridged precursors.<sup>77-79</sup> Owing to the recent interest in the applications of bridged precursors in synthesizing surfactant-templated mesoporous hybrid materials, their kinetic investigation is important. The factors that affect the kinetic behavior of a bridged precursor are the organic and functional groups attached to the silicon site, the hydrocarbon spacer and its length, and the reaction conditions.

Kinetic Investigation of bridged precursor polymerization can answer several vital questions posed below.

1) The tri- and tetra-functional silanes display kinetics distinct from each other based on the organic and functional groups attached to the silicon site. To what extent do these aspects differentiate bridged silanes?

2) How do the kinetics of bridged precursors compare with the kinetics of their non-bridged versions? Comparing bridged silane with a tri-functional silane having same functional and organic groups will help in discovering the subtle advantages bridged precursors provide over their non-bridged but organically modified counterparts.

3) What is the role played by the hydrocarbon spacer of a bridged silane in the nature of the resulting gels or polymeric networks?

4) What is the reason behind quick gelation of bridged silanes despite extensive cyclization?

Figure 1.4 illustrates the range of different investigative tools available for kinetic studies. There are two approaches towards kinetic modeling of silane polymerization: mechanistic and stochastic modeling. The former uses experimental data to build kinetic models based on basic



silane chemistry coupled with reaction engineering fundamentals. It involves devising reaction pathways and intermediate products that provide best fits to the experimental observations. However, as the polymerization reactions progress, it becomes more and more cumbersome to predict the reaction pathways and model the kinetics using a mechanistic approach. To circumvent this, stochastic techniques like Monte Carlo and Molecular Dynamics simulations are generally used to predict the structural details of the polymerizing systems until gelation. These models require only a limited amount of detail to predict overall system behavior and capture correlations not explicitly represented in ordinary differential equations.

#### **1.2.2.2. Mechanistic Modeling**

Mechanistic models are based on experimental observations. In order to build these models, we need concentration profiles of the reactants and products formed during the time the polymerization reactions are monitored. The experimental tools that can be used to procure this data are described in the following section. After sorting out the reactions to be considered in the model, ordinary differential equations are written for each species or silicon site and this system of differential equations is iteratively solved to obtain best fit to the experimental measurements. Using the early time experimental kinetic data, rate constants of the reactions can be determined from kinetic models and then the models can be extrapolated for broader time scales to predict reaction parameters, products and pathways. A comprehensive model representing the sol-gel process must take into account the mathematical form of the reactions 1.1 through 1.4 (section 1.1.3). This would account for innumerable forward and reverse hydrolysis and water / alcohol producing condensation reactions depending upon the functionality of the precursor. Modeling this scenario is insurmountable unless some of these reactions are neglected by making judicious assumptions.

Reaction conditions under which experimental data are collected can help to eliminate some reactions with certainty. In acidic environments, since hydrolysis is fast and reversible, only condensation reaction rates need to be considered. Under basic conditions, phase separation due to fast condensation hinders collection of meaningful kinetic data. Hence, most of the existing kinetic models have been built for reactions in acidic environments.

Modeling silane polymerization reactions first commenced with functional group kinetics. Kay and Assink<sup>52,64</sup> were able to obtain overall rates of hydrolysis and condensation neglecting reversibility of these reactions and also the substitution effects caused due to changes in the

number of reactive groups on different silicon sites. Later experimental research in this field provided more details leading to comprehensive approaches. For systems with moderate to high water content ( $[H_2O]/[Si] > 4$ ), only water producing condensation is dominant.<sup>56,80</sup> Hydrolysis is reversible<sup>74,81</sup> and the reactivity of an OH group for condensation depends on its environment<sup>80,82</sup> indicating that at least first shell substitution effects must be accounted to describe true sol-gel kinetics. More recently, Sanchez et al.<sup>75</sup> developed a kinetic model that allows condensation substitution effects with degree of condensation accounting for hydrolysis reactions using average degree of hydrolysis. Rankin and McCormick<sup>70</sup> stated that hydrolysis pseudo-equilibrium must be considered in order to determine unique condensation rate coefficients. Using this assumption, they have built kinetic models describing first shell substitution effects and cyclization (in some cases) for non-bridged silane systems.<sup>69,83</sup> Since bridged silanes are prone to extensive cyclization, kinetic models must account for cyclization effects. The kinetic models in this dissertation focus on investigating cyclization effects besides testing the above mentioned assumptions for bridged silane polymerization.

### **1.2.2.3. Dynamic Monte Carlo Simulation**

Another tool that is used in the present research is dynamic Monte Carlo (DMC) simulation to investigate the structural evolution of bridged silane polymerization. DMC is based entirely on random selection of reactions based on probabilities and hence can be used to study the evolution of sol-gel polymers until gelation. Predicting gelation behavior of silica precursors using statistical models has witnessed an enormous improvement over years. Flory<sup>44</sup> developed and used random branching theory to confirm that gelation is the result of infinitely large three dimensional networks. Extending his work, Stockmayer<sup>45</sup> calculated the most probable distributions of molecular sizes at the gel point in branched chain polymers. They neglected cyclization phenomena in their studies. A two stage statistical model was developed by Ng et al.<sup>23</sup> to predict the siloxane bond conversion in tetraethoxysilane. They illustrated that cyclization was responsible for the high gel point of tetraethoxysilane. Rankin et al.<sup>46</sup> used the dynamic Monte Carlo approach to model the tetraethoxysilane polymerization which included all the features of alkoxy silane polymerization and their simulations matched the experimental gel point.

Dynamic Monte Carlo method was first developed by Gillespie et al.<sup>84</sup> and later proposed for network polymers by Dušek and coworkers.<sup>85,86</sup> In this method, simulation initiates from a finite

set of monomers and at every step, a condensation reaction occurs between two silicon sites to form a siloxane bond. In the process, the simulation stores the information about the nature of connectivity (involvement in cyclization, neighboring sites etc.) of each silicon site. Hence, it is possible to derive molecular structures and molecular weight distribution to which those sites belong. The only input that this approach needs is the rate coefficients for the reactions included in the model. The local rates of reaction can be defined and distinguished based on cyclization and substitution effects to allow modeling the competition between molecular growth and cyclization. This method is especially useful in modeling bridged silane systems to understand the role of cyclization in gelation. The DMC approach is limited by the finite size of the population that restricts the maximum simulated length scale and leads to erroneous results as the system approaches gelation. However, compared to molecular dynamic simulations (another common statistical thermodynamics based modeling tool), the DMC method is still advantageous because it allows simulations for longer simulation times and for larger ensembles. Computationally, the DMC method is less expensive to simulate sol gel polymerization as the conversion of the system is advanced at every step unlike the diffusion limitations that prolong the computational time in molecular dynamics simulations.

### **1.3. NMR Spectroscopy**

Nuclear Magnetic Resonance (NMR)<sup>87</sup> is one of the most powerful and complex analytical tools that facilitates observing nuclei in different chemical environments to derive structural information. An NMR spectrum can be recorded from isotopes of elements having non-zero nuclear spin. In this method, these nuclei immersed in a static magnetic field are exposed to a second oscillating magnetic field at their resonance frequency. Because of small differences in electronic shielding of the static magnetic field, nuclei in local bonding environments show peaks at different frequencies relative to a reference peak. The difference is referred to as the chemical shift, and is expressed in terms of the ppm difference from the frequency of the reference compound (usually tetramethylsilane). When nuclear relaxation is properly accounted for, the concentration of a particular nucleus in the sample being probed is proportional to the intensity of the peak representing it. Thus, NMR offers the advantage of quantitative analysis of samples. Some of the nuclei that are most frequently used in NMR are  $^1\text{H}$ ,  $^2\text{H}$ ,  $^{13}\text{C}$ ,  $^{19}\text{F}$ ,  $^{31}\text{P}$  and  $^{29}\text{Si}$ .

NMR can be carried out on reacting solutions, which allows in-situ kinetic studies. However, in order to derive meaningful kinetic information, it is important to ensure that the sample being observed by NMR is a liquid. More precisely, it is important that the molecules are mobile enough that dipolar interactions between spins and chemical shift anisotropy (due to directionality of bonding) are averaged out over the time scale of NMR data acquisition. If this is not the case, peaks are broadened tremendously, often enough that the signal is spread across the entire spectrum and it becomes impossible to distinguish signal from noise, or to gain chemical information from the spectrum. This care is specifically important while studying sol-gel reactions as phase separation (due to formation of gels or particles) is frequently encountered at certain compositions leading to peak broadening.

$^{29}\text{Si}$  NMR is employed extensively in this dissertation for studying silane systems and is more specialized than the other characterization techniques referred to. Hence, this technique is introduced in more detail here than in the individual chapters.

### 1.3.1. $^{29}\text{Si}$ NMR

$^{29}\text{Si}$  NMR is the technique that provides most specific information about silane polymerization. The  $^{29}\text{Si}$  nucleus is sensitive to the identity of groups directly attached to the silicon as well as to those attached to its nearest neighbors and sometimes beyond. Numerous chemical environments of a  $^{29}\text{Si}$  nucleus can be identified through the shifts in resonance peaks. Several studies have reported peak assignments associating various chemical shifts with species having different degrees of hydrolysis, condensation and cyclization compared with the monomer resonance peak.<sup>27</sup> However, there are two main drawbacks associated with carrying out  $^{29}\text{Si}$  NMR. First, low natural abundance (4.7%) of the NMR-active  $^{29}\text{Si}$  isotope limits the sensitivity of NMR measurements. This natural abundance is similar to that of  $^{13}\text{C}$ . The second problem (unique to  $^{29}\text{Si}$ ) is slow relaxation, which adds to the difficulties in recording quick good quality spectra. To obtain quantitative data, it is necessary to use a delay between pulses of at least  $3T_1$ , where  $T_1$  is the longest spin-lattice relaxation parameter for any observed nucleus in the sample. For widely used  $^1\text{H}$  NMR,  $T_1$  values are on the order of a few seconds, but for  $^{29}\text{Si}$ ,  $T_1$  is often several minutes which hinders deriving meaningful kinetic information on an NMR time scale. Decreasing  $T_1$  can be accomplished by adding a paramagnetic relaxation agent directly into the solution being studied. Chromium III 2,4-pentanedionate is often used for this purpose.<sup>75,88</sup> However, for kinetic studies, there is the risk that this additive can act as a

catalyst.<sup>89</sup> A preferable approach is to use polarization transfer techniques<sup>28</sup> like INEPT (Insensitive Nuclei Enhanced by Polarization Transfer) or DEPT (Distortionless Enhancement by Polarization Transfer). In these techniques, magnetization from protons is transferred to silicon nuclei, thus increasing the sensitivity up to 5 times (the value of  $\Gamma_{\text{H}} / \Gamma_{\text{Si}}$ , where  $\Gamma$  is the gyromagnetic ratio). Another improvement brought by these techniques is that the pulse repetition rate is dictated by the relaxation time of the attached protons rather than silicon. Recently, many research groups have employed these polarization transfer experiments to investigate various silanes.<sup>22,29</sup> DEPT displays a better tolerance towards experimental imperfections<sup>30</sup> in comparison to INEPT and hence is most frequently used.

### 1.3.2. DEPT <sup>29</sup>Si NMR

The DEPT pulse sequence<sup>87</sup> is illustrated in Figure 1.5. As is evident from this sequence, the proton excitation and magnetization evolve under the influence of the transfer time,  $\Delta$ . Because of the polarization transfer from protons to silicon nuclei, relaxation time and signal to noise ratio of the resulting spectrum now depend upon the highly sensitive and quickly relaxing protons rather than the silicon nuclei present in the system. The DEPT technique also has the potential for spectral editing based on the number of different types of <sup>1</sup>H nuclei coupled to a given <sup>29</sup>Si nucleus, leading to the structure determination and polymerization species identification. Thus, it is possible to extract all the information related to the polymerization kinetics, just by collecting <sup>29</sup>Si DEPT NMR spectra of reacting precursors without the use of any other instrumentation.

As literature reveals, this advantage has not been used to its full extent to explore bridged precursors. First, this is due to the high functionality of these monomers that gives rise to difficulties in the identification of the large number of peaks appearing in the <sup>29</sup>Si NMR spectra. However, this task can be made easy by carrying out the polymerization reactions under controlled conditions which lead to slower reaction rates allowing the unambiguous assignment of the peaks.

Second impediment to applying DEPT to bridged silanes is the determination of long range <sup>29</sup>Si-<sup>1</sup>H scalar spin-spin coupling constants that are required by DEPT pulse sequence in spectrum collection as well as in spectral editing. The transfer time  $\Delta$  is strongly dependent on the heteronuclear spin-spin couplings between <sup>29</sup>Si and <sup>1</sup>H nuclei. Specifically,  $\Delta$  is usually set to  $(1/2J)$  where  $J$  is the <sup>29</sup>Si-<sup>1</sup>H coupling constant that dominates the evolution of magnetization. For

bridged precursors, the strongest coupling that could be used for polarization transfer would be the scalar coupling between  $^{29}\text{Si}$  present at one end of the bridge and the proton that is two bonds away from it and connected to the carbon atom adjacent to it in the bridge.

For spectral editing purposes, Alam<sup>47</sup> has described the formulation of a theoretical transfer function that is a function of  $\Delta$  and the pulse angle,  $\theta$ . The determination of the theoretical intensities requires the knowledge of hetero- and homo- nuclear scalar coupling constants that are present in the spin system. The intensity of each peak in the DEPT spectrum representing a particular silicon environment is proportional to its corresponding theoretical value for particular  $\Delta$  and  $\theta$  used. With the help of theoretical intensities predicted for various polymeric species that are expected to be formed during the reaction for varying  $\Delta$  and  $\theta$ , and the peaks can be identified by comparison with the corresponding changes in the spectral intensities.

### 1.3.3. Selective Decoupling

The NMR coupling constants can be measured from a coupled experimental spectrum. However, sometimes multiple coupling interactions overlap each other calling for selective decoupling experiments to determine the individual coupling constants. Two- and three-bond silicon couplings to protons are of similar magnitude and hence, the  $^{29}\text{Si}$  NMR spectra of silanes show overlapping couplings. Such spectra can be selectively decoupled by using continuous wave decoupling of appropriate protons. The pulse scheme<sup>90</sup> used for this purpose is shown in Figure 1.6. In this experiment, a decoupler tuned to the resonant frequency of the nucleus to be decoupled is used to perform simultaneous excitation of selected protons while observing  $^{29}\text{Si}$  nuclei. The decoupler power is adjusted so that the resonance of interest when excited has no effect on the other resonances present in the spectrum. The resulting spectrum displays all resonances from the coupling of silicon nuclei to protons except the one that is irradiated.

## 1.4. Dissertation Scope

This dissertation is mainly focused on the interface between quantum chemistry and main stream chemical engineering research regarding the physicochemical aspects of silanes and silane-based polymers. The research pathway that led to the development of this thesis includes diverse areas as illustrated in Figure 1.7. The primary motivation for the initiation of this research was to expand the understanding of bridged silsesquioxanes and their formation through kinetic studies of their precursors owing to immense significance attached to such investigation (explained in the earlier sections). At the onset of this work, it was found that

traditional NMR technique fails to work for experimental characterization of certain bridged silane systems due to reaction induced microphase separation during the course of polymerization. This realization led to new avenues of research and in-depth kinetic studies including the effects of varying organic groups, solvents, substituents, and pH on bridged silane polymerization could not be investigated as initially intended. Nevertheless, the tools and techniques that facilitate or compliment NMR studies to easily investigate such effects are established in this dissertation with illustrations on some silane systems. Quantum chemical models of silanes presented in this work provide parameters required for employing improved NMR techniques like DEPT. Not only kinetics but also means to study the structural development of bridged silane polymers using Dynamic Monte Carlo simulations are discussed in this dissertation. In the process of exploring these techniques and customizing them for the bridged silanes systems, basic experimental trends and some differences in the structural evolution of bridged and non-bridged silanes have also been explained. The silanes explored with kinetic interests are limited to methylene and ethylene bridged alkoxy silanes.

In addition to fundamental investigation, this thesis also includes research on the application of siloxane-based polymers as biomaterials and adsorbents. Ordered mesoporous silica materials have emerged as promising materials for adsorption mediated applications due to their high surface areas and easy pore size control. In this thesis, silica systems have been suggested as drug carriers by establishing means to mediate silica toxicity through *in vitro* studies of anti-oxidant enzyme immobilization on silica matrices. The effect of structural parameters such as pore size and orientation, surface area and particle size on enzyme binding and protection are investigated. The effect of enzyme related parameters (size, shape, type etc.) and *in vivo* challenges are not addressed here. The second application, ammonia adsorption on copper sulfate impregnated silica is investigated to explore enhanced silica adsorbents. Adsorbent-adsorbate interactions and selectivity of adsorption are studied through quantum chemical modeling at different degrees of hydration. This investigation is performed at the atomic level to investigate the local interactions and does not include diffusion limitations at macroscopic level.

### **1.5. Dissertation Outline**

The research presented in this dissertation is divided into three parts. The first part deals with quantum chemical modeling of silanes to assist  $^{29}\text{Si}$  NMR characterization of bridged

alkoxysilane polymerization. Kinetic and structure evolution studies of bridged silane systems are presented in the second section. The third section deals with the investigation of siloxane-based polymeric materials as biomaterials and adsorbents.

In Chapter 2, the performance of four basis sets (6-311+G(2d,p), IGLO-III, cc-PVTZ, and 6-31G) is evaluated in order to find a quantum mechanical technique that can be used to accurately estimate  $^{29}\text{Si}$ - $^1\text{H}$  spin-spin coupling constants in organoalkoxysilanes. 6-31G basis set with the B3LYP functional is found to be an accurate, efficient, and cost-effective density functional theory method (DFT) for this purpose. The effects of size and the number of unhydrolyzable alkyl groups attached to silicon and the effects of substitution of alkoxy groups with hydroxyl groups on  $^{29}\text{Si}$ - $^1\text{H}$  spin-spin coupling constants are investigated using this method. The results show that the predicted scalar coupling between silicon and organic groups depends weakly on the degree of hydrolysis of the alkoxysilanes. The effectiveness of this method is also illustrated for the determination of spin-spin coupling constants in a species containing a siloxane bond. This chapter has been published in *The Journal of Physical Chemistry A*. (Ambati, J., Rankin, S.E., "DFT calculation of indirect  $^{29}\text{Si}$ - $^1\text{H}$  coupling constants in organoalkoxysilanes", **2010**, 114, 5279-5286)

The theoretical method established in Chapter 2 is employed to simulate the bridged silane coupling patterns in Chapter 3. In order to facilitate DEPT  $^{29}\text{Si}$  NMR studies of bridged silane systems, we need accurate values of NMR coupling constants. These values cannot be extracted from experiments as  $^{29}\text{Si}$  NMR spectra of bridged silanes, specifically those containing ethylene bridging groups, were found to suffer from second order effects. In these systems, theoretical tools are required to interpret the spectra of even simple molecules. Here, we determine density functional theory estimates of  $^{29}\text{Si}$ - $^1\text{H}$  scalar coupling constants and use these along with homonuclear coupling constant estimates to resolve the non-trivial nature of these spectra. We also report a Karplus equation consistent with the dihedral angle dependence of the three bond homo- and hetero- nuclear couplings in the ethylene bridge. By thermal averaging of DFT coupling constants, a good initial guess of the coupled  $^{29}\text{Si}$  spectral pattern is made, which is easily refined by curve fitting to determine estimates of all coupling constants in the system. This chapter too has been published in *The Journal of Physical Chemistry A*. (Determination of  $^{29}\text{Si}$ - $^1\text{H}$  NMR coupling constants in organoalkoxysilanes with non-trivial scalar coupling patterns", **2010**, 114, 12613–12621)



In Chapter 4, phase behavior of an ethylene bridged monomer, bis(triethoxysilyl)ethane (BTESE) in acidic water-ethanol solutions is discussed. The primary purpose of this investigation is to identify the reaction mixtures that allow meaningful kinetic characterization using  $^{29}\text{Si}$  NMR. A ternary pseudo-phase diagram is constructed to map the phase behavior for varying initial compositions. It is found that some of these solutions are prone to gradual loss of NMR signal due to reactive micro-phase separation of intermediates. The rate of signal loss is found to be dependent on the initial compositions as well as the pH of the solution mixtures. A portion of this chapter has been published in *PMSE Preprints*. (Ambati, J., Rankin, S.E., “ $^{29}\text{Si}$  NMR investigation of the polymerization kinetics of bis(triethoxysilyl)ethane in acidic alcohol/water solution”, **2006**, 94, 610-611). This chapter has also been accepted for publication as an article in the *Journal of Colloid and Interface Science* (Ambati, J., Rankin, S.E., “Reaction-Induced Phase Separation of Bis(triethoxysilyl)ethane upon Sol-gel Polymerization in Acidic Conditions”, **2011**, in press).

Application of DEPT technique in NMR investigation of bridged silanes has been demonstrated in Chapter 5 for characterizing methylene bridged silane polymerization in ethanol and acidic water solutions. For a low water concentration, early time polymerization species were identified from  $^{29}\text{Si}$  NMR spectra. Distortionless Enhancement through Polarization Transfer technique was used to enhance the sensitivity of  $^{29}\text{Si}$  nuclei and assign NMR peaks. DFT calculations were performed to determine  $^{29}\text{Si}$ - $^1\text{H}$  coupling constants used to calculate DEPT transfer efficiencies. These couplings were found to vary with progressive structural changes in the products of polymerization. This variation significantly affected theoretical DEPT intensities and their accurate determination led to identifying the reaction products observed in the DEPT  $^{29}\text{Si}$  NMR spectra through spectra editing. Cyclic dimer and linear dimer remained as the predominant products of condensation for the length of time the reactions were monitored.

In Chapter 6, the polymeric structure evolution and gelation of organoalkoxysilanes are compared based on the size and location of the organic group in the monomers using dynamic Monte Carlo simulations. We first discuss the incorporation of organic groups into the simulation models that were previously developed for tetra-alkoxysilanes.<sup>71</sup> We consider similar first shell substitution effects in bi-molecular reactions and cyclization involving the formation of four-member rings. Our simulation results are consistent with the experimental observations of

bridged precursors exhibiting quick gelation when compared to tri-functional silanes, with an exception of monomers with short hydrocarbonbridges displaying relatively prolonged gelation.<sup>91</sup> We found that the carbosiloxane rings formed from bridged precursors slow down but do not prevent gelation.

In Chapter 7, loading, activity and retention of an anti-oxidant enzyme, catalase on engineered mesoporous silica nanoparticles with different pore size and orientation and particle size are compared. All silica types display the potential for effective catalase loading and protection against the proteolytic enzyme, pronase when compared to non-porous silica. Hollow particles with interconnected pores exhibit higher loading and activity but poor protection compared with the other silica carriers.

Chapter 8 deals with a quantum mechanical investigation of ammonia adsorption on (a) silica, (b) copper sulfate hydrates and (c) a mixture of both of these adsorbents. Hydroxyl group attached to a hydridosilsesquioxane cluster is used to represent an isolated silanol at the surface of silica. B3LYP/6-311G\* level of theory is employed to derive the associated adsorption energies from optimized structures. Simplest system consisting of the dehydrated adsorbents is modeled first and then water is systematically added to these systems to understand its role in adsorption. Results indicate that a combination of silica and copper sulfate exhibits significantly stronger binding with ammonia when compared to the individual adsorbents. This implies that copper sulfate (even if physically bound) is a promising additive for enhanced efficiency of silica adsorbents.

Conclusions and recommendations for future work are presented in the final chapter (Chapter 9) followed by references of the articles cited in preparing this dissertation (Chapter 10).

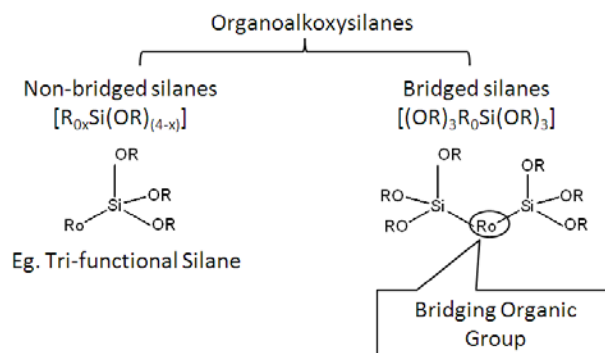


**Figure 1.1.** Classification of organoalkoxysilanes.

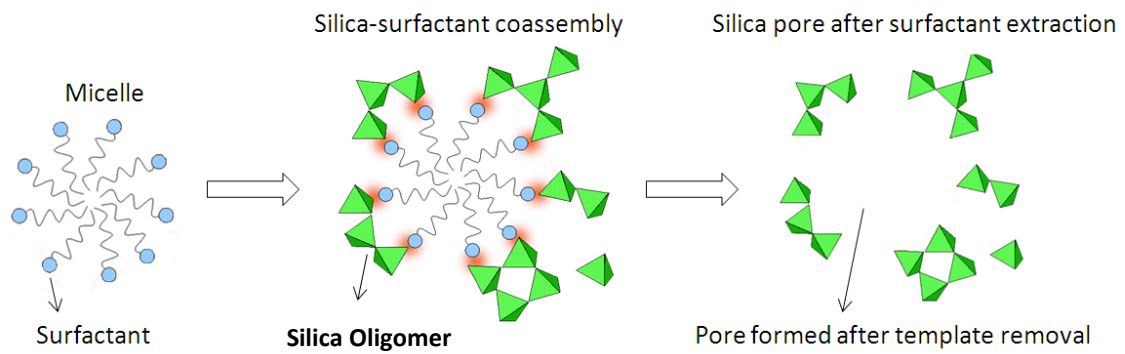


**Figure 1.2.** Synthesis of silica via surfactant templating.

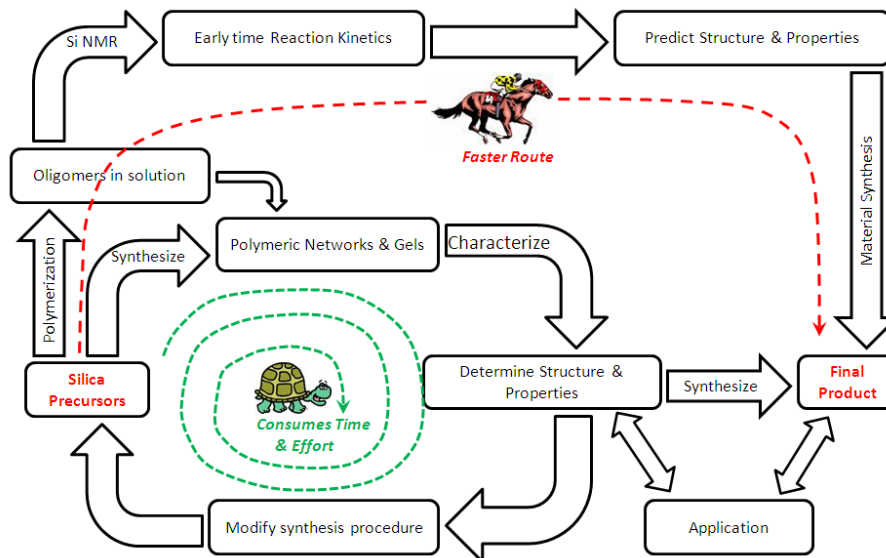


**Figure 1.3.** Significance of kinetic studies of sol-gel polymerization.

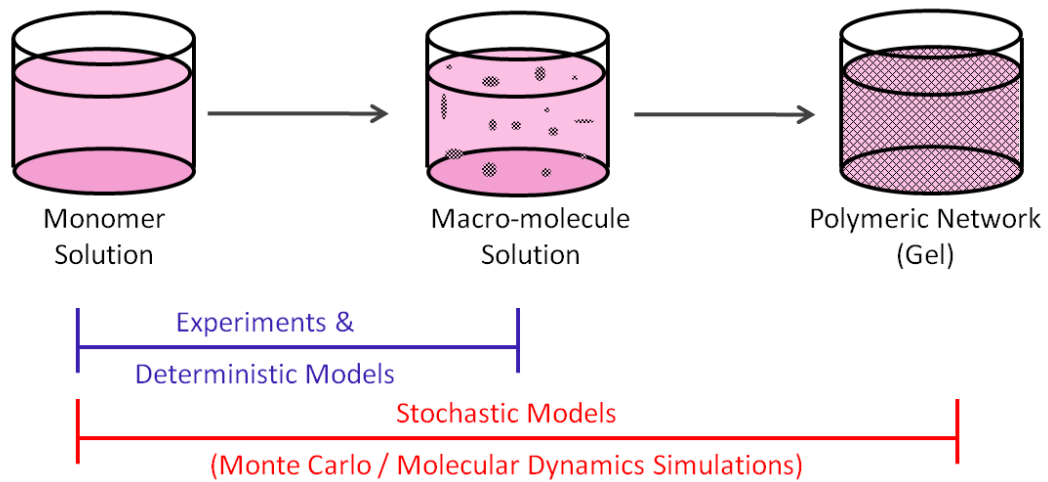


**Figure 1.4.** Limitations of experiments and mechanistic models in kinetic investigation.

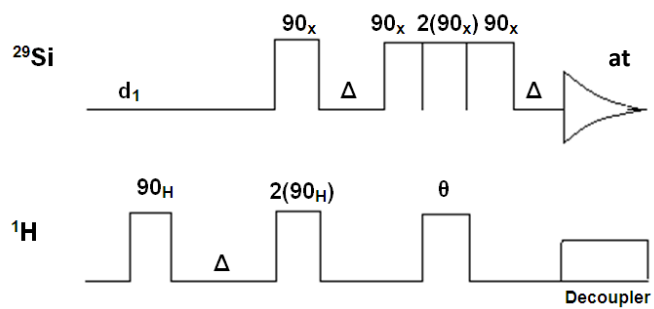


**Figure 1.5.** DEPT <sup>29</sup>Si NMR pulse sequence.

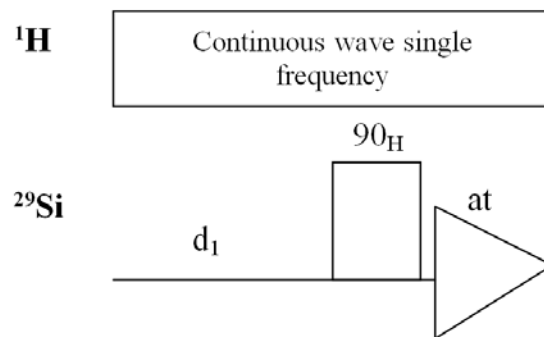


**Figure 1.6.** Pulse scheme for  $^1\text{H}$  single frequency decoupling of  $^{29}\text{Si}$  NMR.



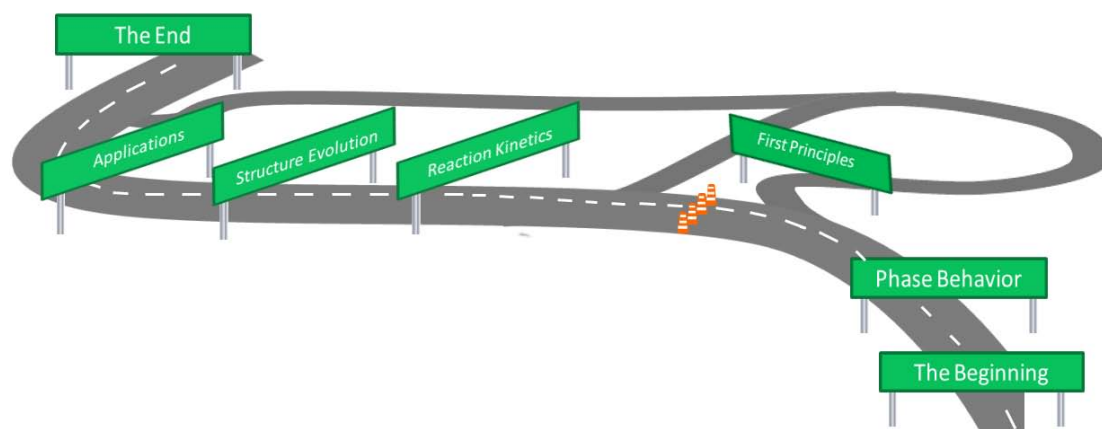


**Figure 1.7.** Dissertation research pathway.

**I DFT Calculations to Assist  $^{29}\text{Si}$  NMR Investigation of Alkoxysilane Polymerization**

## 2. DFT Calculations of Indirect $^{29}\text{Si}$ - $^1\text{H}$ Spin-Spin Coupling Constants in Organoalkoxysilanes

Reproduced with permission from (Ambati, J. and Rankin, S.E., *Journal of Physical Chemistry A* (2010), 114, 5279-5286) Copyright [2010] American Chemical Society

### 2.1. Summary

The performance of four basis sets (6-311+G(2d,p), IGLO-III, cc-PVTZ and 6-31G) is evaluated in order to find a quantum mechanical technique that can be used to accurately estimate  $^{29}\text{Si}$ - $^1\text{H}$  spin-spin coupling constants in organoalkoxysilanes. The 6-31G basis set with B3LYP functional is found to be an accurate, efficient and cost effective density functional theory method for predicting spin-spin coupling constants of organoalkoxysilanes. Knowledge of these scalar coupling constants and their dependence on structural variations is important to be able to fine tune NMR experiments that rely on polarization transfer among nuclei, such as  $^{29}\text{Si}$  Distortionless Enhancement by Polarization Transfer (DEPT). Effects of size and number of unhydrolyzable alkyl groups attached to silicon and effects of substitution of alkoxy groups with hydroxyl groups on  $^{29}\text{Si}$ - $^1\text{H}$  spin-spin coupling constants are investigated using this DFT method. The results show that the predicted scalar coupling between silicon and organic groups depends weakly on degree of hydrolysis of the alkoxysilanes. The effectiveness of this method is also illustrated for the determination of spin-spin coupling constants in a species containing a siloxane bond.

### 2.2. Introduction

Synthesis and application of polysilsesquioxanes has been a subject of growing interest in recent years due to the wide range of potential applications of these materials in the areas of optics, catalysis, thin films, coating of metal surfaces etc.<sup>25,92-95</sup> In the present study, we discuss the calculation of  $^{29}\text{Si}$ - $^1\text{H}$  NMR spin-spin coupling constants of a class of simple organically modified silanes that serve as precursors to some of these hybrid materials. These coupling constants are essential to the design and interpretation of NMR studies of these compounds, as articulated below.

Sol-gel polymerization involves hydrolysis and subsequent condensation of alkoxy groups in silane precursors to form polymeric networks and gels.<sup>1</sup> Structure and properties of polymers thus formed can be predicted from kinetic studies of polymerization well before the formation

of a solid material.<sup>54,60,61,68,69,71,96-101</sup> Although the most detailed information about polymerizing silanes is obtained from  $^{29}\text{Si}$  NMR, its applicability for in-situ kinetic studies is limited by low signal intensities and long data collection times.<sup>102,103</sup>  $^{29}\text{Si}$  NMR can still be made faster and more affordable by employing polarization transfer techniques like DEPT (Distortionless Enhancement through Polarization Transfer)<sup>104</sup> and INEPT (Insensitive Nuclei Enhanced by Polarization Transfer).<sup>105</sup> The usefulness of these techniques in  $^{29}\text{Si}$  NMR kinetic investigation of polymerizing silanes is well established in the literature.<sup>106-110</sup> Here, we will discuss primarily the use of the DEPT sequence, but INEPT also works on similar principles. By applying the DEPT pulse sequence, 1D  $^{29}\text{Si}$  NMR can be tuned for optimum sensitivity for qualitative or quantitative studies.<sup>110</sup> Magnetization evolves under the influence of proton-silicon coupling and polarization transfers from highly abundant protons to the rare  $^{29}\text{Si}$  nuclei to enhance the NMR signal. Also, the delay between successive pulses with DEPT depends on the relaxation rate of protons rather than on silicon nuclei, thus significantly reducing the time required to collect a spectrum.<sup>106,107</sup>

DEPT intensities are very sensitive to the parameters used in its pulse sequence and the coupling parameters of the molecule being observed. Hence, accurate parameter values must be used to extract meaningful kinetic information from DEPT experiments. The transfer time ( $1/2 J(\text{Si-H})$ ) in the DEPT pulse sequence used to control the extent of polarization transfer from protons to silicon nuclei is usually determined from the magnitude of the strongest  $^{29}\text{Si}$ - $^1\text{H}$  coupling interaction in the molecule. However,  $^2J(\text{Si-H})$  coupling between Si and protons in unhydrolyzable organic groups and  $^3J(\text{Si-H})$  coupling between Si and protons in hydrolyzable alkoxy groups constitute the strongest coupling interactions in alkylalkoxysilanes (compared to the direct  $^1J(\text{C-H})$  coupling available in  $^{13}\text{C}$  NMR). Theoretical DEPT intensities can also be predicted from these coupling constants.<sup>106,107</sup>

Due to the multi-functionality of these silane precursors, numerous reactions occur during their polymerization. Hence, NMR spectra of the reacting solutions are often too complex to analyze without spectral editing. DEPT facilitates spectral editing to make unambiguous peak assignments. Therefore, it is important to determine hetero-nuclear couplings and investigate how they change with changes in structure of silanes. Experimental intensities can be matched with theory to distinguish the peaks in the spectra. This has proven to be very useful in the identification of peaks in  $^{29}\text{Si}$  NMR spectra of polymerizing methyltriethoxysilane and tetramethoxysilane.<sup>106,107</sup>

There is a wealth of information available in literature about quantum mechanical NMR calculations performed on several classes of molecules and clusters using diverse model chemistries. Helgaker<sup>111</sup> has provided a review of *ab initio* methods for the computation of NMR shielding tensors and spin-spin coupling constants. The majority of these studies pertain to the calculation of NMR chemical shifts while reports related to spin-spin couplings are less extensive. The complexity of the determination of indirect spin-spin coupling constants increases many-fold in comparison to the chemical shift calculations<sup>112-115</sup> as it often requires large basis sets rendering high computational cost. Several authors have proposed improved basis sets and theoretical methods and demonstrated their applicability and computational efficiency for computing spin-spin couplings in small simple molecules.<sup>116-119</sup> However, there is no established rule that foretells the basis set and methodology that works best for a customized and more complicated set of molecules like the organoalkoxysilanes under consideration. A study focusing exclusively on first principles calculations of the couplings of these silanes using various basis sets is required in order to set up the guiding principle for these kinds of compounds.

The literature contains several reports of *ab initio* calculations performed for silicon-containing molecules. For instance, Cormiboef et al.<sup>120</sup> have calculated geometries and <sup>29</sup>Si NMR chemical shifts of silane derivatives. Heine et al.<sup>121</sup> and Casserly and Gleason<sup>122</sup> have performed DFT calculations of <sup>29</sup>Si NMR chemical shifts of silanes and organosiloxanes respectively. Pereira et al.<sup>123</sup> and Šefčík and Goddard<sup>124</sup> have conducted *ab initio* studies of the chemistry of silanols. Okumoto and Fajita<sup>125</sup> performed a theoretical study of hydrolysis and condensation of methylmethoxysilane. Casserly and Gleason<sup>126</sup> conducted DFT calculations on methyl and methylmethoxysilanes to obtain their enthalpies of formation and reaction. Nevertheless, there has been no study related to the heteronuclear couplings of organosilicon compounds. In the present work, we provide a model chemistry that predicts experimental indirect <sup>29</sup>Si-<sup>1</sup>H spin-spin coupling constants in some simple silica precursors.

The choice of basis set and the method employed play a major role in the accuracy of the results obtained. The applied basis set should be large enough to describe the molecule accurately while being small enough to reduce the computational cost. This work mainly focuses on finding a basis set appropriate for estimating hetero-nuclear couplings in organoalkoxysilanes. The correlation between measured and calculated <sup>2</sup>J(Si-H) and <sup>3</sup>J(Si-H) in

alkylalkoxysilanes and their variation with alkyl groups and degree of hydrolysis will also be discussed.

## 2.3. Computational Details

### 2.3.1. Geometry Optimization

NMR parameter calculations are very sensitive to molecular geometry; hence the model chemistry selected for geometry optimization plays an important role. First, all molecules were built in Argus Lab.<sup>127</sup> Stable geometries were obtained by the UFF molecular mechanics method in Argus Lab and input files for Gaussian03<sup>128</sup> were generated. Further geometry optimization was carried out using Gaussian03 at the B3LYP/6-31G\* level of theory. This methodology was chosen based on literature precedent; Cormiboef et al.<sup>120</sup> employed the hybrid density functional method B3LYP<sup>129,130</sup> in geometry optimization of silane compounds. Also, Franci et al.<sup>131</sup> have proposed the 6-31G\* basis set to be appropriate for the second row elements and it has been used by various researchers for optimizing geometries.<sup>132-134</sup> Vibrational frequency calculations were performed at the same level of theory to check the stability of geometries obtained by confirming the absence of any imaginary frequencies.

### 2.3.2. NMR Calculations

For accurate determination of NMR parameters, it is necessary that the method employed in geometry optimization as well as in estimation of NMR parameters be the same. Also, Helgaker et al.<sup>115</sup> have concluded from their studies that B3LYP provides accurate calculation of NMR shielding tensors and also spin-spin coupling constants. Therefore, in the present work, all NMR calculations were performed with the B3LYP functional using the Gaussian03 program package.

Calculated coupling constants depend strongly on the quality of the basis set.<sup>117</sup> Hence, we surveyed the literature to identify the basis sets which could be anticipated to work well for the class of silanes considered. Helgaker et al.<sup>117</sup> proposed a family of basis sets denoted by cc-pVXZ-*sun* for calculating NMR coupling constants with considerable accuracy for HF and H<sub>2</sub>O systems. 6-311G including various diffuse and polarization functions has been widely used for calculating chemical shifts.<sup>132-137</sup> IGLO basis sets<sup>138-141</sup> are reported by several researchers to be suitable for NMR calculations.<sup>142-144</sup> Helgaker et al.<sup>117</sup> have mentioned in their work that the IGLO basis sets are much smaller than the correlation consistent basis sets (cc-pVXZ series) and are not

systematic with respect to electron correlation, but they can still be used in comparison to the triple zeta (cc-PVTZ) or longer correlation consistent basis sets.

With these considerations, the performance of 6-311+G(2d,p), cc-PVTZ and IGLO –III and also the smaller simpler 6-31G basis set was initially investigated to identify the basis set that gives results comparable to the experiments. Later, the chosen basis set was used with B3LYP functional to determine  $^{29}\text{Si}$ - $^1\text{H}$  coupling constants of the set of silicon-containing compounds illustrated in Figure 2.1.

Reported spin-spin coupling constants are the sum of individual contributions of four Ramsay terms: Paramagnetic Spin Orbital (PSO), Diamagnetic Spin Orbital (DSO), Fermi-contact (FC) and Spin-Dipole (SD) interactions. Computed values and methodology were considered to be acceptable if the results were within 10% of the experimental values. All of the Gaussian calculations were performed on an Intel Xeon-based IBM HS21 blade cluster. All calculations were performed for isolated molecules in a vacuum except for a set of calculations (noted below) to study the effect of solvent modeled using the Polarization Continuum Model (PCM).<sup>145</sup> For the PCM calculations, both geometry optimization and NMR calculations were performed with acetone as the solvent.

The  $^2J(\text{Si-H})$  and  $^3J(\text{Si-H})$  couplings in all methoxysilanes studied and the  $^2J(\text{Si-H})$  values in ethoxysilanes are obtained by taking the arithmetic average of the coupling constants calculated for the three protons in the methyl group assuming rapid internal rotation.  $^3J(\text{Si-H})$  in ethoxysilanes are obtained by taking the arithmetic average of the calculated coupling constants for the  $\text{CH}_2$  protons in the ethoxy moieties unless thermal averaging is specified (see below).

## 2.4. Experimental Section

### 2.4.1. Methods

The samples were prepared by adding approximately 20% by volume deuterated acetone to the monomer and placing it in a 5 mm quartz NMR tube. They were probed with a pulse width of 11.8  $\mu\text{s}$  for  $^{29}\text{Si}$ , 7  $\mu\text{s}$  for  $^1\text{H}$ , and an interpulse delay of 100 s for  $^{29}\text{Si}$  spectra and 5 s for  $^1\text{H}$  spectra on a 400 MHz Varian NMR spectrometer. Appropriate signs were given to the measured coupling constants according to the Dirac vector model<sup>146</sup> unless unsaturated bonds were involved. Since  $^{29}\text{Si}$  has a negative gyromagnetic ratio, according to the Dirac vector model, the sign of the coupling constants alternate as the number of bonds between the nuclei increases,

with an odd number of intervening bonds carrying negative sign. Williams reported that  $^2J(\text{Si-H})$  are usually positive and  $^3J(\text{Si-H})$  negative.<sup>147</sup> For phenyl and vinyl silanes, coupling constant signs were set equal to those from the DFT calculations because of the difficulty predicting signs *a priori*.<sup>148</sup>

$^2J(\text{Si-H})$  or  $^3J(\text{Si-H})$  couplings were isolated by continuous wave  $^1\text{H}$  selective decoupling during acquisition of  $^{29}\text{Si}$  NMR spectra of the precursors wherever overlapping peaks hindered spectral interpretation. This experiment correlates a preferred  $^1\text{H}$  signal with the related  $^{29}\text{Si}$  signal and produces desired coupling information in the observed  $^{29}\text{Si}$  NMR spectrum. Where the couplings did not overlap, the coupling constants were measured from an ordinary coupled  $^{29}\text{Si}$  NMR spectrum.

#### 2.4.2. Materials

All silanes used in this study were acquired from Gelest Inc. at the highest purity available. Isomeric purity of the silanes was confirmed by the presence of one peak in the decoupled  $^{29}\text{Si}$  NMR spectrum of each compound. Deuterated acetone was obtained from Cambridge Isotope Laboratories.

#### 2.5. Results and Discussion

Precursors that are considered in the present study include simple silanes with different organic groups and functionality, namely, trimethoxysilane ( $\text{HSi}(\text{OMe})_3$ ), tetramethoxysilane ( $\text{Si}(\text{OMe})_4$ ), tetraethoxysilane ( $\text{Si}(\text{OEt})_4$ ), methyltriethoxysilane ( $\text{MeSi}(\text{OEt})_3$ ), methyltrimethoxysilane ( $\text{MeSi}(\text{OMe})_3$ ), dimethyldiethoxysilane ( $\text{Me}_2\text{Si}(\text{OEt})_2$ ), dimethyldimethoxysilane ( $\text{Me}_2\text{Si}(\text{OMe})_2$ ), trimethylethoxysilane ( $\text{Me}_3\text{SiOEt}$ ), trimethylmethoxysilane ( $\text{Me}_3\text{SiOMe}$ ), tetramethylsilane ( $\text{Me}_4\text{Si}$ ), vinyltrimethoxysilane ( $\text{ViSi}(\text{OMe})_3$ ), and phenyltrimethoxysilane ( $\text{PhSi}(\text{OMe})_3$ ). Optimized molecular geometries of these molecules are provided in Figure 2.1. We considered methoxy and ethoxy functionality in order to study the effect of the alkoxy substituent (and replacement of the alkoxy with hydroxyls upon hydrolysis) and methyl, vinyl and phenyl groups to study the effect of size and number of alkyl groups on  $^{29}\text{Si}$ - $^1\text{H}$  spin-spin coupling constants. We also studied a siloxane-containing species, hexamethyldisiloxane ( $\text{Me}_3\text{SiOSiMe}_3$ ) to investigate the effect of the presence of a siloxane bond on the ability of our method to predict coupling constants.



### 2.5.1. Selection of Appropriate Basis Set

Table 2.1 compares NMR parameters computed with the B3LYP functional using the 6-311+G(2d,p), cc-PVXZ, IGLO-III and 6-31G basis sets with experimental values for methyltriethoxysilane. We also report  $^{29}\text{Si}$  chemical shifts of methyltriethoxysilane with reference to tetramethylsilane calculated at the same level of theory using the GIAO method. The coupling constants calculated using the 6-31G basis set are within 5% deviation from experiment and are closer to the experimental values than the others. The other three basis sets underestimate the value of two-bond coupling and overestimate the value of the three-bond coupling constant. This finding is surprising because it contradicts previous studies that stress the need for rigorous levels of theory for achieving accurate values of spin-spin coupling constants.<sup>111</sup> Although cc-PVXZ and IGLO genres of basis sets are expected to give accurate descriptions of spin-spin coupling constants they fail to do so for the silanes considered in the present study. It is evident from Table 2.1 that 6-311+G(2d,p) (as expected) is an appropriate basis set for calculating nuclear shielding tensors, although it does not adequately predict scalar coupling constants. Shifts predicted by IGLO-III are close to the experiment, while the prediction of 6-31G basis set has 20% deviation from the experimental value and is not acceptable. This demonstrates that for  $^{29}\text{Si}$  none of these basis sets can be used for prediction of both chemical shifts and spin-spin coupling constants even for small molecules such as organoalkoxysilanes.

While it was not our goal to merely achieve computational expedience, we also observe that the simplicity of the 6-31G basis set allows NMR calculations to execute about two orders of magnitude quicker than the other three basis sets. Calculations for the results in Table 2.1 took 270 minutes for IGLO-III, 360 minutes for cc-PVTZ and only 4 minutes for 6-31G. Since there have been no studies that specifically address the prediction of  $^{29}\text{Si}$ - $^1\text{H}$  coupling constants in silanes, we suggest based on our work that, while it is counterintuitive, the 6-31G basis set is adequate for determining scalar coupling constants in silane-based molecules.

In order to further confirm this finding, we have compared the calculated  $^{29}\text{Si}$ - $^1\text{H}$  coupling constants using the four basis sets for various methylmethoxysilanes. Table 2.2 summarizes the percentage deviation of these calculated values from experimental measurements. We observe that, consistent with the result for  $\text{MeSi}(\text{OEt})_3$ , the values calculated using 6-31G are all within 10% of the experimental measurements while the other three basis sets have larger deviations.

### 2.5.2. Analysis of Contributions to Spin-Spin Coupling

Table 2.3 details the individual contributions to  ${}^2J$  and  ${}^3J$   ${}^{29}\text{Si}$ - ${}^1\text{H}$  coupling constants calculated for methyltriethoxysilane at various levels of theory. The contributions to these coupling constants appear to follow similar trends irrespective of the basis set used in the calculation. Both types of coupling constants are dominated by the Fermi contact (FC) contribution. The next significant contribution is from the paramagnetic spin orbital term. Spin dipole and diamagnetic spin orbital terms are negligible in  ${}^3J(\text{Si-H})$  coupling and have small values in the case of  ${}^2J(\text{Si-H})$ . Therefore, it can be concluded that terms other than FC have little influence on spin-spin coupling constant calculations for methyltriethoxysilane, and we noticed that this is true for other molecules used in the present study as well. This may help to explain why the 6-31G basis set performs well; the absence of d-orbitals in the basis function may allow a more accurate prediction of electron density near the nuclei in silicon-containing species, which determine FC contributions to scalar coupling. It may be possible to define a new basis set which is suitable for accurate prediction of both scalar coupling and nuclear shielding in silanes, but for the rest of this study, we will focus on applying B3LYP/6-31G to scalar coupling calculations of small silane molecules.

### 2.5.3. Calculation of Heteronuclear Coupling Constants

Measured and calculated  ${}^2J$  and  ${}^3J$   ${}^{29}\text{Si}$ - ${}^1\text{H}$  couplings for organoalkoxysilanes with varying organic and alkoxy groups are compared in Table 2.4 and a summary comparison is presented in Figure 2.2. In this series of molecules,  ${}^2J(\text{Si-H})$  seems to be underestimated slightly while there is no particular trend observed for  ${}^3J(\text{Si-H})$ . Overall, calculated values agree well with experiments.  ${}^2J(\text{Si-H})$  values are within 3.1% of the experiment while the deviation is higher (9.7%) for  ${}^3J(\text{Si-H})$ . Nonetheless, both are within an acceptable error of 10%. The sign of calculated  ${}^2J(\text{Si-H})$  in vinyl silane is negative in contradiction to the prediction of Dirac vector model. Exceptions to the Dirac model are not unprecedented<sup>148</sup> but are difficult to predict in molecules with delocalized electrons, so we have applied the signs predicted by the DFT calculations to the experimental magnitudes of  ${}^2J(\text{Si-H})$  of vinyl and phenyl silanes.

To confirm that the predictions made in vacuum can be compared to experimental values, Table 2.4 also lists  $J(\text{Si-H})$  calculated using the DFT method for trimethylmethoxysilane in acetone (calculated using the PCM model). These values match with both the experimental coupling constants and the values calculated in vacuum, thus showing that solvent has little

effect on the calculated coupling constants. Experimental measurements of  $J(\text{Si-H})$  reported by Alam et al.<sup>106</sup> and Brunet<sup>107</sup> in deuterated methanol and deuterated toluene respectively are given in Table 2.4. These values also match closely with our experimental measurements in deuterated acetone further supporting our conclusion that the effect of solvent environment is well within the limits of accuracy established for the applied DFT method.

Larger deviations in  $^3J$  coupling constants found for ethoxysilanes (Table 2.4) may be attributed to lack of adequate averaging among different configurations. To account for this problem, a detailed study of the ethoxy group dihedral angle dependence of scalar coupling in trimethylethoxysilane was performed (discussed in the following section) and the value of  $^3J(\text{Si-H})$  in Table 2.4 was obtained by thermal averaging.

The model chemistry used to study organosilicon compounds can be extended to siloxanes as well. To test this for one simple case, the  $^2J(\text{Si-H})$  coupling constant of hexamethyldisiloxane was calculated, and an exact match with the experimental value was found (Table 2.4). This agreement suggests that the B3LYP method and the 6-31G basis set provide accurate predictions of scalar coupling in simple silicon compounds containing siloxane bonds. More detailed calculations of the geometry dependence on scalar coupling for organoalkoxysilanes undergoing condensation will be presented in a future manuscript.

#### 2.5.4. Dihedral Angle Dependence in Ethoxysilanes

In order to substantiate the strong dihedral angle dependence of  $^3J(\text{Si-H})$  which we hypothesize is responsible for the deviations of calculations from experiments in some ethoxysilanes, we determined  $^3J(\text{Si-H})$  for several configurations of trimethylethoxysilane. There is only one ethoxy group in this molecule, which allows the dihedral angle effect to be isolated. Figure 2.3 shows the variation of  $^3J(\text{Si-H})$  in trimethylethoxysilane with dihedral angle between Si and H along the O-C single bond in the ethoxy group. The geometry was optimized for each calculated point (open diamond) with the dihedral angle constrained at the desired value. The observed trend is consistent with a Karplus relationship (the curve in Figure 2.3) which fits the observed three bond couplings to the following function:

$$^3J = A \cos^2\phi + B \cos\phi + C$$

where  $\phi$  is the dihedral angle and A, B, C are constants that depend on the compound.<sup>149</sup> Fitting the above expression to calculated  $^3J(\text{Si-H})$  values gives values of the constants equal to  $A = -7.1$ ,

B = 2.5 and C = -0.1. Thermal averaging of  $J$  in trimethylethoxysilane was performed over the entire range of dihedral angles as follows:

$$J_{avg} = \frac{\sum_i J(\varphi_i) e^{\frac{-\Delta E_i}{k_B T}}}{\sum_i e^{\frac{-\Delta E_i}{k_B T}}}$$

where  $J_{avg}$  is the average  ${}^3J(\text{Si-H})$ ,  $J(\varphi_i)$  is the calculated  ${}^3J(\text{Si-H})$  for dihedral angle  $\varphi$  in configuration  $i$ , and  $\Delta E_i$  represents the energy associated with internal rotation of the molecule and is determined by the energy of the configuration relative to the global minimum single point energy calculated at the B3LYP/6-31G level of theory. The temperature was set to the experimental temperature of 300 K.

The thermally averaged value of  ${}^3J(\text{Si-H})$  computed for  $\text{Me}_3\text{SiOEt}$  using above eqn. is -2.7 Hz and is within an acceptable 10% deviation from the experimental value provided in Table 2.4. The deviation found in this case may be larger than for other coupling constants because of the estimates of internal rotation energies. Relative energies,  $\Delta E_i$  are plotted against dihedral angles on the secondary axis of Figure 2.3. The energy barrier between different configurations (the maximum being 2.5 kcal/mol between the global minimum at  $60^\circ$  and global maximum at  $240^\circ$ ) indicate hindered rotation. However, the form of the energy landscape suggests a contribution from intramolecular steric interactions; the dihedral angle of  $240^\circ$  corresponds to the distance of closest approach between one of the methyl groups attached to silicon and the methyl of the ethoxy group. More complete sampling of the configurations of the molecule (for instance by Monte Carlo sampling) may give even better agreement with the experiment coupling constant, but is beyond the scope of the current investigation. Other ethoxysilane molecules are likely to have different intramolecular steric interactions that may influence the energies of configurations, but the coupling coefficients themselves seem to be predicted adequately. For comparison, if there were free rotation, the thermal average would become the arithmetic average of the coupling constant with respect to dihedral angle (calculated to be -3.6) in the high temperature limit. Increasing the temperature or lowering intramolecular steric barriers would give a coupling constant between -2.7 and -3.6, which is in the range where the experimental value is found. Hence, it is safe to conclude that in the ethoxy group dihedral angle has a strong effect on  ${}^3J(\text{Si-H})$  of ethoxysilanes but that proper thermal averaging of values estimated using the 6-31G basis set can give a reasonable estimate for trimethylethoxysilane.

To confirm that the deviations found for some ethoxysilanes in Table 2.4 are due to inadequate conformational averaging, Figure 2.3 also displays  $^3J(\text{Si-H})$  obtained from NMR calculations for each ethoxy group in each configuration found in ethoxysilanes with respect to the corresponding dihedral angles. These values all follow the Karplus curve established for  $\text{Me}_3\text{SiOEt}$ , thus suggesting that substitution has negligible effect on  $^3J(\text{Si-H})$  when the dihedral angle is taken into account. It should be noted that for all ethoxysilanes but trimethylethoxysilane, the  $^3J(\text{Si-H})$  values reported in Table 2.4 are arithmetic averages of the values plotted in Figure 2.3 for a selected configuration. Averaging all possible configurations for silanes having more than one ethoxy group is a cumbersome task due to internal degrees of freedom in the molecule and has not been attempted here as the primary goal for NMR studies is being able to predict coupling to protons in nonhydrolyzable organic groups. Based on the similarity in the Karplus relationship for all ethoxysilanes in Figure 2.3, we expect that if thermal averaging were done for each ethoxysilane, the estimates of  $^3J(\text{Si-H})$  would be found to be independent of organic substitution, as is observed experimentally (Table 2.4). This dihedral angle dependence does not seem to be a problem with methoxysilanes despite sampling over a small number of molecular configurations. Methoxy structures have fewer degrees of rotational freedom when compared to ethoxy moieties and averaging among all methyl protons in the methoxy group leads to good agreement with experimental values.

### 2.5.5. Effect of Alkyl and Alkoxy groups

Varying the type and number of alkyl and alkoxy groups attached to silicon changes the electron density around the silicon atom which affects the magnitudes of  $^2J(\text{Si-H})$  and  $^3J(\text{Si-H})$ . As evident in Table 2.4,  $^2J(\text{Si-H})$  is more sensitive to these variations when compared to  $^3J(\text{Si-H})$ . With increase in the number of methyl groups to two,  $^2J(\text{Si-H})$  coupling drops from 8.3 to 6.6 Hz for methyltriethoxysilane but the values are not much different for silanes with two, three or four methyl groups. On the other hand, the magnitude of  $^3J(\text{Si-H})$  is around 4 for methoxysilanes irrespective of the number of methyl groups attached to silicon. As discussed in the previous section, all ethoxysilanes all follow the same Karplus relationship, so deviations in  $^3J(\text{Si-H})$  for ethoxysilanes reported in Table 2.4 with methyl substitution are attributed to inadequate conformational averaging.

There is a significant decrease in the magnitude of the calculated value of  $^2J(\text{Si-H})$  on going from a methyl to a vinyl silane. This is due to the difference in coupling interactions caused by

the double bond in the vinyl group. Unfortunately, this does not match the experimental value of  $^2J(\text{Si-H})$  as well as for methyl groups – perhaps because of  $sp^2$  hybridization or the presence of delocalized electrons. However, delocalized electrons do not prevent accurate prediction of longer-range coupling. The three-bond coupling to the protons in the vinyl group are predicted to be -10.4 (cis) and -19.4 (trans) and these compare favorably to the experimental values of -9.6 and -19.3, respectively. Also, three-bond coupling from silicon to the hydrogens in the phenyl group of  $\text{PhSi}(\text{OMe})_3$  is predicted accurately. This  $^3J(\text{Si-H})$  value is larger in magnitude for the phenyl protons than for coupling to methoxy groups. The conjugate bond in the phenyl group is most likely responsible for this variation. As one further test of the predictive capabilities of the B3LYP/6-31G method, experimental and calculated one-bond  $^{29}\text{Si-}^1\text{H}$  couplings for trimethoxysilane are also reported in Table 2.4. The values agree well, despite the coupling constants being two orders of magnitude larger than two and three bond  $^{29}\text{Si-}^1\text{H}$  couplings.

#### 2.5.6. Effect of Degree of Hydrolysis

Now that we have validated the ability of B3LYP/6-31G calculations to predict two- and three- bond coupling, we illustrate the use of this methodology to confirm a hypothesis common in DEPT studies of silane kinetics – that hydrolysis does not change scalar coupling of  $^{29}\text{Si}$  to protons in unhydrolyzable groups. Table 2.5 lists the  $^{29}\text{Si-}^1\text{H}$  coupling constants calculated with the 6-31G basis set and B3LYP functional for silanes with respect to their degree of hydrolysis. It may be observed from Figure 2.4a that  $^2J(\text{Si-H})$  coupling seems to be independent of the degree of substitution of alkoxy groups for methyl silanes. All products of hydrolysis share almost the same coupling values as their parent alkoxy silanes. For dimethyl, vinyl and phenyl silanes,  $^2J(\text{Si-H})$  increases but the change is not very pronounced. This emphasizes that the couplings of fully hydrolyzed silanes can be used instead of the parent silanes to obtain quick and rough estimates of  $^2J(\text{Si-H})$  coupling constants. This makes the computations relatively inexpensive due to the decrease in the number of atoms. Also, the experimental spectra of fully hydrolyzed species are less complicated and hence, the couplings of these are easier to evaluate from experiment than their parent silanes. Previously, some authors<sup>106,107</sup> have estimated the couplings of fully hydrolyzed species and assumed that they could be applied to their parent silanes. These calculations support the validity of this assumption. Note also that, consistent with the assumptions made during kinetic DEPT experiments, condensation of two  $\text{Me}_3\text{SiOH}$

species to generate  $\text{Me}_3\text{SiOSiMe}_3$  is confirmed (Table 2.4) not to change the  $^2J(\text{Si-H})$  coupling constant.

On average, the magnitude of  $^3J(\text{Si-H})$  coupling also remains unchanged with degree of hydrolysis for all methoxysilanes (Figure 2.4b), except in the case of trimethoxysilane for which  $^3J(\text{Si-H})$  seems to decrease slightly with increasing hydroxyl group substitution. For hydrolyzed ethoxysilanes, coupling constants again show strong dihedral angle dependence consistent with the Karplus relationship in Figure 2.3. It should be noted that, although multiple configurations of the molecules were used to get the reported arithmetic averages for hydrolyzed ethoxysilanes, the changes in  $^3J(\text{Si-H})$  with degree of hydrolysis in Table 2.5 are still attributed to inadequate conformational averaging rather than changes due to hydrolysis. This is because of the strong dihedral angle dependence in the Karplus relationship. Calculation of  $^3J(\text{Si-H})$  in hydrolyzed derivatives tetraethoxysilane by arithmetic averaging would be expected to yield incorrect values for the same reason and hence, the effect of hydrolysis in tetraethoxysilane has not been reported in Figure 2.4.

## 2.6. Conclusions

The literature is constantly being updated with new advanced basis sets for the calculation of indirect spin-spin coupling constants owing to the difficulty of their accurate estimation. Contradicting this, our study has revealed that the small, simple 6-31G basis set is sufficient to provide surprisingly accurate results for organosilicon alkoxides as well as their early products of hydrolysis and condensation. DFT calculations employing the 6-31G basis set and B3LYP functional offer good agreement with experimental coupling constants.

Of the four individual contributions to spin-spin coupling constants, non-contact terms are by far much smaller than Fermi-contact, with paramagnetic spin dipole coupling being the next significant term. This suggests that of the basis sets tested, the 6-31G basis set is best suited to predict electron density near the nuclei of the molecules in silicon-containing species.

$^{29}\text{Si-}^1\text{H}$  coupling constants for a variety of silanes have been determined accurately by arithmetic averaging of all couplings found in a few configurations of the molecules, except for  $^3J(\text{Si-H})$  in ethoxysilanes which required full thermal averaging with consideration of the effect of the Si-O-C-H dihedral angle. There exists a strong dihedral angle dependence of  $^3J(\text{Si-H})$  couplings in ethoxysilanes which makes conformational averaging difficult to achieve in molecules with multiple ethoxides. This has been established by developing a Karplus relation

for  $^3J(\text{Si-H})$  silanes using trimethylethoxysilane calculations. All other ethoxysilanes show coupling constants consistent with this Karplus curve.

$^2J(\text{Si-H})$  is found to be more sensitive to changes in the type and number of alkyl and alkoxy groups attached to silicon when compared to  $^3J(\text{Si-H})$ . However,  $^2J(\text{Si-H})$  is independent of the degree of substitution of alkoxy groups with hydroxyl groups. Hence, fully hydrolyzed products can be used to calculate  $^2J(\text{Si-H})$  coupling constants making the computations relatively inexpensive. For all the silanes considered in this study, the degree of hydrolysis has no pronounced affect on the values of  $^3J(\text{Si-H})$ .

The results reported in the present study will be very useful in the quick estimation of coupling constants which play an essential role in the design and analysis of  $^{29}\text{Si}$  DEPT experiments that are used in the investigation of kinetics of sol-gel polymerization. They also provide a predictive basis for studies of polarization transfer in other silicon-containing systems such as silylated compounds.



**Table 2.1.** Comparison with experimental values of  $^{29}\text{Si}$ - $^1\text{H}$  coupling constants (in Hz) and chemical shifts relative to tetramethylsilane (in ppm) of methyltriethoxysilane calculated at the B3LYP level employing various basis sets.

|               | $^2J(\text{Si-H})$ | $^3J(\text{Si-H})$ | $\delta(\text{ppm})$ |
|---------------|--------------------|--------------------|----------------------|
| 6-311+G(2d,p) | 6.8                | -4.2               | -46.1                |
| IGLO III      | 6.2                | -4.2               | -52.3                |
| cc-PVTZ       | 6                  | -4.1               | -42.9                |
| 6-31G         | 8                  | -3.8               | -8.6                 |
| Experiment    | 8.2                | -3                 | -43.1                |

**Table 2.2.** Percent deviations from experiment for  $J(\text{Si-H})$  calculated using various basis sets in methoxysilanes.

|                                      | 6-311+G(2d,p) | cc-PVTZ | IGLO-III | 6-31G |
|--------------------------------------|---------------|---------|----------|-------|
| $^1J(\text{Si-H})$                   |               |         |          |       |
| HSi(OMe) <sub>3</sub>                | -1.4          | -18.6   | 2.6      | -1.2  |
| $^2J(\text{Si-H})$                   |               |         |          |       |
| MeSi(OMe) <sub>3</sub>               | -15.5         | -25.0   | -23.8    | -1.2  |
| Me <sub>2</sub> Si(OMe) <sub>2</sub> | -25.8         | -32.9   | -33.6    | -8.5  |
| Me <sub>3</sub> SiOMe                | -23.6         | -29.1   | -30.8    | 0.0   |
| $^3J(\text{Si-H})$                   |               |         |          |       |
| Si(OMe) <sub>4</sub>                 | 17.2          | 9.3     | 15.0     | 8.3   |
| HSi(OMe) <sub>3</sub>                | 11.9          | 4.8     | 11.9     | 2.4   |
| MeSi(OMe) <sub>3</sub>               | 12.5          | 37.3    | 16.0     | 2.6   |
| Me <sub>2</sub> Si(OMe) <sub>2</sub> | 16.7          | 13.2    | 16.2     | 2.6   |
| Me <sub>3</sub> SiOMe                | 11.9          | 6.3     | 81.7     | -4.8  |

**Table 2.3.** Individual contributions (in Hz) to  $^2J(\text{Si-H})$  and  $^3J(\text{Si-H})$  spin-spin coupling constants in methyltriethoxysilane.

|                    | FC   | SD   | PSO | DSO  |
|--------------------|------|------|-----|------|
| $^2J(\text{Si-H})$ |      |      |     |      |
| 6-311+G(2d,p)      | 6.7  | -0.1 | 0.3 | -0.1 |
| IGLO III           | 6.1  | -0.1 | 0.3 | -0.1 |
| cc-PVTZ            | 5.9  | -0.1 | 0.4 | -0.1 |
| 6-31G              | 7.9  | -0.4 | 0.4 | -0.1 |
| $^3J(\text{Si-H})$ |      |      |     |      |
| 6-311+G(2d,p)      | -4.2 | 0    | 0.1 | 0    |
| IGLO III           | -4.3 | 0    | 0.1 | 0    |
| cc-PVTZ            | -4.1 | -0.2 | 0.1 | 0    |
| 6-31G              | -4   | 0    | 0.1 | 0    |

**Table 2.4.** Comparison with experiment of  $^{29}\text{Si}$ - $^1\text{H}$  spin-spin coupling constants calculated at the B3LYP/6-31G level.

|                                      | $^2J(\text{Si-H})$ Hz |                       | $^3J(\text{Si-H})$ Hz |                         |
|--------------------------------------|-----------------------|-----------------------|-----------------------|-------------------------|
|                                      | Calc.                 | Exp.                  | Calc.                 | Exp.                    |
| $\text{Si}(\text{OMe})_4$            | -                     | -                     | -3.9                  | -3.6, -3.6 <sup>a</sup> |
| $\text{Si}(\text{OEt})_4$            | -                     | -                     | -0.1                  | -3                      |
| $\text{HSi}(\text{OMe})_3$           | -286.3*               | -289.7*               | -4.3                  | -4.2                    |
| $\text{MeSi}(\text{OMe})_3$          | 8.3                   | 8.4, 8.3 <sup>a</sup> | -4                    | -3.9, -3.9 <sup>a</sup> |
| $\text{MeSi}(\text{OEt})_3$          | 8                     | 8.2, 8.3 <sup>b</sup> | -3.8                  | -3, -3 <sup>b</sup>     |
| $\text{Me}_2\text{Si}(\text{OMe})_2$ | 6.5                   | 7.1                   | -4                    | -3.9                    |
| $\text{Me}_2\text{Si}(\text{OEt})_2$ | 6.5                   | 6.7                   | -3.9                  | -3                      |
| $\text{Me}_3\text{SiOMe}$            | 6.6, 6.7 <sup>c</sup> | 6.6                   | -4, -3.9 <sup>c</sup> | -4.2                    |
| $\text{Me}_3\text{SiOEt}$            | 6.6                   | 6.5                   | -2.7                  | -3                      |
| $\text{Me}_4\text{Si}$               | 6.6                   | 6.6                   | -                     | -                       |
| $\text{ViSi}(\text{OMe})_3$          | -5.6                  | -7.8                  | -4.1                  | -3.6                    |
| $\text{PhSi}(\text{OMe})_3$          | -5.5**                | -5.7**                | -4                    | -3.9                    |
| $\text{Me}_3\text{SiOSiMe}_3$        | 6.6                   | 6.6                   | -                     | -                       |

\*  $^1J(\text{Si-H})$  is reported in the case of  $\text{HSi}(\text{OMe})_3$

\*\*  $^3J(\text{Si-H})$  is reported for H in the ortho position of the phenyl group

<sup>a</sup> Coupling constants measured in deuterated methanol by Alam et al.<sup>106</sup>

<sup>b</sup> Coupling constants measured by simulating the experimental spectrum of polymerizing methyltriethoxysilane in ethanol and deuterated toluene<sup>107</sup>

<sup>c</sup> Coupling constant calculated in acetone using the B3LYP/6-31G method with PCM.

**Table 2.5.** Effect of hydrolysis of alkoxy silanes on calculated  $^{29}\text{Si}$ - $^1\text{H}$  coupling constants.

| # of OH groups                       | $^2J(\text{Si-H})$ Hz |         |         |         | $^3J(\text{SiH})$ Hz |      |      |
|--------------------------------------|-----------------------|---------|---------|---------|----------------------|------|------|
|                                      | 0                     | 1       | 2       | 3       | 0                    | 1    | 2    |
| $\text{Si}(\text{OMe})_4$            | -                     | -       | -       | -       | -3.9                 | -4   | -4.1 |
| $\text{HSi}(\text{OMe})_3$           | -286.3*               | -283.4* | -291.2* | -293.3* | -4.3                 | -4.4 | -4.8 |
| $\text{MeSi}(\text{OMe})_3$          | 8.3                   | 8.2     | 8.3     | 8.3     | -4                   | -4.1 | -4.1 |
| $\text{MeSi}(\text{OEt})_3$          | 8                     | 8.4     | 8.4     | 8.3     | -3.9                 | -2.1 | -3.7 |
| $\text{Me}_2\text{Si}(\text{OMe})_2$ | 6.5                   | 6.9     | 7.3     | -       | -4                   | -3.8 | -    |
| $\text{Me}_2\text{Si}(\text{OEt})_2$ | 6.5                   | 6.9     | 7.3     | -       | -3.9                 | -0.6 | -    |
| $\text{Me}_3\text{SiOMe}$            | 6.6                   | 6.7     | -       | -       | -4                   | -    | -    |
| $\text{Me}_3\text{SiOEt}$            | 6.6                   | 6.7     | -       | -       | -3                   | -    | -    |
| Vi $\text{Si}(\text{OMe})_3$         | -5.6                  | -5.5    | -5.6    | -5.8    | -4.1                 | -4.1 | -4.2 |
| $\text{PhSi}(\text{OMe})_3$          | -5.5**                | -5.6**  | -5.6**  | -5.7**  | -4                   | -4   | -4.2 |

\* $^1J(\text{Si-H})$ \*\* $^3J(\text{Si-H})$

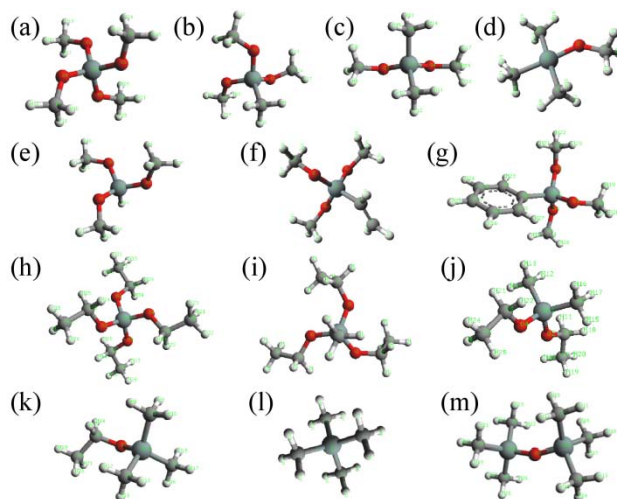


**Figure 2.1.** Optimized geometries of the unhydrolyzed form of the molecules studied here: (a) tetramethoxysilane, (b) methyltrimethoxysilane, (c) dimethyldimethoxysilane, (d) trimethylmethoxysilane, (e) trimethoxysilane, (f) vinyltrimethoxysilane, (g) phenyltrimethoxysilane, (h) tetraethoxysilane, (i) methyltriethoxysilane, (j) dimethyldiethoxysilane, (k) trimethylethoxysilane, (l) tetramethylsilane, and (m) hexamethyldisiloxane.

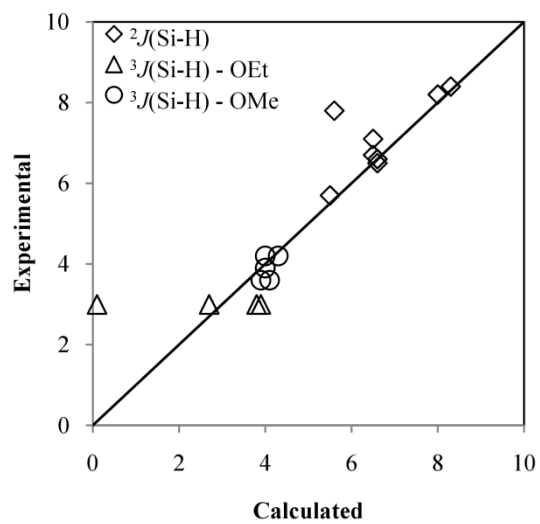


**Figure 2.2.** Correlation between calculated and experimental magnitudes of  $^2J(\text{Si-H})$  and  $^3J(\text{Si-H})$  coupling constants. Coupling constants of ethoxy (OEt) and methoxy (OMe) protons are plotted separately.

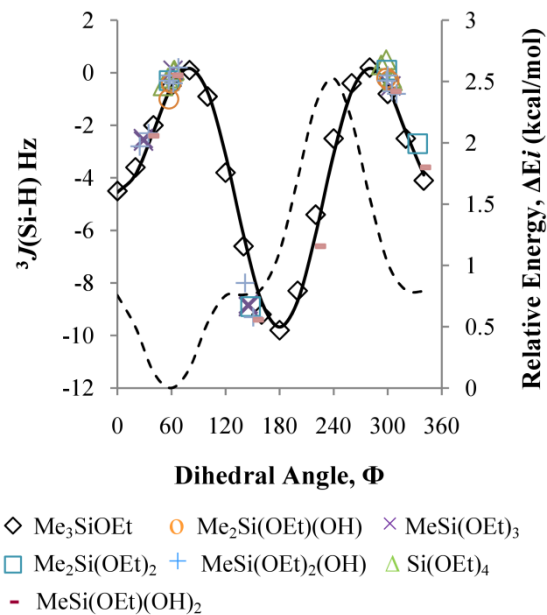


**Figure 2.3.** Variation of  $^3J(\text{Si-H})$  in ethoxysilanes with dihedral angle between silicon and the proton in the ethoxy group along the O-C bond. Points are values calculated by DFT; the solid curve is the best-fit Karplus relationship for  $\text{Me}_3\text{SiOEt}$  and the dashed line is the variation of relative energy with dihedral angle in  $\text{Me}_3\text{SiOEt}$ .



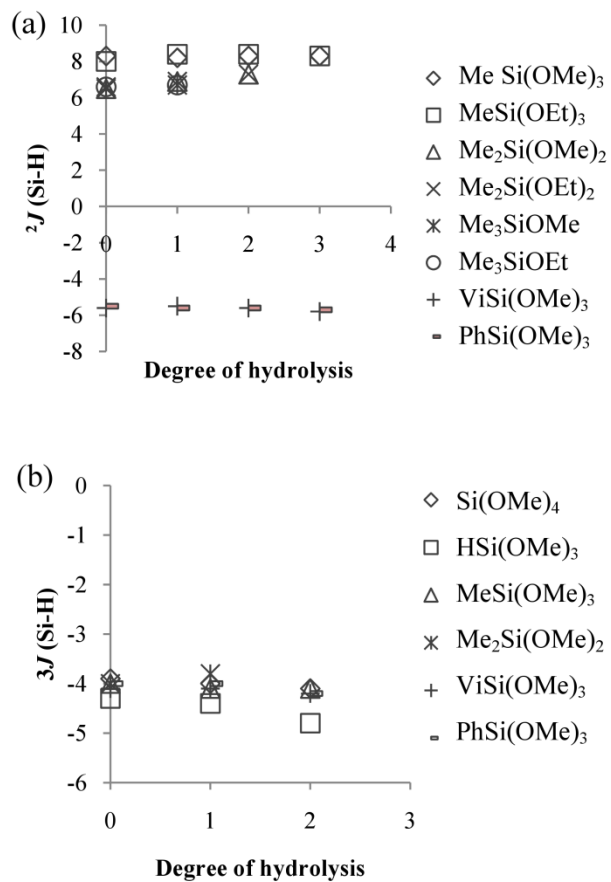


**Figure 2.4.** Variation of magnitude of hetero-nuclear coupling constants with degree of hydrolysis of organoalkoxysilanes: (a)  $^2J(\text{Si-H})$  and (b)  $^3J(\text{Si-H})$ .

### 3. Determination of $^{29}\text{Si}$ - $^1\text{H}$ Spin-Spin Coupling Constants in Organoalkoxysilanes with Nontrivial Scalar Coupling Patterns

Reproduced with permission from (Ambati, J. and Rankin, S.E., *Journal of Physical Chemistry A* (2010), 114, 12613-12621) Copyright [2010] American Chemical Society

#### 3.1. Summary

Application of polarization transfer techniques such as DEPT and INEPT in  $^{29}\text{Si}$  NMR investigation of bridged silane polymerization requires knowledge of indirect  $^{29}\text{Si}$ - $^1\text{H}$  scalar coupling constants in the silane system. However, the fully coupled  $^{29}\text{Si}$  NMR spectra of these molecules, specifically those containing ethylene bridging groups, are too complicated to measure the coupling constants directly by visual inspection. This is because, unlike hydrocarbon systems where one-bond proton-carbon coupling constants exceed other coupling constants by an order of magnitude, in silanes, the closest proton-silicon pairs are separated by two bonds and all coupling coefficients (both homonuclear and heteronuclear) are of similar magnitude. In these systems, theoretical tools are required to interpret the spectra of even simple molecules. Here, we determine density functional theory estimates of  $^{29}\text{Si}$ - $^1\text{H}$  scalar coupling constants and use these along with homonuclear coupling constant estimates to resolve the non-trivial nature of these spectra. We also report a Karplus equation consistent with the dihedral angle dependence of the three bond homo- and hetero- nuclear coupling in the ethylene bridge. By thermal averaging of DFT coupling constants, a good initial guess of the coupled  $^{29}\text{Si}$  spectral pattern is made, which is easily refined by curve fitting to determine estimates of all coupling constants in the system.

#### 3.2. Introduction

Bridged silanes serve as precursors to organic-inorganic hybrid sol-gel materials that have expanded the realm of ceramic applications available today. The source of organic functionality embedded in these materials is the hydrocarbon bridging group present in the precursors. Typically, a bridged silane consists of two tri-functional silicon atoms connected by an organic group. This bridge provides for more structural and functional possibilities than can be achieved by their non-bridged counterparts. Hydrolytic poly-condensation of these precursors leads to polymer networks and gels<sup>1,150</sup> that have a variety of applications in the fields of optics, selective

adsorption, coatings, catalysis and many more. Literature provides several reviews on the synthesis and applications of these hybrid materials.<sup>25,28,151-158</sup>

Investigation of the kinetics of polymerization of silane precursors<sup>60,61,68,69,71,75,96,101</sup> provides the information needed to develop conditions favorable to synthesize desired products, since the structure and properties of the final product can be predicted well before their synthesis. <sup>29</sup>Si NMR offers most detailed information about polymerizing silanes but is limited by low natural abundance (4.7 %) and slow relaxation of NMR active <sup>29</sup>Si nuclei. The low abundance renders low signal intensities hampering the observation of species present in relatively small concentrations. Relaxation times of <sup>29</sup>Si range from 20-135 s in bridged silanes<sup>91</sup> which is too long for collecting meaningful kinetic information under many practically relevant conditions. In order to decrease the relaxation time, a paramagnetic relaxation agent such as chromium (III) acetylacetonate is sometimes added to the samples being probed. However, introduction of a relaxation agent into sol gel samples is questionable because there is a chance it may act as a catalyst, thus impeding true kinetic studies.<sup>159</sup> Polarization transfer techniques<sup>87</sup> like DEPT (Distortionless Enhancement through Polarization Transfer)<sup>104</sup> and INEPT (Insensitive Nuclei Enhanced by Polarization Transfer)<sup>160</sup> are sometimes employed instead of using a paramagnetic relaxation agent. Polarization transfer not only decreases the delay between acquisitions (which is now dependent on the relaxation time of protons) but also enhances the sensitivity of <sup>29</sup>Si NMR. Theoretically, these techniques are expected to improve the <sup>29</sup>Si signal up to a factor of 5 ( $\Gamma_H / \Gamma_{Si}$ , where  $\Gamma$  is gyromagnetic ratio)<sup>87</sup> when polarization is transferred from <sup>1</sup>H to <sup>29</sup>Si. They also facilitate spectral editing of the NMR peaks of polymerizing precursors to help make structural assignments. The work of Alam and coworkers<sup>47,48,51</sup> and Brunet and coworkers<sup>58,161-163</sup> demonstrates the application of these techniques in <sup>29</sup>Si NMR kinetic studies of silanes.

Despite the usefulness of bridged silanes and well established experimental techniques to facilitate kinetic studies, almost all <sup>29</sup>Si NMR investigations available in literature have studied non-bridged silanes. There have been some FT-IR investigations<sup>77,78</sup> but FT-IR is limited only to functional group kinetics unlike <sup>29</sup>Si NMR which gives site-specific details. One reason that bridged silane kinetics remains unexplored is their complex nature when compared to relatively simple non-bridged silanes. <sup>29</sup>Si NMR spectra of polymerizing bridged silanes are potentially more difficult to interpret when compared to the spectra of their non-bridged counterparts. Each species in the former has two silicon environments which may produce two resonances if

substitution has long-range electronic effects. Moreover, due to their hexafunctionality, there is a possibility of several substitution reactions producing numerous peaks. This leads to uncertain peak assignments unless spectral editing is done.

Investigating the kinetics of bridged precursors using DEPT  $^{29}\text{Si}$  NMR has been a recent focus of our research.<sup>164</sup> DEPT can be a powerful solution to relaxation and peak assignment problems but its application requires the values of heteronuclear coupling constants in order to assign the transfer time for acquiring quantitative spectra or to predict the theoretical intensities for spectral editing purposes. Attempting to apply this technique to bis(triethoxysilyl)ethane, BTESE (Figure 3.1) was complicated by difficulty identifying the primary coupling constant to determine the transfer time in the DEPT sequence (usually  $1/[2 \times J(\text{Si-H})]$ ). The transfer time controls the extent of polarization transfer from protons to silicon nuclei and is often determined from the magnitude of the strongest  $^{29}\text{Si}$ - $^1\text{H}$  coupling interaction in the molecule. This should be the two-bond coupling to bridging group protons, which also have the advantage over alkoxy protons of remaining intact during polymerization. Even after selectively decoupling the alkoxy group protons, we found that the splitting pattern in the  $^{29}\text{Si}$  NMR spectrum of BTESE involving silicon coupling only to the bridging group protons is nontrivial (Figure 3.2a). Interpretation of these spectral patterns in order to extract values of heteronuclear coupling constants has been the primary motivation for the present work. The significance of this work lies in providing a validated approach to estimating coupling constants in bridged silanes that generate nontrivial splitting patterns. Understanding the coupling between silicon and protons in bridging organic groups is also essential for estimating and interpreting DEPT intensities.<sup>47,51,58</sup>

To address these challenges here, we systematically discuss hypotheses that are expected to explain the coupling pattern in Figure 3.2a. After all possible physical reasons that could cause such complexity are ruled out, we derive the procedure to obtain the indirect  $^{29}\text{Si}$ - $^1\text{H}$  couplings from a combined analysis of experimental results and DFT calculations. Because the theoretical methodology has not been established for  $^{29}\text{Si}$ - $^1\text{H}$  scalar coupling in bridged silanes, the DFT computational procedure employed is verified by comparing the experimental and calculated results for methylene bridged monomer followed by its application to interpret the nontrivial experimental spectra of ethylene-bridged monomers. To the best of our knowledge, this level of detail has not been applied to bridged silanes before.

### 3.3. Materials and Methods

#### 3.3.1. Experimental Details

The complexity of the fully coupled  $^{29}\text{Si}$  NMR spectra of the precursors discussed here arises partly due to silicon coupling to alkoxy and bridging organic groups overlapping with each other. In order to isolate these two types of couplings, selective continuous wave  $^1\text{H}$  decoupling<sup>165</sup> of  $^{29}\text{Si}$  NMR spectra of the precursors was performed. Since absolute values only can be obtained from the experimental spectra, appropriate signs were assigned to the measured magnitudes of coupling constants according to the Dirac vector model.<sup>166</sup> According to this model, depending on the sign of the gyromagnetic ratio of the nucleus involved, the sign of the coupling constants alternate as the number of bonds between the nuclei increases, with an odd number of intervening bonds carrying same sign.  $^{29}\text{Si}$  has a negative gyromagnetic ratio and the coupling constants with odd number of intervening bonds are negative, that is  $^2J(\text{Si-H})$  are usually positive and  $^3J(\text{Si-H})$  negative.<sup>167</sup> Hence, a negative sign is applied to the magnitude of all measured  $^3J(\text{Si,H})$  and unless otherwise stated, a positive sign to the measured  $^2J(\text{Si,H})$ . The samples were prepared by adding approximately 20% by volume deuterated acetone to the monomer. They were probed in 5 mm NMR sample tubes with a pulse width of 11.8  $\mu\text{s}$  for  $^{29}\text{Si}$ , 7  $\mu\text{s}$  for  $^1\text{H}$ , and an interpulse delay of at least 100 s for  $^{29}\text{Si}$  and 5 s for  $^1\text{H}$  on a 400 MHz Varian NMR spectrometer at  $27\pm 2$  °C.  $^1\text{H}$  NMR spectra were collected on a 600 MHz Varian spectrometer.

#### 3.3.2. Materials

All silanes used in this study were acquired from Gelest Inc. (Morrisville, PA) at their highest available purities. Deuterated acetone was obtained from Cambridge Isotope Laboratories (Andover, MA). All chemicals were used as received.

#### 3.3.3. Computational Details

All *ab initio* calculations were carried out on an Intel Xeon-based IBM HS21 blade cluster using Gaussian03<sup>128</sup> with the DFT functional, B3LYP<sup>129,130</sup>. The input files for Gaussian computations were generated with ArgusLab 4.0.<sup>127</sup> 6-31G\*<sup>131</sup> and 6-31G<sup>131</sup> basis sets were employed for geometry optimization and estimation of NMR spin-spin coupling constants respectively. The optimized 3D structures of the molecules studied in the present work, bis(triethoxysilyl)ethane (BTESE), bis(trimethoxysilyl)ethane (BTMSE), bis(trichlorosilyl)ethane (BTCSE), bis(triethoxysilyl)ethene (BTES=E) and bis(triethoxysilyl)methane (BTESM), are provided

in Figure 3.1. The optimized structure of bis(trihydroxysilyl)methane (BTHSM) is also included in Figure 3.1 as an example of a fully hydrolyzed version of a bridged silane. Vibrational frequency calculations were performed at the same level of theory as geometry optimization (B3LYP/6-31G\*) to confirm the absence of any imaginary frequencies that would indicate unstable geometries. All calculations were performed in vacuum and the solvent effects that could exist in the experimental samples were neglected; this was shown to be a reasonable assumption in our previous study.<sup>168</sup> Unless otherwise indicated, the heteronuclear coupling values reported from DFT calculations are estimates made using fully hydrolyzed molecules. Ground state energies of different conformations of BTMSE and BTESE were calculated using the B3LYP/6-31G\* geometry optimization results. BTMSE energies were also calculated using AM1 and B2LYP/aug-cc-PVTZ computations for comparison with the former. The MOPAC<sup>169</sup> module provided with ChemOffice<sup>170</sup> was used for AM1<sup>171</sup> computations and ORCA<sup>172</sup> package for employing B2LYP method with aug-cc-PVTZ basis set. VNMR 6.1C software (from Varian Inc.) available on the Varian NMR Spectrometer was used to simulate coupled <sup>29</sup>Si and <sup>1</sup>H NMR spectra of the bridging group of BTMSE.

### 3.4. Results and Discussion

#### 3.4.1. Silicon Coupling to Alkoxy Group Protons

Selective decoupling of protons in the bridging group of bridged silanes generates first order spectra. Interpretation of such spectra is straightforward and the <sup>3</sup>J(Si-H) value can be obtained directly from experimental measurement. For example, coupling to the methoxy groups in BTMSE (Figure 3.2b) results in the expected first-order doublet giving <sup>3</sup>J(Si,H) = -3.7 Hz. Theoretical computation of the same coupling constant for ethoxysilanes requires thermal averaging of <sup>3</sup>J(Si,H) over the entire range of Si-O-C-H dihedral angles of the monomer,<sup>168</sup> which also requires extensive geometry optimization. This computation has not been attempted for any molecule in this study, as it can be experimentally measured with relatively little effort. The <sup>3</sup>J(Si,H) values of ethoxysilanes are comparable to values found for non-bridged silanes, and all measured values are listed in Table 3.1.

#### 3.4.2. Silicon Coupling to Bridging Group Protons

Selectively decoupling the protons in the ethoxy moieties in BTESE results in the non-trivial spectrum shown in Figure 3.2a. A similar spectral pattern (Figure 3.2c) is produced by BTMSE as well. Since the BTMSE spectrum is clearer than that of BTESE, further analysis has been

performed using Figure 3.2c. Figure 3.2c is symmetrical with several low intensity peaks on both sides of a central quintet. This spectrum does not follow the coupling pattern that would arise from an  $A_4X$  (5 peaks) spin system if all protons (A) in the bridge were equivalent and hence,  $J(\text{Si-H})$  could not be measured directly from the experimental spectrum.

### 3.4.3. Resolving Non-trivial Coupling Patterns

The best way to experimentally determine coupling constants in this situation is to simulate the spectrum to determine the coupling constants giving the best fit. *Ab initio* calculations also have recently begun to be an accessible tool to aid in this task, although they require the selection of an appropriate method and basis set. These calculations also offer the advantage of supplying the sign of the coupling constants as compared to the absolute magnitudes provided by the experimental techniques. Knowledge of the signs is sometimes essential to start the simulations from initial guesses. Estimating coupling constants for ethylene-bridged silanes requires a combination of these methods because of the sensitivity of the spectral pattern to the coupling constants. Before discussing the quantum mechanical interpretation of the pattern, we discuss how we ruled out other possible reasons for the non-trivial appearance of the spectrum in the following sections. Possible physical reasons include incomplete decoupling to alkoxy groups or overlapping coupling patterns arising from different conformations if rotation were restricted in the molecule.

### 3.4.4. Ruling out Incomplete Decoupling to Alkoxy Protons

To test for incomplete decoupling of alkoxy protons, we collected the fully coupled spectrum ((Figure 3.2d) of bis(trichlorosilyl)ethane, BTCSE. BTCSE has an ethylene bridge identical to BTMSE and BTESE, but has chlorine atoms in place of alkoxy groups. We attribute the broadening observed in the BTCSE spectrum to complex splitting and relaxation phenomena owing to the presence of chlorine nuclei. Close observation and comparison of Figures 3.2d and 3.2c shows that the spectral pattern of BTCSE has features qualitatively similar to the BTMSE spectrum – most importantly the presence not only of a central (broadened) quintet but also of symmetrical broadened satellite peaks spaced at over 10 Hz from the central peak position. This result is consistent with a coupling pattern from the bridging group that is independent of the type of hydrolyzable groups (methoxy, ethoxy, or chloride) attached to the silicon nuclei. More importantly, this observation rules out the possibility that incomplete selective decoupling of  $\text{CH}_2$  group protons in the ethoxy groups of BTESE or coupling to  $\text{CH}_3$  in the methoxy groups of

BTMSE are responsible for the non-trivial pattern of peaks observed in these molecules. For the same reasons, the spectral pattern of BTESE is similar to that of BTMSE.

### 3.4.5. Ruling Out Hindered Rotation

It is expected that the ethylene bridging group is able to readily rotate along the C-C single bond on the time scale of NMR measurements. However, if the molecule were to exist in more than one conformation without rapid exchange, there would be peaks in the spectrum coming from each conformation which could result in a non-trivial spectral pattern. Ethenylene-bridged bis(triethoxysilyl)ethene, BTES=E is a good molecule to illustrate this. Because of the presence of the double bond, BTES=E has restricted rotation and it exists in *cis*- and *trans*- forms. The BTES=E used in the NMR experiments here is reported to have 80% *trans* conformation by the supplier. This is clearly evident in selectively decoupled spectra (Figures 3.2e and 3.2f) of BTES=E. The cluster of peaks arising from the *cis* conformation in the ethoxy-coupled spectrum (Figure 3.2e) is hundreds of Hz upfield from the *trans* peak referenced to 0 Hz, indicating that different conformations would produce different chemical shifts. To further rule out the effect that rotational isomerism might have, spectra were collected for BTMSE at 65 °C and no qualitative difference in the ethylene-coupled  $^{29}\text{Si}$  NMR spectrum could be seen due to faster exchange among rotamers. Effects of solvents on rotation were also ruled out using deuterated benzene and ethanol (and no qualitative difference in the coupled spectrum was seen). Based on these experiments, we conclude that rotational isomerism is not a likely cause for the coupling pattern observed for BTMSE.

### 3.4.6. Simulation of the Non-trivial Coupling Pattern

Now that we have ruled out any physical causes that could produce a nontrivial spectrum (which confirms a quantum mechanical source for the pattern), we address the spectral pattern computationally. In order to simulate the spectrum, the first step is to identify the spin system. Because  $^{29}\text{Si}$  is only 4.7% abundant, we can safely assume that the majority of the molecules contain only one active  $^{29}\text{Si}$  (X) nucleus. The spin system now depends upon the spins of the four protons. From the singlet representing the bridged protons in the  $^1\text{H}$  NMR spectrum of this compound (Figure 3.3a), we know that these protons are chemically equivalent. However, magnetic equivalence remains unknown. If the four protons were magnetically equivalent, the spin system would be  $A_4X$ , which would give rise to a first order quintet. Clearly the observed spectrum is not consistent with this spin system since satellite peaks are observed in addition to



the central quintet in the  $^{29}\text{Si}$  spectrum. This indicates that the four protons are mutually coupled to each other although they all have the same chemical shift, thus producing second order effects.

In a second order spectrum with one X nucleus, the X transitions due to the unmixed spin states of the other nuclei give rise to a symmetrical multiplet about the X resonance ( $\nu_X$ ). The splitting in this multiplet is equal to the average of the heteronuclear couplings involved. For example, the X part of an ABX spin system produces a doublet with separation  $|J_{AX} + J_{BX}|$ .<sup>166</sup> Considering these effects in BTMSE system, the splitting in the quintet in Figure 3.2c is the arithmetic average of  $^2J$  and  $^3J$  (Si-H) couplings. We observed that the satellite peaks also have splittings consistent with this average as indicated during the discussion of the simulated spectra below. Because only average values of heteronuclear couplings are directly observable in the experimental pattern, their individual magnitudes cannot be directly measured experimentally. Therefore, knowing that the system suffers from second order effects alone does not help either in resolving the non-trivial spectrum or in determining the coupling constant values. We need to know the appropriate spin system. From our earlier discussion, we recognize that the bridging protons are not held rigidly in place. So, the other possible options for spin system would be  $A_2A'_2X$  or  $AA'A''A'''X$ . If  $J_{AX}=J_{A'X}$ , the spin system is  $A_2A'_2X$  (two pairs of magnetically equivalent protons) and otherwise it is  $AA'A''A'''X$ . In this notation, primes (') represent the magnetic inequivalence in protons (A) and X represents  $^{29}\text{Si}$ . The exact spin system can only be identified from the magnitude of the couplings involved. *Ab initio* calculations of the coupling constants in BTMSE will help us to determine the relative strengths of the homo- and hetero-nuclear couplings in the bridge, in addition to providing initial guesses for simulation of the experimental spectrum.

### 3.4.7. DFT Method Validation

In our previous study,<sup>168</sup> we observed that the application of the B3LYP/6-31G level of theory to fully hydrolyzed versions of silanes provides accelerated estimation of  $^{29}\text{Si}$ - $^1\text{H}$  coupling constants in non-bridged precursor molecules without compromising accuracy. In this section, we validate the same methodology for bridged silanes by executing DFT calculations for the more tractable BTESM system and verifying the results with experimental measurements.

Upon selective decoupling of ethoxy groups in BTESM, the two equivalent protons in the methylene bridge produce a first order triplet (Figure 3.2g) and hence the heteronuclear

coupling in the bridge can be directly measured from the experimental spectrum.  $^2J(\text{Si-H})$  measured from this spectrum is 11 Hz which exactly matches 10.95 Hz, the DFT result for  $^2J(\text{Si-H})$  of BTESM's fully hydrolyzed form, BTHSM. This validates our computational method and basis set, and also supports the use of fully hydrolyzed bridged molecules to estimate heteronuclear coupling constants.

### 3.4.8. DFT Estimation of Coupling Constants

The DFT calculations of the coupling constants in the fully hydrolyzed form of BTMSE suggest that  $^2J(\text{Si-H})$  and  $^2J(\text{H-H})$  remain constant with free rotation, as expected. However,  $^3J(\text{Si-H})$  and  $^3J(\text{H-H})$  in the bridge depend on the Si-C-C-Si dihedral angle of the bridging group backbone. Figure 3.4 shows the variation of these coupling constants with the dihedral angle in the bridging group of BTMSE. Fitting these curves to the general Karplus equation,  $J(\phi) = A \cos^2\phi + B \cos\phi + C$  (where  $\phi$  is the corresponding dihedral angle), we obtained the Karplus constants for  $^3J(\text{Si-H})$  and  $^3J(\text{H-H})$ .

$$^3J(\text{Si-H}) = -14.95 \cos^2\phi_1 + 3.1 \cos\phi_1 - 0.4$$

$$^3J(\text{H-H}) = 14.9 \cos^2\phi_2 + 0.8 \cos\phi_2 + 0.5$$

Subscripts 1 and 2 of  $\phi$  represent Si-C-C-Si and H-C-C-H dihedral angles respectively. The Karplus curve for  $^3J(\text{H-H})$  in the bridge is similar to that of ethane. The magnitudes of these Karplus constants can be used to compare coupling constants with the values estimated for ethane<sup>173</sup> and butane.<sup>174</sup> The  $^3J(\text{H-H})$  values are close to the values of San Fabian et al.,<sup>175</sup> which are regarded as accurate.<sup>173</sup>  $^3J(\text{Si-H})$  constants are different in sign than for hydrocarbons because of the negative gyromagnetic ratio of silicon, and significantly larger in magnitude than typical  $^3J(\text{C-H})$  values.<sup>174</sup> They are, in fact more similar in magnitude to  $^3J(\text{H-H})$  values, perhaps because Si is only slightly less electronegative than H, while C is significantly more electronegative. The low electronegativity of Si leads to weaker, longer Si-C bonds than comparable C-C bonds and polarization of electron density towards C.<sup>176</sup> Localization of electrons at the carbons of ethylene-bridged silanes may be the reason for stronger long-range  $^3J(\text{Si-H})$  coupling than  $^3J(\text{C-H})$  coupling in comparable hydrocarbons.

For any particular dihedral angle, the actual dihedral angles between  $^{29}\text{Si}$  and each  $^1\text{H}$  are substantially different, and so we found that the magnitudes of  $^3J(\text{Si-H})$  of each proton are considerably different for all conformations, indicating that the four protons in the bridge are

magnetically inequivalent. This establishes the fact that the spin system should be regarded as AA'A''X.

### 3.4.9. Calculating Non-trivial Spectra from DFT Estimates

We observed that the simulated spectral pattern for AA'A''X spin system is very sensitive to the initial guesses of all ten homo- and heteronuclear coupling constants. This clearly establishes the need for good initial guesses in order to obtain a close match with the experimental spectrum. Complete agreement between the calculated spectrum and the experimental pattern would require iterative simulations. However, without good initial estimates, obtaining accurate coupling constants from simulation is not possible, even with regression to improve the match between the simulated and experimental spectra.

Since only the average of the heteronuclear coupling constant values is apparent in the experimental spectrum, the variation of this average splitting in the quintet is plotted in Figure 3.5 as function of the Si-C-C-Si dihedral angle in the ethylene bridge. The experimental splitting falls in the range of calculated values, and is close to the value of the 180° conformer. In order to quantitatively account for the effects of internal rotation, all homo- and heteronuclear coupling constants computed over the entire range of dihedral angles in the bridge are thermally averaged for comparison with the apparent coupling constants of the experimental spectrum. Individual thermal averages of the coupling constants in the bridge were calculated using Boltzmann factors as follows:

$$J_{avg} = \frac{\sum_i J(\varphi_i) e^{\frac{-\Delta E_i}{k_B T}}}{\sum_i e^{\frac{-\Delta E_i}{k_B T}}}$$

where  $J_{avg}$  is the average of  $J(\text{Si-H})$  or  $J(\text{H-H})$  and  $J(\varphi_i)$  is the calculated  $J(\text{Si-H})$  or  $J(\text{H-H})$  for corresponding dihedral angle  $\varphi$  in conformation  $i$ . The temperature was set to the experimental temperature of 300 K.  $\Delta E_i$  represents the energy associated with internal rotation of the molecule and is determined by the energy of the conformation relative to the global minimum single point energy. These energies are calculated at the B3LYP/6-31G\* or AM1 level of theory for B3LYP/6-31G\* optimized BTMSE geometries. The energy landscapes from both of these methods are provided in Figure 3.5 and they appear very distinct from each other. The DFT method predicts three minima at 60, 180 and 300° which is similar to the rotational effect found in hydrocarbons, but which may indicate that the steric effects from the bulky methoxy groups

attached to the silicon nuclei are underpredicted. Improving the DFT methodology by using the B2PLYP functional and aug-ccPVTZ basis set<sup>177</sup> did not change the energy profile. On the other hand, the AM1 energy prediction shows a minimum for 180° conformation alone because of steric interactions between trimethoxysilyl groups. We calculated thermal averages of coupling constants in the bridge in both cases and calculated the corresponding <sup>29</sup>Si NMR spectra displayed in Figures 3.6a and 3.6b. The spectrum from AM1 matches more closely with the experimental spectrum (Figure 3.6d). The splitting in the quintet obtained from AM1 thermal averaging (2.3 Hz) is closer to the experiment than the DFT estimate (1.5 Hz). This may be because the conformations may not be thermodynamically favorable as the dihedral angle recedes from 180°. By virtue of being parameterized with heats of formation, AM1 includes thermochemical corrections to yield heats of formation at 300 K while the DFT average includes only the total ground state energy.<sup>178</sup> While strategies exist to determine accurate heats of formation from DFT total energies, comparative energies at finite temperature are more easily obtained using semi-empirical methods such as AM1.<sup>179</sup>

Energy landscapes of BTESE using B3LYP/6-31G\* method is also provided in Figure 3.5. This profile closely matches with BTMSE's, indicating similar electronic behavior of the ethylene bridge in both these molecules. This theoretically supports the conclusion drawn from experimental observation earlier that the alkoxy groups do not affect the electronic structure (and coupling among nuclei) in the bridge.

In order to articulate the proximity of the calculated spectra with the experiment, Figure 3.7 shows the deviation from experiment of chemical shifts and normalized intensities of the BTMSE spectra calculated using DFT as well as AM1 energies, and the homo- and hetero-nuclear coupling constants obtained from the fully hydrolyzed version of BTMSE. From this figure, it is clear that the spectrum calculated using averaging with DFT energies shows greater deviations than when AM1 energies are used. All the deviations for the AM1 case are concentrated near zero indicating that the combination of AM1 energies and DFT coupling constants yields an accurate prediction of the experimental spectrum. In order to further minimize these deviations, the AM1 calculated spectrum (Figure 3.6b) was refined by regression to provide a better fit to the experimental spectrum (Figure 3.6d) in two steps. First, iterations were performed using the computed heteronuclear coupling constants. In the next step, the resulting values of  $J(\text{Si-H})$  were fixed and homonuclear couplings were iterated to get the best possible fit to the

experimental spectrum (Figure 3.6c). The deviations of intensities and chemical shifts from this best fit are also shown in Figure 3.7. It may be noticed that fitting decreased the deviations from experiment but not by much when compared to those found in Figure 3.6b. Coupling constants resulting from iterative simulation are within 10% of the computed coupling constants.

Table 3.2 shows that the changes in individual homo- and heteronuclear coupling constants made from the computed values to provide the best fit by regression are small. We can conclude that, consistent with our prior study of non-bridged silanes,<sup>168</sup> the B3LYP/6-31G method accurately predicts the homonuclear and heteronuclear coupling constants in a simple bridged silane. This can be further verified from the simulation of <sup>1</sup>H NMR spectrum of BTMSE (Figure 3.3a) using the coupling constants obtained from iterative simulation listed in Table 3.2. The expanded spectrum near the singlet representing the bridged protons is shown in Figure 3.3b. The peak at 21 Hz is believed to be an impurity. The peaks at 20 and -20 Hz are spinning side bands. All other peaks appear symmetrically on either side of the singlet due to second order coupling effects. Using the AA'A'A''X spin system, the calculated contributions to the spectrum from the coupling of <sup>1</sup>H nuclei in the bridge to <sup>13</sup>C and <sup>29</sup>Si nuclei are shown in Figures 3.3c and 3.3d respectively. These simulations closely match the observed experimental spectrum within experimental limitations. In the range of -20 to 20 Hz, the peaks from coupling to <sup>13</sup>C in Figure 3.3c and to <sup>29</sup>Si in Figure 3.3d overlap, and these are embedded in the experimental singlet which is broadened at the base due to multiple interactions. The satellite peaks observed on either side of the singlet between ±50 to 70 Hz are closely reproduced by the simulation in Figure 3.3c.

#### **3.4.10. J(Si-H) Trends**

The monomers considered in this study helped us not only to resolve the intricacies in the NMR spectra of ethylene-bridged precursor but also to further understand the effect of the type of substituent and bridging group on Si-H coupling constants. All of the calculated and experimentally measured heteronuclear coupling constants obtained in the present study are listed in Table 3.1. Note that, because of the complexity of the experimental spectra of ethylene-bridged precursors, the measured net result of silicon coupling to the bridge protons rather than individual coupling constants are provided as the splitting in the central quintet. All calculated values of this parameter are within 5% of the experimental measurements. We report only experimental values of <sup>3</sup>J(Si-H) from alkoxy groups since the values observed

experimentally agree well with other alkoxysilanes, as explained above. These values are comparable to  $^3J(\text{Si,H})$  measured and calculated for other methoxysilanes in our prior study.<sup>168</sup>

When compared to  $J(\text{Si-H})$  of non-bridged silanes in our previous study,<sup>168</sup> the calculated  $^2J(\text{Si-H})$  values have larger magnitudes in bridged silanes, with the methylene bridged silane having the largest magnitude and the ethenylene bridged the lowest. For the alkylene bridges, this effect may be due to some delocalization of bonding electrons due to the reduced electronegativity of silicon compared to carbon.  $^2J$  is larger for Si-C-H bonds<sup>168</sup> than typical values for C-C-H,<sup>180</sup> which is consistent with this idea. The second silicon attached to the methylene bridge enhances this effect. Expanding the bridge (to ethylene) reduces the influence of the second silicon in the bridge, although both  $^2J(\text{Si-H})$  and  $^3J(\text{Si-H})$  are comparable in magnitude to those found in methylalkoxysilanes.<sup>168</sup> Delocalization of electrons in the ethenylene bridge may be the reason that the magnitude of splitting increases again.  $^3J(\text{Si-H})$  is almost the same in all ethylene bridges and does not seem to be affected by the type of alkoxy group while  $^2J(\text{Si-H})$  is reduced in the chlorosilane compound. However, both  $^2J(\text{Si-H})$  and  $^3J(\text{Si-H})$  in the bridge of the *trans* form of the ethenylene bridged silane are strikingly different when compared to ethylene bridged silanes. This may be attributed to the unsaturated nature of the ethenylene bridge. For comparison with another unsaturated monomer, vinyltrimethoxysilane coupling constants are provided in Table 3.3. For both vinyl and ethenylene groups,  $^3J(\text{Si-H})$  in the organic group is larger in magnitude than  $^2J(\text{Si-H})$ . This is opposite to the trend observed in the case of saturated bridges. However, the measured and calculated splittings in the triplet of the ethenylene bridge in BTES=E (Table 3.1) are quite close, establishing the credibility of these magnitudes. The counterintuitive, strong long-range heteronuclear coupling in these ethenyl-based silanes is important to note, and can potentially be exploited for spectral editing and polarization transfer with DEPT.

### 3.5. Conclusions

The fully coupled spectral patterns of bridged silanes have been found to be too complicated for traditional interpretation by visual inspection. Selective decoupling of protons in the bridging group results in first order spectra and the  $^3J(\text{Si-H})$  coupling constants to alkoxy protons can be directly measured from the experimental spectra based on the observed multiplets. However, selective decoupling of alkoxy groups produces non-trivial second order spectra. From the present study, we have established a methodology to derive  $^{29}\text{Si}-^1\text{H}$  coupling

constants in bridged silanes from experimental simulation of second order spectra with the aid of DFT calculations. We observed that the B3LYP/6-31G level of theory produces accurate coupling constants in bridged silanes. We also found the Karplus constants consistent with the dihedral angle dependence of  $^3J(\text{Si-H})$  and  $^3J(\text{H-H})$  in ethylene bridged silanes. Thermally averaged coupling constants using AM1 energies were able to closely predict the non-trivial experimental spectrum of ethylene bridge, thus accurately predicting the apparent homo- and hetero- nuclear coupling constants observed in the experiment.

Coupling interactions in the bridge and in the alkoxy groups are independent of each other.  $^3J(\text{Si-H})$  in the alkoxy groups follow the same trends as observed for non-bridged silanes. However,  $^2J(\text{Si-H})$  in bridging groups have larger magnitudes when compared to those in nonhydrolyzable organic groups in non-bridged silanes. This is hypothesized to be caused by delocalized bonding involving silicon d-orbitals, or the polarity of Si-C bonds. In the presence of unsaturated bonds,  $^2J(\text{Si-H})$  are negative as opposed to the conventional Dirac vector model prediction, and smaller in magnitude than  $^3J(\text{Si-H})$ .

The complications arising from strong heteronuclear coupling in addition to strong homonuclear coupling set this study apart from the other systems exhibiting only strong homonuclear coupling, where spectral simulation is possible without needing very good initial guesses of coupling constants. Thermal averaging of accurate DFT estimates of scalar coupling constants is the key for resolving complicated second order spectra like that of BTMSE by spectrum simulation. The analysis done in the present study can be applied to other silanes suffering from second order effects to estimate Si-H coupling constants for use in polarization transfer  $^{29}\text{Si}$  NMR kinetic studies. This study paves the way for the kinetic investigation of bridged silane polymerization using DEPT  $^{29}\text{Si}$  NMR which would otherwise be difficult to design and interpret.

**Table 3.1.**  $^{29}\text{Si}$ - $^1\text{H}$  coupling constants of various bridged silanes.

| Monomer | Bridging group          |                         |                            |      | Alkoxy group            |
|---------|-------------------------|-------------------------|----------------------------|------|-------------------------|
|         | $^2J(\text{Si-H})$ (Hz) | $^3J(\text{Si-H})$ (Hz) | Splitting in the multiplet |      | $^3J(\text{Si-H})$ (Hz) |
|         | Calc                    | Calc                    | Calc                       | Exp  | Exp                     |
| BTESM   | 11                      | -                       | 11                         | 11   | -2.8                    |
| BTMSE   | 9.8,9.9 <sup>a</sup>    | -5.2,-5.8 <sup>a</sup>  | 2.3,2.1 <sup>a</sup>       | 2.1  | -3.7                    |
| BTCSE   | 7.7                     | -5.2                    | 1.3                        | 1.3  | -                       |
| BTESE   | 9.8,9.9 <sup>a</sup>    | -5.2-5.8 <sup>a</sup>   | 2.3,2.1 <sup>a</sup>       | 2.1  | -2.8                    |
| BTES=E  | -7.2                    | -13.2                   | 10.3                       | 10.9 | -2.9                    |

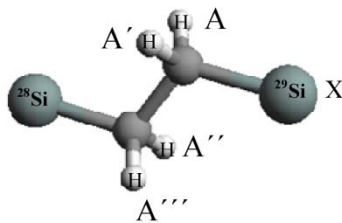
<sup>a</sup>  $J(\text{Si-H})$  that provide best-fit to the experimental spectrum in Figure 3.2c.



**Table 3.2.** Thermal averages of homo- and heteronuclear coupling constants calculated at the B3LYP/6-31G level of theory in the bridging group of fully hydrolyzed BTMSE using BTMSE AM1 energy estimates. Please refer to the adjoining structure for notation.

| Coupling      | Calculated | Iterated |
|---------------|------------|----------|
| $J_{AA'}$     | -20.2      | -19.9    |
| $J_{AA''}$    | 5          | 3.8      |
| $J_{AA'''}$   | 11.2       | 11.7     |
| $J_{AX}$      | 9.5        | 9.6      |
| $J_{A'A''}$   | 11.3       | 12.2     |
| $J_{A'A'''}$  | 6.3        | 6.5      |
| $J_{A'X}$     | 10.1       | 10.3     |
| $J_{A''A'''}$ | -20.3      | -20.3    |
| $J_{A''X}$    | -5.7       | -6.3     |
| $J_{A'''X}$   | -4.7       | -5.3     |

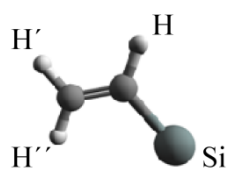
Ethylene Bridge



**Table 3.3.** Comparison of measured  $^{29}\text{Si}$ - $^1\text{H}$  coupling constants with computations at B3LYP/6-31G level of theory in vinyl group of vinyltrimethoxysilane. Please refer to the adjoining structure for notation.

| Coupling constant    | Calculated values (Hz) | Experimental magnitudes (Hz) |
|----------------------|------------------------|------------------------------|
| $^2J(\text{Si-H})$   | -5.6                   | 7.8                          |
| $^3J(\text{Si-H}')$  | -10.4                  | 9.6                          |
| $^3J(\text{Si-H}'')$ | -19.4                  | 19.3                         |

Vinyl group in  
Vinyltrimethoxysilane



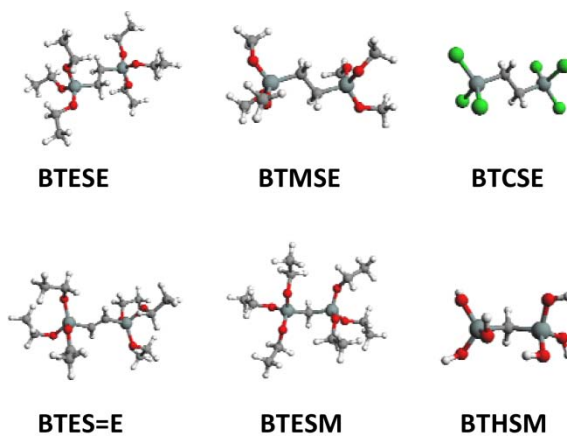


**Figure 3.1.** Optimized 3D geometries of bis(triethoxysilyl)ethane (BTESE), bis(trimethoxysilyl)ethane (BTMSE), bis(trichlorosilyl)ethane (BTCSE), bis(triethoxysilyl)ethene (BTES=E), bis(triethoxysilyl)methane (BTESM) and bis(trihydroxysilyl)methane (BTHSM)

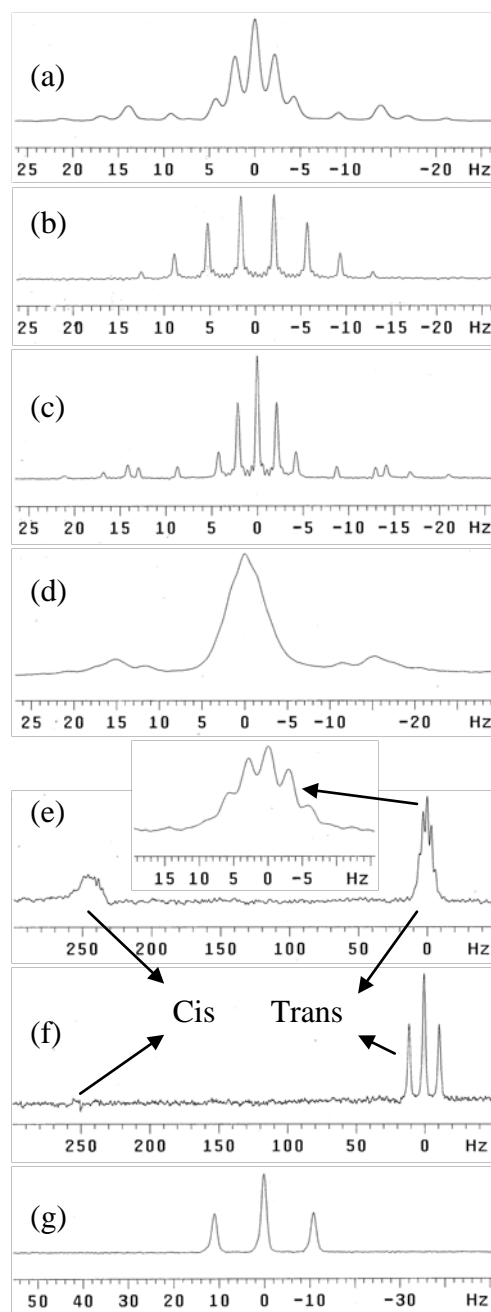


**Figure 3.2.** Selectively decoupled experimental  $^{29}\text{Si}$  NMR spectra displaying silicon coupling to protons in various bridged silanes. Spectra (a), (c) and (g) are the result of selectively decoupling alkoxy groups in (a) BTESE (c) BTMSE and (g) BTESM. Spectrum (b) is the result of selectively decoupling the bridging group protons in BTMSE. (e) and (f) are spectra obtained from selectively decoupling BTES=E bridging groups and ethoxy group respectively. The inset in spectrum (e) is the expanded form of coupling pattern in trans-form of BTES=E. Spectrum (d) is the coupled spectrum of BTCSE.

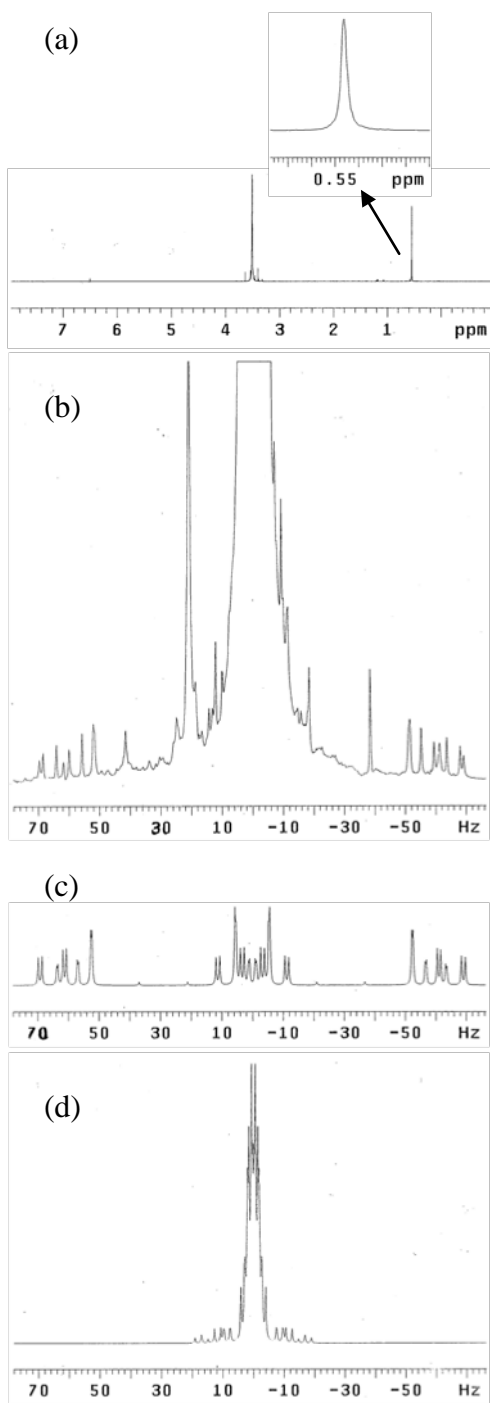


**Figure 3.3.** (a) Experimental  $^1\text{H}$  NMR spectrum of BTMSE referenced to tetramethylsilane. (b) Expanded form of the singlet in the experimental  $^1\text{H}$  NMR spectrum shown in (a); (c)  $^1\text{H}$  NMR spectrum of the singlet simulated using iterated  $J(\text{H-H})$  reported in Table 3.2 and experimental values of  $^1J(\text{C-H})=120$  Hz and  $^2J(\text{C-H})=-4.2$  Hz; (d)  $^1\text{H}$  NMR spectrum of the singlet simulated using iterated  $J(\text{H-H})$  and  $J(\text{Si-H})$  reported in Table 3.2.

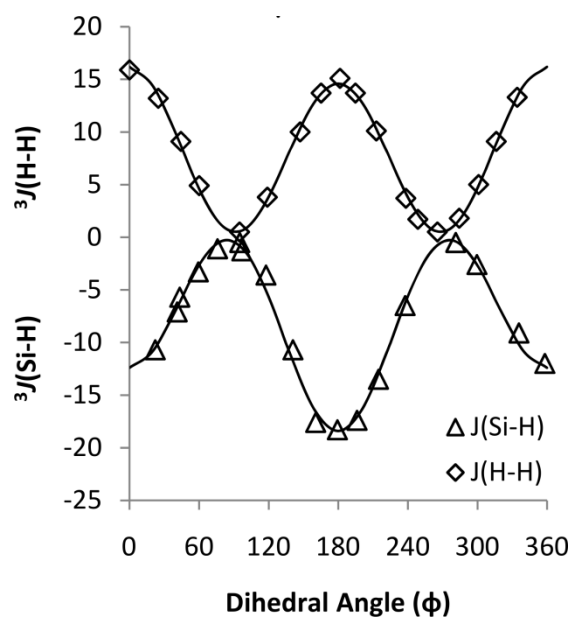


**Figure 3.4.** Variation of  $^3J(\text{Si-H})$  and  $^3J(\text{H-H})$  in the bridging group of bis(trihydroxysilalyethane) with the corresponding Si-C-C-H and H-C-C-H dihedral angles, respectively. Points represent the values obtained from DFT calculations and curves represent the Karplus fits. Karplus constants for these fits are provided in the text.

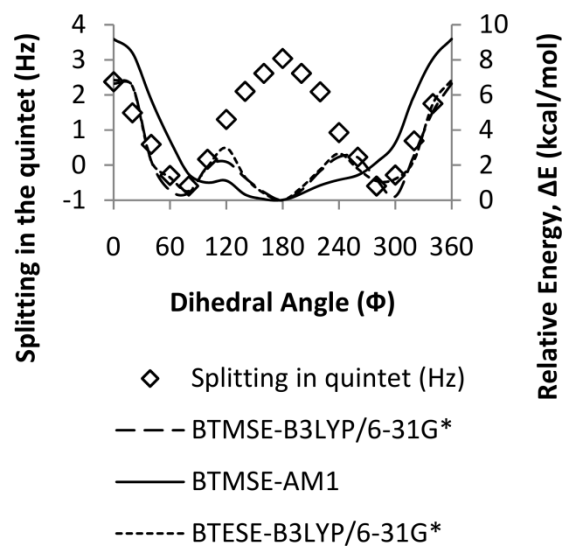


**Figure 3.5.** Variation of splitting in the quintet [=average of ( $^2J(\text{Si-H})$  and  $^3J(\text{Si-H})$ )] of BTMSE spectrum with Si-C-C-Si dihedral angle in the bridging group plotted on primary axis. Relative energies of BTMSE and BTESE obtained from DFT and semi-empirical AM1 methods are compared on the secondary axis.

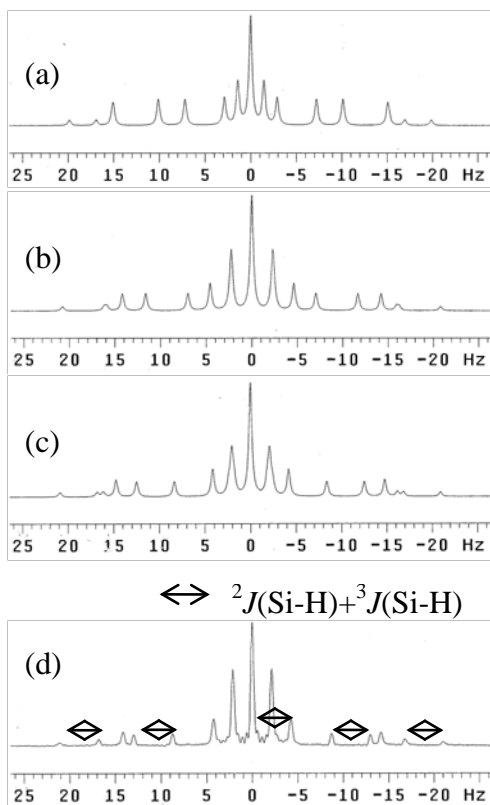


**Figure 3.6.** Simulated  $^{29}\text{Si}$  NMR spectra of the ethylene bridge in BTMSE (a-c) compared with experimental spectrum (d). Coupling constants for the theoretically derived spectra (a and b) are obtained from B3LYP/6-31G, and energies for calculating thermal averages from either B3LYP/6-31G\* (a) or the semi-empirical AM1 method (b). Spectrum (c) is obtained by using regression to better fit the simulated spectrum (b) to the experimental spectrum (d).



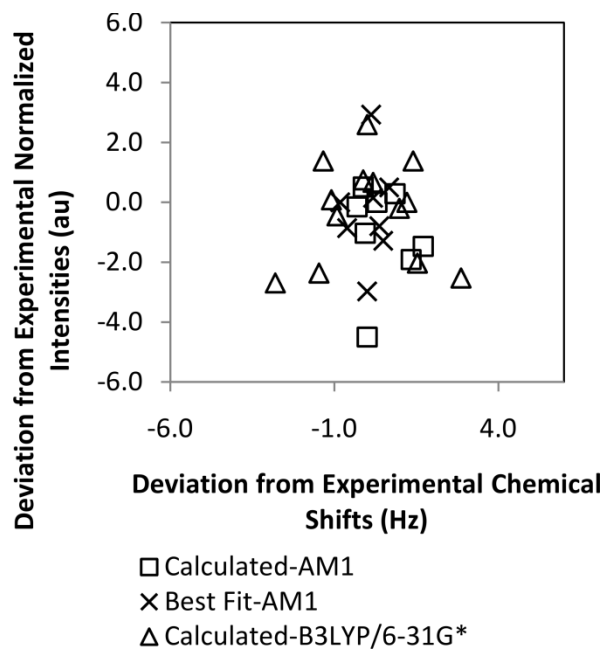


**Figure 3.7.** Deviation from experimental values of chemical shifts and normalized intensities of the spectrum calculated using BTMSE DFT or AM1 energies and homo- and heteronuclear coupling constants obtained by DFT from fully hydrolyzed version of BTMSE. The “Best Fit-AM1” values are the difference between experiment and the best-fit spectrum found by regression using the AM1 coupling constants as initial guesses.

**II Investigation of Kinetic, Structure and Phase Evolution of Bridged Alkoxysilane  
Polymerization**

## 4. Reaction-Induced Phase Separation of Bis(triethoxysilyl)ethane upon Sol-gel Polymerization in Acidic Conditions

Reproduced with permission from (Ambati, J. and Rankin, S.E., *Journal of Colloid and Interface Science*, in press) Copyright [2011] Elsevier. Some material is also reproduced in part from (Ambati, J. and Rankin, S.E., *Proceedings of the ACS Division of Polymeric Materials: Science and Engineering* (2006), 94, 610-611) Copyright [2006] American Chemical Society.

### 4.1. Summary

While organically bridged alkoxysilane precursors such as bis(triethoxysilyl)ethane (BTESE) find increasing use in materials synthesis, their polymerization still has not been subject to detailed kinetic investigations. One factor complicating the measurement and interpretation of the behavior of these monomers is their tendency to aggregate during polymerization into small clusters or particles. Here, the phase behavior and kinetics of BTESE during polymerization in acidic water-ethanol solutions are investigated *in situ* using  $^{29}\text{Si}$  NMR spectroscopy. Based on macroscopic observation of the colloidal stability of the reacting solutions, a ternary pseudo-phase diagram is constructed and solutions that seem from a macroscopic point of view to be favorable for kinetic investigation are probed *in situ* using  $^{29}\text{Si}$  NMR. However, even when the solutions remain optically clear, the polymerization mixtures are sometimes prone to gradual loss of NMR signal. The rate of signal loss is found to be dependent on the initial composition as well as the pH of the reacting mixtures. We speculate that this phenomenon is caused by microphase separation of reaction intermediates formed early in the polymerization process. This phenomenon is likely to affect the formation and distribution of oligomers in the solution that eventually react together to form a material.

### 4.2. Introduction

Because of their unique combinations of properties, nanostructured sol-gel materials that are molecular hybrids of organic and inorganic components are of growing interest for a wide range of applications in diverse fields including environmental science, electronics, catalysis and industrial separations.<sup>151,152,181-183</sup> Acid or base catalyzed hydrolytic polycondensation of alkoxysilane precursors (Section 1.1.3), also known as sol-gel polymerization,<sup>1,2,150</sup> constitutes the most commonly used pathway to the formation of these three-dimensional polymeric

networks and gels. Controlling the structure and properties of these materials to engineer them for specific applications (for instance, for homogeneous incorporation of monomers with diverse functional groups) requires understanding the underlying chemistry and sol-gel kinetics. *In situ* characterization of the early time polymerization reactions provides information about the structural evolution of these polymers that can be used to fine tune the reaction conditions to favor desired properties. This is especially important for network polymers which cannot be readily refined by post-synthesis techniques.

Most of the kinetic studies<sup>60,61,69,71,101,184-186</sup> of silane polymerization have focused on identification and characterization of the hydrolyzed monomers and oligomers present in solution well before gelation using <sup>29</sup>Si NMR. Silicon site-specific details extracted from <sup>29</sup>Si NMR provide a high level of information about the state of the system that enables the development and validation of mechanistic models capable of predicting structure and properties of the materials synthesized from their precursors. However, this extremely useful technique is accompanied by three main drawbacks which need to be addressed for successful application to <sup>29</sup>Si NMR in kinetic studies. First, the samples being probed must be clear homogeneous liquids. The formation of sol-gel materials may be complicated because of the phase behavior of the precursor. The sol sometimes tends to be cloudy depending on the reaction conditions due to either the kinetic growth mechanism or phase separation. Phase separation leads to an uneven distribution of the reaction components making inhomogeneous samples unsuitable for liquid-state NMR characterization. The resulting phase does not need to be a solid to exhibit line broadening that makes NMR impossible; for example, doubly-hydrolyzed tetraethoxysilane monomers have been identified as the species that initially phase separate in base-catalyzed Stöber silica solutions, and no subsequent reaction products can be observed by liquid-state NMR.<sup>187</sup> Second, the low natural abundance (4.1%) of the <sup>29</sup>Si nuclei leads to poor signal intensities. Third, slow spin-lattice relaxation of the <sup>29</sup>Si nuclei requires long delays between the pulses which hinders rapid data collection. The latter two problems can be resolved by isotopic enrichment,<sup>188-190</sup> probe designs without silicon,<sup>191,192</sup> paramagnetic relaxation agents,<sup>79,193-195</sup> and polarization transfer techniques,<sup>196</sup> but the first problem cannot be readily overcome. The purpose of the present work is to establish the conditions that favor meaningful <sup>29</sup>Si NMR characterization of bridged silanes that have not yet been systematically investigated like non-bridged organoalkoxysilanes have.<sup>60,61,69,71,101,184-186</sup>

Bridged silanes are a class of functionally reactive silica precursors with an organic group embedded between two tri-functional silicon atoms. The presence of an organic bridging group<sup>28</sup> provides for more functional and structural possibilities than can be achieved by their tri-functional counterparts. The organic groups are inbuilt into the walls of the polymeric network and do not block the pores like in the polymers formed from non-bridged precursors. Thus they are valuable additions to the sol-gel materials design toolkit that complement organically modified tri-functional or purely inorganic tetra-functional silanes.

In our research, we are specifically interested in the kinetic investigation of an ethylene bridged precursor, bis(triethoxysilyl)ethane (BTESE). Prior kinetic studies of this silane have been limited to hydrolysis reactions only.<sup>197,198</sup> While the reasons for the absence of any reports on BTESE condensation kinetics were not very clear until the onset of the present investigation, reaction conditions that enable BTESE condensation characterization may be expected to be different from those used for non-bridged silanes. The reactivity of BTESE significantly differs from other bridged alkoxysilanes and its non-bridged counterpart, methyltriethoxysilane. BTESE undergoes extensive cyclization of monomers and dimers despite quick gelation<sup>199</sup> while methyltriethoxysilane exhibits slow gelation or sometimes no gelation at all. Other bridged alkoxysilanes with longer organic bridging groups gel relatively quickly.<sup>199</sup>

Owing to its wide range of applications,<sup>200-203</sup> investigating early time kinetics of BTESE to understand the mechanisms behind these peculiar polymerization traits would be of great interest. Successful design of NMR experiments is the first step towards being able to address these issues. Here, we report the phase behavior of BTESE in acidic water-ethanol solutions to identify clear homogeneous reaction mixtures that conform to the constraints of <sup>29</sup>Si NMR. Once the homogeneity conditions are met, the reaction mixtures are probed using DEPT<sup>87</sup> (distortionless enhancement through polarization transfer) <sup>29</sup>Si NMR. The DEPT sequence has been used previously to study non-bridged silanes<sup>49-51,58,59,104,161,162,186</sup> and shown to improve the <sup>29</sup>Si NMR signal intensities and data collection time by transferring the magnetization from highly abundant and quickly relaxing hydrogen nuclei to rarer <sup>29</sup>Si nuclei. Consistent with expectations, we have found that the signal intensities double and the inter-pulse delay can be reduced from 150 s (3\*T<sub>1</sub> of BTESE) to 15 s by the application of DEPT <sup>29</sup>Si NMR for BTESE. However, the surprising finding for this system is that under acidic conditions, macroscopically homogeneous solutions still exhibit loss of NMR signal with progress of the polymerization

reactions, in some cases quite dramatic. The potential causes for this behavior will be discussed in relation to macroscopic observations of phase and gelation behavior. Loss of NMR signal has been observed during the nucleation and aggregation of other systems, and hence is of general interest in colloid science and materials synthesis.

### 4.3. Experimental

#### 4.3.1. Materials

1,2-Bis(triethoxysilyl)ethane (>95% pure) was purchased from Gelest Inc. Deionized ultrafiltered water and concentrated aqueous HCl were obtained from Fisher Scientific, and absolute ethanol (200 proof, 99.5% ACS reagent) from Sigma Aldrich. All materials were used as received.

#### 4.3.2. Phase Behavior Characterization

All samples were prepared by adding acidic water to a mixture of BTESE in ethanol. The pH of the water used for synthesis of the samples was adjusted by the addition of HCl. All reported pH values discussed here are nominal values based on the expected concentration of HCl in the water used to prepare the materials following dilution of 1N HCl. A series of samples was prepared to investigate macroscopic phase separation across the entire range of BTESE/ethanol/water mole ratios. The pH of the water used to prepare these samples was fixed at 3. A subset of these samples that appeared to remain transparent and in a single phase were observed using DEPT  $^{29}\text{Si}$  NMR over a period of 4 days unless they reached gelation first. In addition to this, we also investigated the following set of samples using NMR over a range of time periods. The corresponding compositions are indicated in the ternary diagram (Figure 4.1). The compositions provided below are the final values after mixing together all ingredients and the reported pH is that of the water used to prepare the solutions.

Sample **a**: 1.7 M BTESE,  $\text{H}_2\text{O}/\text{BTESE}=0.5$ , pH=1 and pH=2.2

Sample **b**: 0.6 M BTESE and  $\text{H}_2\text{O}/\text{BTESE} = 6$ , pH=2.1

Sample **c**: 1.4 M BTESE,  $\text{H}_2\text{O}/\text{BTESE} = 4$ , pH=2.4

Sample **d**: 1.2 M BTESE,  $\text{H}_2\text{O}/\text{BTESE}=2$ , pH=1.3 and 3.6

#### 4.3.3. Gel Time Characterization

The samples used to study the gelation characteristics of BTESE were prepared in cylindrical glass vials (2.5 cm diameter, 30 mL capacity) by the addition of water and HCl to BTESE dissolved in ethanol. The molar ratio of ethanol to BTESE ( $y$ ) was varied in order to study the effect of monomer concentration on gelation time. The nominal pH of all solutions was decreased to 2 by adding appropriate amount of 0.1 N HCl to the solution mixtures. Except for the gelation studies described here, all pH values reported in this study correspond to the nominal pH of the water used to prepare the samples. The molar ratio of the components after mixing was BTESE: ethanol:  $H_2O = 1: y: 12$  ( $y = 1, 2, 3, 4, 5, 6$ ). These compositions are indicated by the line  $l$  in the ternary diagram. After shaking the solutions vigorously, the mixtures were left undisturbed in closed glass vials until they became viscous. Gelation time was determined as the time that elapsed from the point of mixing the sample to that at which the liquid ceased flowing upon being tilted by 90 degrees. All of these samples were prepared and observed at room temperature.

#### 4.3.4. NMR Characterization

NMR experiments of optically clear samples were performed without  $^2H$  locking at room temperature ( $21 \pm 1$  °C) on a Varian 400 MHz spectrometer tuned to  $^{29}Si$  at 79.5 MHz. The 90-degree pulse width of  $^{29}Si$  was set to 11.8  $\mu s$  and an inter-pulse delay of 15 s was used. For DEPT experiments, the angle of the last proton pulse was set to 20° and the transfer time to 72 ms. 1 wt% of chromium acetylacetonate, a paramagnetic relaxation agent, was mixed with ethanol used in the samples when DEPT was not employed. This compound is known to reduce the relaxation time of the  $^{29}Si$  nuclei.<sup>204-206</sup>  $^{29}Si$  NMR chemical shift assignments are referenced to the chemical shift of BTESE with respect to tetramethylsilane. For  $^1H$  NMR spectra, a 90-degree pulse width of 7  $\mu s$  and a delay of 5 s were used, and the chemical shifts were referenced to tetramethylsilane. All  $^{29}Si$  NMR spectra were collected with 16 transients and a spectral width equal to 3000 Hz unless specified otherwise.  $^1H$  NMR spectra were collected with 4 scans each and spectral width equal to 6500 Hz. If exponential line broadening (lb) was applied to process the FIDs (free induction decay), it is provided in the Figure captions of the respective spectra.

#### 4.3.5. FTIR Characterization

*In situ* FTIR spectra of sample **b** were acquired at  $21 \pm 1$  °C using a Thermo Nicolet Nexus 470 series spectrometer equipped with a DTGS detector. Each spectrum was averaged over 16 scans and the resolution was  $4.0 \text{ cm}^{-1}$ . A demountable flow-through stainless steel liquid transmission cell (Pike Technologies) equipped with germanium windows separated by two mismatched PTFE spacers (Harrick Scientific) with thicknesses of 0.006 and 0.012 mm was used to hold the sample. The sample was injected by syringe into the cell shortly after mixing all ingredients together and monitored over time by intermittent spectrum collection.

#### 4.4. Results and Discussion

##### 4.4.1. Phase Behavior in Acidic Ethanol-Water Solutions

A ternary pseudo-phase diagram has been constructed by observing the physical nature of BTESE, ethanol and water mixtures and the NMR behavior of transparent solutions. Figure 4.1 summarizes composition regions corresponding to five different appearances of these mixtures. Regions A through C (with subdivisions based on the dynamic evolution of the systems) showed obvious macroscopic phase separation after all ingredients were mixed. Samples appeared to be cloudy suspensions in region A. Region A corresponds to reaction mixtures with high water content and low BTESE and ethanol concentrations. Initially, two cloudy phases were visible which gradually turned into a single phase and formed cloudy gels in this region. Region B (subdivided into B1 and B2) corresponds to the compositions that formed two clear liquid phases. The immiscibility was temporary for samples in region B1, which contained relatively large amounts of solvent and eventually formed clear gels. In contrast, samples in region B2 maintained two clear phases until one of them turned into a transparent gel. Solutions in regions C1 and C2 initially had two phases which were either cloudy (C1) or clear (C2) and eventually formed a white solid precipitate. Mixtures in regions D and E remained macroscopically homogeneous from the time of their preparation. Some of these solutions gradually formed clear gels and the gel times increased with decreasing water content.

Based on the above observations, the phase behavior of these mixtures can be correlated with the composition of the individual components. The miscibility of these mixtures decreases with decreasing quantities of ethanol in the solution (with a boundary of about 40 mol% ethanol required for miscibility across most compositions). The end product is a gel for low BTESE mole



fractions and is a precipitate for higher values. The gels formed with high initial compositions of water were cloudy and those with moderate water content were clear. With decreasing water content, the gelation time increased. No gelation was observed for very low water solutions even after 2 months (sample **a** (pH=2.2), for example). This may be because of limited reactions occurring before equilibrium is established. We monitored the gel times for a subset of these compositions, indicated by the connected dots ( $\bullet$ ) in the ternary diagram (Figure 4.1) but at a pH value of 2 for all of the solution mixtures. Ethanol to BTESE molar ratios greater than 3 resulted in transparent gels (region B1). For  $y \leq 3$ , the compositions fall in region A of the ternary diagram and macroscopic phase separation occurred as expected. The variation of gelation time ( $t_g$ ) as a function of the initial monomer concentration is displayed in Figure 4.2. The decrease of  $t_g$  with an increase in initial concentration of BTESE can be related to the increased rates of hydrolysis and condensation. This variation is described by a power law equation as

$$t_g = A [\text{BTESE}]_0^a$$

with a prefactor  $A \sim 18$  days and  $a \sim -5.4$ . Similar power law dependence was reported for the tetramethoxysilane-water-methanol system under basic conditions.<sup>207</sup> In this case  $A = 6900$  s and  $a = -3.2$ . Also, the gelation time of BTESE is relatively high when compared to other alkylene bridged precursors which gel quite fast under similar conditions.<sup>91</sup> For example, Loy et al.<sup>91</sup> reported that 1,10-bis(triethoxysilyl)decane formed a gel within 6 hours when compared to BTESE that took 720 hours to gel under similar conditions.<sup>199</sup> The prolonged gel time of BTESE may be due to the cyclization process occurring early in the sol-gel process.<sup>91,208</sup> The five-atom cyclic monomer (structure provided in Figure 4.3) formed from the condensation of the monomer, or larger rings formed from the dimers<sup>91</sup> may be reacting very slowly in further polymerization reactions, thus increasing the gelation time. The large power-law coefficient is consistent with cyclization interfering with gelation. Without cyclization, the power would be expected to be -1 because even with first-shell substitution effects, the rates of all bimolecular polycondensation processes scale in the same way such that there should be an inverse relationship between concentration and time to reach the gelation conversion (which is also expected to be fixed in the absence of cyclization).<sup>209</sup> The severe concentration dependence observed here reflects the influence of cyclization, and possibly of additional aggregation phenomena in solution that delay gelation severely as the BTESE concentration decreases.

The regions of interest for NMR experiments are D and E where the mixtures remained optically clear. However, it was observed that samples in region D are prone to gradual loss of NMR signal. Notable signal intensities were completely absent for some samples (sample **b** for example). Only the reaction mixtures in region E are favorable for NMR experiments, as they exhibited negligible signal loss over the course of observation. The characterization of these solutions and the possible causes of signal loss are discussed in the remainder of this paper.

#### 4.4.2. Characterization under NMR-Favorable Conditions

Figure 4.3 shows a series of DEPT  $^{29}\text{Si}$  NMR spectra collected over a period of 15 hours for sample **a** (pH=1). For this experiment, the composition chosen is such that the solution remains macroscopically clear and homogeneous throughout the experiment and the sample does not display any apparent signal loss (discussed below). Similar results were found using water with pH=3 although the time scale for a comparable change in the spectra was 144 hours. Some peaks in the spectra (Figure 4.3) are identified according to the assignment patterns of Myers et al.<sup>210</sup>. The monomer appears at -46.1 ppm. Similar to other ethoxysilanes, BTESE shows a small downfield shift, to -43.9 ppm, upon hydrolysis of the monomer. Accompanying the appearance of this hydrolyzed monomer peak, the unhydrolyzed silicon site at the other end of the bridged precursor shifts downfield to -45.6 ppm. These types of shifts due to hydrolysis at a remote site are not normally visible in sol-gel NMR spectra of non-bridged organoalkoxysilane precursors, and may indicate unusually strong electronic coupling between the silicons at both ends of the bridged precursor. As expected, the intensities of the two silicon sites at both ends of the single-hydrolyzed monomer remain equal throughout the reaction. The peak with the greater chemical shift change relative to BTESE is assigned to the hydrolyzed end because the electronic effect of substituting an ethoxyl group with a hydroxyl group is expected to be greatest at that end.

In addition to hydrolysis products, condensation products are also visible in Figure 4.3. The resonance near -41.0 ppm that is shifted far downfield from the monomer is attributed to a 5-atom cyclic structure formed by the condensation between the silicon sites at both ends of the bridge.<sup>39,91,211</sup> Even though the formation of a siloxane bond normally causes an upfield shift, the distortions in electron density and shielding caused by ring formation lead to strong downfield shifts.<sup>59,69,75</sup> This condensation peak is the first to appear but interestingly, the intensity of the 5-atom cyclic species passes through a maximum, indicating that it is a metastable intermediate.

Over the course of polymerization, two additional peaks at -51 ppm and -53.3 ppm appear upfield from the monomer and grow in intensity. Loy et al.<sup>91</sup> assigned these peaks to a bicyclic dimer species (shown in Figure 4.3). However, this assignment is ambiguous in the present case because the peaks are not always equal in intensity. The bicyclic dimer contains an equal number of singly- and doubly-condensed silicon sites, so we would have anticipated that both peaks would appear simultaneously and would grow in intensity together. Spectral editing using the DEPT pulse sequence would be required to make definitive peak assignments, but for now we can safely state that these are condensed silicon sites not involved in rings as highly strained as the cyclic monomer. Continued evolution of the system leads to the appearance of more condensed products which can potentially be assigned through spectral editing and reaction parameter variations, but the focus of the current work is the surprising case in which no macroscopic phase separation occurs but NMR signal is still lost.

#### **4.4.3. Characterization under Signal Loss Conditions**

The observed loss of NMR signal could be associated with spectrometer irregularities, changes in the parameters that influence the DEPT pulse sequence during reaction, or reaction abnormalities specific to the systems being studied. We performed the following investigations to gain further insight on the cause of the signal loss.

##### **4.4.3.1. Characterization using FTIR**

FTIR can be employed to complement the NMR experiments without the homogeneity constraint (since negligible light scattering is observed in the macroscopically homogeneous systems). However, it provides only functional group information and therefore, is not as detailed as the NMR technique. Here, we used FTIR to confirm that NMR signal loss is not due to any discrepancies in the polymerization reactions of the samples. Sample **b** did not show any detectable signal by <sup>29</sup>Si NMR 20 minutes after its preparation (Figure 4.4a). Note that the Free Induction Decay (FID) of this sample also shows a complete absence of signal under conditions where samples with a comparable total dissolved silicon concentration show obvious intensity. FTIR spectra collected for the same sample for a period of 1 hour are shown in Figure 4.5 as an illustration of the types of band changes associated with the polymerization reactions that occur. The bands representing H<sub>2</sub>O, ethoxy and hydroxyl groups attached to silicon sites and CH<sub>3</sub>CH<sub>2</sub>OH indicated in Figure 4.5 are assigned in agreement with the work of Pu et al.<sup>197</sup> From 2.85 min. to 57.85 min., the peaks corresponding to water (1650 cm<sup>-1</sup>) and ethoxy groups (1167

$\text{cm}^{-1}$ ) in BTESE are observed to decrease as expected if hydrolysis reactions are occurring. The band corresponding to silanol ( $950 \text{ cm}^{-1}$ ) first increases due to hydrolysis and then gradually decreases due to subsequent condensation reactions. These trends are consistent with prior FTIR studies of BTESE<sup>197,212</sup> and similar bridged alkoxysilanes<sup>212</sup> and provide evidence of the progress in polymerization reactions showing that the observed absence or loss of NMR signal is not because of a drastic change in the nature of the reactions that proceed in the NMR mixtures (for instance, there is no evidence that condensation has become the rate-determining step in these mixtures).

#### 4.4.3.2. DEPT <sup>29</sup>Si NMR vs. Single Pulse <sup>29</sup>Si NMR

Another possible reason for the apparent loss of NMR signal intensity could be the use of a constant delay  $\Delta$  in the DEPT experiments. To maximize the intensity of the spectra when using DEPT to enhance signal intensity, this value is usually set to  $\Delta = 1/(2J)$  where  $J$  is the strongest silicon-to-proton scalar coupling constant for the molecule (here  $J = 6.9 \text{ Hz}$ ). We expect the strongest coupling in BTESE to come from  $^2J(\text{Si,H})$  between a silicon site and the protons in the ethylene bridge. However, the splitting pattern induced by coupling to bridging protons in BTESE is influenced by second-order effects<sup>213</sup> and DEPT intensities may not be as constant as they are in non-bridged monomers such as methyltriethoxysilane. Also, the scalar spin-spin couplings that govern the polarization transfer may be changing with the structure of the oligomers, which would be expected to change DEPT intensities. In order to check whether this is the cause for the apparent signal loss that we observed, we collected <sup>29</sup>Si NMR spectra of sample **c** with and without employing DEPT (Figure 4.6a and 4.6b). While signals are improved in the DEPT spectra (Figure 4.6a), there is signal loss evident without the use of DEPT (Figure 4.6b) as well. This confirms that the loss of signal cannot solely be attributed to inconsistencies in use of the DEPT technique for oligomers of different structure.

#### 4.4.3.3. <sup>29</sup>Si NMR vs <sup>1</sup>H NMR

As another check on whether the signal loss is somehow unique to the challenges of <sup>29</sup>Si NMR, we compared ordinary <sup>29</sup>Si NMR and <sup>1</sup>H NMR for the same sample **c**. Figure 4.6b shows a series of <sup>29</sup>Si NMR spectra collected at different times over a period of 10 hours for this sample. The species observed during the first few minutes of reaction can be unambiguously assigned to the monomer and its product after being hydrolyzed once, as explained earlier. After 4 h of reaction, the monomer is not observed anymore. The progress in reaction is evident from the

peaks appearing downfield and upfield of -46.1 ppm (where the monomer peak had been observed) which can be associated with the products of hydrolysis and condensation respectively (see above for discussion of peak assignments). The peaks from hydrolyzed species disappear after 10 h of reaction with an increased range of observed chemical shifts from condensation products, but the overall intensity of the integrated  $^{29}\text{Si}$  NMR spectrum declines by 70% from its initial value at this point (Figure 4.7).

In order to rule out specific abnormalities associated with  $^{29}\text{Si}$  NMR, the same sample was probed by  $^1\text{H}$  NMR. There are four sets of peaks observed at the onset of polymerization by  $^1\text{H}$  NMR (Figure 4.6c). The singlet at 0.3 ppm (referenced to tetramethylsilane) belongs to the four equivalent hydrogen nuclei in the ethylene bridge of the monomer. There are two triplets near 1 ppm that represent the  $\text{CH}_3$  protons in the ethoxy groups of the monomer and in ethanol. The  $\text{CH}_2$  protons from the same functional groups are represented by the quadruplets downfield to the triplets between 3.5 and 4 ppm. The protons in the OH groups of ethanol and water are represented by the singlet at 4.9 ppm. With progress in reactions, the OH peak broadens and shifts downfield due to rapid exchange among water, ethanol and silanols. The other peaks broaden somewhat and overlap with each other and the distinct  $\text{CH}_2$  proton peak from the ethoxy groups disappears, although it is not clear whether this is simply due to hydrolysis. The best indication of the state of the system comes from the protons in the bridging group, which seem to spread across a range of chemical shifts as diverse structures of oligomers are formed. This broadening of the variety of chemical shifts and the intensity of the solvent peaks makes it difficult to visually observe whether the intensity of the  $^1\text{H}$  signal associated with the siloxane products is preserved. Therefore, the integral of the bridging proton peak is measured with time and plotted in Figure 4.7. In the absence of signal loss this integral would remain constant, which is not observed to be the case; discernable signal is essentially gone after 12 hours of reaction in sample **c**. The rate of signal loss is observed to be faster in  $^1\text{H}$  NMR than in  $^{29}\text{Si}$  NMR. This may either be due to the slower tumbling of bridged protons in the interior of the aggregates formed during microphase separation, or greater sensitivity to the solid-like signal broadening from the single bridging  $^1\text{H}$  peak compared to the array of  $^{29}\text{Si}$  NMR peaks used to determine the total integrated intensity. Nevertheless, the qualitative agreement in conditions causing signal loss confirms that signal loss is due to the physical state of the system, which affects both  $^{29}\text{Si}$  and  $^1\text{H}$  NMR, and thus rules out the possibility that the DEPT parameters or

other measurement irregularities associated with  $^{29}\text{Si}$  cause the observed loss of NMR signal in region D.

#### 4.4.3.4. Effect of Water Content on Signal Loss

Now that we have established that the signal loss phenomenon is not an artifact of the behavior of  $^{29}\text{Si}$ , the effects of composition on the signal loss are further explored. First,  $^{29}\text{Si}$  NMR spectra of sample compositions falling in regions D and E for varying  $\text{H}_2\text{O}/\text{BTESE}$  ratios are discussed. Normalized total integrated signal intensities measured with time from the single pulse  $^{29}\text{Si}$  NMR spectra collected for samples **a** ( $\text{H}_2\text{O}/\text{BTESE} = 0.5$ ) and **c** ( $\text{H}_2\text{O}/\text{BTESE} = 4$ ) are plotted in Figure 4.7. For sample **b** ( $\text{H}_2\text{O}/\text{BTESE} = 6$ ), signal was completely lost immediately after sample preparation (Figure 4.4a). If the solutions remain in a single liquid phase, the total integrated intensity of NMR peaks would be expected to remain constant with time as long as adequate time is permitted for complete relaxation of all species between pulses. From Figure 4.7, it is obvious that the signal loss is gradual and increases with increasing amounts of water in the system. For sample **a** there is no apparent loss of signal over the entire time the reactions were monitored. In contrast, for sample **c** with more water added to promote hydrolysis, signal is gradually lost as the reaction proceeds. For sample **b** with still more water, NMR signal is lost immediately but FTIR indicates that the trends in reaction rates are consistent with any other acid-catalyzed ethoxysilane. It is also observed from Figure 4.1 that region D is associated with higher concentrations of water than region E, consistent with the effect of water on the rate of signal loss. Large amounts of water are expected to promote more complete hydrolysis of the silane species in solution and a greater variety of oligomeric intermediates which may only exist as isolated species in solution at concentrations below the level of detection by NMR. Free water may also play a role in signal loss, although even sample **b** has only the stoichiometric amount of water needed for complete hydrolysis of BTESE.

#### 4.4.3.5. Effect of pH on Signal Loss

$^{29}\text{Si}$  NMR spectra collected for samples with the composition of sample **d** and with water pH=3.6 and 1.3 are shown in Figure 4.8a and 4.8b respectively. At a pH of 3.6, condensation is slower than at pH=1.3. It is observed from Figure 4.8a that the monomer hydrolyzes at a slow pace and condensation is not very prevalent even after 15 hours of reaction. The peaks from hydrolyzed species decrease in intensity without the appearance of any peaks from condensed species, indicating that the loss of signal is due to products from further reactions of the

hydrolyzed monomeric species. This is analogous to the situation observed for sol-gel solutions under Stöber synthesis conditions in which Lee and McCormick implicated double-hydrolyzed monomers as the species that initiates the loss of NMR signal.<sup>187</sup> An important difference is the fate of those species, however; the tetraethoxysilane species rapidly aggregate into colloidal droplets that eventually become solid particles. Assuming that BTESE is consistent with other silanes, a lower pH implies increased catalyst concentration which should accelerate the sol-gel reactions, although the net effect on the competition between hydrolysis and condensation depends on the point of zero charge of the precursor. At pH=1.3, signal loss occurs at a faster rate than at high pH and the signal almost disappears after 1.1 hours of reaction, indicating that increase in reaction rate increases the rate of signal loss. However, species are detected upfield of the monomer after 36.5 minutes, which indicates that condensed products are detectable, and perhaps somewhat more stable in solution than at pH 3.6.

#### 4.4.4. Correlation between Signal Loss and $T_2$

As noted above, conditions that favor loss of signal also favor faster reactions and therefore lead to diversification of the chemical shifts of the species in solution. This can have the undesired consequence of introducing many low-intensity peaks into the spectrum that are difficult to fully observe, whereas loss of signal due to solid-like behavior can be confirmed by short spin-spin relaxation times ( $T_2$ ). As representative samples, we consider two samples, **a** (pH=2.2) and **b**, the first of which exhibits no NMR signal loss (Figure 4.4c) and the other exhibits significant signal loss (Figure 4.4a and 4.4b). As discussed above, sample **b** shows complete signal loss after 20 min. of reaction (Figure 4.4a) even though the solution appears to be a single homogeneous phase. After 2 months of reaction, there is only a broad peak from the same reaction mixture (Figure 4.4b), which is found downfield from the peak originating from the glass of the NMR tube (near -110 ppm). The sample whose spectra are shown in Figure 4.4c remained an optically clear solution and did not lose the signal even after 2 months of reaction. Due to limited water, a large concentration of monomer remains unreacted but condensation products are clearly observed upfield of the monomer. Peaks from hydrolyzed species are not observed in the spectra after 3 hours of reaction indicating complete condensation of the hydrolyzed species. The insets in these figures show the FIDs of the spectra. The FID in Figure 4.4a and 4.4b decayed completely within 0.002 s (indicating a  $T_2$  value significantly less than that) while the FID for the spectra in Figure 4.4c decay within 0.1 s, indicating that  $T_2$  is roughly 2

orders of magnitude smaller in samples exhibiting signal loss. Therefore, the broad peak observed in sample **b** (Figure 4.4b) is not from a broad distribution of species with liquid-like  $T_2$  values, but instead is a result of the species having short, solid-like  $T_2$  values. This occurs despite the homogeneous, clear appearance of the solution which indicates negligible formation of particles large enough to scatter light.

#### 4.4.5. Explanation by Microphase Separation

From the results above, the most likely explanation for signal loss in samples with large water and ethanol contents (region D in Figure 4.1) is that the hydrolyzed intermediate products of BTESE polymerization enter into an environment where fast tumbling cannot occur, most likely due to microphase separation (or molecular aggregation). Various instances of the loss of NMR signal due to change of phase of silicon-containing species have been reported in literature. As mentioned above, McCormick's group<sup>187</sup> confirmed through mass balance calculations that the Si lost from the NMR spectra collected during Stöber silica particle synthesis can be attributed to particles that are detectable with photon correlation spectroscopy. The doubly hydrolyzed monomer ( $\text{Si}(\text{OC}_2\text{H}_5)_2(\text{OH})_2$ ) was identified as the unstable species that first disappeared from the spectra. It is not known whether the particles were fully rigid at the point that signal was lost, but the particles are facile enough to undergo aggregation early in their formation<sup>214</sup> while still finally adopting a spherical shape. Perhaps a better analogy was found in the report of Rankin et al.,<sup>72</sup> who observed the loss of NMR signal 20 minutes after the polymerization reaction of trimethylethoxysilane was initiated. In their case, the system did not (and could not since the only condensation product is a liquid at room temperature) produce any solid precipitates. Therefore, they concluded that the formation of a solid phase is not necessary to observe loss of  $^{29}\text{Si}$  NMR signal in sol-gel solutions. Unlike zeolite synthesis solutions, the trimethylethoxysilane solutions contained no quaternary ammonium ions either, so spontaneous microphase separation or aggregation among hydrolyzed species is the most likely cause for signal loss. Eventually the solutions did separate into two liquid phases and the signal was regained when an appreciable amount of the second phase was formed, but prior to the phase forming signal loss was observed. Signal loss in this case was attributed to hexamethyldisiloxane microphase separation and accompanied with a new chemical shift in the spectrum.<sup>72</sup> In a similar fashion, Kirschhock et al.<sup>215</sup> also detected changes in  $^{29}\text{Si}$  NMR chemical



shift when organic solvent selectively interacted with small silicate entities providing a different environment from the original aqueous phase.

This phenomenon of signal loss due to microphase separation in optically clear liquids is analogous to what is commonly observed during nucleation in clear solution zeolite synthesis.<sup>216-218</sup> Fedeyko et al.<sup>219</sup> and Rimer et al.<sup>220</sup> reported evidence that silica oligomers co-assemble with alkylammonium cations above a critical aggregate concentration, with accompanying changes in pH and conductivity. Follens et al.<sup>221</sup> characterized clear solutions obtained during silicalite-1 synthesis using liquid <sup>29</sup>Si NMR. They observed that the dissolved silicate oligomers gave sharp peaks while particles produced broad signals. Petry et al.<sup>222</sup> showed that the nanoparticles found in clear zeolite synthesis solutions initially form by aggregation of silicate oligomers, which subsequently condense further into particles that begin to be detectable when they are 8-10 Å in size. Petry et al. attributed signal broadening in nanoparticles to chemical shift variability in the particles, but another possibility is a decrease in T<sub>2</sub> due to a decreased rate of tumbling of the nanoparticles in solution. While it has not been associated with complete signal loss, such broadening has been observed in pre-micellization of amphiphilic compounds below their critical micelle concentration.<sup>223</sup> Mintova and Valtchev<sup>224</sup> found that the size of the primary species in the precursor mixtures is strongly dependent on the silica source employed. To search for evidence that BTESE is undergoing a similar phenomenon, we used dynamic light scattering to observe our solution mixtures. However, we were unable to clearly detect the presence of particles. This may be because of the low refractive index variation between the two phases or because the aggregates are too small and too dilute to cause appreciable light scattering. Nevertheless, by analogy with the studies cited here, we suspect that in region D, the hydrolysis products of BTESE self-assemble into aggregates which do not tumble quickly enough to appear as liquids in NMR. This self-assembly may occur because of the amphiphilic nature of partially hydrolyzed organoalkoxysilanes. Analogous assembly occurs in zeolite precursor solutions; Kragten et al.<sup>225</sup> extracted well-defined sub-colloidal particles observed during the clear solution synthesis of silicalite-1 to characterize them. The ability to extract these particles from an aqueous solution suggests that they had appreciable non-polar character and thus that self-assembly played a role in their formation.

Another secondary contribution to signal loss may be from the diverse array of species found during BTESE polymerization. Cheng and Shantz<sup>226</sup> examined by <sup>29</sup>Si NMR, solutions

containing 2 nm particles along with a small fraction of 20 nm particles as part of an investigation of silica speciation during silicalite-1 synthesis. The larger particles were not observable in  $^{29}\text{Si}$  NMR because of their low number density when compared to the smaller ones. Along similar lines, in our systems, the species present during microphase formation may represent very low concentrations of a large number of species that are below the threshold of NMR detection. This is more likely to be a problem with bridged precursors due to their high functionality and long-range sensitivity of chemical shift to substitution reactions. Clearly there are more possible oligomer structures that could result from reactions of bridged precursors, potentially causing detection difficulties in NMR characterization not encountered with non-bridged silanes. However, broadening due to oligomer diversity is usually not a problem in the absence of microphase separation and at least the degrees of hydrolysis, siloxane bond connectivity and cyclization of species can be quantified by  $^{29}\text{Si}$  NMR in non-bridged silane systems, as is evident from their extensive studies using this technique.<sup>49-51,54,60-63,96,185,227,228</sup> Thus, the more likely explanation for signal loss in macroscopically homogeneous phases is aggregation into molecular clusters where restricted motion leads to broadening of the peaks of species to the point that they are no longer detectable under the conditions of the experiment.

#### 4.5. Conclusions

The results reported here illuminate significant and somewhat surprising challenges involved in applying NMR technique to characterize bis(triethoxysilyl)ethane polymerization systems. The phase behavior of bis(triethoxysilyl)ethane was studied in acidic water-ethanol solutions over the entire range of compositions of these three components and summarized in the form of a ternary diagram to identify the conditions favorable for  $^{29}\text{Si}$  NMR characterization. As with all alkoxy silanes, the starting monomer and water are immiscible, so it was not surprising to find two-phase regions and regions that produce cloudy gels or particles. However, it was also found that some macroscopically homogeneous solutions exhibited signal loss during NMR experiments. The loss of signal was demonstrated to occur not only when the DEPT pulse sequence was employed, but also with single-pulse  $^{29}\text{Si}$  NMR and  $^1\text{H}$  NMR. The rate of signal loss increased with decreasing pH and increasing water content in the systems, both of which favor rapid accumulation of partially hydrolyzed monomers and oligomers. The FIDs of spectra collected for samples losing signal indicated that the broadening of signal was not only caused by chemical shift diversification in liquid-phase species, but also that  $T_2$  of the samples

decreased substantially, consistent with the loss of rapid tumbling of liquid-like species in solution. These results together suggest that aggregation or microphase separation of partially hydrolyzed monomers/oligomers is responsible for the loss of signal in polymerizing BTESE solutions with large water to monomer ratios. The bridging organic may accentuate this aggregation compared to previous observations of non-bridged organoalkoxysilane systems. This phenomenon is analogous to the aggregation of oligomers that occurs during nucleation in clear solution zeolite synthesis. Phase separation in organically modified silicates and mixtures of silicates and organic templates is vitally important in materials synthesis, and will be worth further exploration, although new tools will be needed to supplement liquid-state NMR.

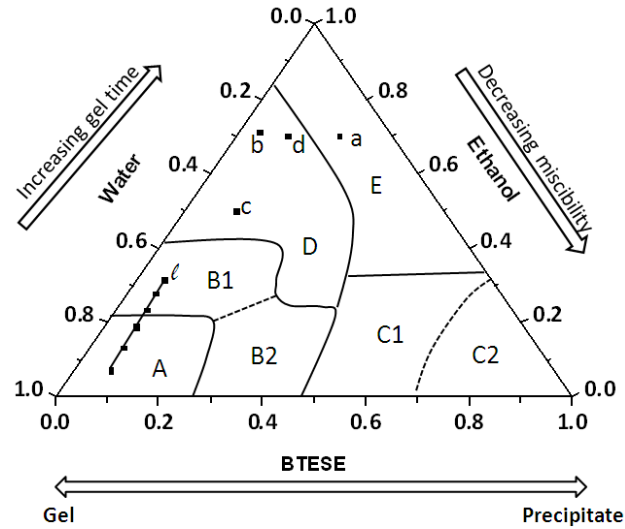


**Figure 4.1.** Ternary pseudo-phase diagram of BTESE, ethanol and water (pH=3) mixtures. The axes are mole fractions of the labeled components. The line  $l$  represents the compositions used for developing the gelation power law (Figure 4.2). The regions correspond to (A) 2-phase systems that formed a cloudy gel, (B) 2-phase systems that formed a clear gel, (C) 2-phase systems that formed precipitates, (D) 1-phase systems that remained clear but lost NMR signal at some rate, and (E) 1-phase systems that were clear and preserved NMR signal intensity.

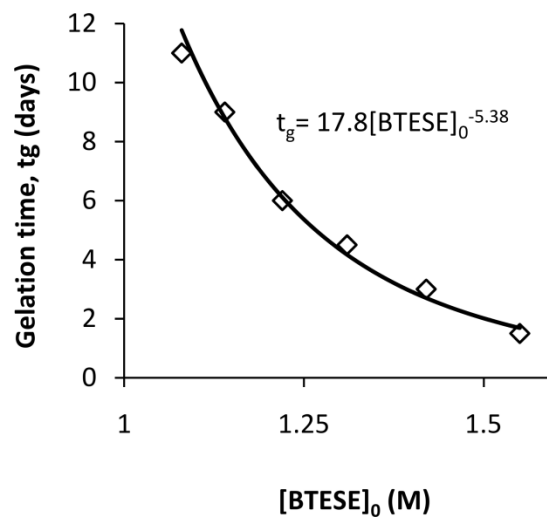


**Figure 4.2.** Variation of gel time ( $t_g$ ) as a function of initial concentration of BTESE for solutions (pH=2) prepared with a H<sub>2</sub>O: BTESE ratio of 12. Points are measured gel time values and the curve is a power law fit giving the equation shown on the plot.

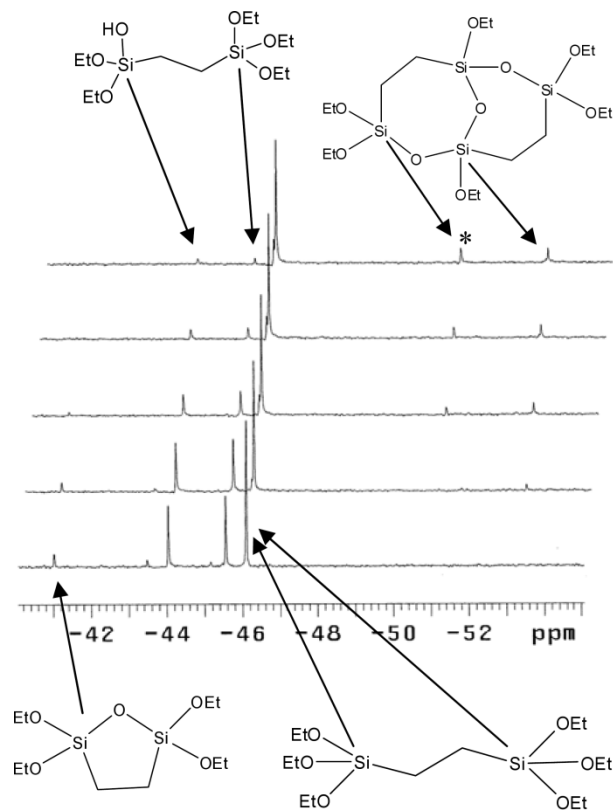


**Figure 4.3.** DEPT  $^{29}\text{Si}$  NMR spectra of sample **a** (pH=1) processed with line broadening parameter  $lb=1$ . From bottom to top, the spectra were collected 0.1, 0.8, 3.6, 8, and 15.3 h after mixing all ingredients together. The total integrated intensity of the NMR signal was preserved over the course of observation. Peak assignments marked with an \* have been adapted from reference.<sup>91</sup>

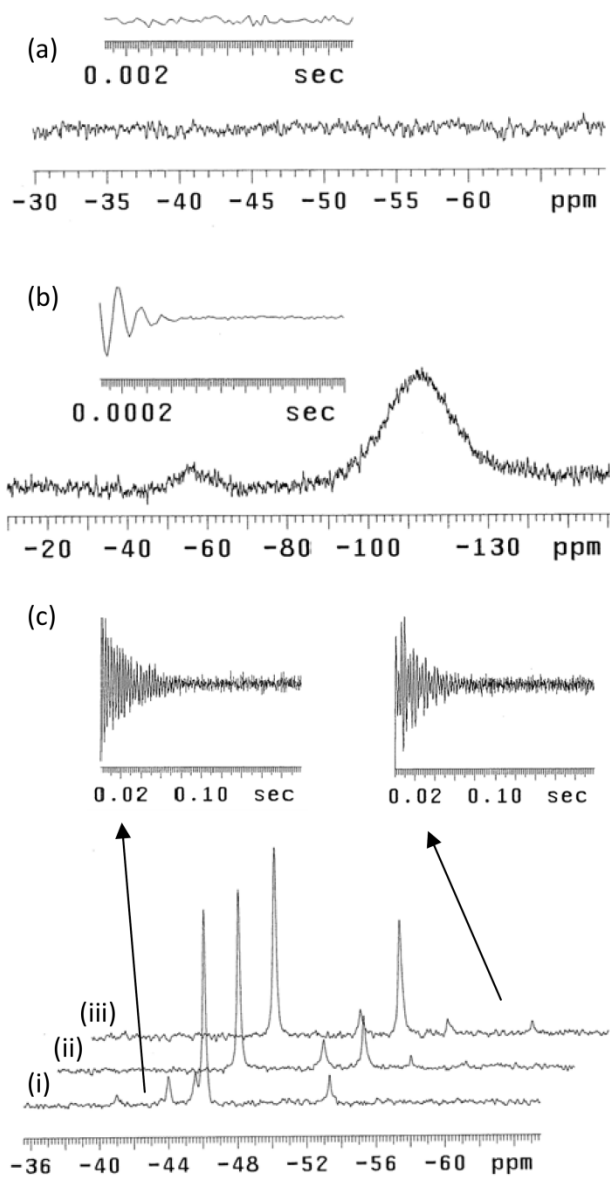


**Figure 4.4.** Single-pulse  $^{29}\text{Si}$  NMR spectra collected for (a) sample **b** (pH=2.1) after 20 min. of reaction with  $l_b=5$  and averaging of 64 scans over a spectral width of 3000 Hz; (b) sample **b** (pH=2.1) after 2 months of reaction with a spectral width of 50000 Hz, an average of 64 scans and  $l_b=10$ ; (c) sample **a** (pH=2.2) after (i) 1.5 min, (ii) 2.7 h and (iii) 2 months of reaction. Spectra in (c) are averages of 16 scans over a spectral width of 5000 Hz and  $l_b=5$  is applied. The insets are the FIDs of the spectra adjacent to them or as indicated by arrows.

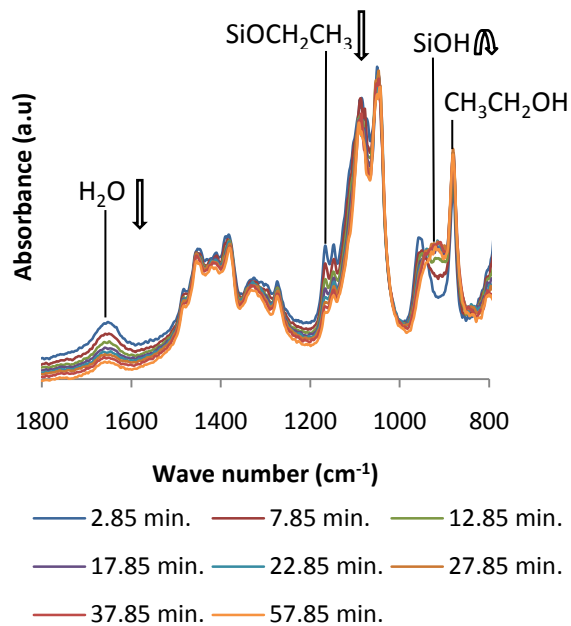


**Figure 4.5.** (a) FTIR spectra of sample **b** (pH=2.1) collected for a period of 1 hour. The arrows indicate the direction of evolution (increase or decrease) of the corresponding species with time. The legend indicates the time at which each spectrum was collected.



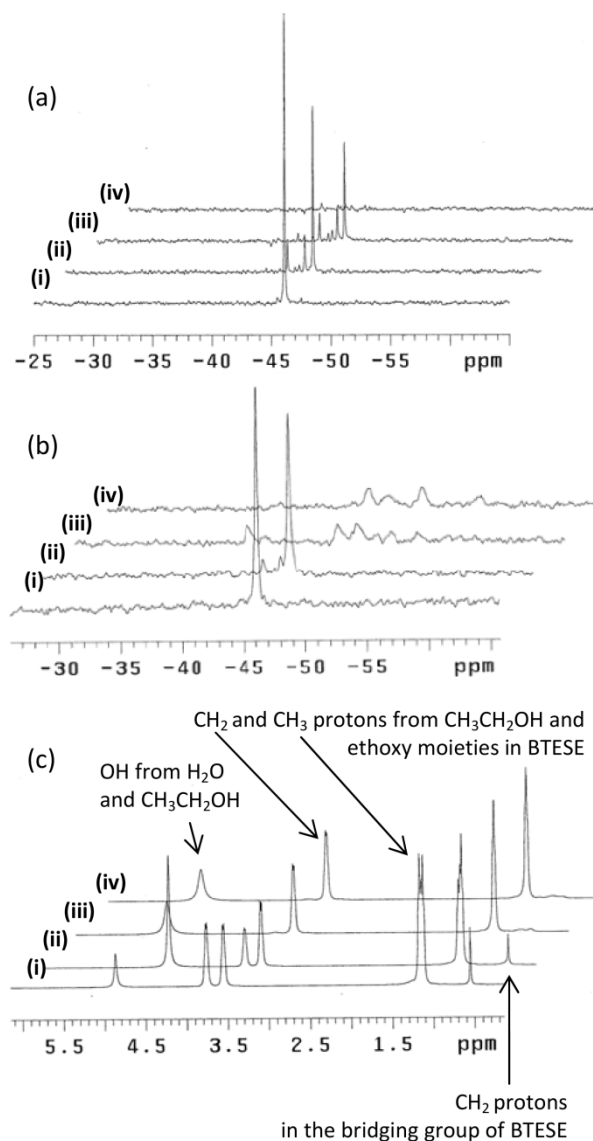


**Figure 4.6.** (a) DEPT  $^{29}\text{Si}$  NMR ( $l_b=5$ ) spectra of (i) 1.4 M BTESE in ethanol, and sample **c** (pH=2.4) collected after (ii) 6 min., (iii) 19 min. and (iv) 36 min. of reaction. (b) Single-pulse  $^{29}\text{Si}$  NMR ( $l_b=10$ ) spectra of (i) 1.4 M BTESE in ethanol, and sample **c** (pH=2.4) collected after (ii) 6 min., (iii) 4 h and (iv) 10 h of reaction and (c)  $^1\text{H}$  NMR spectra of (i) 1.4 M BTESE in ethanol, and sample **c** (pH=2.4) collected after (ii) 6 min., (iii) 4 h and (iv) 10 h of reaction.

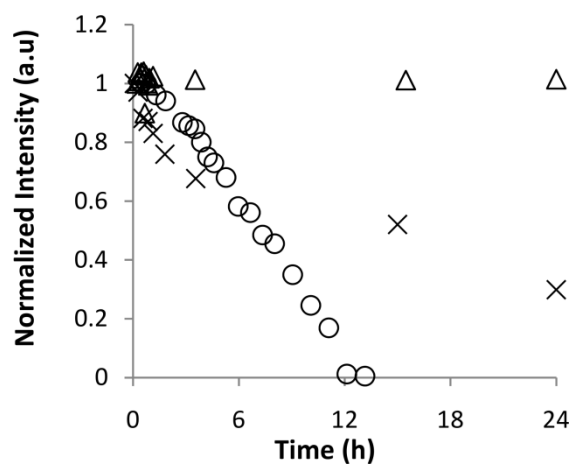


**Figure 4.7.** Normalized total integrated NMR intensities measured with time for sample **a** (pH=2.2) using single-pulse  $^{29}\text{Si}$  NMR of the spectra ( $\Delta$ ) shown in Figure 4.4c, for sample **c** (pH=2.4) using single-pulse  $^{29}\text{Si}$  NMR in spectra (X) shown in Figure 4.6b and  $^1\text{H}$  NMR spectra (o) shown in Figure 4.6c. The plotted intensities are the total integrated intensities of all the peaks in each spectrum except the  $^1\text{H}$  NMR intensities which are the total integrated intensities of the bridging group protons peak at  $\sim 0.5$  ppm (labeled in Figure 4.6c).

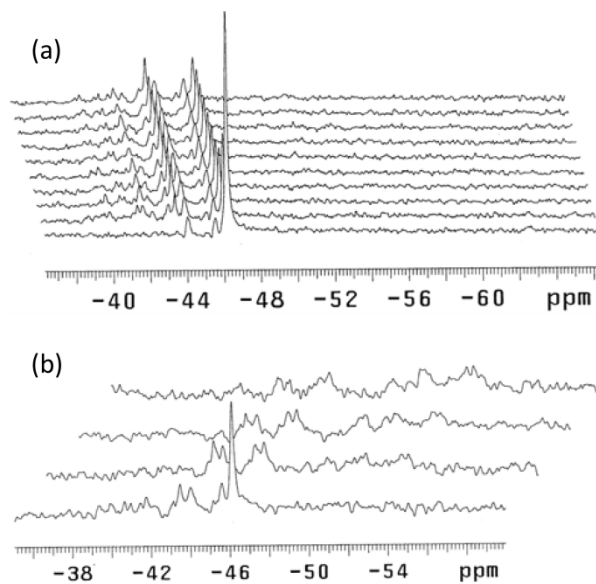


**Figure 4.8.** Single-pulse  $^{29}\text{Si}$  NMR spectra collected for sample **d** prepared using water with (a) pH=3.6 (lb=5) and (b) pH=1.3 (lb=10). Both the samples were probed over a spectral width of 5000 Hz and pw=11.8  $\mu\text{s}$ . First spectrum (close to the chemical shift axis) in Figure (a) was collected after 14 minutes of reaction, second spectrum 45 minutes after the first, and the rest at intervals of 100 minutes. Spectra in Figure (b) were collected at regular intervals of 30 minutes after 1.5 minutes of reaction from bottom to top.

## 5. Kinetic Modeling of Sol gel Polymerization of Bis(triethoxysilyl)methane using DEPT $^{29}\text{Si}$ NMR

### 5.1. Summary

This chapter addresses the hydrolytic polycondensation of bis(triethoxysilyl)methane (BTESM) in acidic ethanol / water solution. For a low water concentration, species generated during the early stages of polymerization are identified from  $^{29}\text{Si}$  NMR spectra. Distortionless Enhancement through Polarization Transfer (DEPT) is used to enhance the sensitivity of  $^{29}\text{Si}$  nuclei. A cyclic dimer and linear dimer are found to be the predominant products of condensation for the length of time the reactions were monitored. For other species, such as partially hydrolyzed monomers, the pairs of silicon sites connected by the bridging organic group give rise to two distinct resonances unless the sites are symmetrical. The chemical shift trends upon hydrolysis and condensation of the silicon sites are found to be consistent with those observed for non-bridged silanes, although differences in the effects of cyclization are noted. In addition to chemical shift assignments, a kinetic model describing the early-time reaction evolution is developed and validated by fitting to concentrations found from  $^{29}\text{Si}$  NMR.

### 5.2. Introduction

Bis(triethoxysilyl)methane (BTESM) (Figure 5.1a) is the simplest of the class of precursors to siloxane-based sol gel polymers with organic groups embedded in their framework.<sup>93</sup> The presence of an organic bridging group imparts more structural and functional flexibility to the periodic organosiloxanes derived from bridged silanes than the non-bridged tri- and tetra-functional silanes. The nature of its bridging group provides unique characteristics to polymeric networks and gels formed from BTESM. The short methylene bridge drives the polymerization reactions towards cyclic oligomers specific to BTESM. It also imparts rigidity to the polymer structures formed which is not possible with tri-functional silanes carrying the same amount of organic component. BTESM is used as a coupling agent<sup>229</sup> as well as a precursor to produce porous organic inorganic hybrid materials with enhanced mechanical, chemical and physical properties like low dielectric constant,<sup>230</sup> high thermal stability,<sup>231</sup> and increased chemical accessibility.<sup>232</sup> The applications of BTESM-based sol-gel materials include but are not limited to their use as substrates in biological assays,<sup>233</sup> membranes in separations<sup>234</sup> and insulating films in semiconductor devices.<sup>235</sup> BTESM is also being used as a silicon source in the synthesis of

hybrid zeolitic frameworks with morphology and textural properties similar to conventional zeolites.<sup>231</sup> Derivatives of BTESM (BTESM forms cage-like rigid and symmetrical structures) are being used as building blocks for the synthesis of silica based materials.<sup>236</sup> These versatile applications make the study of early time kinetics of BTESM polymerization significant to be able to predict *a priori* the structure and properties of the materials.

Despite its wide spread use in material synthesis, investigation of the polymeric structure evolution from BTESM has been very limited. Shea and Loy<sup>93,237</sup> identified certain cyclic carbosiloxanes that are initially formed from BTESM through mass spectrometry studies. Kuge and coworkers<sup>236</sup> investigated the kinetics of forming of a cage-like hybrid species that BTESM forms under certain conditions. Here, we perform a systematic study of the early stage polymerization reactions of BTESM to model the reaction pathways and identify initial oligomers using DEPT <sup>29</sup>Si NMR characterization.

Since the dawn of sol-gel chemistry, <sup>29</sup>Si NMR has been one of the most power sources of experimental data for kinetic modeling<sup>50,58,80,238</sup> and for identifying reaction intermediates and the composition of building blocks that comprise the final products.<sup>93</sup> This knowledge is useful to fine tune the reaction conditions to force the reactions towards desired pathways in order to obtain preferred final products. Progressive hydrolysis and condensation reactions (Section 1.1.3) follow specific trends in <sup>29</sup>Si NMR chemical shifts which aid in the assignment of NMR peaks to the species present in the reaction mixture. These trends have been well established for tri- and tetra-functional silanes.<sup>239-242</sup> However, this task is quite challenging for bridged silane polymerization and much less has been reported in this area.<sup>93,237,243</sup> Each molecule of the bridged monomer has two silicon environments with three attached functional groups that can undergo displacement reactions. This causes multiple resonances depending upon the degree of hydrolysis and condensation of each silicon end. Several intermediates result from the high functionality of a bridged silane precursor even at very early stages of reaction leading to numerous peaks appearing in the <sup>29</sup>Si NMR spectrum. Moreover, the low sensitivity and long relaxation time of <sup>29</sup>Si nuclei impede capturing intensities of species in low concentrations. In the present study, we overcome this impediment by employing DEPT (Distortionless Enhancement of Polarization Transfer)<sup>87</sup> <sup>29</sup>Si NMR. The DEPT technique enhances the sensitivity and lowers the relaxation time of <sup>29</sup>Si nuclei to produce meaningful quantitative data for kinetic

investigations. To the best of our knowledge, the present study is the first to implement the DEPT technique for characterizing a bridged silane system using  $^{29}\text{Si}$  NMR.

We develop a kinetic model to describe the hydrolytic polycondensation of BTESM based on species identified in the experimental spectra and fit the model to the experimental transients. Our kinetic model follows in the footsteps of the comprehensive quantitative models that have been developed for tri- and tetra-functional silane polymerization by McCormick's group.<sup>70,75</sup> Under hydrolysis pseudoequilibrium, their models described condensation kinetics at the silicon sites considering first shell substitution effects. However, these models fail to distinguish between the oligomers the silicon sites belong to. In our study, we develop a species-specific kinetic model. Modeling reactions specific to species in the polymerization mixture is usually cumbersome due to large number of reactions that need to be considered. Also, similar chemical environments in different species produce the same chemical shifts in the absence of long range effects making it impossible to identify individual oligomers. However, in the present study, the water concentration is low enough to limit the reactions as well as their rates and this facilitated monitoring the evolution of individual oligomers present in BTESM polymerization mixtures.

### 5.3. Application of DEPT for BTESM Polymerization

By applying the DEPT pulse sequence,  $^{29}\text{Si}$  NMR can be tuned to gain optimum sensitivity and qualitative information. A  $90^\circ$  proton pulse is applied at the beginning of the sequence after which the magnetization evolves under the influence of proton-silicon coupling. Due to the 100% natural isotopic abundance of  $^1\text{H}$  nuclei and the higher gyromagnetic ratio of  $^1\text{H}$  compared to  $^{29}\text{Si}$ , transfer of polarization from protons to desired (Si) nuclei enhances NMR signal by up to five times, depending on the number of protons involved in polarization transfer.<sup>244</sup> Because the source of the polarization (which is the basis for the observed signal) is  $^1\text{H}$ , the delay ( $d_1$ ) between successive pulses depends on the relaxation time of  $^1\text{H}$  rather than  $^{29}\text{Si}$ , thus significantly reducing the time to collect a spectrum. In addition, the broad signal of the NMR sample tube that appears at around -110 ppm is suppressed because of the lack of attached protons.

The DEPT technique has been used by Brunet<sup>58</sup> and by Alam and Assink<sup>50</sup> to analyze tri-functional silane polymerization. Brunet<sup>58</sup> derived an expression (eqn. 1) for predicting theoretical DEPT transfer efficiencies of methyltriethoxysilane and its derivatives which have an

$I_n I'_m I''_p$  S spin system. In this spin system, S represents a  $^{29}\text{Si}$  nucleus, I represents the protons in the methyl group attached to the silicon nucleus (which can be replaced by a methylene bridge in our case), and I' and I'' represent the  $\text{CH}_2$  and  $\text{CH}_3$  protons, respectively, in the ethoxy moieties coupled to the silicon nucleus. In this spin system,  $n$  is the number of protons I,  $m$  is the number of protons I', and  $p$  is the number of protons I''. Since both ends of the methylene bridging group in BTESM have the same attached protons as MTES, BTESM also has the same spin system, considering only one end of the bridge (this is reasonable because the  $^{29}\text{Si}$  isotope is only 4.7% abundant). Therefore, the expression for polarization transfer efficiency  $F(\Delta, \theta)$  (eqn. 5.1) as provided by Brunet<sup>58</sup> holds for our system as well.

$$F = n s_\theta [s_\Delta^I]^2 \left( [c_\Delta^I]^2 + c_\theta [s_\Delta^I]^2 \right)^{n-1} \left( [c_\Delta^{I'}]^2 + c_\theta [s_\Delta^{I'}]^2 \right)^m + m s_\theta [s_\Delta^{I'}]^2 [c_{2\Delta}^{I''}]^3 \left( [c_\Delta^{I'}]^2 + c_\theta [s_\Delta^{I'}]^2 \right)^{m-1} \left( [c_\Delta^I]^2 + c_\theta [s_\Delta^I]^2 \right)^n \quad (5.1)$$

where  $s_\Delta^I = \sin(\pi J_{IS}\Delta)$ ,  $c_\Delta^I = \cos(\pi J_{IS}\Delta)$ ,  $s_\Delta^{I'} = \sin(\pi J_{I'S}\Delta)$ ,  $c_\Delta^{I'} = \cos(\pi J_{I'S}\Delta)$ ,  $s_\theta = \sin\theta$ ,  $c_\theta = \cos\theta$

and  $c_{2\Delta}^{I''} = \cos(2\pi J_{I''S}\Delta)$ . In this expression,  $J$  is the scalar spin-spin coupling constant between the subscripted spin nuclei. The transfer efficiency of each silicon site changes with a change in the number of protons attached to it as the reactions progress. We will use  $T_i^j - T_k^l$  to represent two  $T_{ij}$  sites connected by a bridging organic.  $T$  represents a tri-functional Si, subscript  $i/k$  is the number of siloxane bonds attached to a site, and superscript  $j/l$  is the degree of hydrolysis. Since the methylene bridge in BTESM remains attached to the silicon sites regardless of the polymerization reactions,  $n$  is always equal to 2.  $m$  varies depending on the number of ethoxy groups attached to the silicon. Therefore,  $m=6$  for  $T_{\theta^3}$ ,  $m=4$  for  $T_{\theta^2}$ ,  $m=2$  for  $T_{\theta^1}$  and  $m=0$  for  $T_{\theta^0}$ . Since  $n$  remains the same for all silicon sites, polarization transfer efficiency only varies with the number of attached ethoxy groups for each type of silicon site (assuming that the scalar coupling constants remain constant). Due to fast exchange of hydroxyl groups between hydrolyzed silicon sites and the solvent, the silicon nucleus does not experience coupling to this proton on an NMR time scale and hence, protons in the hydroxyl groups do not contribute to magnetization transfer.

#### 5.4. Kinetic Model

Sol-gel polymerization involves concurrent hydrolysis and water or alcohol producing condensation of the alkoxy groups in the precursor (Section 1.1.3). The concentration of the

precursor(s), H<sub>2</sub>O/Si ratio and pH govern the relative rates of the reactions that occur. The reaction pathways can be understood by characterizing the polymerizing silanes *in situ*. From the experimental spectra described later, it is clear that monomer (M) (Figure 5.1a), linear dimer (D) (Figure 5.1b) and cyclic dimer (C) (Figure 5.1c), and their products of hydrolysis are the only species present in the polymerization mixture for the length of time the reactions were monitored. Based on this, we propose the following reaction pathways assuming that (1) condensation is irreversible, (2) all hydrolysis/esterification reactions are in quasi-equilibrium as condensation reactions are rate limiting under acidic conditions,<sup>70</sup> and (3) all hydrolysis reactions have the same equilibrium coefficient.<sup>70</sup> Only water producing condensation is considered here, as it is not possible to distinguish water and alcohol producing condensation from a single experiment.<sup>70</sup>



If extent of hydrolysis,  $\chi$  is defined as the fraction of uncondensed groups that are hydrolyzed,

$$\chi = \frac{[SiOH]}{[SiOH] + [SiOR]} \quad (5.4)$$

then under hydrolysis pseudoequilibrium,  $\chi$  can be calculated using hydrolysis equilibrium coefficient<sup>70</sup>,  $K_h = \frac{\chi_{eq}}{(1-\chi_{eq})} \frac{(E + \chi_{eq}(1-\alpha) + \alpha)}{(W - \chi_{eq}(1-\alpha) - \alpha/2)}$ . This expression is quadratic in  $\chi_{eq}$  and can be rearranged to calculate  $\chi_{eq}$  as given below.

$$\chi_{eq} = \frac{-b - \sqrt{b^2 - 4ac}}{2a} \quad (5.5)$$

where:

$$a = (K_h - 1)(1 - \alpha)$$

$$b = -(K_h(1 + W - 1.5\alpha) + \alpha + E)$$

$$c = K_h \left( W - \frac{\alpha}{2} \right)$$

$$\alpha = \frac{2[SiOSi]}{[SiOR]_0}$$

$$W = \frac{[H_2O]_0}{[SiOR]_0}$$



$$E = \frac{[C_2H_5OH]_0}{[SiOR]_0}$$

The differential equations for the evolution of species according to rate equations 5.2 and 5.3 are as follows.

$$\frac{d[M]}{dt} = -k_M(6\chi[M])^2 \quad (5.6)$$

$$\frac{d[D]}{dt} = \frac{1}{2}k_M(6\chi[M])^2 - k_D(3\chi)^2[D] \quad (5.7)$$

$$\frac{d[C]}{dt} = k_D(3\chi)^2[D] \quad (5.8)$$

In rate equations 5.6-5.8, the concentration of hydrolyzed sites of the reactants is based on the average number of hydroxyls per molecule, which is a function of the siloxane conversions described in equation 5.5. For monomer, there are 6 functional groups, and hence the average number of hydrolyzed SiOH groups per molecule is  $6\chi$ . Similarly, the average number of SiOH groups at one end a linear dimer is  $3\chi$ , as each silicon end-site has 3 functional groups. The rate of monomer consumption is a bimolecular reaction and is proportional to  $(6\chi[M])^2$ . Since the consumption of linear dimer to form cyclic dimer is a unimolecular reaction which still depends on the average number of hydrolyzed functional groups on each end of the molecule, its rate is proportional to  $(3\chi)^2[D]$ . The concentrations of species with various degrees of hydrolysis can also be obtained from the total concentrations of M, D and C by assuming that the probability of each uncondensed group being hydrolyzed is given by  $\chi$  (so the probability of an alkoxy group being attached is given by  $(1-\chi)$ ). The fraction of differently hydrolyzed species therefore depends on the combined probabilities of having the required number of uncondensed groups hydrolyzed. For example, any one of the ethoxy groups could be hydrolyzed to generate a singly-hydrolyzed monomer ( $T_0^1 - T_0^0$ ), leading to 6 possible combinations of 1 hydroxyl group and 5 unhydrolyzed ethoxy groups. Therefore,  $[T_0^1 - T_0^0] = 6\chi(1-\chi)^5[M]$ . Unhydrolyzed monomer, linear and cyclic dimer are the most prevalent species in the NMR spectra, and their concentrations are given by,

$$[T_0^0 - T_0^0] = (1-\chi)^6[M],$$

$$[T_0^0 - T_1^0 - T_1^0 - T_0^0] = (1-\chi)^{10}[D], \text{ and}$$

$$\begin{bmatrix} T_{1c}^0 - O - T_{1c}^0 \\ | \\ T_{1c}^0 - O - T_{1c}^0 \end{bmatrix} = (1-\chi)^8[C].$$

## 5.5. Experimental Section

### 5.5.1. Source of Materials

BTESM was procured from Gelest Inc., ethanol from Alfa Aesar, de-ionized ultra-filtered water from Fisher Scientific and acetone-d<sub>6</sub> was obtained from Cambridge Isotope Laboratories. 5 mm thin walled quartz NMR sample tubes were purchased from Wilmad. All materials were used as purchased.

### 5.5.2. Sample Preparation

<sup>29</sup>Si NMR spectra used to verify DEPT parameters were collected with a sample containing BTESM and deuterated acetone in the volume ratio 4:1. The BTESM polymerization mixture was prepared by mixing together monomer, ethanol and acidic water (pH=1). The monomer concentration was 1.78 M in solution and the H<sub>2</sub>O/BTESM ratio was 0.5. The sample was mixed by vigorous shaking to ensure homogeneity and immediately transferred to the NMR sample tube for data collection.

### 5.5.3. NMR Experiments

DEPT <sup>29</sup>Si NMR spectra of BTESM polymerization mixture were collected on a 400 MHz Varian Spectrometer at 27 °C for a period of 6 h. Pulse widths of 22 μs and 12 μs for <sup>1</sup>H and <sup>29</sup>Si and inter-pulse delay of 5 s were used. A spectral width of 10000 Hz was used after confirming that the signal from the NMR glass tube did not interfere with peaks from the sample. An acquisition time of 1 s was used to ensure complete decay of the fid. The delay between consecutive acquisitions was set to 15 s (three times the spin-lattice relaxation time of protons). 16 scans were averaged to obtain each spectrum. DEPT <sup>29</sup>Si NMR spectra of BTESM in acetone-d<sub>6</sub> were collected at varying values of pulse angle to verify theoretical predictions.

## 5.6. Computational Details

### 5.6.1. Solution Procedure

The set of differential rate equations (5.6-5.8) were solved simultaneously using the Adams-Moulton predictor-corrector method. Optimal values of the rate constants,  $k_M$  and  $k_D$ , and hydrolysis equilibrium coefficient,  $K_h$  were obtained by fitting the model-derived concentrations with the corresponding experimental data using the Levenberg-Marquardt algorithm.<sup>245</sup> The experimental intensities of singly hydrolyzed monomer ( $T_0^1 - T_0^0$ ), unhydrolyzed monomer

$(T_0^0 - T_1^0)$ , unhydrolyzed linear dimer  $(T_0^0 - T_1^0 - O - T_1^0 - T_0^0)$  and cyclic dimer  $\begin{pmatrix} T_{1c}^0 - O - T_{1c}^0 \\ | \quad | \\ T_{1c}^0 - O - T_{1c}^0 \end{pmatrix}$  were used for this purpose. The program for running these calculations was written in the C language. The convergence criteria for optimization were  $\left| \frac{\varphi_{i+1} - \varphi_i}{\zeta + \varphi_i} \right| < 10^{-5}$  or  $\left| \frac{k_{j,i+1} - k_{j,i}}{\zeta + k_{j,i}} \right| < 10^{-5}$  whichever occurred first. Here,  $\varphi_i$  and  $\varphi_{i+1}$  are the sum of squares of the differences between the experimental and calculated concentrations, and  $k_{j,i+1}$  and  $k_{j,i}$  represent the rate constants of rate equation,  $j$  in any two successive iterations,  $i$  and  $i+1$ .  $\zeta$  was set to a small value, 0.001. The reported uncertainties of the optimized rate constants are the standard deviations obtained from the variance-covariance matrix.<sup>246</sup>

### 5.6.2. Density Functional Theory Calculations

The initial 3D geometric structures of the molecules for DFT calculations were built in Argus Lab 4.0<sup>127</sup> and the geometry optimization was carried out in vacuum at the B3LYP/6-31G\* level of theory on an Intel DLX cluster using Gaussian 03.<sup>128</sup> The <sup>29</sup>Si NMR chemical shieldings were calculated using the optimal geometries with the B3LYP/6-311G+(2d,p) method and referenced to tetramethylsilane to obtain the chemical shifts. This method has been found to provide reasonable estimates of <sup>29</sup>Si NMR chemical shifts for silanes.<sup>247</sup>

## 5.7. Results and Discussion

### 5.7.1. Optimal Sensitivity

The DEPT parameters,  $\Delta$  and  $\theta$  were set based on the theoretical predictions of the transfer efficiencies for all  $T$  sites using equation 5.1. For BTESM,  $J_{1s} = {}^2J(\text{Si-H}) = 11$  Hz and  $J_{1s} = {}^3J(\text{Si-H}) = -2.8$  Hz.<sup>213</sup> The CH<sub>3</sub> protons in the ethoxy groups are not affected by the coupling to silicon.<sup>213</sup> Hence,  $J_{11'} = {}^3J(\text{H-H})$  was set to 7.3 Hz, measured for CH<sub>3</sub>CH<sub>2</sub>OH.<sup>58</sup> Since the methylene bridge is always attached to Si site regardless of the polymerization reactions, we choose bridging group protons for transferring polarization to achieve optimum sensitivity. Therefore, transfer time,  $\Delta$  ( $=1/2J(\text{Si-H})$ )<sup>58</sup> is set to 45 ms with  $J = 11$  Hz for optimal signal to noise ratio. Figure 5.2 shows the variation of transfer efficiency with pulse angle,  $\theta$  for different  $T$  sites with  $\Delta$  set to 45 ms. Transfer efficiencies for all  $T$  types are maximum at  $\theta=40^\circ$ . Hence,  $\theta=40^\circ$  was chosen for attaining optimal sensitivity.

### 5.7.2. Experimental Verification of DEPT Theoretical Intensities

Figure 5.3 shows experimental intensities compared with theoretically predicted intensities in order to verify the accuracy of DEPT transfer efficiencies. The experimental intensities are the heights of the monomer peak obtained from DEPT  $^{29}\text{Si}$  NMR spectra of BTESM in acetone- $d_6$  collected for varying  $\theta$  at  $\Delta = 45$  ms. Theoretical intensities relative to experimental NMR intensities were calculated considering the maximum experimental intensity equivalent to maximum transfer efficiency at  $\theta=40^\circ$ .

Theoretical intensity = Height of the peak x (Maximum F / Maximum intensity of the peak)

Experimental intensities in Figure 5.3 match well with the theoretical trend confirming that  $\Delta=45$  ms and  $\theta=40^\circ$  are optimum to obtain maximum signal to noise ratio when probing BTESM polymerization mixtures.

### 5.7.3. Peak Assignments

Figure 4.4 shows the evolution of products of BTESM polymerization in DEPT  $^{29}\text{Si}$  NMR. Peak assignments are labeled in Figures 5.4a and 5.4b, and tabulated in Table 5.1. The peak at -46.4 ppm is assigned to the unhydrolyzed monomer ( $T_0^0 - T_0^0$ ) with reference to tetramethylsilane. Other peak assignments are discussed below.

*Single hydrolysis at one end ( $T_0^1 - T_0^0$ ).* Singly hydrolyzed monomer produces two resonances with nearly equal intensities downfield from monomer at -45.7 and -44.7 ppm. The hydrolyzed end of this monomer ( $T_0^1$ ) shifts 1.7 ppm and causes the unhydrolyzed end ( $T_0^0$ ) to shift 0.7 ppm downfield from the unhydrolyzed monomer. The smaller change in chemical shift at the unhydrolyzed end is consistent with it being further removed from the effects of substituting an ethoxyl group with a hydroxyl group. The slightly larger intensity of the singly hydrolyzed site ( $T_0^1$ ) compared with the unhydrolyzed Si site ( $T_0^0$ ) is consistent with the higher transfer efficiency of  $T_0^1$  ( $m=4$ ) than  $T_0^0$  ( $m=6$ ) (Figure 5.2). In the absence of polarization transfer both of these peaks would be expected to have equal intensities.

*Single hydrolysis at both ends ( $T_0^1 - T_0^1$ ).* Hydrolysis of one ethoxy group at both ends of the bridge makes the two Si sites equivalent and hence the doubly hydrolyzed monomer ( $T_0^1 - T_0^1$ ) generates only one resonance at -43.9 ppm. Consistent with the magnitudes of the chemical shifts changed upon the first hydrolysis, hydrolysis at both ends shifts the peak 0.8 ppm downfield at the end further removed from the hydrolysis reaction (relative to the singly

hydrolyzed Si site of  $T_0^1 - T_0^0$ ) and 1.8 ppm downfield at the end where hydrolysis occurs (relative to the unhydrolyzed Si site of  $T_0^1 - T_0^0$ ).

*Two hydrolyzed sites on one end ( $T_0^2 - T_0^0$ ).* Hydrolysis of two ethoxy groups on one end of the monomer generated two resonances at -45 ppm and -43.1 ppm. The unhydrolyzed end ( $T_0^0$ ) of this double hydrolyzed monomer shifted 0.7 ppm downfield from unhydrolyzed site of the single hydrolyzed monomer ( $T_0^1 - T_0^0$ ). Its hydrolyzed end ( $T_0^2$ ) is 1.6 ppm downfield from  $T_0^1$  site of ( $T_0^1 - T_0^0$ ).

*Three hydrolyzed sites ( $T_0^2 - T_0^1$ ).* Both  $T_0^2$  and  $T_0^1$  resonances appear at -42.4 ppm and -43.1 ppm which is downfield of the corresponding sites observed in the other hydrolyzed species discussed above. The doubly hydrolyzed end ( $T_0^2$ ) of this monomer is 1 ppm downfield from its singly hydrolyzed end ( $T_0^1$ ) and 0.7 ppm downfield from the  $T_0^2$  site of  $T_0^2 - T_0^0$ .

*Linear dimer ( $T_0^0 - T_1^0 - O - T_1^0 - T_0^0$ ).* There are two peaks with nearly equal intensities at -52.4 ppm and -47.1 ppm. These correspond to linear dimer that has two Si sites ( $T_1^0$ ) connected to each other with a siloxane bond and two unconnected and unhydrolyzed Si sites ( $T_0^0$ ) at the ends. The unconnected ends of the dimer ( $T_0^0$ ) moved 0.7 ppm upfield from the unhydrolyzed monomer, while condensation caused 5.3 ppm upfield shift upon going from monomer to dimer. This shift is somewhat smaller than what is observed for condensation of MTES,<sup>58,69</sup> but of the right order of magnitude.

*Cyclic dimer*  $\begin{pmatrix} T_{1c}^0 - O - T_{1c}^0 \\ | \qquad \qquad | \\ T_{1c}^0 - O - T_{1c}^0 \end{pmatrix}$ . The peak at -54.4 ppm is assigned to cyclic dimer. This species

produces only one peak due to its symmetrical structure, and there is no other peak in the spectrum that follows the intensity of this peak, so the cyclic species seems to be the appropriate assignment. However, it is surprising that cyclization leads to an upfield shift in this case, in comparison to the downfield shift usually observed upon formation of 8-atom siloxane rings.<sup>69</sup> Therefore, DFT calculations were used to support this assignment. The optimized geometric structure of cyclic dimer compared with monomer and linear dimer (Figure 5.5) show that SiOSi and SiCSi bond angles (Table 5.2) are strained enough (indicated by larger bond angles in cyclic dimer when compared to those in monomer and linear dimer) to cause an upfield shift of  $T_{1c}^0$  sites from  $T_1^0$  of the linear dimer. The known chemical shifts of the hydrolyzed and unhydrolyzed monomer and linear dimer match closely with experimental shifts (Table 5.2, average deviation from experimental = 2.3 ppm) validating the accuracy of the theoretical

methodology used for calculating these shifts. The calculated chemical shift of the cyclic dimer appears 1.7 ppm upfield of the linear dimer, which is similar to the experimental upfield shift of 2 ppm (for the  $T_1^0$  sites) thus justifying our assignment. The increase in Si-O-Si angle is the reason for this shift; strained siloxane rings usually have Si-O-Si bond angles less than the relaxed value of siloxane systems (near 120°) and thus cause a chemical shift change opposite in sign.

#### 5.7.4. Chemical Shift Trends

The two silicon sites connected by the methylene bridge are found to be influenced by substitution at either end of the organic bridge. Symmetric ends of the bridge are observed to produce a single resonance and unsymmetric sites produced two resonances. For example, hydrolysis at one end of the bridge makes the two silicon sites unsymmetric generating two resonances for  $T_0^1 - T_0^0$ . For every hydrolysis, the peak representing the hydrolyzed end is shifted 1.6-1.8 ppm downfield, as has been reported for non-bridged silanes,<sup>248</sup> while the unhydrolyzed end of the molecule shows a shift 0.7-0.8 ppm downfield from its parent (unhydrolyzed) peak. This means that when the ends of a molecule differ by one degree of hydrolysis, the difference between their chemical shifts is ~1ppm (as in  $T_0^2 - T_0^1$  for example). Condensation is found to shift the connected Si site 5.4 ppm upfield from the monomer similar to that observed in non bridged silanes.<sup>248</sup> This also induces a shift at the other end of the organic bridges, although smaller in magnitude (0.7 ppm). Cyclization in an 8-atom carbosiloxane ring moves the chemical shift of singly connected silicon sites 2 ppm further upfield, unlike in non-bridged silanes where connected silicon sites belonging to cyclic species are observed to move downfield.<sup>58</sup> As noted above, this is most likely due to an expansion of the Si-O-Si bond angle in the carbosiloxane ring due to the rigidity of the Si-C-Si bond, whereas the Si-O-Si bond angle is reduced in an 8-atom siloxane ring.

#### 5.7.5. Reaction Pathways

The reaction pathways for the species identified in DEPT <sup>29</sup>Si NMR spectra follow the reactions occurring at the local silicon sites. Monomer ( $T_0^0 - T_0^0$ ) undergoes hydrolysis to form ethanol and monomers hydrolyzed once or twice at one or both ends of the methylene bridge. Only the singly hydrolyzed monomer ( $T_0^1 - T_0^0$ ) is observed at high concentrations. The intensities of other hydrolyzed monomers are not very high indicating that the average degree of hydrolysis is low under the conditions of this experiment. The hydrolyzed linear dimers

undergo condensation involving the two ends to form cyclic dimer and are not observed to accumulate.

### 5.7.6. Hydrolysis Pseudo-equilibrium

Under hydrolysis pseudo-equilibrium conditions mentioned in the earlier section, all uncondensed groups are assumed to hydrolyze to the same extent. Because  $\chi$  represents the probability that a randomly selected uncondensed group is hydrolyzed, the fraction of silicon sites,  $f(T_i^j)$  with varying degrees of hydrolysis can be obtained as follows.

$$f(T_0^0) = (1-\chi)^3 \quad (5.9)$$

$$f(T_0^1) = 3\chi(1-\chi)^2 \quad (5.10)$$

$$f(T_0^2) = 3\chi^2(1-\chi) \quad (5.11)$$

$$f(T_0^3) = \chi^3 \quad (5.12)$$

The fraction of  $T_i^j$  sites obtained from experimental data match with those calculated from the above equations (5.9-5.12) (Figure 5.6) indicating that the reaction mixture attained hydrolysis pseudoequilibrium by the time the first spectrum was collected, and that hydrolysis pseudoequilibrium was maintained throughout the course of the experiment.

### 5.7.7. Condensation Kinetics

Now that we know that hydrolysis pseudoequilibrium exists in the reaction mixture studied, the proposed model could be considered to aptly describe the structure evolution of this system. The best fits obtained from the model are compared with the experimental concentrations in Figures 5.7a (W=0.09). The best fit to the experimental data gave  $k_M=0.45\pm 0.01$  L/mol/h,  $k_D=16.6\pm 1.2$  /h and a very large  $K_h$ . Since the water concentration is very low, any source of experimental error (an external source of water like the solvent, ethanol used in the experiment, for instance) would make a huge difference.  $K_h$  has been observed to be 11.3 for trimethylethoxysilane polymerization.<sup>70</sup> When the value of W was adjusted to 0.1 (Figure 5.7b) the model predicted a reasonable estimate of  $K_h$ . The optimal rate constants associated with W=0.1 are  $k_M=0.42\pm 0.007$  L/mol/h and  $k_D=21\pm 0.9$  /h, and  $K_h = 11.4\pm 0.93$ . The value of  $k_M$  is consistent with the magnitude of dimerization rate constants observed for tri- and tetra-functional silane systems.<sup>23</sup> The relatively high  $k_D$  value is consistent with no net accumulation of hydrolyzed dimers; they quickly react to form cyclic dimer. The magnitude of  $k_D$  is an order of

magnitude higher than cyclization rates found for non-bridged silanes<sup>69,249,250</sup> and is consistent with extensive cyclization observed in bridged alkoxy silane polymerization.<sup>91</sup>

## 5.8. Conclusions

This study demonstrates the use of DEPT <sup>29</sup>Si NMR for quantitative kinetic modeling of bridged silane polymerization. The evolution of products of polymerization of BTESM was monitored *in situ*. Due to its hexa-functionality, BTESM has the tendency to form numerous oligomers with a wide range of silicon environments making the <sup>29</sup>Si NMR spectra too complex to interpret. However, when a small amount of water was provided for polymerization, the spectra could be clearly interpreted which helped to derive meaningful kinetic information. The DEPT technique was successfully employed to tune <sup>29</sup>Si NMR for optimal sensitivity and low data collection times. Signal enhancement through polarization transfer also aided in the detection of low intensity peaks which would otherwise be lost in noise. Various species resulting from progressive hydrolytic polycondensation of BTESM were identified. The reaction mixture was found to attain hydrolysis pseudoequilibrium, and linear and cyclic dimer were the predominant oligomers. A kinetic model describing the formation of these oligomers provided calculated concentrations consistent with fast consumption of linear dimer to form cyclic dimer.



**Table 5.1.**  $^{29}\text{Si}$  NMR chemical shifts and peak assignments of species formed during early time sol-gel polymerization of BTESM.

| Oligomer                            | Si site    | $\delta(\text{ppm})$ |
|-------------------------------------|------------|----------------------|
| $T_0^0 - T_0^0$                     | $T_0^0$    | -46.4                |
| $T_0^1 - T_0^0$                     | $T_0^0$    | -45.7                |
|                                     | $T_0^1$    | -44.7                |
| $T_0^1 - T_0^1$                     | $T_0^1$    | -43.9                |
| $T_0^2 - T_0^0$                     | $T_0^0$    | -45.0                |
|                                     | $T_0^2$    | -43.1                |
| $T_0^2 - T_0^1$                     | $T_0^1$    | -43.4                |
|                                     | $T_0^2$    | -42.4                |
| $T_0^0 - T_1^0 - O - T_1^0 - T_0^0$ | $T_0^0$    | -47.1                |
|                                     | $T_1^0$    | -52.4                |
| $T_{1c}^0 - O - T_{1c}^0$           |            |                      |
|                                     | $T_{1c}^0$ | -54.4                |
|                                     |            |                      |
| $T_{1c}^0 - O - T_{1c}^0$           |            |                      |

**Table 5.2.** Average SiCSi and SiOSi bond angles and chemical shifts calculated at B3LYP/6-311+G(2d,p) level of theory for the optimized structures in Figure 5.5.

| Oligomer   | SiCSi(°) | SiOSi(°) | $\delta_{\text{calc.}}$ (ppm) |
|--|----------|----------|-------------------------------|
| $T_0^0 - T_0^0$  | 120      | ---      | -48.9                         |
| $T_0^0 - T_1^0 - O - T_1^0 - T_0^0$  | 119      | 118      | -47.4<br>-57.5                |
| $\begin{array}{c} T_{1c}^0 - O - T_{1c}^0 \\   \qquad \qquad   \\ T_{1c}^0 - O - T_{1c}^0 \end{array}$ | 117      | 150      | -59.2                         |

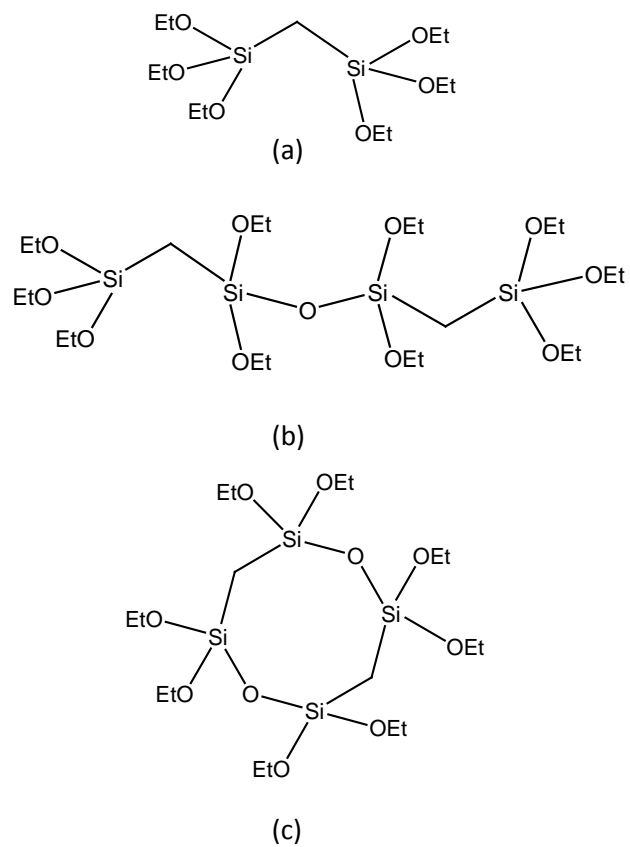


**Figure 5.1.** Structures of (a) BTESM (b) Linear dimer and (c) cyclic dimer.

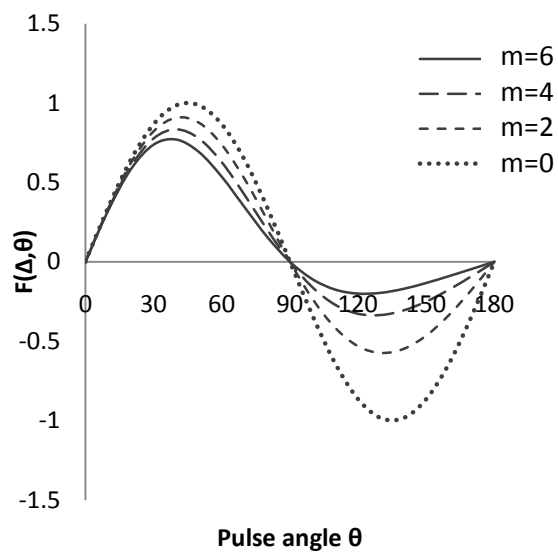


**Figure 5.2.** Polarization transfer efficiency as a function of pulse angle for varying  $m$  at transfer time,  $\Delta = 45$  ms.  $m$  is the total number of protons in the ethoxy groups attached to a silicon site.

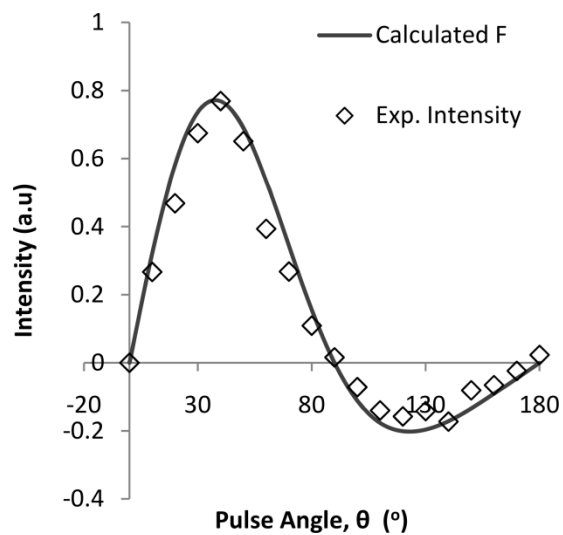


**Figure 5.3.** Comparison of theoretical and experimental intensities of unhydrolyzed BTESM for varying pulse angle at transfer time,  $\Delta=45$  ms.

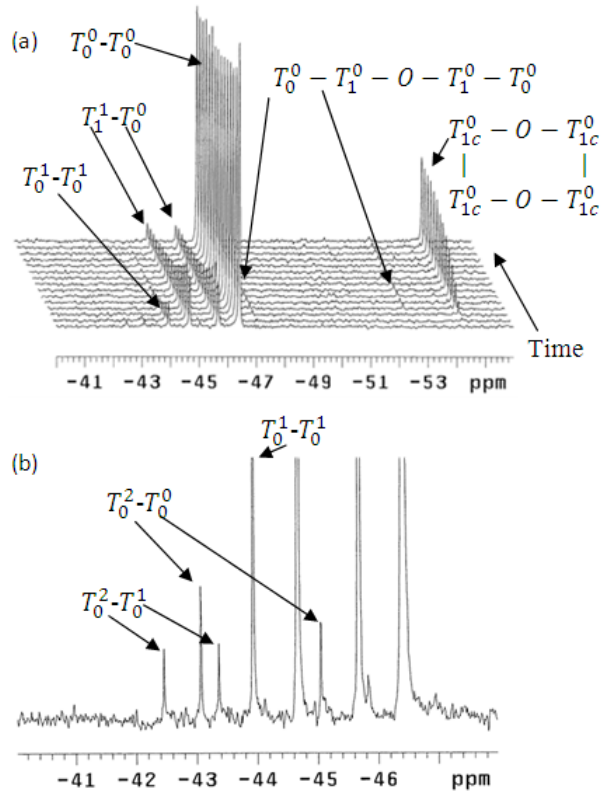


**Figure 5.4.** (a) DEPT  $^{29}\text{Si}$  NMR spectra of BTESM polymerization sample collected with  $\Delta=45$  ms &  $\theta=40^\circ$  after 2 minutes of reaction every 20 minutes and (b) an expanded view of part of the first spectrum of the series spectra in (a) to indicate low intensities peaks.

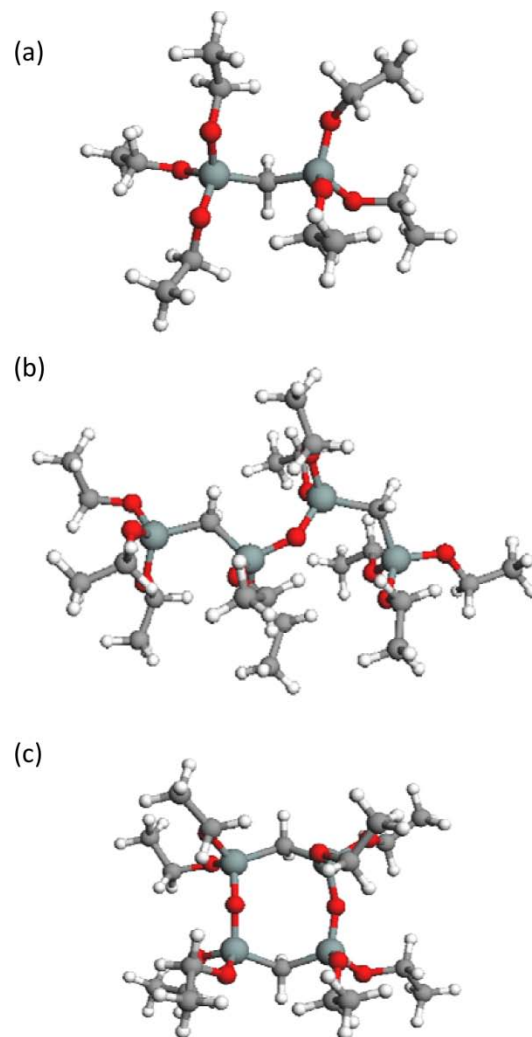


**Figure 5.5.** 3D-Optimized geometric structures of (a) BTESM (b) linear dimer (c) cyclic dimer.

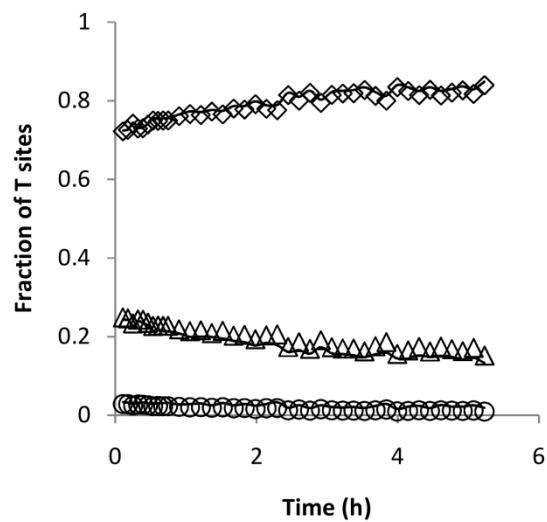


**Figure 5.6.** Fraction of ( $\diamond$ )  $T_0^0$ , ( $\triangle$ )  $T_0^1$  and ( $\circ$ )  $T_0^2$  sites derived from experimental data (dots) compared with those calculated using equations 5.9-5.12 (lines).



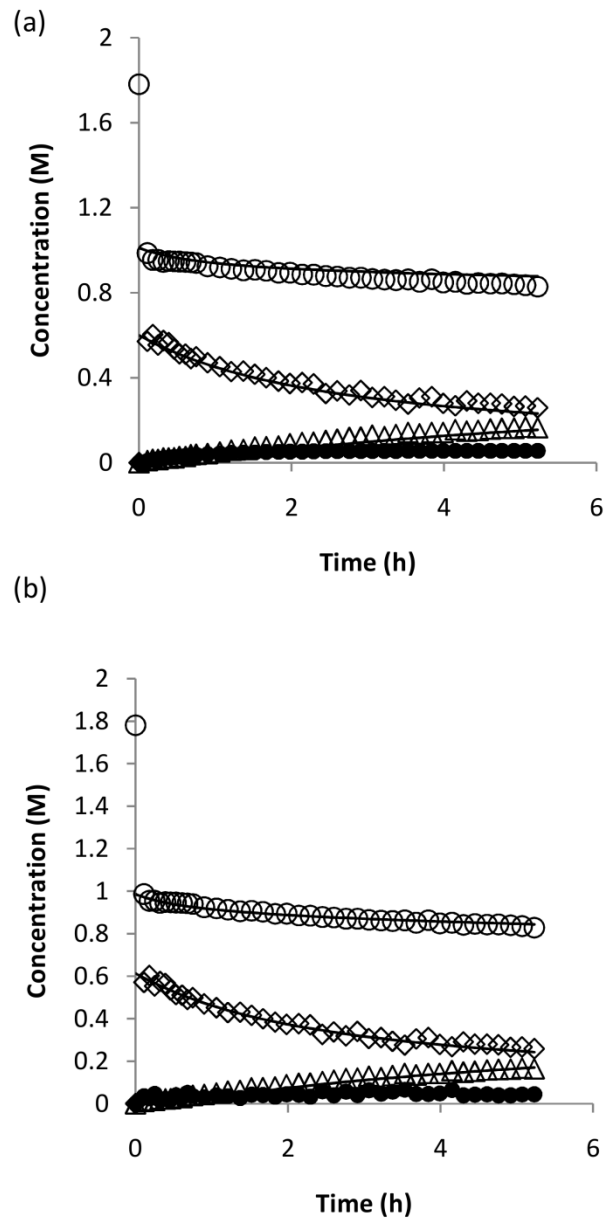


**Figure 5.7.** Experimental (dots) concentration profiles of (o) unhydrolyzed monomer, ( $\diamond$ ) singly hydrolyzed monomer, ( $\bullet$ ) unhydrolyzed linear dimer and ( $\Delta$ ) unhydrolyzed cyclic dimer compared with model predictions (lines) (a)  $W=0.09$  and (b)  $W=0.1$ .

## 6. Dynamic Monte Carlo Investigation of the Effects of Organic Bridges on the Gelation Behavior of Alkoxysilanes

### 6.1. Summary

In this work, we use dynamic Monte Carlo simulations (DMC) to compare the polymeric structure evolution and gelation of organoalkoxysilanes based on the size and location of the organic group in the monomer. The organic group in bridged monomers is sandwiched between two trifunctional silicon ends while their non-bridged versions have an organic group attached to a trifunctional silicon site. We first discuss the incorporation of organic groups into the simulation models that were previously developed for tetraalkoxysilanes [*Macromolecules*, **2000**, *33*, 7639]. We consider similar first shell substitution effects for bimolecular reactions and cyclization involving the formation of four-member rings. Our simulation results are consistent with the experimental observations that bridged precursors exhibit quick gelation when compared to trifunctional silanes, with the exception of monomers with short hydrocarbon bridges, which display relatively prolonged gelation [*J. Am. Chem. Soc.*, **1999**, *121*, 5413]. When the carbosiloxane rings formed from bridged precursors are assumed to react at a rate comparable to siloxane rings with a comparable number of silicon sites, cyclization slows down but does not prevent gelation.

### 6.2. Introduction

Bridged silanes (Figure 7.1a) are a class of organoalkoxysilanes with an organic group sandwiched between two silicon sites. Their non-bridged counterparts are trifunctional silanes (Figure 7.1b) with an organic group attached to a silicon site. These silanes undergo hydrolytic polycondensation (Section 1.1.3) in the presence of water to form polymeric networks and gels with inbuilt organic and inorganic components. The hybrid materials thus formed can be engineered to possess well ordered porous structures that have a wide variety of applications.<sup>5,28,151,152,154,183,251,252</sup> The presence of the bridging group imparts structural and functional flexibility to the bridged silanes which leads to an added control over the properties of the materials formed from them.<sup>25,28</sup> In order to utilize this benefit, it is important to understand the role played by the bridging organic group in polymerization. Experimental reports suggest that despite their close structural similarity, the polymerization behavior of

bridged and non-bridged silanes is very different. Trifunctional silanes form silsesquioxane cages which cannot polymerize any further and hence, may never gel. However, these cages are reversible which can lead to eventual gelation. On the other hand, bridged silanes exhibit quick gelation.<sup>28</sup> We hypothesize that although bridged silanes are trifunctional at their ends and can participate in forming similar siloxane-based cages, they have the ability to form gels because these cages are connected together by the organic bridges introduced via the monomers. Loy and coworkers monitored the gel times of alkylene bridged silanes in acidic conditions and found that short bridged silanes are an exception to this rule, and exhibit relatively long gelation times.<sup>91,199</sup> They hypothesized that monomers with short bridges are able to form carbosiloxane rings which are slow to react further, thus delaying gelation. This hypothesis and other reasons for these differences can be understood by studying the evolution of polymeric structures by computational methods.

While experimental characterization can provide meaningful insights into the kinetics of the sol-gel reactions, as the polymerization progresses identifying the oligomers and building deterministic models becomes challenging. Theoretical simulations using statistical or stochastic models are very helpful in such situations.<sup>253-255</sup> Usually the only input that such models need would be the reaction rates that can be inferred from early time kinetic investigation. Previously several studies described simulations of sol gel polymerization processes<sup>256-259</sup> to aid in the design of material synthesis procedures for applications.<sup>260-262</sup> For instance, Rankin et al.<sup>263</sup> have successfully compared the results of their Monte Carlo simulations with experimental data, thus justifying the use of simplified kinetic schemes to predict larger-scale phenomena such as gelation. Li and Rankin<sup>264,265</sup> used dynamic Monte Carlo (DMC) simulations in modeling the drying of sol gel silica films. The present study is an attempt towards fully understanding the role of the bridging group to explain the gelation behavior of bridged silanes by comparing the predictions of DMC simulations obtained for gelation of bridged and trifunctional silanes.

Rankin et al.<sup>266</sup> have shown that dynamic Monte Carlo simulation is by far the most suitable technique to predict the structural evolution of sol-gel polymers from the initial monomer solution up until the point of gelation. Using this approach, they were the first to present a single modeling strategy able to predict experimentally observed gel conversions for tetraethoxysilane by incorporating cyclization effects in addition to first shell substitution effects. Considering the significance of cyclization for formulating realistic predictions,<sup>83</sup> this

method represents a significant improvement over previously developed statistical<sup>267,268</sup> and Monte Carlo methods<sup>263,269,270</sup> and combined statistical / Monte Carlo approaches.<sup>271</sup> Despite all of the improvements made in the ability of the DMC method to simulate kinetics and gelation, all reports based on this approach pertain only to tetrafunctional systems. Taking into account, the potential applications of organoalkoxysilanes and the usefulness of such simulations, it is important to build models that incorporate organic components. The present study is a starting step toward modeling organically functionalized silsesquioxanes and will be a valuable addition to the existing sol gel simulation studies.

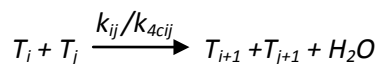
We extend the dynamic Monte Carlo approach used by Rankin et al.<sup>266</sup> and Li<sup>272</sup> to describe trifunctional and bridged silane systems by incorporating organic groups into their model. In the present work, our specific aim is to study the effect on polymer structure and gelation of adding a bridge between pairs of trifunctional sites. Specifically, we perform simulations comparing trifunctional silanes and bridged silanes under the assumption that both systems exhibit the same reaction kinetics at the level of the silicon site reactions involved in the polymerization process. We implement both of the known key non-ideal aspects of the sol-gel polycondensation process: first shell substitution effects (FSSE) and cyclization. In keeping with the importance of four-member (8-atom) rings in siloxane systems, we consider unlimited cyclization to form four member rings. These rings are the building blocks of the experimentally observed silsesquioxane cages formed predominantly from tri- and tetra-functional silanes.<sup>184,267,273,274</sup> Four member rings are also the building blocks of the carbosiloxane rings reported to be observed in the intermediate and final products of ethylene bridged silane polymerization.<sup>91</sup> Due to the method adopted for choosing cyclization sites (explained in the following section), the model best accounts for the heavy level of intra-molecular cyclization observed in the polymerization of silanes with short bridges (such as ethylene). Long (e.g. hexylene) or stiff (e.g. phenylene) bridges, on the other hand, sterically behave like linear oligomers and do not form carbosiloxane rings. This feature is easily implemented in our model by forbidding the participation of organic bridges in ring formation. In the present work, we use the DMC method to compare structure evolution between the trifunctional and bridged silane polymerization by monitoring traits such as site distributions, degree of polymerization, gel conversion and gel time. The main goals are to address (1) the effect of adding a bridge on the cyclization rate and gelation, (2) the effect of carbo-siloxane ring formation in bridged system polymerization and (3) the competition between cyclization and molecular growth in both the

bridged and non-bridged cases. We also discuss the implications of using unlimited cyclization to model this process and propose avenues for further improvements.

### 6.3. Modeling Approach

#### 6.3.1. Kinetic Model

Hydrolytic polycondensation consists of subsequent hydrolysis and condensation reactions as described in section 1.1.3 for each functional group attached to a silicon site. Each silicon site (designated with a T in the subsequent discussion) either in the trifunctional silane or bridged silane system can be uniquely identified by its degree of hydrolysis (number of hydroxyl (OH) groups) and connectivity (number of siloxane (OSi) bonds). In acid catalyzed systems, hydrolysis reactions are very fast when compared to condensation. Rankin and his coworkers<sup>69,70,75</sup> have modeled sol-gel polycondensation by describing hydrolysis reactions using ‘extent of hydrolysis’. They have established that when enough water is added for hydrolysis, the extent of hydrolysis remains constant with time<sup>70</sup> and also that it does not change very significantly with respect to the degree of hydrolysis of the silicon site.<sup>275</sup> Based on these observations, it is reasonable to assume that all the monomers are completely hydrolyzed before condensation begins and therefore, we start our simulation with fully hydrolyzed monomers. Accounting for incomplete hydrolysis would only require modifying all rate coefficients in the same way (the square of the degree of hydrolysis) and therefore would not affect the evolution of the polycondensation process. Due to this assumption, every silicon site (T) in our model can be identified by just the degree of connectivity, an integer that can range from 0 to a functionality of 3 for trifunctional silicon sites. We neglect alcohol producing condensation and consider only water producing condensation reactions that are either bi-molecular or uni-molecular. These reactions can be expressed as



where  $k_{ij}$  and  $k_{4cij}$  are the rate constants for the bimolecular and uni-molecular reactions respectively between silanol groups of the trifunctional sites  $T_i$  and  $T_j$  with connectivities  $i$  and  $j$ . Uni-molecular reactions lead to the formation of rings in the molecule while bi-molecular reactions contribute towards molecular growth and network formation. In both cases, for every siloxane bond that is formed, the connectivity of the reacting sites increases by 1. The rate constants depend on the connectivities of the reacting sites and the type of the reaction (bi-

molecular or uni-molecular) as described below. As we will describe, the population of potential rings (bond blocks) is used to define the rate of cyclization in a physically consistent way.

### 6.3.2. Dynamic Monte Carlo Algorithm

The DMC method for simulation of chemically reacting systems was first developed by Gillespie et al.<sup>84</sup> and later developed for network polymers by Dusek and coworkers.<sup>85,86</sup> In this section, we briefly outline the basic DMC algorithm we employed. The simulation initiates from a finite set of  $N$  ( $2 \times 10^5$ ) monomers and at every step, a condensation reaction occurs between two silicon sites to form a siloxane bond. To select which type of reaction occurs, the rates of each type of condensation reaction are calculated and one of the reactions is randomly selected using probabilities proportional to the rates of the reactions. The sites to be involved in the chosen reaction are randomly selected from the pool of all sites having the required connectivities, and in the case of cyclization reactions, connected by a bond block of the appropriate length. The changes in the population of oligomers and their average properties caused by this event are updated after each step and the DMC steps are repeated until one of the stopping criteria are met. These criteria are either reaching (a) the gel point (defined later) or (b) 100% condensation conversion. Specific details about the storage of information in data structures, the procedure for random selection of reactions and reacting sites and updating the event-driven changes at every step of the simulation for modeling tetrafunctional silanes are discussed in previous reports.<sup>266,276</sup> Here, we describe only the modifications made to extend this model to bridged and trifunctional silanes.

### 6.3.3. Accounting for Organic Components

The DMC model developed for tetrafunctional silanes can be easily customized for trifunctional silanes by simply setting the functionality of the monomers to 3. This allows only three condensable groups on each silicon site and the fourth group can be considered to be the organic component attached to each trifunctional site (such as a methyl group). The simulated polymers are equivalent to polymers resulting from trifunctional silanes comprising organic groups dangling in the network of connected silicon sites. For bridged silanes however, the task of defining the monomeric precursors is more complex. To do this, we build hexafunctional monomers and define bridging groups attached to each trifunctional site whose behavior may be different from siloxane bonds. Within the context of the existing program, we do this by first forming dimers from an even number ( $N$ ) of tetrafunctional monomers. This first bond between

each pair of monomers is always the organic bridge. After creating the dimers, the condensation conversion is reset and the sites are treated as trifunctional sites. Thus, at the onset of simulation, when compared to unconnected silicon sites in trifunctional monomers, all sites in the bridged monomers have an inherent connectivity equal to 1. This approach not only helps to identify the bridging group at any point in the simulation but also allows treatment of each silicon site as a trifunctional site analogous to the independent sites in the trifunctional silane case.

#### 6.3.4. Accounting for Cyclization Phenomena

For both bridged and non-bridged monomers represented by the DMC model, we consider formation of four-member rings. In non-bridged silanes, these rings form from the reaction between the unconnected ends of trimeric units (four silicon sites connected to each other with siloxane bonds) which may exist as isolated trimers or may be a part of larger oligomers. In our model, we keep track of these three bond segments by using the bond block concept of Rankin et al.<sup>266</sup> For example, Figure 7.2 shows a three bond block consisting of the silicon sites numbered 3, 4, 5 and 6 which is a part of a linear oligomer containing silicon sites numbered 1 through 7. This three bond block can be closed to form a four-member ring by connecting sites 3 and 6. For organically bridged silanes, we treat cyclization of siloxane-only bonds exactly the same way as for non-bridged silanes. However, carbosiloxane rings do not necessarily behave the same way and here we consider two extreme cases. For short bridged silanes (such as silanes with ethylene bridges), we treat the organic bridge just like a siloxane bond and allow formation of four-member rings involving bridges (carbosiloxane rings) to occur at the same rate as siloxane-only bridges. It is likely that carbosiloxane cyclization would in reality have different bond length dependent kinetics than siloxane cyclization, but this simplification reduces the number of parameters needed to allow carbosiloxane rings to form. The other case considered corresponds to either long or stiff bridges in which carbosiloxane rings are not prevalent. In this case, we restrict the bridges from engaging in the formation of rings by choosing only those trimeric units that do not contain bridges to react. In either case, four member ring cyclization is implemented by keeping track of all the three bond blocks at every Monte Carlo step. Li<sup>265,276,277</sup> and Rankin et al.<sup>266</sup> have described how to incorporate ring formation in the Monte Carlo algorithm and those details are not repeated here.

### 6.3.5. Accounting for First Shell Substitution Effects

Unlike hydrolysis, condensation reactions exhibit strong negative first shell substitution effects; in other words, the reactivity of a silicon site decreases with increasing connectivity of that site.<sup>80</sup> For tri- and tetra-ethoxysilanes under acidic conditions, the trend in the rate coefficients of the bi-molecular reactions that mimics the experimental trend is one in which they drop 90% when both reacting sites increase in connectivity and 10% when one of the reacting sites keeps the same connectivity.<sup>69,75</sup> Using these trends, the rate coefficient matrix for a trifunctional silane can be written as

$$\mathbf{k}_{non-bridged} = k_{00} \begin{bmatrix} 1.0 & 0.9 & 0.81 \\ & 0.1 & 0.09 \\ & & 0.01 \end{bmatrix}$$

The corresponding rate coefficient trend is not known for bridged silanes. However, in another study, we observed that bridged silanes follow similar functional group kinetics as their non-bridged versions when they are compared in solutions with equal initial alkoxy group concentrations.<sup>278</sup> This suggests that it is safe to assume that the nearest-neighbor effects in bridged silanes follow similar trends as in trifunctional silanes. Hence for bridged silane bi-molecular reactions, we used the same trends as observed for ethoxysilanes mentioned above. Since we start our simulations with dimers of tetrafunctional silanes representing the bridged monomers, the first row of the rate coefficient matrix can be ignored. Therefore, the bimolecular rate coefficient matrix for bridged silane simulations is input as

$$\mathbf{k}_{bridged} = k_{11} \begin{bmatrix} \bar{\phantom{1.0}} & \bar{\phantom{0.9}} & \bar{\phantom{0.81}} \\ & 1.0 & 0.9 \\ & & 0.1 & 0.09 \\ & & & 0.01 \end{bmatrix}$$

The substitution effects for cyclization reactions have never been directly measured. However, in keeping with prior simulation studies, we assume that the rates of ring closure depend on the connectivity of the end sites of the three bond blocks according to the same substitution effect trends for cyclization as for bi-molecular reactions. Hence the rate coefficient matrices for unimolecular reactions for the trifunctional and short bridged monomer cases are

$$\mathbf{k}_{4c,non-bridged/bridged} = k_{4c11} \begin{bmatrix} 1.0 & 0.9 \\ & 0.1 \end{bmatrix}$$



### 6.3.6. Reaction Rates

The reaction rates for the trifunctional sites in bridged and non-bridged cases are derived from the expressions provided by Li<sup>272</sup> and are summarized below.

$$\text{Bimolecular reaction rate, } R_{ij} = \begin{cases} k_{ij}(3-i)(3-j)[T_i][T_j] & i \neq j \\ \frac{k_{ij}}{2}(3-i)(3-j)[T_i][T_j] & i = j \end{cases}$$

$$\text{Uni-molecular reaction rate, } R_{4cij} = k_{4cij}(3-i)(3-j)[{}^3B_{ij}] \quad i \neq j$$

$[T_i]$  and  $[T_j]$  are the concentrations of the reacting sites,  $T_i$  and  $T_j$  respectively.  $[{}^3B_{ij}]$  is the concentration of the three bond blocks with end site connectivities  $i$  and  $j$ . The numbers of all  ${}^3B_{ij}$  segments are updated continuously by tracing the new bond pathways and changed pathways after each reaction.

### 6.3.7. Model Parameters

We make use of the following parameters to describe and understand the statistics of our simulations.

*Site Distribution  $[T_i]$ :* The concentration of each type of silicon site is obtained by enumerating the number of sites with different degrees of connectivity in the DMC calculation.

*Gel Conversion ( $\alpha_g$ ) and Gel Time ( $t_g$ ):* At any point in the simulation, cumulative condensation conversion is calculated by  $\alpha = \frac{2 \times \text{total number of DMC steps}}{3 \times N}$ <sup>276</sup> and, the Monte Carlo time to reach this conversion is calculated by  $t = t_{\text{prev}} + \Delta t$  where  $t_{\text{prev}}$  is the Monte Carlo time in the previous DMC step,  $\Delta t = \frac{\ln(\frac{1}{x})}{(\frac{N}{[Si]}) \sum (R_{ij} + R_{4cij})}$ <sup>263</sup> is the time elapsed during each bond addition,  $x$  is

a random number between 0 and 1, and  $[Si]$  is the silicon site concentration. The gel conversion and gel time correspond to the conversion and time when the weight average degree of polymerization diverges. In cases where the system doesn't gel, the condensation conversion would reach 100% when the simulation stops.

*Degree of Polymerization ( $DP_w$ ):*  $DP_w$  is the weight-averaged degree of polymerization defined as

$$DP_w = \frac{1}{N} \sum_{i=1}^N L(i)^2$$

where  $N$  is the number of molecules and  $L(i)$  is the size of molecule,  $i$ .

*Cyclization Tendency (K)*: To characterize cyclization tendency of the system, we use the dimensionless parameter defined by  $K = \frac{k_{4c(1,1)}}{k_{11}[Si]}$ .<sup>266</sup> The ratio of the cyclization and bi-molecular rate constants gives a measure of the competition between molecular growth and cyclization.  $K = 0$  indicates the extreme case of no cyclization and increasing  $K$  value increases the rate of cyclization. For low  $K$ , bimolecular reactions are predominant. This parameter is also useful to model the sensitivity of structure evolution with initial concentration, thus providing a quantitative connection with the experimental reaction conditions.

*Ring Involvement (I)*: Ring involvement gives a measure of the extent of cyclization in the local network. It is defined as the average number of rings any randomly chosen silicon site is involved in. Since cyclization reactions involve the formation of one ring,  $I$  is increased by  $3/N$  after every ring closure. It ranges from 0 (indicating no rings) to a maximum value equal to the functionality of the silicon site. Therefore, any given silicon site can be involved in at most 3 rings except for bridged silanes, when carbosiloxane formation is allowed and maximum ring involvement can be as large as 4.

## 6.4. Results and Discussion

### 6.4.1. Model Validation

We validate our models by comparing the results of simulation for ideal polycondensation with theory. In ideal polymerization, the functional groups react randomly, independent of the neighboring connectivities. That is, substitution and cyclization effects are not considered. This is implemented in our models by setting all rate constants equal to  $k_{00}$  and  $K=0$ . Ideal polymerization can be described by random branching theory developed by Flory<sup>279</sup> and Stockmayer<sup>280</sup> to obtain properties of a non-linear polymerization system. We use the following expressions derived from this theory<sup>281,282</sup> to determine fractional site distributions  $f(T_i)$ , weight-average degree of polymerization ( $DP_w$ ) and gel conversion ( $\alpha_g$ ) from condensation conversion ( $\alpha$ ).

$$f(T_0) = \frac{T_0}{N} = (1 - \alpha)^3$$

$$f(T_1) = \frac{T_1}{N} = 3 \alpha (1 - \alpha)^2$$

$$f(T_2) = \frac{T_2}{N} = 3 \alpha^2 (1 - \alpha)$$

$$f(T_3) = \frac{T_3}{N} = \alpha^3$$

$$DP_w = \frac{1 + \alpha}{1 - (f - 1)\alpha}$$

$$\alpha_g = \frac{1}{1 - f}$$

Figure 7.3a compares the fractional site distributions obtained from simulations with the theoretically derived profiles given above for ideal bridged and non-bridged silane polymerization. Under random branching conditions, only bi-molecular reactions occur and the reactivity of the bridged sites does not depend on the presence of the bridge. Hence, the site distributions are same for bridged and non-bridged cases. Figure 7.3b compares with theory the progress of  $DP_w$  with  $\alpha$  for both types of monomers under the ideal conditions.  $DP_w$  gradually increases with conversion and suddenly diverges. This is an indication of the gel point. Gel points match with the theoretical values for both simulations. The presence of the bridging organic group in bridged silanes provides for additional connectivity in the network as opposed to unconnected organic groups in the trifunctional system. This causes gelation at lower conversion (20%) in bridged silanes when compared to 50% in the non-bridged case. In both the figures, simulations are equivalent to the theoretically derived profiles illustrating the accuracy of the DMC model used. The simulated profiles slightly deviate from the theoretical towards high  $DP_w$  values due to the finite population of monomers in the simulation. With increasing system size, the simulated profiles have been shown to match better with theory.<sup>283</sup>

#### 6.4.2. Effect of Cyclization

Figures 7.4a and 7.4b show the site distributions in bridged and non-bridged versions under non-ideal polycondensation conditions for low ( $K=0.5$ ) and relatively high ( $K=10$ ) cyclization rates. For  $K=0.5$ , we observe similar local connectivities for bridged and trifunctional system (Figure 7.4a). When  $K$  is increased to 10, the bridged profiles deviate from non-bridged and the gel conversion of the bridged system surpassed that of the trifunctional system, illustrating that cyclization increases gel conversion. The same effect is observed in Figures 7.5a and 7.5b depicting the variation of  $DP_w$  with  $\alpha$  for trifunctional and bridged systems respectively for a range of cyclization tendencies. In the absence of cyclization, the gel conversions are slightly higher than the ideal cases due to the substitution effects. In both cases, gel conversion increases with  $K$ . This is consistent with the hypothesis that cyclization delays gelation. For  $K \leq 2$ ,

the gel conversions in trifunctional system remain higher than bridged as bi-molecular reactions are predominant. However, for  $K > 2$ , the cyclization phenomenon causes the gel conversion of bridged silanes to overtake the values of the corresponding non-bridged system for the same cyclization rates.

In the trifunctional system, gel conversions increase gradually with  $K$  for  $0 \leq K < 10$  (Figure 7.5a). For  $K \geq 10$ , the cyclization rate has no effect on  $DP_w$  profiles and gel conversions. The system reaches a gel point for all values of  $K$  and the maximum simulated gel conversion is 95% for  $K \geq 10$ . However, experimental observations show that the formation of silsesquioxane cages prevents gelation in trifunctional silanes. The gelation predictions of simulations are most likely due to the irreversible model of polymerization used in the DMC model and the use of only one type of cyclization reaction so that, for instance, trimers are unable to participate in cyclization. On the other hand, in the bridged systems, gel conversions remain very low for low values of  $K$  and increase quickly to  $>90\%$  for  $K > 2$ . With increasing  $K$ , the system reaches 100% conversion for a low  $DP_w$  of 10 without reaching the gel point. This indicates that the model exaggerates the effects of cyclization, but also predicts the formation of cage-like silsesquioxanes that do not gel. The effect of cyclization is more severe here because we start with bridged monomers containing two silicon sites and the first reaction generates dimers containing four silicon sites, which quickly react by cyclization.

#### **6.4.3. Molecular Growth vs Cyclization**

Plots of gel conversion and gel time vs.  $K$  articulate the competition between molecular growth and cyclization. Figures 7.6a and 7.6b show that they follow a sigmoidal relationship with cyclization. For  $K < 2$ , bridged silanes gel at 20% conversion. There is an inflection in gel conversion and gel time as cyclization becomes dominant. Dimers formed from bridged silanes are very reactive towards cyclization causing the rapid rise in gel conversion. Bridged monomers delay the rise in gel conversion when compared to trifunctional but they do not prevent it. This is because the carbosiloxane rings link together siloxane rings, thus allowing network formation even in the presence of strong cyclization effects. For  $K > 10$ , both the types have almost 100% conversion. Gel time increases with cyclization rate for bridged and non-bridged silanes. Bridged silanes gel quickly when compared to trifunctional monomers at high concentrations/low cyclization.

#### 6.4.4. Implications of Unlimited Cyclization

The effect of uncontrolled cyclization noted above can be found by observing the evolution of cyclic structures as described by the ring involvement vs. conversion profiles for non-bridged and bridged monomers in Figures 7.7a and 7.7b respectively. For trifunctional sites, the maximum ring involvement would be 3 and for bridged (since we are including bridges in rings), the theoretical value would be 4. For trifunctional sites at high  $K$ , the maximum value is  $I=2$  (Figure 7.7a). If cages were dominant,  $I$  would be 3. Because the maximum observed ring involvement is significantly less than the maximum possible, this explains the deviation from the experimental trend (of silsesquioxane cages preventing gelation). For the bridged monomer,  $I \geq 4$  (Figure 7.7b) for  $K \geq 5$  which means that cages involving carbosiloxane rings are formed. In addition to this, the current simulation treats all three bond blocks the same way leading to ring closures that may not be physically possible. There could be some practically impossible molecules that lead to closed structures as indicated by  $I > 4$  for bridged, delaying gelation. Such physically unreasonable values for  $I$  ( $I > 4$ ) even for  $K > 2$  indicate the need to limit cyclization. Since we are starting with all dimers that have even number of molecules, four member carbosiloxane rings are favored by the simulation. We can limit this growth by setting carbo-siloxane rate co-efficients different from the other rates of cyclization.

#### 6.4.5. Role of Carbosiloxane Rings

In order to understand the role played by carbosiloxane rings in the gelation of bridged silanes, we consider long bridges which are stiff enough not to participate in ring closures. We account for this feature in our simulation by excluding formation of carbosiloxane rings. In the absence of such rings, Figures 7.8a and 7.8b show that there is no  $K$  large enough to influence gel conversion or gelation rate. Figure 7.8a shows that there is not much cyclization without the involvement of bridges when compared to extensive cyclization due to carbosiloxane ring involvement in the short bridged silanes. In the absence of carbosiloxane rings, gel conversions remain low and are not sensitive to cyclization. This means that carbosiloxanes are the only type of rings that delay gelation for bridged silanes. This conclusion supports the delayed gelation exhibited by short bridged silanes forming carbosiloxane rings.<sup>91</sup>

#### 6.5. Conclusions

We performed dynamic Monte Carlo Simulations for bridged and non-bridged silanes and evaluated the effects of the inclusion of an organic bridge on gelation behavior. We included

substitution effects and allowed four-member ring formation, and treated four-site rings involving short organic bridges like a siloxane bond. We found that both types of silanes have similar local connectivities at low rates of cyclization but that deviations increase with increasing cyclization tendency. We addressed the implications of bridging group length by simulating polycondensation in the presence and absence of carbo-siloxane rings. The results of the simulation indicate that cyclization delays gelation in general and particularly in bridged silanes only carbosiloxane rings delay gelation. Silanes with long bridges exhibit low gel times because they do not form carbo-siloxane rings. Current simulations favor the formation of carbosiloxane rings from dimers in bridged systems resulting exaggerated effects of cyclization which can be averted by limiting the growth of carbosiloxanes.

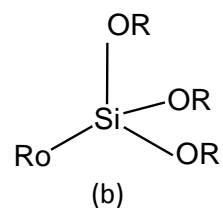
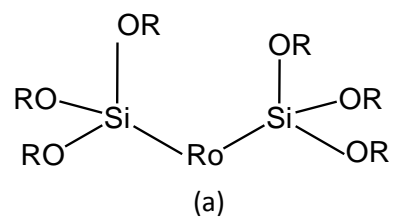


**Figure 6.1.** General structure of (a) Bridged silanes (b) Non-bridged silanes. Notation:  $R_o$  – organic group; OR – alkoxy group.

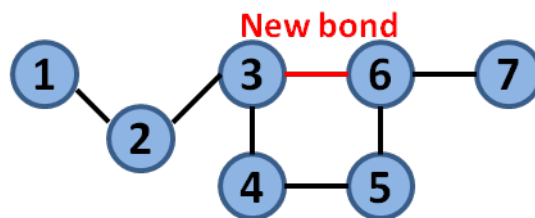


**Figure 6.2.** Formation of a four-member ring from a three bond block. Circles are silicon sites and lines represent the siloxane bonds or bridges wherever applicable.



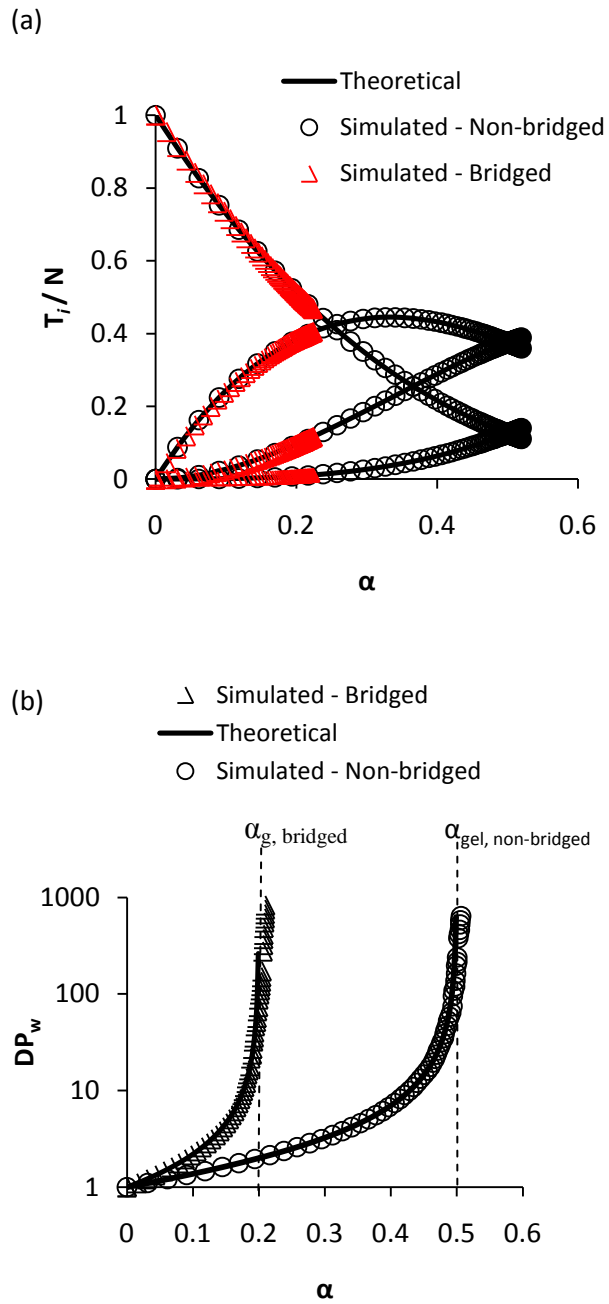


**Figure 6.3.** Bridged and non-bridged random branching theoretical profiles compared with simulations of ideal polycondensation until gelation (a) site distributions (b) degree of polymerization.

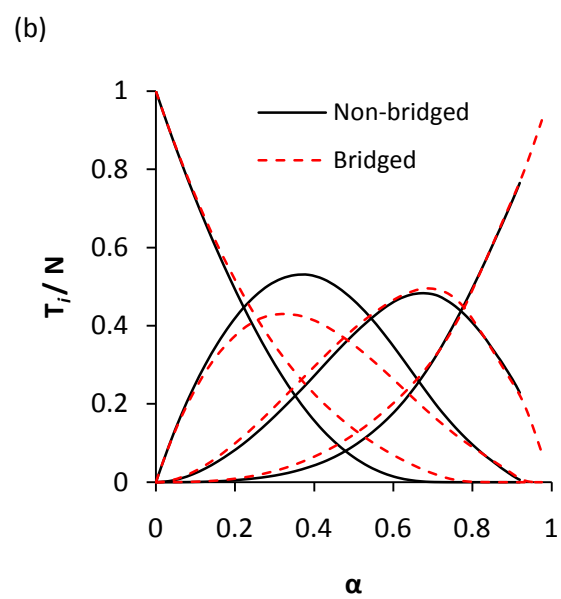
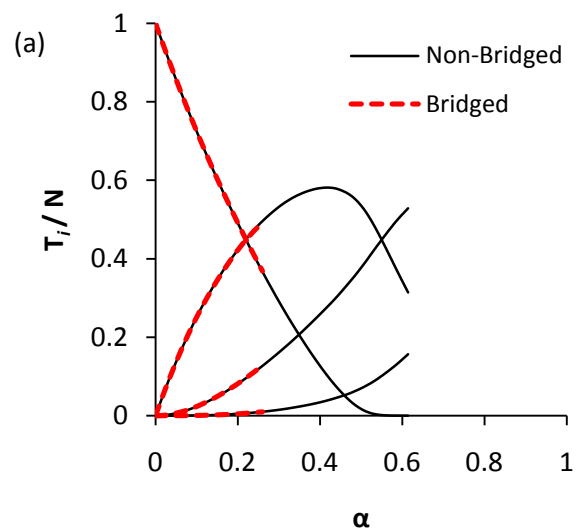


**Figure 6.4.** Site distributions of bridged case compared with non-bridged for non-ideal polycondensation (a)  $K=0.5$  (b)  $K=10$ .

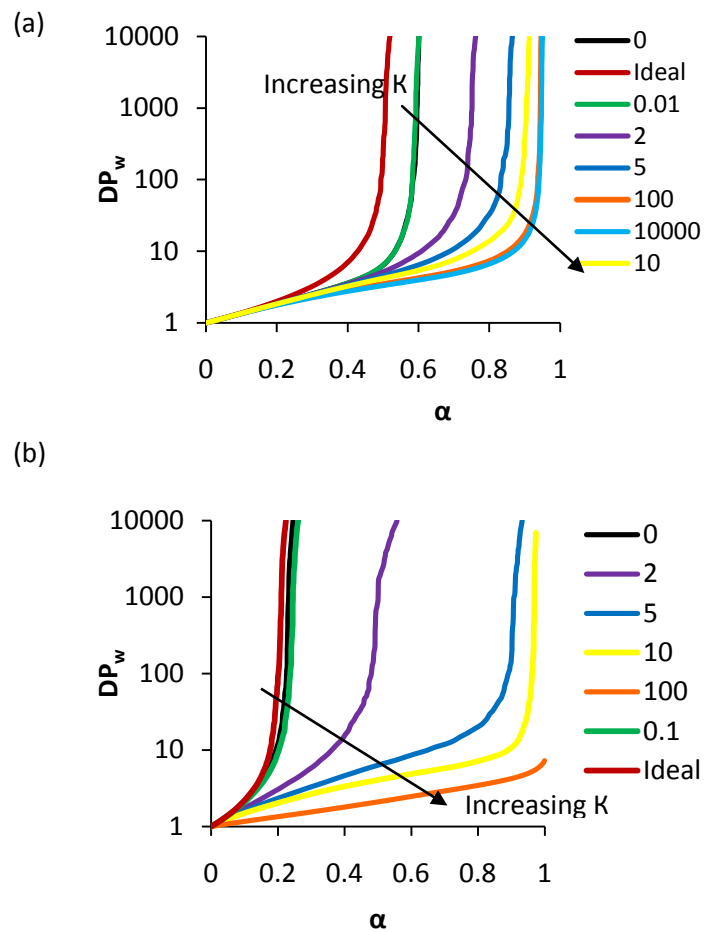


**Figure 6.5.** Variation of Degree of Polymerization with gel conversion for various cyclization tendencies for (a) Non-bridged (b) Bridged.

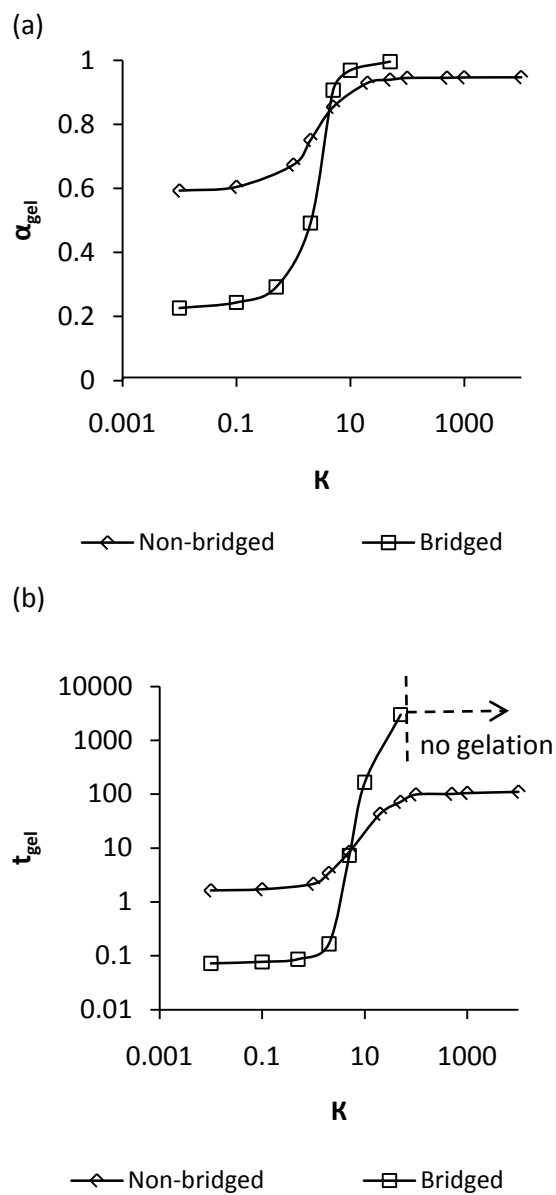


**Figure 6.6.** Variation of (a) gel conversion and (b) gel time with cyclization rate in non-bridged and bridged silanes.

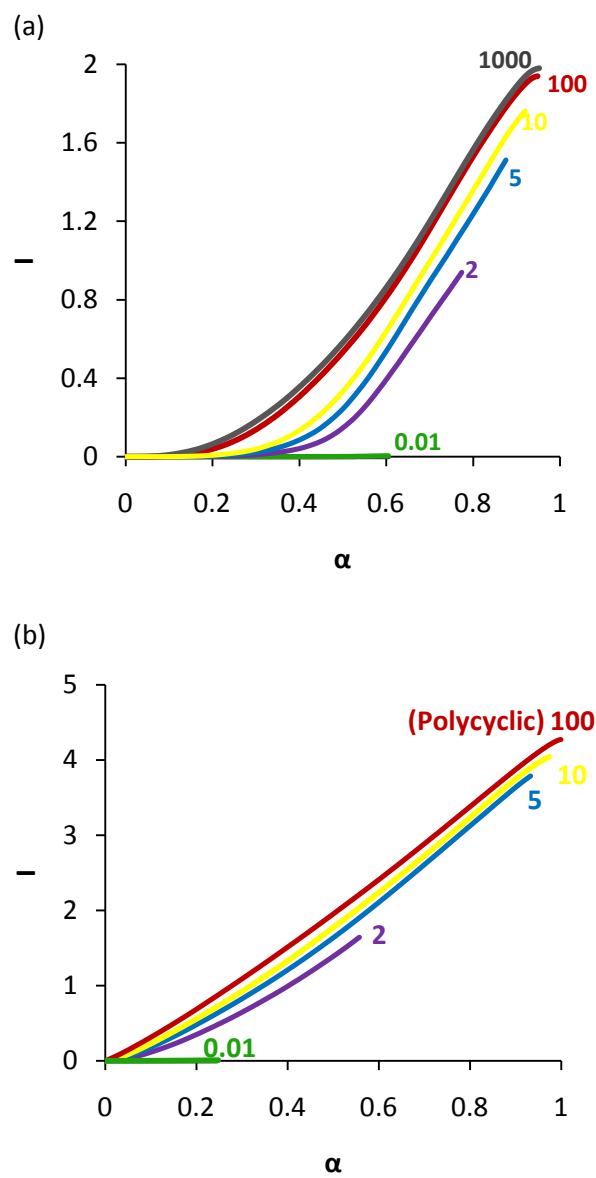


**Figure 6.7.** Variation of Ring Involvement with gel conversion for (a) Non-bridged (b) Bridged.

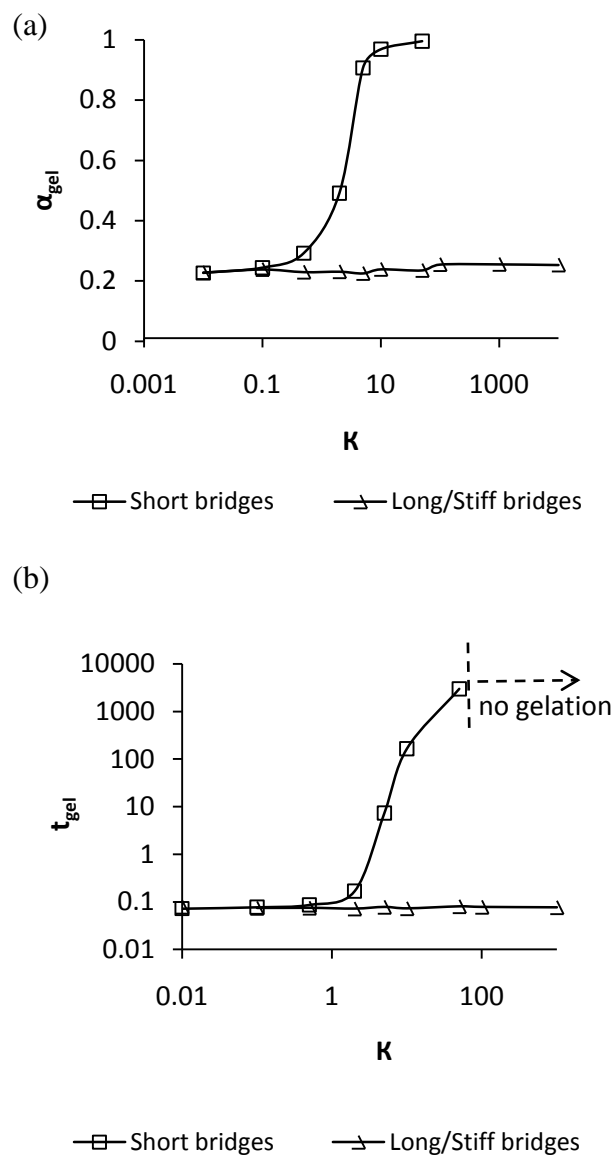


**Figure 6.8.** Variation of (a) gel conversion and (b) gel time with cyclization rate short and long bridged silanes.

### **III Application of Siloxane Based Materials in Adsorption Technologies**

## 7. Loading and Protection of Antioxidant Enzyme on Engineered Silica

### 7.1. Summary

Ordered mesoporous silica materials have emerged as promising bio-materials for tissue engineering and drug delivery due to their high surface areas and easy pore size control. There exist several *in vitro* demonstrations of controlled retention and release of pharmaceuticals from silica systems in literature. However, practical implementation of such carriers is limited by the adverse health effects associated with oxidative stress induced by silica. We hypothesize that loading mesoporous silica with anti-oxidant enzymes helps to control oxidative stress, thus making silica carriers bio-compatible. Based on this hypothesis, in the present study, we compared loading, activity and retention of an anti-oxidant enzyme, catalase, on four engineered mesoporous silica types: non-porous silica (NPSP), spherical silica with radially oriented pores (SP-R) and hollow spherical silica particles with pores oriented either parallel to the hollow core (HSSP-P) or expanded, interconnected bimodal pores (HSSP-I). All of these silica types displayed the potential for effective catalase loading and protection against the proteolytic enzyme pronase when compared to non-porous silica. Hollow particles with interconnected pores exhibit higher loading and activity than the other materials but poor protection against proteolysis. Further pore size tuning may be necessary to obtain protection without compromising loading.

### 7.2. Introduction

Biomedical research on mesoporous silica<sup>284-286</sup> has gained unbridled momentum since they were first reported as prospective drug delivery systems in 2001.<sup>287</sup> Their exceptional properties *viz.* well-ordered structure, high surface area and easy pore size control have made mesoporous silica promising bio-materials for tissue engineering<sup>288,289</sup> and drug delivery.<sup>10,21,290</sup> Serving as effective orthopedic materials, mesoporous silica have the potential for enhanced osteogenic bioactivity when compared to traditional silica bio-glass due to their large pore size and pore volume which accelerates apatite formation.<sup>291</sup> They can also be coated over metallic prosthesis to promote osseointegration. These materials can also be customized to have pores similar to the molecular size of most drugs and hence, can serve as potential carriers for oral as well as parenteral (intramuscular or intravenous) drug delivery. Drugs can also be embedded in mesoporous silica designed for tissue regeneration or reconstruction for local drug release so as



to prevent inflammatory responses and infections. These materials can be loaded not only with drugs that have therapeutic effects but also with proteins and peptides that promote tissue growth or mimic cell functions (e.g. enzymes). Vallet-Regi recently reviewed<sup>13</sup> the growing biomedical applications of nanostructured mesoporous silica matrices.

The literature in this area encompasses several in-vitro studies that have demonstrated controlled retention and release of pharmaceuticals from silica systems.<sup>292-297</sup> However, these materials may present clinical challenges due to the adverse health effects associated with biological exposure to nanoparticles.<sup>290,298-300</sup> There is considerable evidence that silica generates Reactive Oxygen Species (ROS) in living cells and leads to the induction of oxidative stress.<sup>301-304</sup> Oxidative stress damages cells by the alteration of macromolecules such as polyunsaturated fatty acids in membrane lipids, protein denaturation and ultimately damaging DNA. Besides the well known condition silicosis,<sup>305,306</sup> (an occupational lung disease caused by exposure to particulate silica), silica has also been associated with the development of several carcinogenic, autoimmune and other lung diseases.<sup>304,307-309</sup> Injected nanoparticles may redistribute to other sites in the body causing systemic failures also. One way to address this setback of otherwise medically efficacious silica materials is by using antioxidant enzymes. We hypothesize that loading silica particles with an anti-oxidant enzyme would overcome the oxidative stress that induces silica toxicity. Our hypothesis mimics the natural mechanism occurring in living cells that balances the production of ROS. ROS - namely superoxide, hydrogen peroxide and hydroxyl radicals, are usually scavenged by the action of superoxide dismutase (SOD), catalase, or glutathione (GSH) peroxidase<sup>310</sup> (Figure 7.1). These anti-oxidant enzymes are in turn degraded by proteolytic enzymes. Hence, an ideal silica carrier should be able to provide stable residence to the anti-oxidants while protecting them from proteolytic degradation. In order to begin addressing our hypothesis and to provide a basis for designing silica carriers, in the present study we aim to determine the effect of structural parameters (pore size, surface area, particle size etc.) on the enzyme attributes (loading, activity and retention). This research is directed not only towards addressing a potential roadblock in the practical use of silica carriers but also towards impacting the existing therapeutic technologies involving oxidative stress control.

In the present study, we investigate an antioxidant enzyme, catalase, loaded into and onto selected mesoporous silica types ranging from non-porous to silica designed with pores large

enough to freely accommodate catalase. In addition to loading, we study the resistance to proteolysis of supported enzyme by pronase. We compare the loading, activity and protection offered by the mesoporous silica particles with those of bare silica. We also investigate the stability of catalase in each of these materials.

### 7.3. Experimental Details

#### 7.3.1. Source of Materials

Aqueous polystyrene latex microspheres for hollow silica particle templating (0.356  $\mu\text{m}$ ) were purchased from Polysciences, Inc and supplied as a 2.64% aqueous dispersion. Aqueous ammonia (27 wt% ammonia), absolute ethanol and ultra filtered de-ionized water were obtained from Fisher Scientific. Tetraethoxysilane (TEOS, 98%), cetylpyridinium chloride ( $\text{C}_{16}\text{PyCl}$ , > 99%), cetyltrimethylammonium bromide (CTAB, >99%), hydrogen peroxide ( $\text{H}_2\text{O}_2$ , 30 wt% in water), protease from *Streptomyces griseus* and Phosphate Buffered Saline (PBS) (used to make 0.01 M PBS solution, pH 7.4) were purchased from Sigma-Aldrich, and bovine liver catalase (24700 M.W.) from EMD Biosciences. All materials and reagents were used as received.

#### 7.3.2. Nanoparticle Synthesis

Silica materials employed in the present study were synthesized by Alex Lopez from recipes developed and utilized previously in the Rankin group.<sup>311, 312,313</sup>

*Synthesis of NPSP.* Nonporous (NPSP) silica was synthesized using the same compositions of water, ethanol and ammonia as used for SP-R (see below) in the absence of surfactant. This gives a composition approximately in the range used for Stöber silica particle synthesis. 20.9 g  $\text{H}_2\text{O}$ , 26.8 g  $\text{C}_2\text{H}_5\text{OH}$ , and 6.9 g concentrated aqueous ammonia were mixed together and stirred for 30 min. 2.1 g of TEOS was quickly added to the solution and was aged for 2 hours by continuous stirring at room temperature. The solution was centrifuged and washed to recover the particle precipitate. The precipitate was dried overnight and calcined in air at 500  $^\circ\text{C}$  for 4 hours in a muffle furnace.

*Synthesis of SP-R.*<sup>311</sup> 1.1 g of CTAB was added to a mixture of 20.9 g  $\text{H}_2\text{O}$ , 26.8 g  $\text{C}_2\text{H}_5\text{OH}$ , and 6.9 g concentrated aqueous ammonia. This mixture was stirred for 30 min. and 2.1 g of TEOS was added slowly with continuous stirring for 1 minute. The solutions became turbid and the solution was aged for 2 hours by continuous stirring at room temperature. This process resulted

in a white precipitate which was filtered and washed with deionized water. After drying overnight, the powder was calcined in air at 500°C for 4 hours in a muffle furnace.

*Synthesis of HSSP-P.*<sup>312</sup> After stirring a mixture of 0.9 g polystyrene latex dispersion, 0.09 g CTAB and 9 g of concentrated aqueous ammonia for 30 min., 0.46 g TEOS was added slowly. The solution was aged for 2 h with stirring, filtered, dried overnight and then calcined at 550°C in air for 4 hours in a muffle furnace.

*Synthesis of HSSP-I1 and HSSP-I2.*<sup>313</sup> Hollow silica particles with porous interconnected shells were prepared using a two-step procedure. In the first step, 2.7 g polystyrene latex dispersion and 0.6 g C<sub>16</sub>PyCl were added to 27.3 g of concentrated aqueous ammonia. After stirring the mixture for 30 min., 1.4 g TEOS was slowly added to this solution which yielded a white precipitate after aging for 2 h. The precipitate was filtered, washed with deionized water and the resulting powder was dried at 50°C. In the second step, 1 g of this as-made sample was added to a mixture of 63.5 ml H<sub>2</sub>O and 4.1 ml concentrated aqueous ammonia, sealed in a Teflon lined autoclave and heated in an oven at 100°C for 72 hours. The resulting solution was filtered, washed and dried at 50°C overnight and then calcined in air at 550°C for 5 hours in a muffle furnace. The particles in the second step were more homogeneously dispersed in HSSP-I2 than in HSSP-I1.

### **7.3.3. Nanoparticle Characterization**

The synthesized materials were characterized for particle size distribution and indications of hollow cores using Scanning Electron Microscopy (SEM) on a Hitachi s-4300 microscope. The SEM samples were prepared by loading the silica powders on PELCO carbon tape and coating by sputtering with gold under vacuum. The surface area and pore size measurements were performed using N<sub>2</sub> adsorption-desorption on a Micrometrics Tristar 3000 instrument at 70 K. The samples were degassed under flowing nitrogen at 120°C for 4 hours before analysis. Reported specific surface areas of the particles were determined using the isotherm of Brunauer, Emmett and Teller (BET)<sup>314</sup> and the average pore size was determined from the distribution generated by the method of Barrett, Joyner and Halenda (BJH).<sup>315</sup>

### **7.3.4. Enzyme Loading and Analysis**

10 mg / mL of silica nanoparticles was prepared in PBS and used as a stock solution. A 10 mg/ml radiolabeled <sup>125</sup>I-catalase was prepared as previously described. 1.4 mg/ml of catalase

and 1 mg/ml of each nanoparticle were suspended in PBS (pH=7.4) buffer solution. After incubating for 1 hour at room temperature, the enzyme loaded particles were centrifuged and used for analyses. Each individual particle solution was prepared in triplicate. Loading and protection of catalase were monitored through two independent processes, radio-tracing and enzyme activity. The amount of enzyme adsorbed on to the particles was determined by measuring  $^{125}\text{I}$  labeled catalase content in solution pre- and post-loading using a gamma counter (Perkin Elmer). The activity of catalase was determined after specific intervals of incubation using a Varian Cary Eclipse UV-Vis spectrophotometer from 0.1 mg/ml loaded nanoparticles in PBS added to 4.5 mM  $\text{H}_2\text{O}_2$ . The degradation of  $\text{H}_2\text{O}_2$  was monitored by measuring absorbance with time at 242 nm. One unit of catalase activity is defined as the amount of catalase that will decompose 1.0 micromole of hydrogen peroxide per minute at pH 7.0 at 25 °C at a substrate concentration of 50 mM hydrogen peroxide. For protection studies, enzyme loaded particles were re-suspended in PBS solution with 0.2 wt% pronase and incubated for an hour before activity measurements. Loading experiments were performed by David Cochran and activity experiments by Alex Lopez.

### **7.3.5. Statistical Analysis**

All of the values reported in the figures are given in terms of means and standard errors. Loading, activity and protection results were analyzed using MINITAB 15 to identify a statistically significant difference between different types of silica nanoparticles. Where appropriate, one-way Analysis Of Variance (ANOVA) was performed using a general linear model with a p-value of 0.05. Post-hoc analysis was performed using Bonferroni test with 95% confidence interval.

## **7.4. Results and Discussion**

### **7.4.1. Nanoparticle Design Attributes**

Figure 7.2 displays a schematic of the silica nanoparticles used in the present study. Non-porous silica (NPSP) is used as a control. Other particles possess well ordered pore structures which favor homogeneity of the adsorption and release stages. SP-R are spherical particles with radially oriented pores. Compared to bare silica, the mesopores in SP-R provide a higher specific surface area and the radial orientation provides pore accessibility. HSSP-P silica are hollow spherical particles with pores oriented parallel to the hollow core. Although the hollow core offers a large volume for enzyme loading in principle, the parallel orientation of the mesopores in the shell makes it inaccessible. This setback is overcome in HSSP-I, hollow spherical particles

with interconnected bimodal pores. The mesopores oriented parallel to the hollow core are interconnected by larger pores in HSSP-I. Hypothetically, HSSP-I particles are expected to exhibit the maximum enzyme loading and protection due to the presence of hollow core and ease of its accessibility by the enzyme.

#### 7.4.2. Nanoparticle Properties

SEM micrographs of the silica nanoparticles in Figure 7.3 confirm their spherical morphology. A small fraction of hollow particles (Figure 7.3c, 7.3d and 7.3e) appear to be broken. These defects are clearly visible in HSSP-I1 (Figure 7.3d) verifying the hollow structure of the HSSP group of materials. All particle sizes (determined from SEM images, reported in Table 1) are found to be nearly uniform except SP-R's which exhibits a wide range from 0.15 to 0.85 nm. Figure 7.3f provides the particle size distribution of SP-R determined from the SEM image in Figure 7.3b. The size of NPSP particles was measured to be 0.3 nm. The HSSP groups of particles have a narrow size distribution. The small range of HSSP-P (0.56-0.65 nm) particle size indicates the presence of thinner mesoporous shells in HSSP-P than in HSSP-I particles which have a relatively large range (0.56 – 85 nm).

Nitrogen adsorption-desorption isotherms and the corresponding BJH pore size distributions are plotted in Figures 7.4 and 7.5. The non-porous nature of NPSP is confirmed by its nearly zero-volume sorption isotherms in Figure 7.4a. SP-R and HSSP-P (Figure 7.4a) isotherms are Type IV indicating uniform mesopores. The BJH pore diameters obtained from N<sub>2</sub> sorption are 2.9 and 3.1 nm for SP-R and HSSP-P particles respectively. The hysteresis loops of HSSP-I1 and HSSP-I2 (Figure 7.4b) indicate the presence of broad bimodal mesopore distributions. HSSP-I1 has predominantly 3.8 nm pores with a small distribution of larger pores represented by the shoulder at 5.4 nm in the pore size distribution. HSSP-I2 has a broader pore size distribution than HSSP-I1 with peaks at 4.2 and 7.5 nm. Since the size of catalase is (ca. 7 nm × 8 nm × 10 nm; PDB, 1TGU), HSSP-I pores should be readily accessible for enzyme loading. BET surface areas obtained from nitrogen sorption experiments are given in Table 1. All of the mesoporous silica samples have high total surface areas ranging from 600-800 m<sup>2</sup>/g when compared to NPSP (10 m<sup>2</sup>/g). SP-R has largest total surface area (802 m<sup>2</sup>/g) followed by HSSP-I with the lowest being HSSP-I2 (617 m<sup>2</sup>/g). External surface area of each particle was calculated (neglecting the effects of particle aggregation) from  $(\frac{3r^2}{\rho R^3})$  where  $r$  is the particle radius measured from SEM micrographs and  $R = r$  for NPSP and SP-R and  $R = r - r_{core}$  for HSSP group of particles.  $r_{core}$  is the

radius of the latex microspheres used as templates for hollow cores.  $\frac{1}{\rho} = (\frac{1}{\rho_s} + V_p)$ .  $\rho_s = 2.2 \text{ g/cm}^3$  and  $V_p$  is the specific mesopore volume obtained from corresponding adsorption isotherms. HSSP-P is found to have the largest external surface area of  $118 \text{ m}^2/\text{g}$  followed by HSSP-I particles. SP-R ( $9.9 \text{ m}^2/\text{g}$ ) has low external surface area close to that of NPSP ( $9.1 \text{ m}^2/\text{g}$ ).

#### 7.4.3. Loading Analysis

Figure 7.6 illustrates the amount of catalase initially absorbed by the nanoparticles and the amount left on the particles after an hour of incubation under pronase activity. In comparison to NPSP (which is non-porous) and HSSP-P (which is practically non-porous due to its pore orientation), SP-R exhibits higher loading. Presumably the pores are too small to admit catalase, so this suggests that mesoporosity helps stabilize catalase on the silica surface. For the same reason, despite the presence of a hollow core, HSSP-P displays lower loading than HSSP-I particles. HSSP-I2 exhibits the highest loading of all the particles by absorbing  $1.1 \text{ mg/mg}$  silica. However, the loading decreased to  $0.4 \text{ mg/mg}$  silica after the action of pronase. The large pores in HSSP-I2 may be providing accessibility to pronase in addition to catalase leading to poor protection. The advantage of silica particles as catalase carriers is clearly seen, as the best performing material, HSSP-I2 possesses 52 wt% and 28 wt% catalase pre- and post- pronase digestion, respectively. This is in stark contrast to polymer particles synthesized by the Dzuibla group which although effective therapeutically *in vivo*, contained only 2 wt% and 0.5 wt% catalase pre- and post- pronase, respectively.<sup>316</sup> NPSP and HSSP-P exhibit the lowest performance with an initial loading of  $0.2 \text{ mg/mg}$  in both the materials. After proteolysis, NPSP retained the least amount of catalase ( $0.03 \text{ mg/mg}$ ). Surprisingly, HSSP-P retained the largest amount of loaded catalase after proteolysis. The greater amount of retention observed in HSSP-P particles may be attributed to the protection provided by the hollow cores that were accessed by catalase through defects in the porous shells, radially oriented pores, or broken particles.

#### 7.4.4. Activity Analysis

The activities of catalase measured per mass of silica particles before and after proteolysis are plotted in Figure 7.7. HSSP-I2 exhibits the highest catalase activity with 107 units per mg of silica followed by SP-R and HSSP-I1, both with an activity of 64 units/mg. NPSP showed the lowest initial activity of 14 units/mg. After proteolysis HSSP-I1 and HSSP-I2 retained the greatest

levels of activity (24 and 20 units/mg respectively), followed by HSSP-P (14 units /mg silica). SP-R and NPSP respectively retained only 7 and 5 units of the initial activity.

SP-R exhibits higher initial activity when compared to NPSP. High SP-R activity indicates that mesoporosity helps in binding the enzyme to the particle and in maintaining activity. However, after proteolysis SP-R activity drops to a level comparable to that of NPSP. Because the SP-R pore size is much less than the size of catalase, the enzyme may be binding only on the external surface of SP-R without entering the pores. Hence, SP-R offers poor protection to the bound catalase.

HSSP-P has lower activity but offers more protection than SP-R. The inaccessible pores in HSSP-P lead to low loading and in turn low activity. Another possible reason for low activity could be the difference in the surface structure (similar to that of NPSP) when compared to the porous texture of SP-R which seems to promote stronger binding with the enzyme. High loading in HSSP-I particles resulted in high initial activity but their performance after proteolysis was very poor. This may be a result of loss in mass due to degradation by protease or the enzyme leaching out of the particles.

Because the particles differ in size and surface area, stability of the enzyme on the silica surface is best described by activity per mass of catalase (Figure 7.8). Initially, HSSP-P has the largest amount of active catalase per mg of catalase loaded followed by SP-R and HSSP-I1. All particles except NPSP displayed loss of active catalase after proteolysis. The increase in activity in NPSP indicates that proteolysis resulted in loss of inactive catalase.

#### **7.4.5. Protection from Pronase**

Percentage protection offered by the silica nanoparticles against proteolytic degradation of loaded catalase observed from mass loading and activity measurements are compared in Figure 7.9a and 7.9b respectively. If loss in activity is purely a result of loss in mass due to degradation by protease or the enzyme leaching out of the particles, activity and loading are expected to follow the same trend. However, the percentages of protection obtained from mass loading and activity analyses are found to follow different trends. This indicates that the surface structure and mesoporosity are playing an important role in enzyme binding and degradation. All mesoporous silica offer greater protection with respect to mass loading than bare silica indicating that mesoporosity promotes stronger binding of the enzyme with the silica particles. This may result from a rougher surface texture compared to NPSP. Despite low loading, HSSP-P

surprisingly displays greater protection (88%) from proteolysis when compared to HSSP-I1 (61%). This could be an artifact caused by the defects in HSSP-P (Figure 7.4c) admitting catalase into the protected pore space. As expected HSSP-I particles retain more enzyme than SP-R and NPSP due to the presence of hollow cores and ease of their accessibility. Low protection in SP-R (25%) clearly indicates that its pores are too small for catalase. Hollow particles, HSSP-P (33%), HSSP-I1 (37%) and HSSP-I2 (19%) offer more protection to active catalase than SP-R (11%) as the enzyme loaded on SP-R is easily accessible to pronase. Surprisingly NPSP (39%) offers more protection than SP-R which may be an artifact caused by difficulty in accurate activity measurements of NPSP. A low percentage of protection in HSSP-I2 when compared to the other hollow particles can be attributed to the large pores which provide accessibility of the loaded catalase to pronase.

#### **7.4.6. Stability of Catalase**

In order to understand the stability of loaded catalase, activities were monitored for a period of 24 hours. The activities reported in Figure 7.10 are normalized with respect to initial activity observed after an hour of incubation for each particle. NPSP and SP-R particles exhibit decreasing activity, much like free catalase, and retain approximately 50% of active catalase after 24 hours in solution. Activity increases with time for the HSSP group of particles, which is a surprising outcome. The large pores in these particles may be promoting easy movement of the enzyme into and out of the pores. Catalase may be initially protected but deactivated, and gradually released from the hollow cores with time. Hence, the low protection offered by HSSP-I particles could be a combined effect of loaded catalase accessibility to pronase and catalase leaching out of the particles.

#### **7.5. Conclusions**

All the mesoporous silica particles displayed the potential for effective catalase loading and protection when compared to non-porous silica. As expected, non-porous and radially oriented particles do not protect catalase from degradation. However, high loading and activity in SP-R indicate that mesoporosity aids in enzyme loading, perhaps because their rough porous surface permits better catalase anchoring to the surface. Particles with hollow cores displayed higher loading, activity and protection against pronase when compared to SP-R and NPSP, consistent with the hypothesized role of a hollow core in promoting enzyme loading and activity. HSSP-I2 exhibited the highest loading due to the presence of hollow cores and large mesopores, but



poor protection which can be attributed to the loaded catalase accessibility to pronase, and perhaps catalase leaching out of the particles. Surprisingly, HSSP-P offered the greatest enzyme protection and retained active catalase despite having inaccessible pores. Defects in the HSSP-P structures are hypothesized to be admitting catalase into a protected interior pore space. These results indicate that while promising trends are observed with existing particle synthesis recipes, pore size tuning will be necessary to obtain even greater enzyme protection without compromising loading.

**Table 7.1.** Structural properties of the particles used for enzyme studies.

| Material | BET Surface Area<br>(m <sup>2</sup> /g) | External Surface Area<br>(m <sup>2</sup> /g) | BJH Pore Dia<br>(nm) | Particle Diameter<br>(μm) |
|----------|---|--|----------------------|---------------------------|
| NPSP     | 10.2                                    | 9.1  | -                    | 0.3                       |
| SP-R     | 801.4                                   | 9.9  | 2.9                  | 0.15-85                   |
| HSSP-P   | 673.4                                   | 118.4  | 3.1                  | 0.58-0.65                 |
| HSSP-I1  | 761.4                                   | 107.1  | 3.8, 5.4             | 0.58-0.86                 |
| HSSP-I2  | 617.3                                   | 108.4  | 4.2, 7.5             | 0.58-0.86                 |

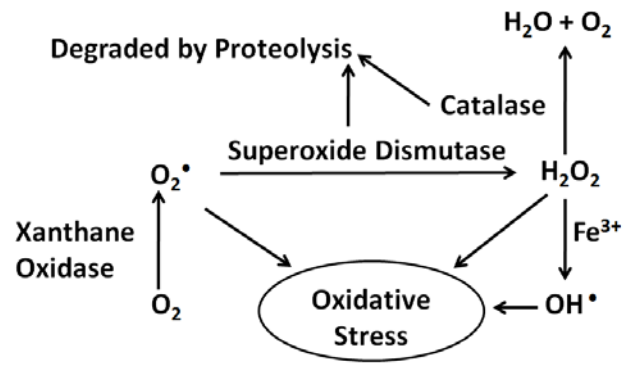


**Figure 7.1.** Mechanism of generation and elimination of free radicals through the action of anti-oxidant enzymes.

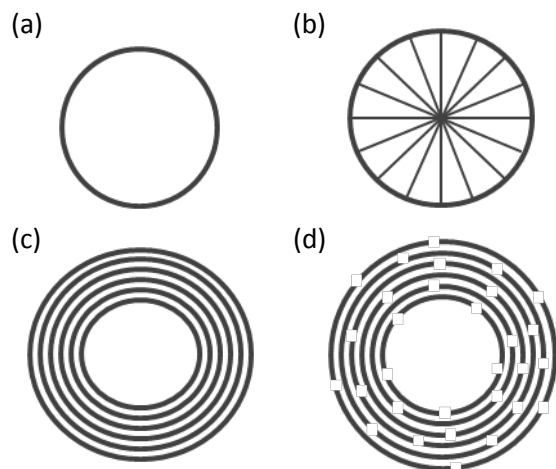


**Figure 7.2.** Idealized representations of mesoporous silica types: (a) nonporous silica (NPSP) (b) silica particles with radially oriented pores (SP-R) (c) hollow spherical silica particles with pores oriented parallel to the hollow core (HSSP-P) (d) hollow spherical silica particles with expanded, interconnected bimodal pores (HSSP-I).

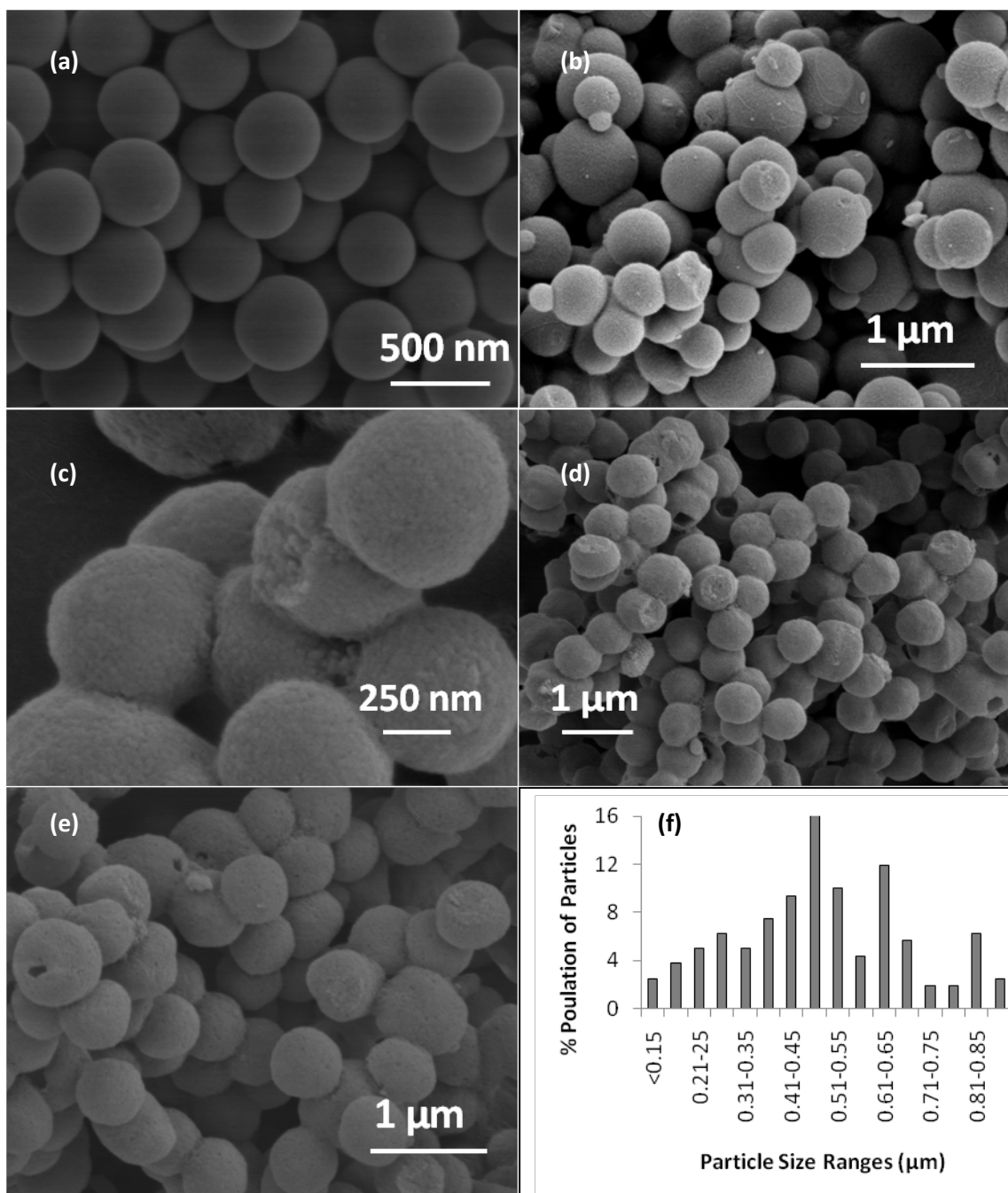


**Figure 7.3.** SEM micrographs of (a) NPSP (b) SP-R (c) HSSP-P (d) HSSP-I1 and (e) HSSP-I2 particles, and (f) particle size distribution of SP-R derived from SEM.

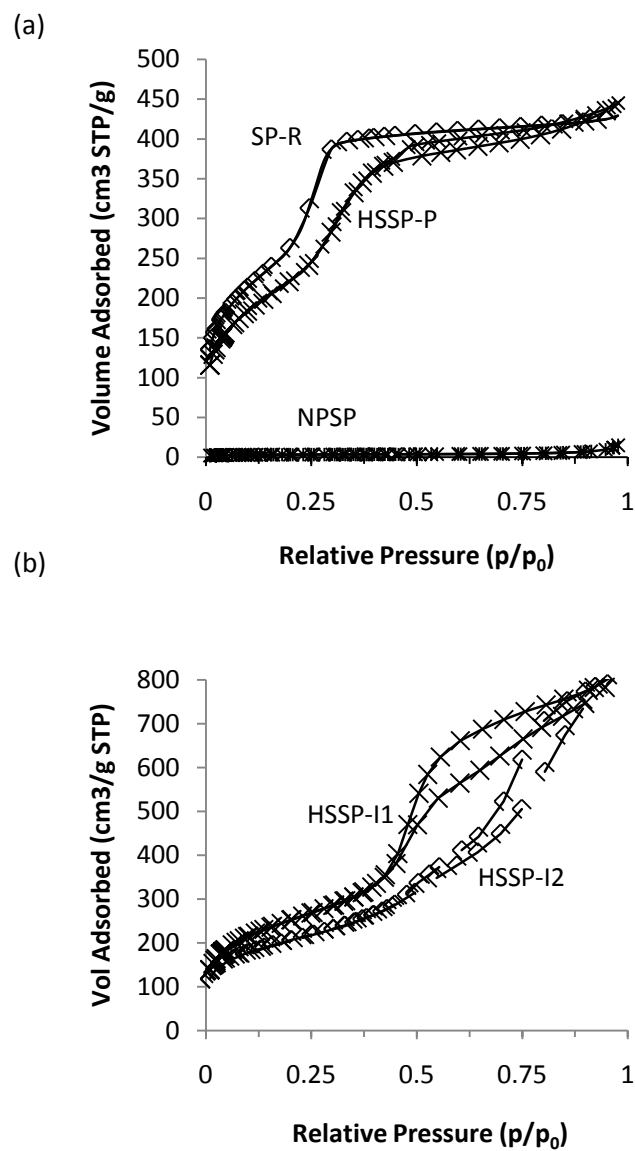


**Figure 7.4.** Nitrogen adsorption-desorption isotherms of (a) NPSP, SP-R, and HSSP-P; and (b) HSSP-I1 and HSSP-I2.

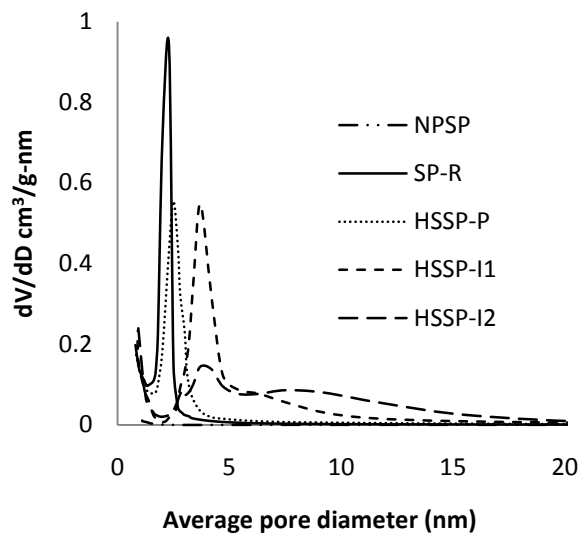


**Figure 7.5.** BJH adsorption pore size distributions calculated using the adsorption branch of the nitrogen adsorption isotherm of the silica particles.

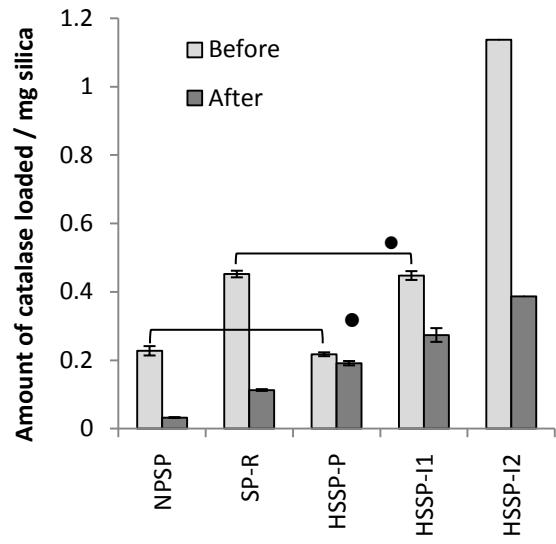


**Figure 7.6.** Amount of catalase loaded per mg silica nano particles obtained from I<sup>125</sup> labeled catalase studies before and after 1 h of proteolysis. One way ANOVA showed that all the silica types before proteolysis are significantly different from each other with  $p < 0.05$ . All pairs except those indicated by ● are statistically significant within 95% confidence interval.



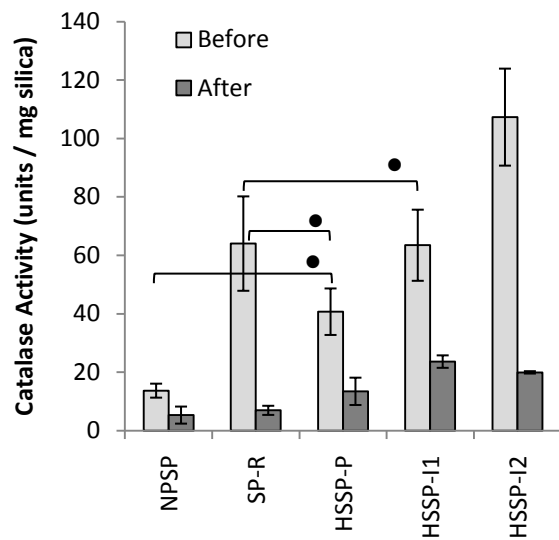


**Figure 7.7.** Activity of catalase loaded per mg silica nano particles obtained from H<sub>2</sub>O<sub>2</sub> degradation studies before and after 1 h of proteolysis. One way ANOVA showed that all the silica types before proteolysis are significantly different from each other with p<0.05. All pairs except those indicated by ● are statistically significant within 95% confidence interval.

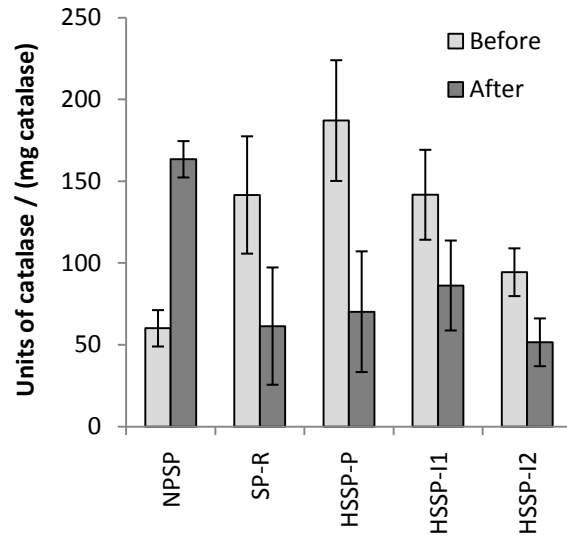


**Figure 7.8.** Activity per mg of catalase before and after 1 h of proteolysis.

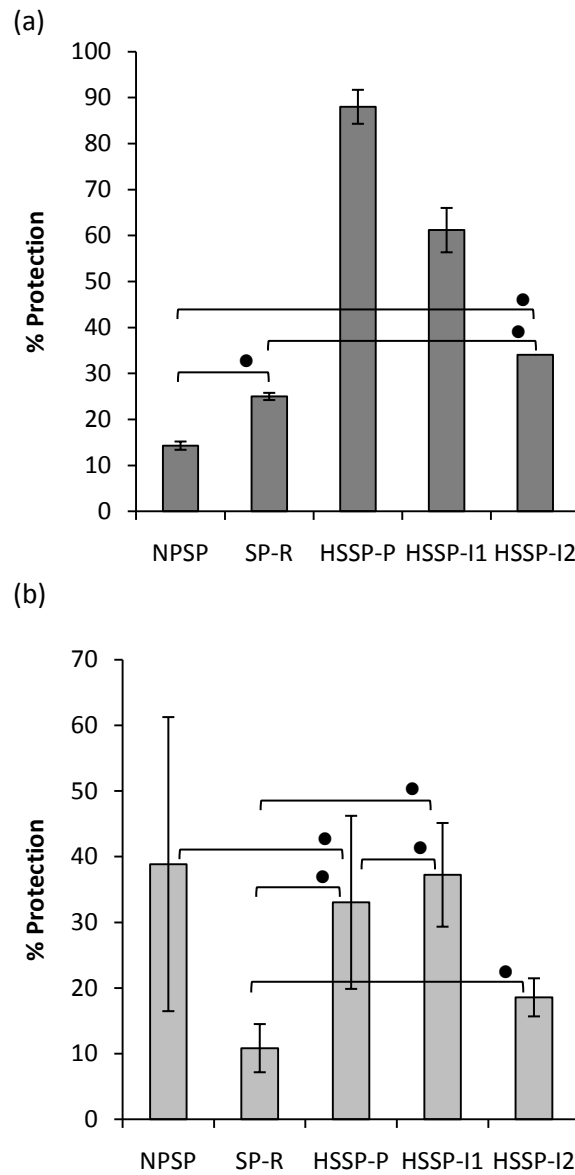


**Figure 7.9.** Percentage protection after 1 h of proteolysis measured by (a) mass loading and (b) H<sub>2</sub>O<sub>2</sub> elimination activity. One way ANOVA showed that all the silica types are significantly different from each other with  $p < 0.05$ . All pairs except those indicated by • are statistically significant within 95% confidence interval.

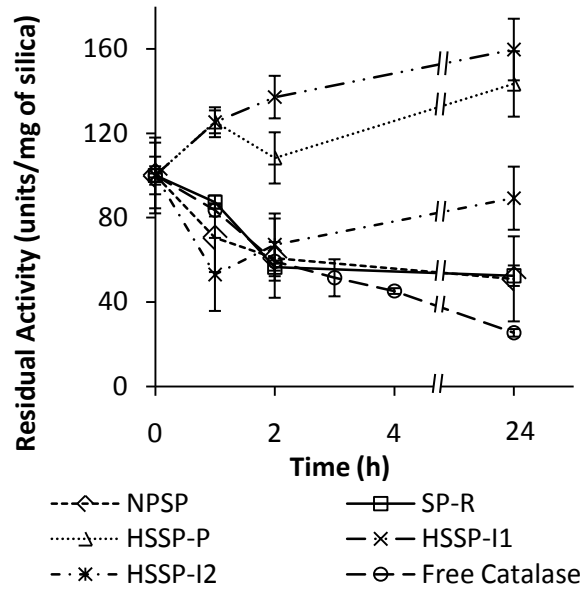


**Figure 7.10.** Activity of catalase with time. One way ANOVA showed that all the silica types are significantly different from each other with  $p < 0.05$ . HSSP-I2, HSSP-P; Free Catalase, NPSP and HSSP-I2, HSSP-P pairs are statistically insignificant within 95% confidence interval at time=24h.

## 8. DFT Investigation of NH<sub>3</sub> Physisorption on CuSO<sub>4</sub> Impregnated SiO<sub>2</sub>

### 8.1. Summary

In this quantum chemical investigation, NH<sub>3</sub> physisorption onto a model of copper sulfate impregnated silica is compared with pure silica and copper sulfate adsorbents. The physisorption process is modeled as direct binding of the NH<sub>3</sub> molecule to the adsorption site of the dry adsorbents and as displacement of a H<sub>2</sub>O molecule by NH<sub>3</sub> in the hydrated complexes. The surface of silica is represented by a hydroxyl group attached to a silsesquioxane cage, H<sub>7</sub>Si<sub>8</sub>O<sub>12</sub>(OH) and silica impregnated with CuSO<sub>4</sub> by the most stable configuration of the cluster containing a CuSO<sub>4</sub> ion pair placed adjacent to the silica cage. H<sub>2</sub>O is systematically added to the dehydrated adsorbents to investigate the role of water in NH<sub>3</sub> adsorption. Modeling hydrated environments of each type of adsorbent is focused on H<sub>2</sub>O molecules that directly coordinate with the active sites. The results indicate that the binding energy of adsorbing NH<sub>3</sub> onto the mixed adsorbent is greater than in pure silica. This enhanced binding in the mixed adsorbent is consistent with improved Brønsted acidity of the silanol in the presence of CuSO<sub>4</sub>.

### 8.2. Introduction

Siliceous materials have been used as adsorbents, catalysts and catalyst supports in a wide range of adsorption mediated applications<sup>317</sup> for several decades. Recent introduction of well ordered mesoporosity<sup>37</sup> leading to enhanced surface areas and pore volumes has brought the applications of these materials on par with conventional zeolites.<sup>318</sup> Several reviews have summarized the demonstrated potential of mesoporous silica as suitable adsorbents for separations,<sup>5</sup> hydrogen storage,<sup>319</sup> catalysis,<sup>320</sup> adsorption<sup>321</sup> and biotechnological applications.<sup>251,322</sup> Surface silanols in silica are the only groups that can interact with the adsorbate molecules. Hence, transition metals or other heteroatoms are introduced into the silica framework to enhance the adsorbent-adsorbate interactions,<sup>323-330</sup> thus gaining the advantages of both worlds. One of the methods of incorporating metals into inert silica matrices is by impregnation with metallic salts.<sup>331</sup> Impregnation takes place by complexation in which the surface sites of silica occupy the coordination sites or displace the ligands of the metal complex.<sup>332</sup>

In the present study, adsorption properties of silica mixed with  $\text{CuSO}_4$  are investigated. Sulfated copper-silica catalysts have been proposed as active catalysts for selective catalytic reduction of  $\text{NO}_x$  with ammonia<sup>333-335</sup> and are found to be more active than their unsulfated versions.<sup>331,336,337</sup> Using this experimental basis for potential adsorption properties of  $\text{CuSO}_4$ -impregnated  $\text{SiO}_2$ , we perform a density functional theory (DFT) investigation to explore its atomic level interactions with  $\text{NH}_3$ .  $\text{NH}_3$  adsorption is of significant research interest not only due to its widespread industrial applications but also due to its extensive use as a probe molecule for acid site characterization in prospective catalysts.<sup>338-340</sup> There exist several theoretical investigations employing DFT that report  $\text{NH}_3$  adsorption on different surfaces including  $\text{V}_2\text{O}_5$  based clusters,<sup>341</sup> anatase  $\text{TiO}_2$  (001),<sup>342,343</sup>  $\text{Nb}(100)$ ,<sup>344</sup> Cl-terminated  $\text{Si}(001)$ ,<sup>345</sup> sulfated  $\text{ZrO}_2$ ,<sup>346</sup> Pt supported on  $\text{SiO}_2$ ,<sup>347</sup> hetero-atom doped SBA-15,<sup>340</sup> and pure  $\text{SiO}_2$ .<sup>348-352</sup> The models of the adsorbent surfaces in these structures are either described as clusters of pure metal oxide or periodic slabs of metal oxides or heteroatoms chemically bound to the metal oxide. However, none of these studies deal with metallic salt physically bound to metal oxide matrix like  $\text{CuSO}_4$  impregnated  $\text{SiO}_2$  studied here.

While the unknown structure of  $\text{CuSO}_4$  impregnated  $\text{SiO}_2$  rules out the possibility for periodic slab models, building clusters even with single moieties of each constituent of the mixed adsorbent is complicated. Due to variable coordination of  $\text{Cu}^{2+}$ , there is a possibility of multiple coordination geometries and isostructures. Also, inter-molecular interactions between the ligands influence the structure favored by metal ion coordination. In the present work, the best model to represent the mixed adsorbent is identified by studying the relative stability of  $\text{CuSO}_4$  at various sites of the  $\text{SiO}_2$  cluster. The structure and energetics of  $\text{NH}_3$  physisorption as a mono-dentate species on the mixed adsorbent ( $\text{SiO}_2/\text{CuSO}_4$ ) are probed and compared with  $\text{SiO}_2$  and  $\text{CuSO}_4$ . Since silica is known to be hygroscopic, the adsorbents' selectivity towards  $\text{NH}_3$  is also tested in the presence of water. This is also done because commercially available  $\text{CuSO}_4$  is in hydrated form and would be expected to yield a hydrated mixed adsorbent upon impregnation at low temperatures. Understanding the effect of solvation is also significant in itself because water deactivated silica<sup>15,353</sup> and hydrated  $\text{CuSO}_4$ <sup>354</sup> have extensive application in chromatography to selectively adsorb polar substances. Hence, the effect of hydration and the nature of local interactions that lead to favorable bonding scenarios are addressed based on the geometric structures and  $\text{NH}_3$  adsorption energies. Modeling hydrated environments of each type of adsorbent is focused on  $\text{H}_2\text{O}$  molecules that directly coordinate with the active sites and

the effect of secondary H<sub>2</sub>O is briefly discussed. While this study is entirely theoretical, the results presented here indicate the promising adsorption properties of CuSO<sub>4</sub>-impregnated silica, and thus provide a predictive basis to design and compare such adsorbents. This approach may also help to interpret experimental characterization of the adsorption and catalytic processes of impregnated silica materials.<sup>330,347,355,356</sup>

### 8.3. Modeling Approach

Surface interactions of silica are primarily modeled as interactions with an isolated silanol on the silica surface. Many clusters have been proposed to model the surface silanol group, ranging from the simplest H<sub>3</sub>SiOH<sup>357,358</sup> to larger cage like structures derived from the class of recently synthesized<sup>359</sup> and characterized<sup>360-363</sup> hydridosilsesquioxanes. However, the type of model to be considered for accurate predictions is strongly dependant on the property being investigated.<sup>364</sup> In this study, we adopt a hydroxyl group attached to an octa-hydrosilsesquioxane, H<sub>7</sub>Si<sub>8</sub>O<sub>12</sub>(OH) (**1**) (Figure 8.1), a double four-membered silicate ring structure. This and similar cage like structures<sup>364-366</sup> are the building units observed during zeolite synthesis<sup>367-370</sup> and hydrolytic polycondensation of alkoxysilanes,<sup>24,267</sup> and have been extensively investigated theoretically. They were first proposed as models of silica surface sites by Sauer and Hill<sup>364</sup> and have been used by Ugliengo's group to compute vibrational modes<sup>213,351,364</sup> and NMR shieldings<sup>364,371</sup> of the silanol group that matched closely with experiments. Civalleri et al. used these structures to model and study stability of zeolitic frameworks.<sup>372</sup> The suitability of H<sub>7</sub>Si<sub>8</sub>O<sub>12</sub>(OH) to model the interactions with NH<sub>3</sub> molecule was established by Civalleri et al.<sup>351</sup> and Roggero et al.<sup>352</sup> In the present study, we extend this model to represent CuSO<sub>4</sub> impregnated SiO<sub>2</sub> in which a single moiety of CuSO<sub>4</sub> (**2**) interacts with the silsesquioxane cage. For comparison, pure CuSO<sub>4</sub> is modeled as a single moiety rather than alternating chains of corner-sharing SO<sub>4</sub><sup>2-</sup> tetrahedra and octahedrally coordinated Cu<sup>2+</sup> sites observed in its crystal structure.<sup>360,373</sup> The possibility of variable coordination numbers in the Cu<sup>2+</sup> ion offers several possibilities for its interaction with SiO<sub>2</sub> in the mixed adsorbent. Hence, the cluster that best represents the mixed adsorbent is evaluated based on the total energies of the equilibrium geometries of four different configurations (structures **5**, **10**, **11**, **12** in Figure 8.2) based on the proximity of CuSO<sub>4</sub> with the surface silanol.

The adsorption process is modeled as physisorption of NH<sub>3</sub> on the active site of the adsorbents. Because the hydroxyl group and Cu<sup>2+</sup> are both amenable to binding with adsorbate

molecules, both of these scenarios are considered for all  $\text{SiO}_2/\text{CuSO}_4$  complexes. In order to understand the role of sulfate,  $\text{NH}_3$  adsorption on sulfate physically bound to silica is also modeled. Except for completely dehydrated adsorbents where  $\text{NH}_3$  directly binds to the adsorption site, we hypothesize that  $\text{NH}_3$  adsorption occurs through displacement of physically bound water. In order to prove this hypothesis and understand the role of water, ammonia adsorption mechanisms on these adsorbents are investigated at different degrees of hydration. While  $\text{NH}_3$  is adsorbed on the silanols in hydrated silica, hydration in the mixed adsorbent depends on the extent of hydration of  $\text{Cu}^{2+}$ . In copper sulfate pentahydrate, the most common form of hydrated  $\text{CuSO}_4$ , the crystal structures show four equatorial waters and two axial sulfate ions interacting with  $\text{Cu}^{2+}$  ion<sup>361,362,374</sup> indicating that four water molecules are in the primary coordination environment. However, the coordination number and hence degree of primary hydration are likely to be different in the presence of a large silica ligand. Hence, we systematically add water to the dehydrated mixed adsorbent in order to locate the water molecules that directly coordinate with  $\text{Cu}^{2+}$ . The same procedure is followed to obtain comparable  $\text{CuSO}_4$  hydration models as the coordination of  $\text{Cu}^{2+}$  in unsaturated  $\text{CuSO}_4$  may be different from that observed in the pentahydrate.

#### 8.4. Computational Details

All of the molecular structures were built and visualized in Argus Lab 4.0<sup>127</sup> and all calculations were performed in vacuum using the Gaussian09<sup>375</sup> software package. The hybrid density functional method, UB3LYP (spin-unrestricted version of Becke's three parameter exchange functional<sup>5</sup> with Lee-Yang-Parr correlation terms<sup>376</sup>), was employed with the 6-311G\* basis set for geometry optimization. Doublet multiplicity was used when  $\text{Cu}^{2+}$  was present in the adsorbent system while pure silica clusters were optimized in a singlet state. All structures carried an overall charge of zero. Geometry optimization of hydrated adsorbents was carried out successively after the addition of every water molecule. When specified, constraints were imposed by freezing certain bond angles to confine the location of the water molecules. Constraining the geometry to prevent hydrogen bonding between water molecules from drawing them into a secondary coordination sphere is a common method in modeling hydrated systems.<sup>341</sup> The total ground state energies resulting from geometry optimization were used to calculate energy change upon  $\text{NH}_3$  adsorption. Adsorption energy,  $\Delta E_{\text{ads}}$  was computed as the difference between the sum of ground state energies of products and reactants as



$$\Delta E_{\text{ads}} = \sum E_{\text{products}} - \sum E_{\text{reactants}}$$

The strength and nature of bonding were analyzed using Wiberg bond indices<sup>377-379</sup> (WBI) obtained from Gaussian NBO<sup>380</sup> (Natural Bond Orbitals) analysis, version 3.1.

## 8.5. Results

### 8.5.1. SiO<sub>2</sub>/CuSO<sub>4</sub> Model

The optimized structures (**5**, **10**, **11**, **12**) of the SiO<sub>2</sub>/CuSO<sub>4</sub> complexes considered here are provided in Figure 8.2. All four of the structures have square planar configuration at their Cu<sup>2+</sup> centers. Cu<sup>2+</sup> interacts with different pairs of oxygen atoms in the Si-O linkages of the silsesquioxane cage and with the two oxygen atoms singly bonded to the sulfur atom in the SO<sub>4</sub><sup>2-</sup> anion. In structure **5**, Cu<sup>2+</sup> interacts with oxygen in the hydroxyl group and an oxygen atom attached to the silanol in addition to the oxygens in the sulfate ion. Cu<sup>2+</sup> interacts with two siloxane oxygen atoms closest to the hydroxyl group in structure **10** and with the next closest pair of siloxane oxygens of the 4-silicon ring in structure **11**. In structure **12**, CuSO<sub>4</sub> is placed away from the hydroxyl group. Total energies obtained from optimal geometries of these structures are provided in Table 8.1. Structure **5** is considered to be the most stable as it has the lowest ground state energy among the four variations and is chosen as the model representing SiO<sub>2</sub>/CuSO<sub>4</sub> for further computations in this study.

### 8.5.2. Hydration Models

Here, we systematically add water molecules to the dehydrated adsorbent models until the added H<sub>2</sub>O falls in the secondary coordination environment. Although there may be a variety of isomeric structures for hydrated CuSO<sub>4</sub> and SiO<sub>2</sub>/CuSO<sub>4</sub>, we adopt one of several optimized structures for every degree of hydration. Preliminary studies showed that the difference in energy among isomers due to changing water position were minor. Hydration models considered for each type of adsorbent are described below.

#### 8.5.2.1. SiO<sub>2</sub>

Figure 8.3 shows the optimized structures of SiO<sub>2</sub> up to two degrees of hydration. In the mono-hydrate (**13**), the H<sub>2</sub>O molecule is hydrogen bonded to the hydroxyl group of the silica

cluster. On adding another H<sub>2</sub>O molecule to SiO<sub>2</sub>·H<sub>2</sub>O, the second H<sub>2</sub>O hydrogen bonds to the H<sub>2</sub>O that is directly bound to the silanol and also to the oxygen in the silanol (**14**).

#### 8.5.2.2. CuSO<sub>4</sub>

Structures **17** and **18** of the mono- and di- hydrates of CuSO<sub>4</sub> in Figure 8.4 are obtained by simple geometry optimization without imposing any constraints. The third water molecule added to this system drifted away during geometry optimization to participate in hydrogen bonding either to the other two water molecules or to the oxygen atoms in the sulfate (**22** in Figure 8.5). The optimized structures of CuSO<sub>4</sub>·4NH<sub>3</sub> (**23**) and CuSO<sub>4</sub>·5H<sub>2</sub>O (**24**) without imposing any constraints are also provided in Figure 8.5 as examples to illustrate the influence of hydrogen bonding on the structure of hydrated CuSO<sub>4</sub>. In order to avoid hydrogen bonding effects among the water molecules, the optimized structure of the tri- hydrate (**20** in Figure 8.4) was obtained by freezing the oxygen atoms of the three water molecules at right angles relative to Cu<sup>2+</sup>. Further addition of a water molecule (CuSO<sub>4</sub>·4H<sub>2</sub>O) and imposition of symmetry constraints did not lead to convergence during geometry optimization even after 600 iterations (indicating that no favorable configuration exists for the imposed constraints) and such structures are not presented here. For the same reason, H<sub>2</sub>O in the secondary hydration shell of CuSO<sub>4</sub> was not modeled.

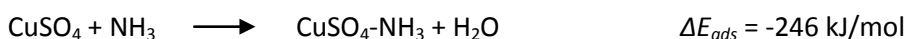
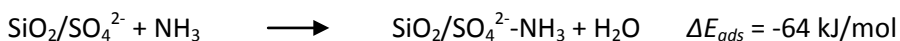
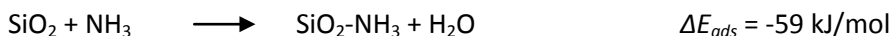
#### 8.5.2.3. SiO<sub>2</sub>/CuSO<sub>4</sub>

In the primary shell, hydration of SiO<sub>2</sub>/CuSO<sub>4</sub> (**5**) is driven by one H<sub>2</sub>O interacting with a silanol plus the number of additional H<sub>2</sub>O molecules directly interacting with Cu<sup>2+</sup>. In these models, the initial placement of H<sub>2</sub>O was dependent on the site considered for adsorption. Two mono-hydrate systems are considered in which H<sub>2</sub>O either interacts with silanol (**25**) or Cu<sup>2+</sup> (**26**) as shown in Figure 8.6. Di-hydrate systems are modeled in three ways (Figure 8.7). In one model, the two H<sub>2</sub>O molecules interact with Cu<sup>2+</sup> (**28**) and in another, one H<sub>2</sub>O interacts with silanol and another with Cu<sup>2+</sup> (**30**). In the third di-hydrate model (**33**), a secondary H<sub>2</sub>O is bound to the silanol. In the tri-hydrate (**35** in Figure 8.8), while two water molecules directly coordinate with Cu<sup>2+</sup> and silanol sites, a third water molecule is located the secondary coordination environment of Cu<sup>2+</sup>.

### 8.5.3. Physisorption on Dry Adsorbents

The optimized structures obtained upon ammonia adsorption on dehydrated SiO<sub>2</sub> (**1**) and CuSO<sub>4</sub> (**2**) are structures **3** and **4** (Figure 8.1) respectively. Interaction of NH<sub>3</sub> with the silanol or with Cu<sup>2+</sup> in the mixed adsorbent, SiO<sub>2</sub>/CuSO<sub>4</sub> (**5**) is also shown in Figure 8.1 as structures **6** and **7**. Adsorption on SiO<sub>2</sub>/SO<sub>4</sub><sup>2-</sup> (**8** and **9** in Figure 8.1) is also considered to investigate if sulfate plays a role in adsorption. For comparison with the second-most stable structure of SiO<sub>2</sub>/CuSO<sub>4</sub> (structure **11**), an NH<sub>3</sub> molecule was placed in the proximity of the silanol, but it did not yield an optimized structure even after 300 iterations.

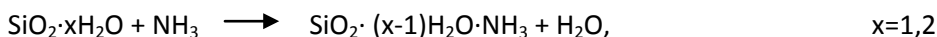
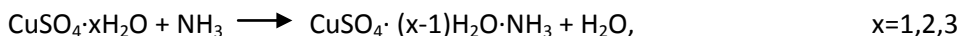
NH<sub>3</sub> interaction with dehydrated adsorbents is modeled as direct binding of NH<sub>3</sub> to the adsorption site (silanol or Cu<sup>2+</sup>) as described by the reactions below, which also indicate the energies of adsorption:

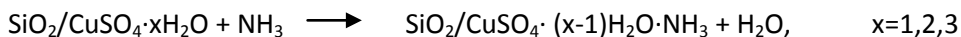


CuSO<sub>4</sub> has the lowest adsorption energy (-246 kJ/mol) indicating highest affinity towards ammonia in a dry state. Physically adsorbing SO<sub>4</sub><sup>2-</sup> to the SiO<sub>2</sub> cluster lowered the adsorption energy by a small amount (5 kJ/mol) from -59 kJ/mol of silica to -64 kJ/mol. On the other hand, NH<sub>3</sub> adsorption affinity of the mixed SiO<sub>2</sub>/CuSO<sub>4</sub> at both of its adsorption sites (-146 or -141 kJ/mol at the silanol or at Cu<sup>2+</sup>, respectively) is enhanced by a factor of 2.5 when compared to pure silica.

### 8.5.4. Physisorption on Hydrated Adsorbents

For the hydrated systems discussed in the earlier section, adsorption is modeled as displacement of H<sub>2</sub>O with an NH<sub>3</sub> molecule. The optimized structures of the adsorbents with different degrees of hydration and the resulting complexes after NH<sub>3</sub> adsorption are provided in Figures 8.3, 8.4 and 8.6-8.8. The associated reactions are provided below and the corresponding adsorption energies are compared with those of their anhydrous counterparts in Table 8.2.





#### 8.5.4.1. SiO<sub>2</sub>

Upon NH<sub>3</sub> adsorption on the monohydrate of SiO<sub>2</sub> (**13**), the adsorption energy increases by 49.3 kJ/mol from -9.9 kJ/mol when compared to completely dehydrated silica (**1**). In the dihydrate of silica (**14**), the adsorption energy is +2.7 kJ/mol because the displaced water molecule is hydrogen bonded to the silanol as well as a secondary H<sub>2</sub>O. The displacement of the secondary H<sub>2</sub>O with NH<sub>3</sub> yielded an energy change of -0.4 kJ/mol.

#### 8.5.4.2. CuSO<sub>4</sub>

In CuSO<sub>4</sub>, the magnitude of the NH<sub>3</sub> adsorption energy decreases with an increase in the degree of primary hydration from 0 to 3. The increase in energy of adsorption is very steep (+191 kJ/mol) on going from dry CuSO<sub>4</sub> (**2**) to its mono-hydrate (**17**), and the value gradually levels off with only a +17 kJ/mol increase on going from mono- to di-hydrate (**18**) and +2.8 kJ/mol on going from di- to tri-hydrate (**20**).

#### 8.5.4.3. SiO<sub>2</sub>/CuSO<sub>4</sub>

Regardless of whether the interaction is with Cu<sup>2+</sup> or silanol, the magnitude of the adsorption energies in the mixed adsorbent are greater than in pure silica (Table 8.2). The effects of hydration on NH<sub>3</sub> adsorption at the silanol and Cu<sup>2+</sup> sites in the mixed adsorbent are slightly different however.

*Adsorption at the silanol site.* The NH<sub>3</sub> adsorption energy on the monohydrate (**25**) increases by 109.5 kJ/mol to -36.2 kJ/mol when compared to its dehydrated version (**5**). In the presence of a second H<sub>2</sub>O molecule coordinating with Cu<sup>2+</sup> in the di-hydrate (**30**), the adsorption energy decreases to -57.8 kJ/mol. In the tri-hydrate (**35**), the adsorption energy increases slightly, to -47.4 kJ/mol. Displacing a secondary H<sub>2</sub>O bound to the silanol (**33**) yields a positive energy of displacement (+8.4 kJ/mol), which is a little higher than for displacement of a water in the dihydrate of pure SiO<sub>2</sub>. Thus, the overall trend among the hydrates is that there is an optimal degree of hydration (the di-hydrate) which gives the strongest energy of adsorption of ammonia.

*Adsorption on the Cu site.* When NH<sub>3</sub> displaces H<sub>2</sub>O bound to Cu<sup>2+</sup> in the mono-hydrate (**25**), the adsorption energy steeply increases by +84.3 kJ/mol to -56.9 kJ/mol when compared to adsorption on the same site in the completely dehydrated adsorbent (**5**). The adsorption energy

further increases to -20.4 kJ/mol with an increase in the primary coordination of  $\text{Cu}^{2+}$  to two  $\text{H}_2\text{O}$  molecules (**28**). In the presence of  $\text{H}_2\text{O}$  bound to the silanol site in the di-hydrate (**30**), the adsorption energy upon displacing  $\text{H}_2\text{O}$  bound to  $\text{Cu}^{2+}$  (**31**) decreases to -41.3 kJ/mol. In the presence of a secondary water bound to  $\text{Cu}^{2+}$  in the tri-hydrate (**35**), the adsorption energy to displace a primary  $\text{H}_2\text{O}$  bound to  $\text{Cu}^{2+}$  (**37**) is -14.2 kJ/mol and displacing the secondary  $\text{H}_2\text{O}$  (**38**) yielded -3 kJ/mol. In this case, the monohydrate shows the most favorable adsorption energy out of all hydrated complexes.

### 8.5.5. Physisorption Mechanism and Stability Analysis

The net charge on  $\text{NH}_3$  and the bond indices at the adsorbent-adsorbate interface provide insights into the strength and type of bonding and in turn the stability of the physisorbed complex. The net charge on  $\text{NH}_3$  on each adsorbed complex is indicated by the small numbers next to ammonia in each of the figures. The net charge on  $\text{NH}_3$  is less than 0.1 when adsorbed on a silanol in pure silica clusters, around 0.1 when adsorbed on a  $\text{Cu}^{2+}$  site on all  $\text{CuSO}_4$  and  $\text{SiO}_2/\text{CuSO}_4$  clusters and it is between 0.7 and 0.9 when adsorbed on silanol sites in  $\text{SiO}_2/\text{CuSO}_4$  clusters.

Wiberg bond indices between oxygen and hydrogen of the silanol and between the silanol hydrogen and nitrogen of  $\text{NH}_3$  adsorbed at the silanol site in the mixed adsorbent and pure silica are compared in Table 8.3. There is a decrease in the strength of the O-H bond from 0.75 to 0.63 upon  $\text{NH}_3$  adsorption to the silanol of  $\text{SiO}_2$ . The O-H bond index is further reduced to 0.59 when  $\text{NH}_3$  and water are both adsorbed to the silanol ( $\text{SiO}_2\cdot\text{H}_2\text{O}\cdot\text{NH}_3$ , **15**). The strength of hydrogen bonding between the hydroxyl group and the  $\text{NH}_3$  molecule are very weak when compared to the OH bond in both  $\text{SiO}_2\cdot\text{NH}_3$  (WBI = 0.1) and  $\text{SiO}_2\cdot\text{H}_2\text{O}\cdot\text{NH}_3$  (WBI = 0.14). In the  $\text{SiO}_2/\text{CuSO}_4$  system, the strength of the H-N bond is much greater than that of O-H, indicating that the silanol site now acts more as a Brønsted acid site than a Lewis acid site. The WBI values are not as sensitive to hydration in this case, and stay near WBI = 0.09 (for O-H) and near WBI = 0.7 (for N-H).

## 8.6. Discussion

### 8.6.1. Role of $\text{CuSO}_4$ Impregnation

Adsorption energies of all adsorbents are compared in Table 8.2 to summarize the potential for synergistic effects on ammonia binding affinity in the mixed adsorbent. A lower adsorption

energy indicates greater relative stability of the adsorbed complex, and therefore that the simulated species should be a more favorable site for adsorption. The decreased adsorption energies in the mixed adsorbent when compared to pure silica indicate that physisorption of  $\text{NH}_3$  on silica is enhanced by  $\text{CuSO}_4$  impregnation. This is true regardless of the degree of hydration of the complex. This enhancement gives adsorption energies comparable to  $\text{NH}_3$  adsorption on super-acid  $\text{TiO}_2$  (-104.6 kJ/mol)<sup>342</sup> and sulfated  $\text{ZrO}_2$  (-141.4 kJ/mol)<sup>346</sup> indicating the high potential of  $\text{SiO}_2/\text{CuSO}_4$  for ammonia adsorption and ammonia-based catalysis. In the presence of sulfate anion only, the affinity of  $\text{NH}_3$  binding to silica improved by a mere 5 kJ/mol. This is consistent with the literature reports that sulfated samples are more active than unsulfated ones.<sup>331,336,337</sup> The presence of sulfate stabilizes the interactions of the active sites with water or ammonia by allowing hydrogen bonding to sulfate to stabilize the adsorbed complex. This is clearly evident in the di-hydrate in which two water molecules interact with  $\text{Cu}^{2+}$  (**28**). This structure is stabilized by the formation of  $\text{HSO}_4^-$  as indicated by the decreased WBI of the O-H silanol bond (WBI = 0.06) and increased WBI between that same hydrogen and an oxygen from the sulfate (WBI = 0.66) in **28** (Table 8.3). All cases of ammonia binding at the silanol site of the  $\text{SiO}_2/\text{CuSO}_4$  complex (**6**, **32** and **36**) show indications of hydrogen bonding to the sulfate ion to stabilize the adsorbed species.

### 8.6.2. $\text{CuSO}_4$ Dispersion in $\text{SiO}_2$ Matrix

The total energies of different configurations of  $\text{SiO}_2/\text{CuSO}_4$  provided in Table 8.1 suggest which are the most favorable sites of  $\text{CuSO}_4$  binding with silica matrix. Structure **5** has the lowest ground state energy and the next lowest energy was found for structure **11**. In both of these cases, direct involvement of the hydroxyl group offers flexibility to stabilize the interactions with  $\text{CuSO}_4$  and allows a lower energy configuration when compared to binding arrangements involving two rigid siloxane oxygens as in structures **10** and **12** (Figure 8.2). The proximity of  $\text{CuSO}_4$  with the hydroxyl group in the more energetically favorable configurations suggests that  $\text{CuSO}_4$  binds strongly to the silica surface or that  $\text{CuSO}_4$  dispersion on the surface of silica promotes better interaction of  $\text{CuSO}_4$  with  $\text{SiO}_2$ . However, not all configurations involving interactions between hydroxyl groups and  $\text{CuSO}_4$  facilitate  $\text{NH}_3$  adsorption. Although relatively stable, structure **11** (the second most stable configuration) did not yield an optimized structure when  $\text{NH}_3$  was modeled as being bound to the hydroxyl group due to its sterically rigid configuration. This indicates that the performance of the mixed adsorbent is strongly influenced

by  $\text{CuSO}_4$  dispersion on the silica matrix and is a very crucial design factor to be considered to take advantage of its enhanced adsorption affinity. The best dispersion occurs when  $\text{Cu}^{2+}$  is able to interact directly with the SiOH oxygen, and this configuration enhances the acidity and adsorption affinity of the silanol.

### 8.6.3. Modeling Hydration

Using our modeling approach, we observed that the structures of systems containing multiple  $\text{H}_2\text{O}$  molecules are strongly influenced by inter-molecular hydrogen bonding. This phenomenon has been observed in other hydrated cluster models before. For example, Gao et al.<sup>381</sup>, Adrian-Scotto et al.<sup>382</sup> and Buzko et al.<sup>383</sup> have modeled sulfate anion,  $\text{Mg}^{2+}$  and  $\text{La}^{3+}$  sulfates with different degrees of hydration using DFT calculations. However, in this case, the symmetry of the structure and charge distribution on the ion caused a symmetric distribution of the water molecules around the cation leading to straightforward analysis of solvation. However, this is not the case with hydrated  $\text{CuSO}_4$ . Figure 8.5 clearly indicates that hydrogen bonding among water molecules interferes with the formation of symmetrical hexacoordinated complexes in hydrated  $\text{CuSO}_4$  (**22** and **24**). In  $\text{CuSO}_4 \cdot 5\text{H}_2\text{O}$  (**24**) it only vaguely appears that four of the five water molecules belong to the primary solvation shell. Contrary to the complications involved with water hydration, a perfectly octahedral structure was obtained upon geometry optimization of  $\text{CuSO}_4 \cdot 4\text{NH}_3$  (**23**) (without imposing any geometry constraints). Unlike  $\text{H}_2\text{O}$ ,  $\text{NH}_3$  has only one lone-pair which is oriented towards  $\text{Cu}^{2+}$  in each ligand in the complex and hence hydrogen bonding effects among the complexing ligands are not observed in **23**. In crystalline  $\text{CuSO}_4 \cdot 5\text{H}_2\text{O}$  system, the five water molecules arrange themselves to satisfy the coordination of  $\text{Cu}^{2+}$  while maintaining the inter-water hydrogen bonding interactions as observed from its crystal structure.<sup>361,362,374</sup> However, this arrangement is observed in the solid state crystal structure and may be stabilized by the proximity of other ions and water molecules in the unit cell which are beyond the scope of the current calculations. To more fully understand the configurations available in a single hydrated  $\text{CuSO}_4$  cluster should involve statistical thermodynamic sampling, for instance using Molecular Dynamics (MD). On an analogous system, MD simulations were used by Rahman et al. to sample stable geometric structures of  $\text{CuCl}_2/\text{water}$  clusters.<sup>363</sup> To rule out the effects of hydrogen bonding among water, the hydrated  $\text{CuSO}_4$  and  $\text{SiO}_2/\text{CuSO}_4$  models considered here are the optimal geometries selected such that they showed little influence of hydrogen bonding between the water molecules.

#### 8.6.4. Cu<sup>2+</sup> Coordination

The optimized structure of completely dehydrated CuSO<sub>4</sub> (**2**) indicates that Cu<sup>2+</sup> coordinates with two oxygen atoms of the sulfate anion. Shubina and Clark have also considered the same structure as used in this study for DFT investigation of Cu<sup>2+</sup> catalyzed rearrangement of quadricyclane to norbornadiene on the anhydrous CuSO<sub>4</sub> surface.<sup>384</sup> For mono- (**17**), di- (**18**) and tri- (**20**) hydrates of CuSO<sub>4</sub> also, the interaction of Cu<sup>2+</sup> with the sulfate oxygens is maintained. Chaban et al.<sup>385</sup> also observed a similar interaction in DFT optimized models of MgSO<sub>4</sub> up to three degrees of hydration. In all of these structures, the oxygens in the sulfate and the two of the H<sub>2</sub>O molecules occupy the corners of the square plane centered at Cu<sup>2+</sup>. Cu<sup>2+</sup> has a square planar arrangement in the di-hydrate (**18**) while the tri-hydrate (**20**) has a square pyramidal geometry with an axial water molecule. Although these structures do not reflect the observed crystal structures of anhydrous<sup>360,373</sup> and pentahydrate<sup>361,362,374</sup> CuSO<sub>4</sub>, these models are best suited for a fair comparison with the mixed adsorbent. In all of the mixed adsorbent structures, Cu<sup>2+</sup> favors a square planar arrangement with the ligands (although slightly distorted in some cases) as opposed to the expected John Teller<sup>386</sup> distorted octahedral geometry suggested by its d9 electronic configuration. In the dehydrated (**5**), mono-hydrated (**25** and **26**) and di-hydrated (**33**) SiO<sub>2</sub>/CuSO<sub>4</sub>, Cu<sup>2+</sup> interacts with a silanol oxygen, a neighboring siloxane oxygen, and two sulfate oxygens. In **26**, where water interacts with Cu<sup>2+</sup>, the structure is square pyramidal with water occupying the axial position. In di- (**28**, **30**) and tri- (**35**) hydrates however, Cu<sup>2+</sup> interacts with only one silanol oxygen and directly coordinates with the H<sub>2</sub>O molecule. In the presence of two coordinating H<sub>2</sub>O molecules (**28**), Cu<sup>2+</sup> coordinates with only one oxygen of the sulfate and the silanol oxygen. This is due to three reasons. First, H<sub>2</sub>O offers structural flexibility when compared to the bulky sulfate and silica ligands. Second, Cu<sup>2+</sup> interacts solely with H<sub>2</sub>O molecules when compared to the multi-dentate sulfate and siloxane oxygens. Third, in the presence of water/ ammonia interacting with Cu<sup>2+</sup>, the structures are stabilized by hydrogen bonding between water/ ammonia and the siloxane oxygen.

Addition of water to the system is stabilized by the rotation of the sulfate ion. NH<sub>3</sub> adsorption did not alter the square planar coordination of Cu<sup>2+</sup> that existed before adsorption in all models except in **27** formed from mono-hydrated SiO<sub>2</sub>/CuSO<sub>4</sub> (**26**). In **27**, Cu<sup>2+</sup> loses its interaction with siloxane oxygen and coordinates with NH<sub>3</sub> upon water displacement. When



only sulfate is bound to silica (**8**), the oxygens with negative charges in the anion orient towards the silicon atoms of the silsesquioxane cage.

#### 8.6.5. Effects of Hydration

For all three types of adsorbents, the magnitudes of the energies of adsorption on dehydrated adsorbents are significantly larger than for their hydrated counterparts (Table 8.2). The largest effect of hydration is seen for  $\text{CuSO}_4$ . The decreased binding ability upon hydration indicates that these adsorbents are more effective under dry conditions. This is perhaps not surprising given that in the silanol, lone pairs are available for interaction with incoming species in the dehydrated adsorption, and in the case of  $\text{CuSO}_4$ ,  $\text{Cu}^{2+}$  has not yet reached its most favorable coordination environment. When water is present on the adsorption sites, internal hydrogen bonding of  $\text{H}_2\text{O}$  has to be overcome by adsorbing  $\text{NH}_3$  and this leads to a smaller magnitude of  $\text{NH}_3$  adsorption energy. Relative to the effect of the first water of hydration, the adsorption energies varied only slightly with increasing degree of hydration. However, the performance of the mixed adsorbent is better than the corresponding pure silica complex for all degrees of hydration considered. The results indicate that di-hydrate is the most favorable among all hydrated complexes for adsorption on silanol and the mono-hydrate for adsorption at  $\text{Cu}^{2+}$ . Both of these complexes show enhanced magnitudes of the energy of adsorption compared with the monohydrate of  $\text{CuSO}_4$ . Thus, in situations where the system is likely to be moderately hydrated (under most practical conditions), the impregnated  $\text{CuSO}_4/\text{SiO}_2$  system shows a certain degree of synergy in enhancing the binding of  $\text{NH}_3$  relative to either pure component. This synergy stems from the enhancement of acidity of the silanol due to  $\text{Cu}^{2+}$  binding combined with the ability of  $\text{SO}_4^{2-}$  to stabilize adsorbed ammonia through hydrogen bonding.

In the presence of a secondary water in  $\text{SiO}_2$  (**14**), the adsorption energy is positive for displacing the primary  $\text{H}_2\text{O}$  (**15**) with  $\text{NH}_3$ , indicating that this reaction is unfavorable. However, displacing the secondary  $\text{H}_2\text{O}$  (**16**) by  $\text{NH}_3$  is more favorable as indicated by the negative value of the adsorption energy. This shows that the outermost layer is displaced in the event of multilayer adsorption of water on the silica surface. This result is consistent with the mechanism of water adsorption on silica proposed by Hair and Hertl<sup>387</sup> that two water molecules can be adsorbed on the same hydroxyl group. However, the adsorption energy is very close to zero (-0.4 kJ/mol) indicating that silica surface is deactivated for ammonia adsorption when it is

saturated with H<sub>2</sub>O. This energy to displace a secondary water of hydration increases to +8.4 kJ/mol in the presence of CuSO<sub>4</sub> (**34**). The sulfate anion stabilizes the secondary water through hydrogen bonding in **33**, thus making displacement of this water less favorable. Displacing the primary H<sub>2</sub>O bound to Cu<sup>2+</sup> in the presence of secondary water (**37**) in the mixed adsorbent yields a lower value (-14.2 kJ/mol) than displacing primary H<sub>2</sub>O in pure SiO<sub>2</sub>. When a second water molecule is directly interacting with Cu<sup>2+</sup> (**28**), the energy to displace H<sub>2</sub>O by NH<sub>3</sub> (**29**) is -20 kJ/mol, 21 kJ/mol higher than when only one water directly binds to Cu<sup>2+</sup> (**30**) due to hydrogen bonding of displaced water with the siloxane oxygen.

#### 8.6.6. Adsorption Mechanism

Upon NH<sub>3</sub> adsorption, the lone pairs of nitrogen interact with the hydrogen of the silanol or with Cu<sup>2+</sup>. In hydrated adsorbents, all energies of adsorption are negative except for the formation of **15** and **34**. The negative energies indicate that the reactions are favorable and that NH<sub>3</sub> easily displaces water physically bound to the adsorbents; these adsorbent surfaces are not deactivated in the presence of H<sub>2</sub>O. In **15** and **34**, hydrogen bonding interactions strongly bind water to the complex thus making their displacement unfavorable.

The physisorption of NH<sub>3</sub> on silanol occurs either through hydrogen bonding interactions or through the transfer of a proton leading to the formation of an NH<sub>4</sub><sup>+</sup> species. The net charge on NH<sub>3</sub> is very small when adsorbed on a silanol in pure silica clusters while it is close to +1 when adsorbed on silanol sites in SiO<sub>2</sub>/CuSO<sub>4</sub> clusters. This indicates that the silanol acts as a Lewis acid and accepts electron density from the lone pair of electrons of NH<sub>3</sub> ordinarily, but in SiO<sub>2</sub>/CuSO<sub>4</sub> the silanol acts more like a Brønsted acid leading to the formation of NH<sub>4</sub><sup>+</sup>. Higher H-N WBI than O-H WBI in SiO<sub>2</sub>/CuSO<sub>4</sub> systems (Table 8.3) also lead to the same conclusion. The origin of protonation may also be assisted by the presence of the sulfate anion near the binding site. Thus, the presence of CuSO<sub>4</sub> improves the Brønsted acidity of silanols.

For both SiO<sub>2</sub> and SiO<sub>2</sub>/CuSO<sub>4</sub> adsorbents, the strength of hydrogen bonding between the silanol and ammonia increases upon hydration of the adsorbent as indicated by a decrease in O-H WBI and an increase in N-H WBI. This information is useful in choosing adsorbents for applications, as stronger binding may influence regeneration of the adsorbent. A moderate degree of hydration appears to enhance the adsorption efficacy of the adsorbents, although too much can lead to a secondary hydration shell that stabilized the primary hydration shell and thus makes water displacement more difficult.

### 8.6.7. Comparison with Literature Reports

The main conclusion of this work that the presence of copper improves silanol acidity in silica is consistent with the observations of improved Brønsted acidity in zeolites<sup>388</sup> and amorphous aluminosilicates in the presence of heteroatoms.<sup>376</sup> For example, Crépeau et al. found that acidic OH groups in amorphous aluminosilicate samples containing a silica/alumina mixed phase as well as in materials with separate alumina clusters and pure silica regions correspond to the silanol groups located in close vicinity to an Al<sup>3+</sup> atom.<sup>376</sup> This depicts the importance of CuSO<sub>4</sub> dispersion on silica support.

Among the results discussed in this study, NH<sub>3</sub> adsorption energy on SiO<sub>2</sub> is the only parameter that can be directly compared with experimental measurements. The adsorption energy (-59 kJ/mol) obtained for SiO<sub>2</sub> here is comparable to -51.5 kJ/mol obtained for the same cluster using ONIOM (B3-LYP/DZP: HF/3-21G) method by Rogerro et al.<sup>352</sup> However, these values are overestimated compared to the experimental enthalpy of -37 kJ/mol reported by Hair and Hertl<sup>387</sup> and -40 kJ/mol by Fubini et al.<sup>389</sup> Deviations from experiment may be expected for various reasons. Spin contamination due to open shell calculations may add to the error from zero point energy and thermal energy that are not rectified in the values reported here. Civalleri et al. obtained a value of 29 ± 3 kJ/mol for NH<sub>3</sub> adsorption on silica cluster after applying energy corrections.<sup>351</sup> Therefore, correcting the energies for spin contamination error may improve the match with experiments.

### 8.7. Conclusions

In this study, NH<sub>3</sub> physisorption on copper sulfate impregnated silica (SiO<sub>2</sub>/CuSO<sub>4</sub>) is compared with physisorption to pure SiO<sub>2</sub> and CuSO<sub>4</sub> adsorbents. The mixed adsorbent is modeled as a cluster consisting of CuSO<sub>4</sub> and silica bound through electrostatic interactions. The results indicate that CuSO<sub>4</sub> dispersion on the surface silanol groups of the silica matrix facilitates stronger binding of CuSO<sub>4</sub> with SiO<sub>2</sub> and that the mixed adsorbent has stronger binding to NH<sub>3</sub> than pure silica. Cu<sup>2+</sup> coordinates with oxygens from silanols, siloxanes and sulfate anions in the absence of flexible water or NH<sub>3</sub> molecules bound to it. The complexes are found to be stabilized not only by the direct interaction of the lone pair of electrons from NH<sub>3</sub> with the active site but also due to inter-molecular hydrogen bonding. The mechanism of adsorption on silanol is through hydrogen bonding of the hydrogen of a silanol with the nitrogen of NH<sub>3</sub> in pure silica, and through proton transfer leading to the formation of an NH<sub>4</sub><sup>+</sup> species in the mixed adsorbent.

Thus, the presence of  $\text{CuSO}_4$  stabilizes the adsorbate molecule on the silica surface and also produces Brønsted acid sites on silica.

Hydration severely decreases the binding affinity of the adsorbents resulting in higher adsorption energies with increasing degree of primary hydration. The presence of water in the secondary coordination shell is also found to decrease adsorption affinity. Internal hydrogen bonding stabilizes the water molecules leading to higher energies for displacement by ammonia. This indicates that all adsorbents function best at low degrees of hydration.  $\text{NH}_3$  adsorption affinity of completely dehydrated  $\text{SiO}_2/\text{CuSO}_4$  is enhanced by a factor of 2.5 when compared to pure silica at both its adsorption sites and the adsorption energies of mixed hydrated systems are comparable to that of corresponding  $\text{CuSO}_4$  systems. Adsorption energies of anhydrous mixed adsorbent are comparable to the theoretical values of super acidic titania and zirconia based adsorbents provided in literature indicating the potential of  $\text{CuSO}_4$  impregnation in enhanced adsorption on silica surface. When hydrated environments cannot be avoided, the mixed adsorbents are found in these calculations to give adsorption affinities as good or better than pure copper sulfate and much better than silica alone, and to retain high binding affinities at higher degrees of hydration than either pure adsorbent.

**Table 8.1.** Total energies of optimized SiO<sub>2</sub>/CuSO<sub>4</sub> complexes with variable final position of the Cu<sup>2+</sup> and SO<sub>4</sub><sup>2-</sup> ions. See Figure 8.2 for the corresponding geometries.

| SiO <sub>2</sub> /CuSO <sub>4</sub> Structure | Total Energy (kJ/mol) |
|---|-----------------------|
| <b>5</b>                                      | -213.4                |
| <b>10</b>                                     | -167.9                |
| <b>11</b>                                     | -209.1                |
| <b>12</b>                                     | -165.7                |

**Table 8.2.** NH<sub>3</sub> adsorption energies ( $\Delta E_{\text{ads}}$ , kJ/mol) for different adsorbents at varying degrees of hydration. Except when marked with a superscript, all adsorption energies are for NH<sub>3</sub> directly interacting with the active adsorption site.

| Adsorbent                           | Adsorption Site  | Degree of Hydration |       |                           |  |
|-------------------------------------|------------------|---------------------|-------|---------------------------|--|
|                                     |                  | 0                   | 1     | 2                         | 3                                      |
| SiO <sub>2</sub>                    | OH               | -59.2               | -9.9  | 2.7, -0.4 <sup>a</sup>    | -                                      |
| CuSO <sub>4</sub>                   | Cu <sup>2+</sup> | -246.6              | -54.9 | -37.8                     | -35.0                                  |
| SiO <sub>2</sub> /CuSO <sub>4</sub> | OH               | -145.7              | -36.2 | -57.8, 8.4 <sup>a</sup>   | -47.4                                  |
|                                     | Cu <sup>2+</sup> | -141.2              | -56.9 | -41.3, -20.4 <sup>b</sup> | -14.2 <sup>b</sup> , -3.0 <sup>a</sup> |

<sup>a</sup> NH<sub>3</sub> displaces secondary H<sub>2</sub>O

<sup>b</sup> 2 H<sub>2</sub>O molecules interact with Cu<sup>2+</sup>

**Table 8.3.** Wiberg Bond Indices of O-H and H-N in adsorbents and NH<sub>3</sub> adsorbed complexes. O-H represents the bond between oxygen and hydrogen in the silanol and H-N represents the bond between hydrogen of silanol and the nitrogen of NH<sub>3</sub>.

| Adsorbent  | O-H  | H-N               |
|--|------|-------------------|
| SiO <sub>2</sub> ( <b>1</b> )  | 0.75 |                   |
| SiO <sub>2</sub> ·NH <sub>3</sub> ( <b>3</b> )                                       | 0.63 | 0.1               |
| SiO <sub>2</sub> ·H <sub>2</sub> O·NH <sub>3</sub> ( <b>15</b> )                     | 0.59 | 0.14              |
| SiO <sub>2</sub> /CuSO <sub>4</sub> ·NH <sub>3</sub> ( <b>6</b> )                    | 0.09 | 0.69              |
| SiO <sub>2</sub> /CuSO <sub>4</sub> ·H <sub>2</sub> O·NH <sub>3</sub> ( <b>32</b> )  | 0.08 | 0.71              |
| SiO <sub>2</sub> /CuSO <sub>4</sub> ·2H <sub>2</sub> O·NH <sub>3</sub> ( <b>36</b> ) | 0.09 | 0.69              |
| SiO <sub>2</sub> /CuSO <sub>4</sub> ·2H <sub>2</sub> O ( <b>28</b> )                 | 0.06 | 0.66 <sup>a</sup> |

<sup>a</sup> O-H WBI between oxygen in the sulfate ion and hydrogen in water hydrogen bonded to silanol in structure **28**.

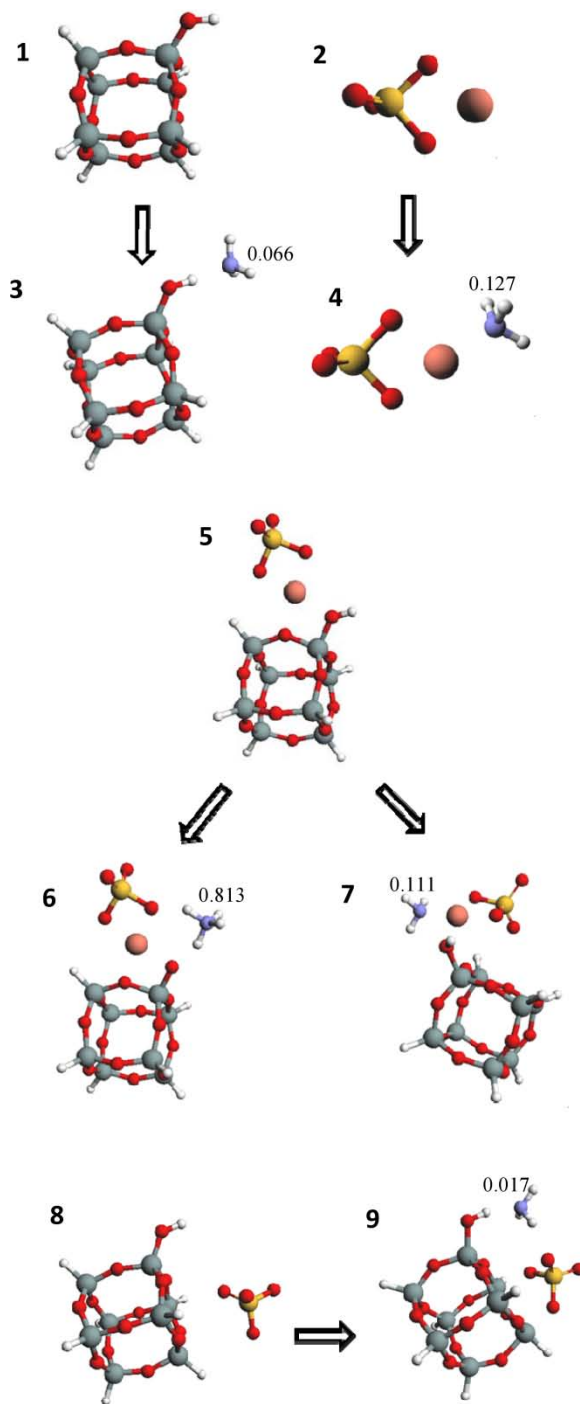


**Figure 8.1.** 3D optimized structures of the dehydrated adsorbents (1) SiO<sub>2</sub>, (2) CuSO<sub>4</sub> (5) SiO<sub>2</sub>/CuSO<sub>4</sub>, (8) SiO<sub>2</sub>/SO<sub>4</sub><sup>2-</sup> and NH<sub>3</sub> adsorbed on (3) SiO<sub>2</sub>, (4) CuSO<sub>4</sub> (6/7) SiO<sub>2</sub>/CuSO<sub>4</sub> and (9) SiO<sub>2</sub>/SO<sub>4</sub><sup>2-</sup>. The numbers indicate charges on the ammonia molecule.



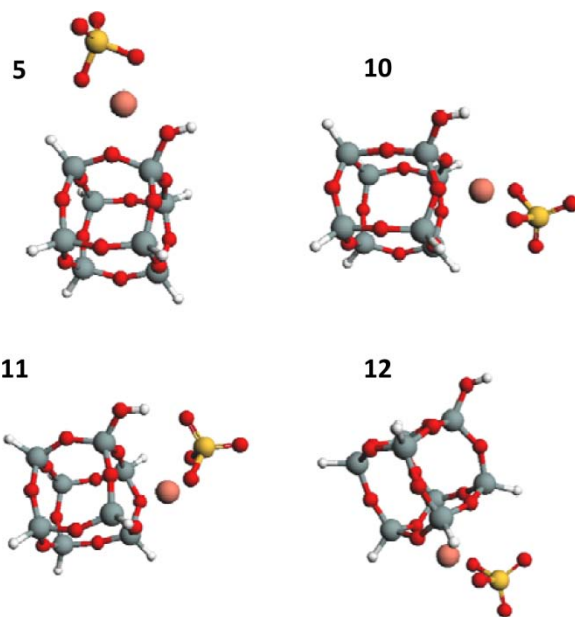


**Figure 8.2.** 3D Optimized geometries of various configurations of SiO<sub>2</sub>/CuSO<sub>4</sub>.

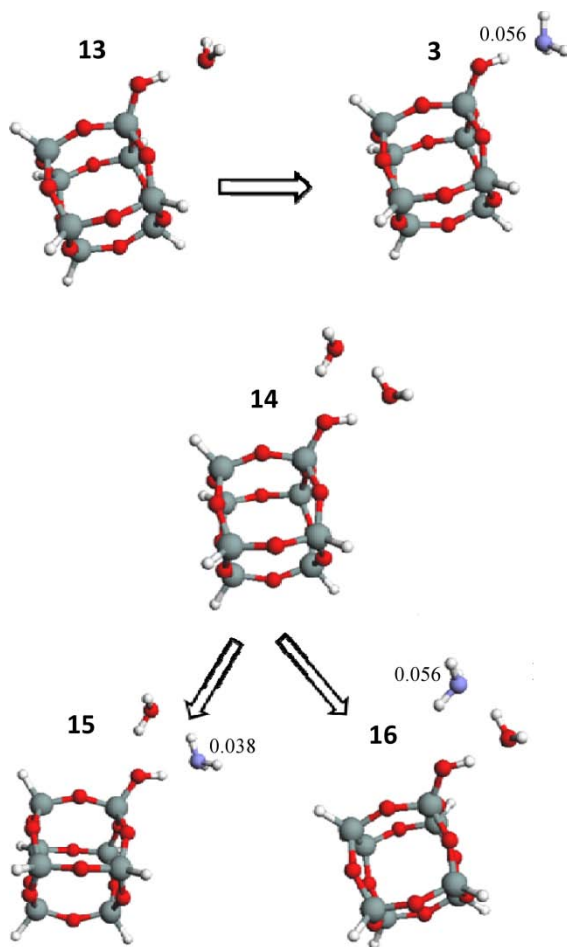


**Figure 8.3.** 3D optimized structures of  $\text{SiO}_2 \cdot x\text{H}_2\text{O}$  ( $x = 1$  or  $2$ ) and the corresponding complexes after  $\text{NH}_3$  adsorption by displacement of one  $\text{H}_2\text{O}$ . The numbers indicate the charge on the adjacent ammonia molecule.

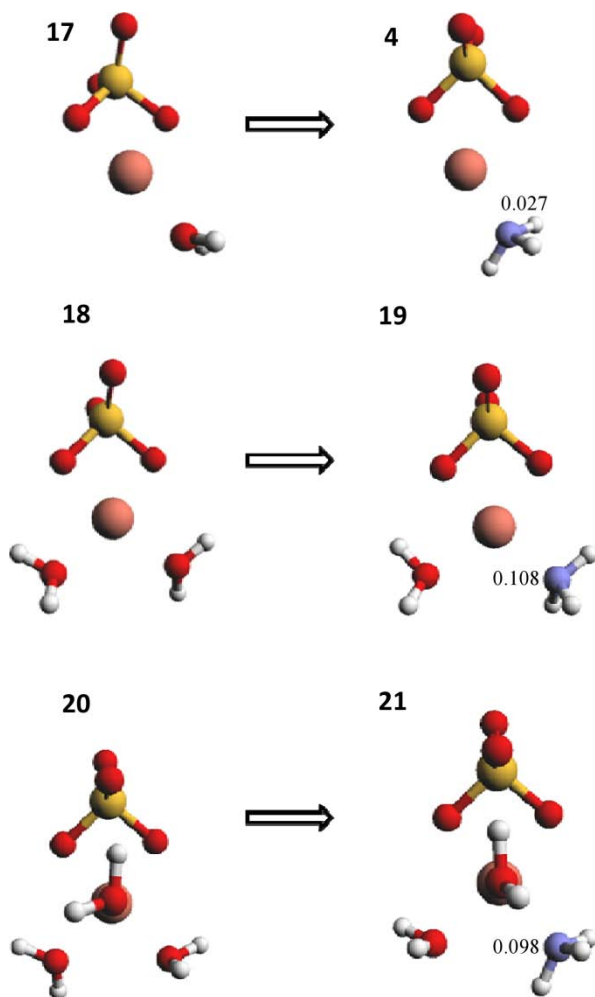


**Figure 8.4.** 3D optimized structures of  $\text{CuSO}_4 \cdot x\text{H}_2\text{O}$  ( $x=1,2,3$ ) and the corresponding complexes after  $\text{NH}_3$  adsorption. Symmetry constraints were imposed to obtain structures **18** and **20**. The numbers indicate the charge on the adjacent ammonia molecule.

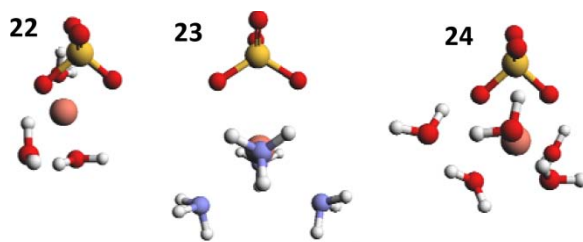


**Figure 8.5.** Structures demonstrating the influence of hydrogen bonding in hydrated  $\text{CuSO}_4$ . (**22**)  $\text{CuSO}_4 \cdot 3\text{H}_2\text{O}$  (**23**)  $\text{CuSO}_4 \cdot 4\text{NH}_3$  and (**24**)  $\text{CuSO}_4 \cdot 5\text{H}_2\text{O}$ .

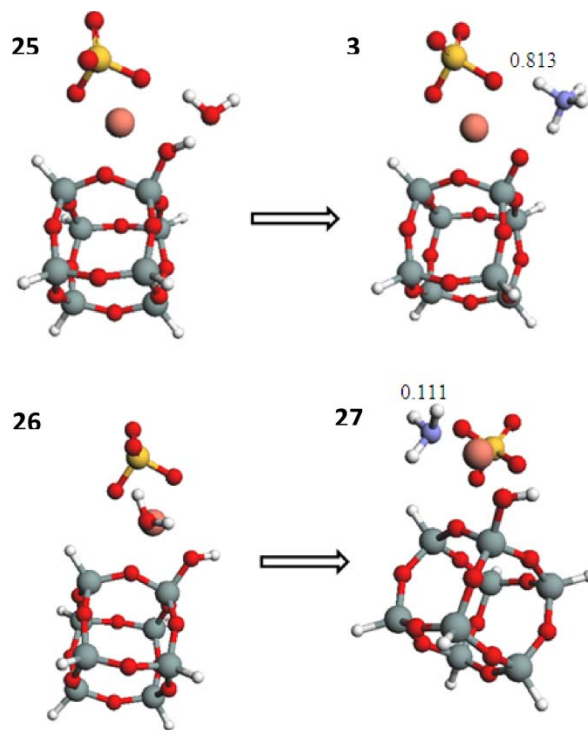


**Figure 8.6.** 3D optimized structures of  $\text{SiO}_2/\text{CuSO}_4 \cdot \text{H}_2\text{O}$  and the corresponding complexes after  $\text{NH}_3$  adsorption. Numbers indicate charges on the adjacent ammonia molecules.

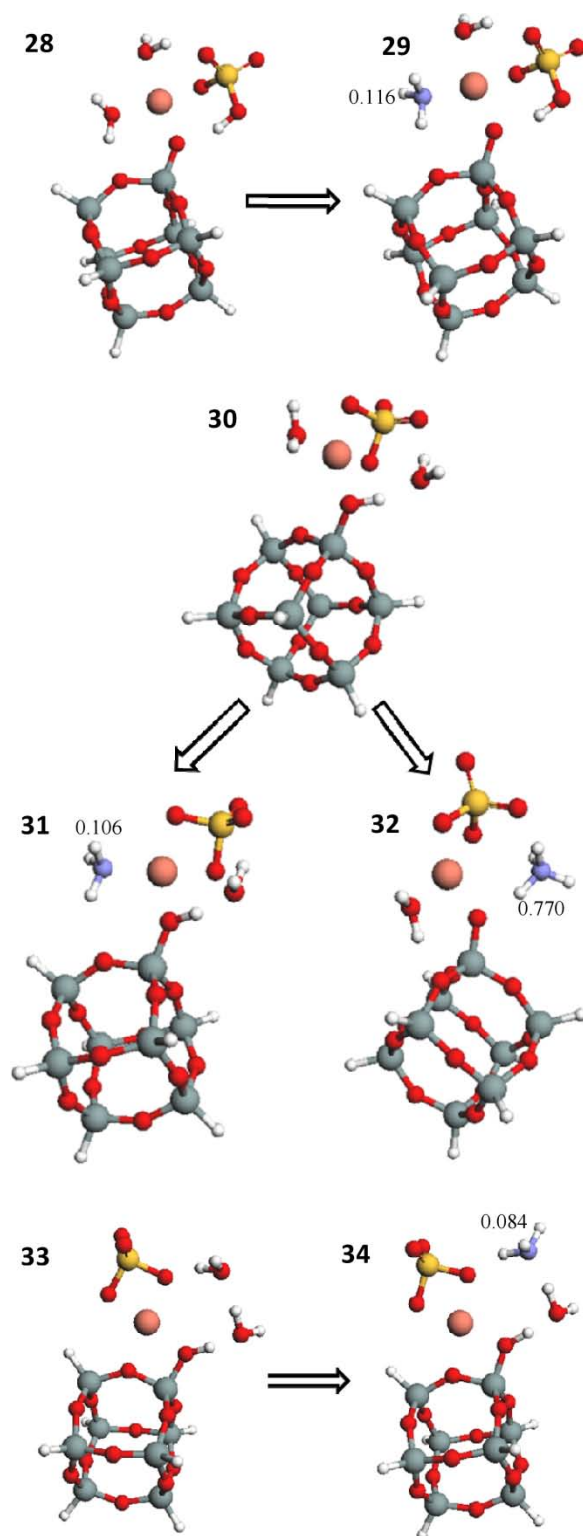


**Figure 8.7.** 3D optimized structures of  $\text{SiO}_2/\text{CuSO}_4 \cdot 2\text{H}_2\text{O}$  and the corresponding complexes after  $\text{NH}_3$  adsorption. Numbers indicate charges on the adjacent ammonia molecules.

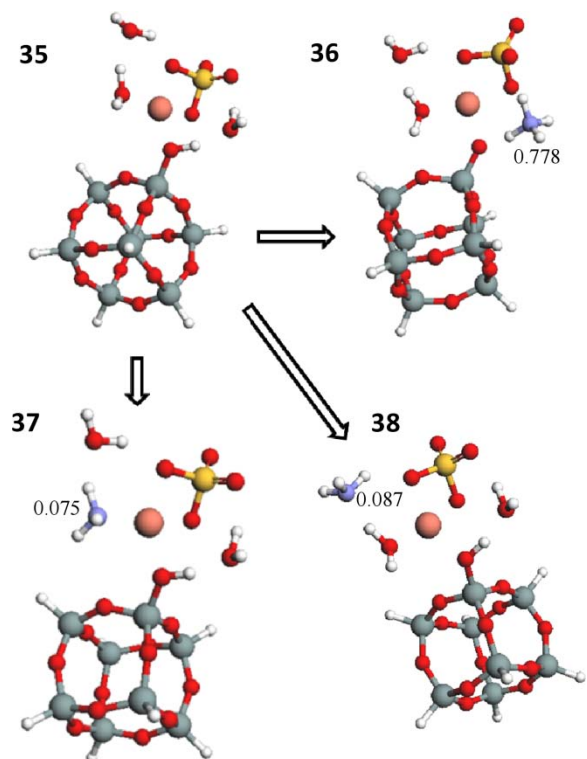


**Figure 8.8.** 3D optimized structures of  $\text{SiO}_2/\text{CuSO}_4 \cdot 3\text{H}_2\text{O}$  and the corresponding complexes after  $\text{NH}_3$  adsorption. Numbers indicate charges on the adjacent ammonia molecules.

#### **IV Closing Notes**



## **9. Dissertation Outcomes, Implications and Future Prospects**

### **9.1. Research Challenges and Outcomes**

#### **9.1.1. Kinetic Investigation**

Knowledge of sol gel polymerization of silica precursors to form organic-inorganic hybrid materials is absolutely important considering the valuable insights kinetic studies can provide to aid their synthesis and processing for a wide range of applications. While the kinetics of non-bridged alkoxysilanes has been extensively investigated, attempts to study bridged silane kinetics remained scarce. This dissertation research has documented some of the complexities involved in characterizing bridged alkoxysilane polymerization reactions which is probably the explanation for the dearth of research existing in this area. The following are the significant conclusions of this research.

##### **9.1.1.1. Phase Separation**

Phase separation affects the formation and distribution of various components in the solution that progressively forms a gel and hence, could have severe implications in synthesis and control of properties of the materials. It was found that ethylene bridged ethoxysilane polymerization produces intermediates that lead to micro-phase separation for certain initial compositions under acidic conditions. This was a surprising result as this has not been a predominant observation under reaction conditions employed for kinetic investigation of non-bridged silanes. The micro-phase separation was evident from the gradual loss of NMR signal in optically transparent solutions. The decrease in total integrated signal intensities increased with increasing reactivity in the solution mixtures depending on water and catalyst concentrations. This clearly indicates that the rate of signal loss is a measure of the concentration of the non-compatible components in the reaction mixture.

##### **9.1.1.2. Characterization and Modeling**

Two tools to understand the kinetic and structural evolution of bridged silica precursors have been explored in this dissertation - NMR and Monte Carlo simulations. The loss of signal narrowed the window of kinetic characterization using  $^{29}\text{Si}$  NMR, the conventional source for deriving silane kinetic information. Samples with no apparent signal loss were probed using DEPT (Distortionless Enhancement through Polarization Transfer)  $^{29}\text{Si}$  NMR to achieve sensitivity enhancement in  $^{29}\text{Si}$  NMR spectra which otherwise suffer from low signal intensities and long

inter-pulse delays that hinder meaningful kinetic characterization. For the first time, application of polarization transfer technique to characterize bridged silane systems is demonstrated for a methylene bridged silane system. From theoretical DEPT intensity expressions, optimal DEPT parameter (transfer time and pulse angle) values were found for signal enhancement. The accurate prediction of theoretical intensities depended on the accuracy of the hetero- and homo-nuclear coupling constants involved. NMR peaks were identified by matching experiments with theory. From the quantification obtained by the analysis of DEPT spectra, the composition of each hydrolyzed and condensed species was determined and a kinetic model describing the kinetics of evolution of monomer and dimers observed in the experimental spectra was developed using these data.

In order to understand the role of the bridging organic group in the overall structural evolution, dynamic Monte Carlo simulations (DMC) were performed on bridged and non-bridged silanes. The bridged silane was modeled as two connected tetra-functional silicon sites. The simulations start with fully hydrolyzed monomers. Substitution effects were included by varying the rates of reaction based on the connectivity of the reacting silicon sites. The model also included four-member ring formation reactions which have been observed to be predominant in experiments. The model distinguishes the short bridges from long based on the formation of carbo-siloxane rings in short bridged silanes.

#### **9.1.1.3. Kinetic Trends**

The results obtained from kinetic characterization and modeling reveal several characteristics of bridged silanes studied.

1. Cyclization is observed to be predominant right from the onset of polymerization in methylene and ethylene-bridged silanes.  $^{29}\text{Si}$  NMR spectra showed the formation of cyclic dimer from bis(triethoxysilyl)methane (BTESM) for low water concentrations. The kinetic model developed for this system is also consistent with early cyclization, with hydrolyzed ends of the linear dimer quickly reacting to form cyclic dimer. Cyclic species were observed in the  $^{29}\text{Si}$  NMR spectra of the BTESE polymerization system as well. The predominance of cyclization in BTESE was also evident from the large power-law coefficient in the empirical expression developed for describing the dependence of gelation time on initial monomer concentration for systems with excess water.

2. The rate of dimerization of BTESM showed that the rates of bi-molecular reactions in bridged silane systems are similar to those observed for non-bridged systems. The rate of cyclization of the linear dimer of BTESM, however, was an order of magnitude higher than in non-bridged systems which is consistent with relatively quick gelation in bridged silane systems.

3. Although bridged and non-bridged silane systems differ in reaction pathways, they follow similar functional group kinetics. The DMC simulations predicted similar local connectivities for bridged and non-bridged versions of silanes at low rates of cyclization. However, deviations in structure of the oligomer distribution increased with increasing cyclization tendency.

3. Another main conclusion from kinetic studies in this dissertation is the rationale behind experimentally observed gelation trends in bridged alkoxy silanes in acidic conditions. We addressed the implications of bridging group length by simulating poly-condensation in the presence and absence of carbo-siloxane rings. The results of the simulation indicate that cyclization delays gelation in general, and particularly in bridged silanes only carbosiloxane rings delay gelation. Silanes with long bridges exhibit low gel times because they do not form carbo-siloxane rings and hence, the bridging organics serve to maintain connectivity among siloxane clusters even when the siloxane ring formation tendency is large.

#### 9.1.1.4. NMR Coupling Constants

Knowledge of the scalar coupling constants and their dependence on structural variations is important to be able to fine-tune NMR experiments that rely on polarization transfer techniques. Hetero-nuclear  $^{29}\text{Si}$ - $^1\text{H}$  spin-spin coupling constants required in DEPT  $^{29}\text{Si}$  NMR experiments were computed using the B3LYP/6-31G density functional theory method. This model chemistry was found to be computationally inexpensive and to accurately predict scalar coupling constants for organoalkoxy silanes and siloxanes. This type of quantum chemical modeling of silanes was necessitated by the inability to measure these values for ethylene bridged silanes directly from their coupled experimental spectra. The observed non-trivial coupling patterns in these silanes were shown to be due to the second order effects generated by the similar magnitudes of  $^2J(\text{Si-H})$ ,  $^3J(\text{Si-H})$  and  $^3J(\text{H-H})$  couplings in the ethylene bridge. The bridging group resonances were calculated from thermal averages of homo- and hetero-nuclear coupling constant estimates obtained from the B3LYP/6-31G method. The calculations were iteratively fit to the experimental coupling patterns to determine estimates of all coupling constants in the system. In addition, coefficients of the Karplus equation consistent with the

dihedral angle dependence of the three-bond homo- and hetero-nuclear couplings in the ethylene bridge and ethoxy groups of ethoxysilanes are also reported. Karplus relationships are interesting tools for understanding electronic structure and chemical bonding in molecules.

### **9.1.2. End-use Investigation**

In addition to kinetic studies, this dissertation includes some insights for application of siliceous materials as biomaterials and adsorbents.

#### **9.1.2.1. Biomaterial Application**

Loading and activity of anti-oxidant enzyme on engineered silica nanoparticles was studied to suggest silica systems for therapeutic applications. All of the mesoporous silica carriers studied exhibited effective loading and those with hollow core offered more protection of enzyme from proteolysis than the others. The results showed that mesoporous surface may be contributing towards enhanced binding of the enzyme with the nanoparticle surface. These results show promising prospects for further research in this area.

#### **9.1.2.2. Adsorption Application**

In this quantum chemical study, copper sulfate, silica and their mixed adsorbent are modeled as clusters with varying degrees of hydration and compared for adsorption of ammonia molecule on their surface. The physisorption process is considered to occur through direct bonding of  $\text{NH}_3$  molecule to the adsorption site in the super dry adsorbents and through displacement of a  $\text{H}_2\text{O}$  molecule by  $\text{NH}_3$  in the hydrated complexes. The results indicate that copper sulfate impregnation on silica matrix stabilizes the adsorbate molecule on silica surface and also enhances the adsorption of ammonia by producing Brønsted acid sites on silica.

### **9.2. Implications**

Theoretical and experimental investigations in this dissertation are all focused on characterization of silanes and their polymers. Characterization is an integral part of material science engineering and knowledge of the techniques and their limitations aids in determining structure, property, performance and processing relationships of these materials. This research provides the tools required to characterize bridged silane systems while focusing on their polymeric evolution. Following are the implications of the results presented in this dissertation.

### **9.2.1. Fundamental Research**

First principles calculations are extensively used to gain fundamental understanding of experimental observations and also to gather information required for kinetic experiments. Efficient and inexpensive model chemistry for predicting spectroscopic properties of organoalkoxsilanes provides a predictive basis for kinetic investigation of silane based molecules and opens the doors for bridged silane system characterization which was not clear before this study.

The non-trivial coupling patterns of bridged silanes and their deconstruction into individual coupling contributions are an important discovery for the silane community. The thermal averaging method to simulate experimental patterns is useful for protein and carbohydrate structure research where this method is extensively used for analysis.

The dissertation also demonstrated the application of an improved analytical technique, DEPT (Distortionless Enhancement through Polarization Transfer)  $^{29}\text{Si}$  NMR for bridged silane characterization. The kinetics and structural evolution models presented in this dissertation could be used in process design and product development involving bridged silanes. This research has revealed phase separation characteristics specific to BTESE polymerization. The ternary pseudo-phase diagram and the power law equation developed for BTESE could serve as a guide to identify initial composition for the synthesis and control of properties of the materials resulting from BTESE polymerization.

### **9.2.2. Applied Research**

The work on anti-oxidant enzyme immobilization on silica nanoparticles is a stepping stone for addressing the controversial nature of silica with respect to its toxicity and its potential as a biomaterial. This study provides insights into the significance of various structural parameters that affect enzyme loading and new possibilities to improve bio-medical technology by suggesting ways to reduce toxicity posed by nanoparticles. The quantum chemical investigation of ammonia adsorption provides meaningful insights that would help in designing enhanced siliceous adsorbents. In addition to this, this work also provides an avenue to model adsorption on hydrated clusters.

### **9.3. Prospective Future Research**

Numerous opportunities for further research emerging from this dissertation are briefly discussed in the following sections.

#### **9.3.1. NMR Characterization**

Application of DEPT  $^{29}\text{Si}$  NMR employed to study BTESM polymerization can be further extended to other bridged silanes. However, theoretical expression consistent with the associated spin system must be derived. Another avenue that remains to be explored in this regard is spectral editing of  $^{29}\text{Si}$  NMR spectra using DEPT. One main reasons for the complexity in interpreting  $^{29}\text{Si}$  NMR spectra of bridged silane polymerization systems is the appearance of numerous peaks, and spectral editing should prove effective in making unambiguous peak assignments

#### **9.3.2. Kinetic Modeling**

The BTESM kinetic model developed in this dissertation is consistent with cyclization being a predominant phenomenon right from the onset of bridged silane polymerization. The model presented here can be further extended to compare bridged and non-bridged silanes for a range of reaction conditions. The substitution effects in bridged silane system polymerization can be further explored from these models.

#### **9.3.3. Structural Modeling**

DMC simulations were able to mimic the quick gelation of short bridged silanes. This encouraging result could be further extended to limit cyclization rate for more realistic predictions. Knowledge of rate constants will be beneficial for this, and these can be found from early time kinetic studies as presented for BTESM polymerization in this dissertation. Incorporation of the evolution of cyclic monomer and bicyclic dimer may provide insights into the polymerization characteristics of BTESE which is difficult to characterize experimentally due to microphase separation. The simulation models presented here can also be customized for other bridged silane systems.

#### **9.3.4. Therapeutic Applications**

Successful and effective loading and activity of anti-oxidant enzyme on mesoporous silica nanoparticles has been observed in the present work. Pore sizes of the materials used can be

further engineered to achieve effective protection. This study can also be extended to a range of enzymes and a broader array of materials for gaining more insights. *In vivo* cell and animal studies will be the next step towards testing the underlying hypothesis of combating oxidative stress through antioxidant enzymes.

#### **9.3.5. Siliceous Adsorbents**

The study in this regard shows the potential of  $\text{CuSO}_4$  impregnation to enhance the adsorption capacity of silica. Knowledge of the effect of hydration and selectivity towards water is very useful when employing the adsorbents for specific applications. This study was limited to modeling the primary coordination of water with the adsorbents and only one among the multiple optimal structures of the clusters is studied here. Molecular dynamics simulations can be employed to model the diffusion of water molecules and to sustain the co-ordination of copper ions. All possible stable geometries of each cluster studied here can be sampled out from molecular dynamics predictions to expand the scope of results predicted by these cluster models.

## 10. References

- (1) Brinker, C. J.; Scherer, G. W. *Sol-gel Science: The Physics and Chemistry of Sol-Gel Processing*; Academic: Boston, 1990.
- (2) Hench, L. L.; West, J. K. *Chem. Rev.* **1990**, *90*, 33.
- (3) Klein L.C., E. *Sol-gel Technology for thin films, fibers, preforms, electronics, and especially shapes*; Noyes: Park Ridge, N.J., 1988.
- (4) Ebelmen, M. *Ann. Chimie Phys.* **1846**, *16*, 129.
- (5) Kumar, P.; Gulians, V. V. *Micropor. Mesopor. Mat.* **2010**, *132*, 1.
- (6) Ju, Y. H.; Webb, O. F.; Dai, S.; Lin, J. S.; Barnes, C. E. *Ind. Eng. Chem. Res.* **2000**, *39*, 550.
- (7) Brown, J.; Mercier, L.; Pinnavaia, T. J. *Chem. Commun.* **1999**, 69.
- (8) Feng, X.; Fryxell, G. E.; Wang, L.-Q.; Kim, A. Y.; Liu, J.; Kemner, K. M. *Science* **1997**, *276*, 923.
- (9) Han, Y. J.; Stucky, G. D.; Butler, A. J. *Am. Chem. Soc.* **1999**, *121*, 9897.
- (10) Manzano, M.; Colilla, M.; Vallet-Regi, M. *Expert Opin. Drug Deliv.* **2009**, *6*, 1383.
- (11) Kim, H. M. *J Ceram. Soc. Jpn.* **2001**, *109*, S49.
- (12) Bottcher, H. J. *J Prakt. Chemie* **2000**, *342*, 427.
- (13) Vallet-Regi, M. *J. Intern. Med.* **2010**, *267*, 22.
- (14) Collinson, M. M. *Crit. Rev. Anal. Chem.* **1999**, *29*, 289.
- (15) McGowin, A. E. In *Chromatographic Science Series*; 3 ed.; Nollet, L. M. L., Ed.; CRC Press: 2006, p 584.
- (16) Brunel, D. *Micropor. Mesopor. Mat.* **1999**, *27*, 329.
- (17) Jones, C. W.; Tsuji, K.; Davis, M. E. *Nature* **1998**, *393*, 52.
- (18) Sanchez, C.; Lebeau, B. *MRS Bull.* **2001**, *26*, 377.
- (19) Sanchez, C.; Lebeau, B. *Curr. Opini. Solid St. M* **1999**, *4*, 11.
- (20) Gomez-Romero, P. *Adv. Mat.* **2001**, *13*, 163.
- (21) Slowing, I.; Trewyn, B. G.; Giri, S.; Lin, V. S. Y. *Adv. Funct. Mater.* **2007**, *17*, 1225.
- (22) Kasemann, R.; Schmidt, H. *New J Chem.* **1994**, *18*, 1117.
- (23) Plueddemann, E. P. *Silane coupling agents*; Plenum Press: Newyork, 1982.
- (24) Li, G.; Wang, L.; Ni, H.; Jr., C. U. P. J. *Inorg. Organomet. P.* **2001**, *11*, 123.
- (25) Shea, K. J.; Loy, D. A. *Chem. Mater.* **2001**, *13*, 3306.
- (26) Sanchez, C.; Ribot, F. *New J Chem.* **1994**, *18*, 1007.
- (27) Sanchez, C.; Ribot, F. *Journal De Physique Iv* **1993**, *3*, 1349.
- (28) Loy, D. A.; Shea, K. J. *Chem. Rev.* **1995**, *95*, 1431.
- (29) Devreux, F.; Boilot, J. P.; Chaput, F. *Phys. Rev. A* **1990**, *41*, 6901.
- (30) Ng, L. V.; Thompson, P.; Sanchez, J.; Macosko, C. W.; McCormick, A. V. *Macromolecules* **1995**, *28*, 6471.
- (31) Zhao, X. S.; Lu, G. Q. M.; Millar, G. J. *Ind. Eng. Chem. Res.* **1996**, *35*, 2075.
- (32) Matos, J. R.; Kruk, M.; Mercuri, L. P.; Jaroniec, M.; Asefa, T.; Coombs, N.; Ozin, G. A.; Kamiyama, T.; Terasaki, O. *Chem. Mater.* **2002**, *14*, 1903.
- (33) Dag, O.; Yoshina-Ishii, C.; Asefa, T.; MacLachlan, M. J.; Grondy, H.; Coombs, N.; Ozin, G. A. *Adv. Funct. Mater.* **2001**, *11*, 213.
- (34) Kuroki, M.; Asefa, T.; Whitnal, W.; Kruk, M.; Yoshina-Ishii, C.; Jaroniec, M.; Ozin, G. A. *J. Am. Chem. Soc.* **2002**, *124*, 13886.
- (35) Burleigh, M. C.; Jayasundera, S.; Thomas, C. W.; Spector, M. S.; Markowitz, M. A.; Gaber, B. P. *Colloid Polym. Sci.* **2004**, *282*, 728.
- (36) Ciesla, U.; Schuth, F. *Micropor. Mesopor. Mat.* **1999**, *27*, 131.



- (37) Kresge, C. T.; Leonowicz, M. E.; Roth, W. J.; Vartuli, J. C.; Beck, J. S. *Nature* **1992**, *359*, 710.
- (38) Beck, J. S.; Vartuli, J. C.; Roth, W. J.; Leonowicz, M. E.; Kresge, C. T.; Schmitt, K. D.; Chu, C. T. W.; Olson, D. H.; Sheppard, E. W. *J. Am. Chem. Soc.* **1992**, *114*, 10834.
- (39) Huo, Q. S.; Margolese, D. I.; Ciesla, U.; Feng, P. Y.; Gier, T. E.; Sieger, P.; Leon, R.; Petroff, P. M.; Schuth, F.; Stucky, G. D. *Nature* **1994**, *368*, 317.
- (40) Huo, Q. S.; Margolese, D. I.; Ciesla, U.; Demuth, D. G.; Feng, P. Y.; Gier, T. E.; Sieger, P.; Firouzi, A.; Chmelka, B. F.; Schuth, F.; Stucky, G. D. *Chem. Mater.* **1994**, *6*, 1176.
- (41) Cheng, G.; Liu, C. *Mat. Chem. Phys.* **2003**, *77*, 359.
- (42) Che, S.; Garcia-Bennett, A. E.; Yokoi, T.; Sakamoto, K.; Kunieda, H.; Terasaki, O.; Tatsumi, T. *Nat. Mater.* **2003**, *2*, 801.
- (43) Yokoi, T.; Yoshitake, H.; Tatsumi, T. *Chem. Mater.* **2003**, *15*, 4536.
- (44) Tanev, P. T.; Pinnavaia, T. J. *Science* **1995**, *267*, 865.
- (45) Bagshaw, S. A.; Prouzet, E.; Pinnavaia, T. J. *Science* **1995**, *269*, 1242.
- (46) Selvam, P.; Bhatia, S. K.; Sonwane, C. G. *Ind. Eng. Chem. Res.* **2001**, *40*, 3237.
- (47) Alam, T. M. *Spectrochim. Acta* **1997**, *53A*, 545.
- (48) Alam, T. M.; Assink, R. A.; Douglas, L. A. *Chem. Mater.* **1996**, *8*, 2366.
- (49) Alam, T. M.; Assink, R. A.; Loy, D. A. *Mat. Res. Soc. Symp. Proc.* **1996**, *435*, 421.
- (50) Alam, T. M.; Assink, R. A.; Prabakar, S.; Loy, D. A. *Magn. Res. Chem.* **1996**, *34*, 603.
- (51) Alam, T. M.; Assink, R. A.; Prabhakar, S.; Douglas, L. A. *Magn. Reson. Chem.* **1996**, *34*, 603.
- (52) Assink, R. A.; Kay, B. D. *J. Non-Cryst. Solids* **1988**, *99*, 359.
- (53) Assink, R. A.; Kay, B. D. *J. Non-Cryst. Solids* **1988**, *107*, 35.
- (54) Assink, R. A.; Kay, B. D. *Annu. Rev. Mater. Sci.* **1991**, *21*, 491.
- (55) Assink, R. A.; Kay, B. D. *Abstr. Pap. Am. Chem. Soc.* **1991**, *202*, 256.
- (56) Assink, R. A.; Kay, B. D. *Colloid Surface A* **1993**, *74*, 1.
- (57) Brinker, C. J.; Keefer, K. D.; Schaefer, D. W.; Assink, R. A.; Kay, B. D.; Ashley, C. S. *J. Non-Cryst. Solids* **1984**, *63*, 45.
- (58) Brunet, F. *J. Non-Cryst. Solids* **1998**, *231*, 58.
- (59) Brunet, F.; Cabane, B.; Dubois, M.; Perly, B. *J. Phys. Chem.* **1991**, *95*, 945.
- (60) Dong, H. J.; Lee, M.; Thomas, R. D.; Zhang, Z. P.; Reidy, R. F.; Mueller, D. W. *J. Sol-Gel Sci. Techn.* **2003**, *28*, 5.
- (61) Dong, H. J.; Zhang, Z. P.; Lee, M. H.; Mueller, D. W.; Reidy, R. F. *J. Sol-Gel Sci. Techn.* **2007**, *41*, 11.
- (62) Doughty, D. H.; Assink, R. A.; Kay, B. D. *Adv Chem Ser* **1990**, 241.
- (63) Jiang, H. M.; Zheng, Z.; Li, Z. M.; Wang, X. L. *Ind. Eng. Chem. Res.* **2006**, *45*, 8617.
- (64) Kay, B. D.; Assink, R. A. *J. Non-Cryst. Solids* **1988**, *104*, 112.
- (65) Malier, L.; Boilot, J. P.; Chaput, F.; Devreux, F. *Phys. Rev. A* **1992**, *46*, 959.
- (66) Osterholtz, F. D.; Pohl, E. R. *J. Adhes. Sci. Technol.* **1992**, *6*, 127.
- (67) Prabakar, S.; Assink, R. A.; Raman, N. K.; Myers, S. A.; Brinker, C. J. *J. Non-Cryst. Solids* **1996**, *202*, 53.
- (68) Rankin, S. E.; Macosko, C. W.; McCormick, A. V. *J Polym. Sci. A* **1997**, *35*, 1293.
- (69) Rankin, S. E.; Macosko, C. W.; McCormick, A. V. *AIChE J.* **1998**, *44*, 1141.
- (70) Rankin, S. E.; McCormick, A. V. *Chem. Eng. Sci.* **2000**, *55*, 1955.
- (71) Rankin, S. E.; McCormick, A. V. *Macromolecules* **2000**, *33*, 7743.
- (72) Rankin, S. E.; Sefcik, J.; McCormick, A. V. *J. Phys. Chem. A* **1999**, *103*, 4233.
- (73) Sanchez, A.; Galan, M. *J Phys. Chem.* **1996**, *100*, 18415.

- (74) Sanchez, J.; McCormick, A. V. *J Phys. Chem.* **1992**, *96*, 8973.
- (75) Sanchez, J.; Rankin, S. E.; McCormick, A. V. *Ind. Eng. Chem. Res.* **1996**, *35*, 117.
- (76) Smith, K. A. *Macromolecules* **1987**, *20*, 2514.
- (77) Pu, Z.; Van Ooij, W. J.; Mark, J. E. *J. Adhes. Sci. Technol.* **1997**, *11*, 29.
- (78) Tan, B.; Rankin, S. E. *J Phys. Chem. B* **2006**, *110*, 22353.
- (79) Spirk, S.; Madl, T.; Pietschnig, R. *Organometallics* **2008**, *27*, 500.
- (80) Pouxviel, J. C.; Boilot, J. P. *J. Non-Cryst. Solids* **1987**, *94*, 374.
- (81) Ro, J. C. C., I. J. *J. Non-Cryst. Solids* **1989**, *110*, 26.
- (82) Brunet, F.; Cabane, B. *J. Non-Cryst. Solids* **1993**, *163*, 211.
- (83) Rankin, S. E.; Macosko, C. W.; McCormick, A. V. *Chem. Mater.* **1998**, *10*, 2037.
- (84) Gillespie, D. T. *J Comput. Phys.* **1976**, *22*, 403.
- (85) Mikes, J.; Dusek, K. *Macromolecules* **1982**, *15*, 93.
- (86) Somvarsky, J.; Dusek, K. *Polym. Bull.* **1994**, *33*, 377.
- (87) Claridge, T. M. *High Resolution NMR Techniques in Organic Chemistry*; Elsevier Inc.: San Diego, CA, 1999; Vol. 19.
- (88) Sugahara, Y.; Okada, S.; Sato, S.; Kuroda, K.; Kato, C. *J. Non-Cryst. Solids* **1994**, *167*, 21.
- (89) Delak, K. M.; Farrar, T. C.; Sahai, N. *J. Non-Cryst. Solids* **2005**, *351*, 2244.
- (90) Stebbins, J. F.; Smyth, J. R.; Panero, W. R.; Frost, D. J. *Am. Mineral.* **2009**, *94*, 905.
- (91) Loy, D. A.; Carpenter, J. P.; Alam, T. M.; Shaltout, R.; Dorhout, P. K.; Greaves, J.; Small, J. H.; Shea, K. J. *J. Am. Chem. Soc.* **1999**, *121*, 5413.
- (92) Baney, R. H.; Itoh, M.; Sakakibara, A.; Suzuki, T. *Chem. Rev.* **1995**, *95*, 1409.
- (93) Loy, D. A.; Shea, K. J. *Chem. Rev.* **1995**, *95*, 1431.
- (94) Wu, J.; Mather, P. T. *Polym. Rev.* **2009**, *49*, 25.
- (95) Zhao, J. Q.; Fu, Y.; Liu, S. M. *Polym. Polym. Compos.* **2008**, *16*, 483.
- (96) Brus, J.; Kotlik, P. *Chem. Listy* **1996**, *90*, 316.
- (97) Malier, L.; Boilot, J. P.; Chaput, F.; Devreux, F. *Phys. Rev. A* **1992**, *46*, 959.
- (98) Osterholtz, F. D.; Pohl, E. R. *J. Adhes. Sci. Technol.* **1992**, *6*, 127.
- (99) Pouxviel, J. C.; Boilot, J. P.; Beloeil, J. C.; Lallemand, J. Y. *J. Non-Cryst. Solids* **1987**, *89*, 345.
- (100) Sanchez, J.; Rankin, S. E.; McCormick, A. V. *Ind. Eng. Chem. Res.* **1996**, *35*, 117.
- (101) Zhang, Z. P.; Gorman, B. P.; Dong, H. J.; Orozco-Teran, R. A.; Mueller, D. W.; Reidy, R. F. *J. Sol-Gel Sci. Technol.* **2003**, *28*, 159.
- (102) Cypriak, M. *Polimery* **2007**, *52*, 730.
- (103) Wrackmeyer, B. In *Annual Reports on Nmr Spectroscopy*; Academic Press Inc: San Diego, 2006; Vol. 57, p 1.
- (104) Doddrell, D. M.; Pegg, D. T.; Bendall, M. R. *J. Magn. Reson.* **1982**, *48*, 323.
- (105) Morris, G. A.; Freeman, R. *J. Am. Chem. Soc.* **1979**, *101*, 760.
- (106) Alam, T. M.; Assink, R. A.; Prabakar, S.; Loy, D. A. *Magn. Reson. Chem.* **1996**, *34*, 603.
- (107) Brunet, F. *J. Non-Cryst. Solids* **1998**, *231*, 58.
- (108) Brunet, F.; Lux, P.; Virlet, J. *New J Chem.* **1994**, *18*, 1059.
- (109) Knight, C. T. G.; Kinrade, S. D. *Anal. Chem.* **1999**, *71*, 265.
- (110) Lux, P.; Brunet, F.; Virlet, J.; Cabane, B. *Magn. Reson. Chem.* **1996**, *34*, 173.
- (111) Helgaker, T. *Chem. Rev.* **1999**, *99*, 293.
- (112) Contreras, R. H.; Barone, V.; Facelli, J. C.; Peralta, J. E. *Ann. Rep. NMR Spectrosc.* **2003**, *51*, 167.

- (113) Contreras, R. H.; Peralta, J. E.; Giribet, C. G.; Azua, M. C. R. D.; Facelli, J. C. *Ann. Rep. NMR Spectrosc.* **2000**, *41*, 55.
- (114) Fukui, H. *Nuclear Magnetic Resonance* **2006**, *35*, 130.
- (115) Helgaker, T.; Watson, M.; Handy, N. C. *J Chem. Phys.* **2000**, *113*, 9402.
- (116) Deng, W.; Cheeseman, J. R.; Frisch, M. J. *J Chem. Theor. Comput.* **2006**, *2*, 1028.
- (117) Helgaker, T.; Jazunski, M.; Ruud, K.; Gorska, A. *Theor. Chem. Acc.* **1998**, *99*, 175.
- (118) Jensen, F. *J Chem. Theor. Comput.* **2006**, *2*, 1360.
- (119) Watson, M. A.; Salek, P.; Macak, P.; Jaszunski, M.; Helgaker, T. *Chem. Eur. J* **2004**, *10*, 4627.
- (120) Corminboeuf, C.; Heine, T.; Weber, J. *Chem. Phys. Lett.* **2002**, *357*, 1.
- (121) Heine, T.; Goursot, A.; Seifert, G.; Weber, J. *J Phys. Chem. A* **2001**, *105*, 620.
- (122) Casserly, T. B.; Gleason, K. K. *J. Phys. Chem. B* **2005**, *109*, 13605.
- (123) Pereira, J. C. G.; Catlow, C. R. A.; Price, G. D. *Chem. Commun.* **1998**, *13*, 1387.
- (124) Sefcik, J.; Goddard, W. A. *Geochim. Cosmochim. Ac* **2001**, *65*, 4435.
- (125) Okumoto, S.; Fajita, N. *J Phys. Chem. A* **1998**, *102*, 3991.
- (126) Casserly, T. B.; Gleason, K. K. *Plasma Processes and Polymers* **2005**, *2*, 669.
- (127) Thompson, M. A. *ArgusLab 4.0.1, Planaria Software LLC, Seattle, WA* **2009**.
- (128) Frisch, M. J.; Trucks, G. W.; Schlegel, H. B.; Scuseria, G. E.; Robb, M. A.; Cheeseman, J. R.; Montgomery, J. A., Jr., T. V.; Kudin, K. N.; Burant, J. C.; Millam, J. M.; Iyengar, S. S.; Tomasi, J.; Barone, V.; Mennucci, B.; Cossi, M.; Scalmani, G.; Rega, N.; Petersson, G. A.; Nakatsuji, H.; Hada, M.; Ehara, M.; Toyota, K.; Fukuda, R.; Hasegawa, J.; Ishida, M.; Nakajima, T.; Honda, Y.; Kitao, O.; Nakai, H.; Klene, M.; Li, X.; Knox, J. E.; Hratchian, H. P.; Cross, J. B.; Bakken, V.; Adamo, C.; Jaramillo, J.; Gomperts, R.; Stratmann, R. E.; Yazyev, O.; Austin, A. J.; Cammi, R.; Pomelli, C.; Ochterski, J. W.; Ayala, P. Y.; Morokuma, K.; Voth, G. A.; Salvador, P.; Dannenberg, J. J.; Zakrzewski, V. G.; Dapprich, S.; Daniels, A. D.; Strain, M. C.; Farkas, O.; Malick, D. K.; Rabuck, A. D.; Raghavachari, K.; Foresman, J. B.; Ortiz, J. V.; Cui, Q.; Baboul, A. G.; Clifford, S.; Cioslowski, J.; Stefanov, B. B.; Liu, G.; Liashenko, A.; Piskorz, P.; Komaromi, I.; Martin, R. L.; Fox, D. J.; Keith, T.; Al-Laham, M. A.; Peng, C. Y.; Nanayakkara, A.; Challacombe, M.; Gill, P. M. W.; Johnson, B.; Chen, W.; Wong, M. W.; Gonzalez, C.; Pople, J. A. *Gaussian, Inc., Wallingford CT* **2004**.
- (129) Becke, A. D. *J Chem. Phys.* **1993**, *98*, 5648.
- (130) Lee, C.; Yang, W.; Parr, R. G. *Phys. Rev. B* **1988**, *37*.
- (131) Franci, M. M.; Pietro, W. J.; Hehre, W. J.; Binkley, J. S.; Gordon, M. S.; DeFrees, D. J.; Pople, J. A. *J. Chem. Phys.* **1982**, *77*, 3654.
- (132) Cypryk, M. *Bull. Pol. Acad. Sci.* **1999**, *47*, 33.
- (133) Xue, X.; Kanzaki, M. *Physi. Chem. Min.* **1998**, *26*, 14.
- (134) Xue, X.; Kanzaki, M. *Solid State Nucl Mag* **2000**, *16*, 245.
- (135) Casanovas, J.; Illas, F.; Pacchioni, G. *Chem. Phys. Lett.* **2000**, *326*, 523.
- (136) Casanovas, J.; Pacchioni, G.; Illas, F. *Mat.Sci. Eng. B* **1999**, *68*, 16.
- (137) Tsantes, G.; Auner, N.; Miiller, T. In *Organo Silicon Chemistry V: from Molecules to Materials*; Auner, N., Miiller, T., Eds.; Wiley-VCH Verlag GmbH & Co. KGaA: Weinheim, Germany, 2003, p 334.
- (138) Huzinaga, S. *J Chem. Phys.* **1965**, *42*, 1293.
- (139) Huzinaga, S. *Approximate atomic functions. Internal report of the Department of Chemistry.*, University of Alberta, 1971.
- (140) Kutzelnigg, W.; Fleischer, U.; Schindler, M. In *NMR Basic Principles and Progress*; 1st ed.; Diehl, P. F., E.; Gnther, H.; Kosfeld, R.; Seelig, J., Ed.; Springer-Verlag: Berlin, Germany, 1991; Vol. 23, p 165.
- (141) Schindler, M.; Kutzelnigg, W. *J Chem. Phys.* **1982**, *76*, 1919.

- (142) Osipova, A. L.; Vyboishchikov, S. F.; Dorogova, K. Y.; Kuzmina, L. G.; Howard, J. A. K.; Lemenovskii, D. A.; Nikonov, G. I. *Chem. Commun.* **2005**, 26, 3349.
- (143) Sykora, J.; Blechta, V.; Sychrovsky, V.; Hetflejš, J.; Sabata, S.; Soukupova, I.; Schraml, J. *Magn. Reson. Chem.* **2006**, 44, 669.
- (144) Vyboishchikov, S. F.; Nikonov, G. I. *Chem. Eur. J* **2006**, 12, 8518.
- (145) Cammi, R.; Mennucci, B.; Tomasi, J. *J. Phys. Chem. A* **2000**, 104, 5631.
- (146) Harris, R. K. In *Nuclear Magnetic Resonance Spectroscopy A Physicochemical View*; Pittman Publishing Inc.: London, 1983, p 213.
- (147) Williams, E. A.; Cargioli, J. D. *Annu. Rep. NMR Spectr.* **1983**, 15, 235.
- (148) Del Bene, J. E.; Elguero, J. *Chem. Phys. Lett.* **2003**, 382, 100.
- (149) Minch, M. J. *Concepts Magn. Reson.* **1994**, 6, 41.
- (150) Sakka, S. *Handbook of sol-gel science and technology: processing, characterization and applications*; Kulwer Academic Publishers: Massachusetts, U.S.A, 2005; Vol. 1.
- (151) Dabrowski, A.; Barczak, M. *Croat. Chem. Acta* **2007**, 80, 367.
- (152) Hunks, W. J.; Ozin, G. A. *J. Mater. Chem.* **2005**, 15, 3716.
- (153) Krishnan, P. S. G.; Joshi, M. In *Polymeric Nanostructures and Their Applications*; Nalwa, H. S., Ed. 2007, p 153.
- (154) Lebeau, B.; Gaslain, F.; Fernandez-Martin, C.; Babonneau, F. In *Ordered Porous Solids* Valtchev, V., Mintova, S., Tsapatsis, M., Eds. 2009, p 283.
- (155) Moreau, J. J. E.; Vellutini, L.; Bied, C.; Man, M. W. C. *J. Sol-Gel Sci. Technol.* **2004**, 31(1/2/3), 151.
- (156) Shea, K. J.; Loy, D. A. *MRS Bull.* **2001**, 26, 368.
- (157) Wada, K.; Mitsudo, T. *Catal. Surv. Asia* **2005**, 9, 229.
- (158) Zhao, X. S.; Chong, A. S. M.; Lu, G. Q. *Series on Chemical Engineering* **2004**, 4 (*Nanoporous Materials*), 393.
- (159) Delak, K. M.; Farrar, T. C.; Sahai, N. *J. Non-Cryst. Solids* **2005**, 351, 2244.
- (160) Morris, G. A.; Freeman, R. *J. Am. Chem. Soc.* **1979**, 101, 760.
- (161) Brunet, F.; Lux, P.; Virlet, J. *New J. Chem.* **1994**, 18, 1059.
- (162) Lux, P.; Brunet, F.; Virlet, J.; Cabane, B. *Magn. Reson. Chem.* **1996**, 34, 100.
- (163) Lux, P.; Brunet, F.; Virlet, J.; Cabane, B. *Magn. Reson. Chem.* **1996**, 34, 173.
- (164) Ambati, J.; Rankin, S. E. *PMSE Prepr* **2006**, 94, 610.
- (165) Berger, S.; Braun, S. *200 and more NMR Experiments-A Practical Course*; WILEY-VCH Verlag GmbH & Co. KGaA: Weinheim, 2004.
- (166) Harris, R. K. *Nuclear magnetic resonance spectroscopy : a physicochemical view*; Pitman Pub. Co., 1983; Vol. 1.
- (167) Williams, E. A. *Annu. Rep. NMR Spectr.* **1983**, 15, 235.
- (168) Ambati, J.; Rankin, S. E. *J Phys. Chem. A* **2010**, 114, 5279.
- (169) Stewart, J. J. P. *MOPAC (2002)*; Fujitsu Limited, Tokyo, Japan.
- (170) Schaefer, T. *Can. J Chem.* **1959**, 37, 882.
- (171) Dewar, M. J. S.; Zebisch, E. G.; Healy, E. F.; Stewart, J. J. P. *J. Am. Chem. Soc.* **1985**, 107, 3902.
- (172) Neese, F. *Orca, revision 2.6.35* Universita't Bonn: Germany, 2008.
- (173) Alkorta, I.; Elguero, J. *Theor Chem Acc* **2004**, 111, 31.
- (174) Palermo, G.; Riccio, R.; Bifulco, G. *J. Org. Chem.* **2010**, 75, 1982.
- (175) Sanfabian, J.; Guilleme, J.; Diez, E.; Lazzarotti, P.; Malagoli, M.; Zanasi, R.; Esteban, A. L.; Mora, F. *Mol. Phys.* **1994**, 82, 913.

- (176) Gibson, S. E. *Organic Synthesis : The Roles of Boron and Silicon*; Oxford University Press: New York, 1991.
- (177) Rakow, J. R.; Tu"llmann, S.; Holthausen, M. C. *J Phys. Chem. A* **2009**, *113*, 12035.
- (178) Stewart, J. J. P. *J. Comput. Chem.* **1989**, *10*, 209.
- (179) Stewart, J. J. P. *Mol. Model.* **2004**, *10*, 6.
- (180) Miyazima, G.; Utsumi, Y.; Takahashi, K. *J. Phys. Chem.* **1969**, *73*, 1370.
- (181) Gomez-Romero, P.; Sanchez, C. In *Functional Hybrid Materials*; Gomez-Romero, P., Sanchez, C., Eds.; Wiley-VCH Verlag GmbH & Co. KGaA: Weinheim, FRG, 2004, p 1.
- (182) Lebeau, B.; Gaslain, F.; Fernandez-Martin, C.; Babonneau, F. In *Ordered Porous Solids*; Valtchev, V., Mintova, S., Tsapatsis, M., Eds. 2009, p 283.
- (183) Li, G.; Wang, L.; Ni, H.; Pittman, C. U. J. *J. Inorg. Organomet. P.* **2001**, *11*, 123.
- (184) Matejka, L.; Dukh, O.; Hlavata, D.; Meissner, B.; Brus, J. *Macromolecules* **2001**, *34*, 6904.
- (185) Pouxviel, J. C.; Boilot, J. P.; Beloeil, J. C.; Lallemand, J. Y. *J. Non-Cryst. Solids* **1987**, *89*, 345.
- (186) Lux, P.; Brunet, F.; Desvaux, H.; Virlet, J. *Magn. Res. Chem.* **1993**, *31*, 623.
- (187) Lee, K.; Look, J. L.; Harris, M. T.; McCormick, A. V. *J. Colloid Interf. Sci.* **1997**, *194*, 78.
- (188) Cho, H.; Felmy, A. R.; Craciun, R.; Keenum, J. P.; Shah, N.; Dixon, D. A. *J. Am. Chem. Soc.* **2006**, *128*, 2324.
- (189) Knight, C. T. G.; Wang, J.; Kinrade, S. D. *Phys. Chem. Chem. Phys.* **2006**, *8*, 3099.
- (190) Stebbins, J. F.; Smyth, J. R.; Panero, W. R.; Frost, D. J. *Am. Mineral.* **2009**, *94*, 905.
- (191) Hoebbel, D.; Reinert, T.; Schmidt, H. *J. Sol-Gel Sci. Technol.* **1996**, *7*, 217.
- (192) Kinrade, S. D.; Swaddle, T. W. *Inorg. Chem.* **1988**, *27*, 4253.
- (193) Gansow, O. A.; Burke, A. R.; Vernon, W. D. *J. Am. Chem. Soc.* **1972**, *94*, 2550.
- (194) Kintzinger, J. P.; Marsmann, H. *Oxygen-17 and Silicon-29 NMR*; Springer Verlag: Berlin, 1981; Vol. 17.
- (195) Levy, G. C.; Cargioli, J. D.; Juliano, P. C.; Mitchell, T. D. *J Magn. Reson.* **1972**, *8*, 399.
- (196) Blinka, T. A.; Helmer, B. J.; West, R. In *Advances in Organometallic Chemistry*; Stone, F. G. A., Robert, W., Eds.; Academic Press: 1984; Vol. 23, p 193.
- (197) Pu, Z.; Van Ooij, W. J.; Mark, J. E. *J. Adhes. Sci. Technol.* **1997**, *11*, 29.
- (198) Dıaz-Benito, B.; Velasco, F.; Martınuez, F. J.; Encinas, N. *Colloid Surface A* **2010**, *369*, 53.
- (199) Shea, K. J.; Loy, D. A. *Acc. Chem. Res.* **2001**, *34*, 707.
- (200) Matinlinna, J. P.; Lassila, L. V.; Dahl, J. E. *Silicon* **2010**, *2*, 87.
- (201) Na, W.; Wei, Q.; Lan, J.-N.; Nie, Z.-R.; Sun, H.; Li, Q.-Y. *Microporous Mesoporous Mater.* **2010**, *134*, 72.
- (202) Shiraiishi, Y.; Ohara, H.; Hirai, T. *New J Chem.* **2010**, *34*, 2841.
- (203) Yang, H.; Han, X.; Li, G.; Ma, Z.; Hao, Y. *J. Phys. Chem. C* **2010**, *114*, 22221.
- (204) Hook, R. J. *J. Non-Cryst. Solids* **1996**, *195*, 1.
- (205) Sugahara, Y.; Okada, S.; Kuroda, K.; C. Kato *J. Non-Cryst. Solids* **1992**, *139*, 25.
- (206) Taylor, R. B.; Parbhoo, B.; Fillmore, D. M. In *Chemical Analysis*; Smith, A. L., Ed.; Wiley: New York, 1991; Vol. 112.
- (207) Ponton, A.; Warlus, S.; Griesmar, P. *J. Colloid Interf. Sci.* **2002**, *249*, 209.
- (208) Loy, D. A.; Carpenter, J. P.; Myers, S. A.; Assink, R. A.; Small, J. H.; Greaves, J.; Shea, K. J. *J. Am. Chem. Soc.* **1996**, *118*, 8501.

- (209) Nielsen, L. B.; McCormick, S. P.; Ng, J. N.; Pierotti, V.; Shizuya, H.; Young, S. G. *Circulation* **1996**, *94*, 3686.
- (210) Myers, S. A.; Assink, R. A.; Loy, D. A.; Shea, K. J. *J. Chem. Soc. Perk. T 2* **2000**, 545.
- (211) Bischoff, J. R.; Kim, D. H.; Williams, A.; Heise, C.; Horn, S.; Muna, M.; Ng, L.; Nye, J. A.; SampsonJohannes, A.; Fattaey, A.; McCormick, F. *Science* **1996**, *274*, 373.
- (212) Tan, B.; Rankin, S. E. *The Journal of Physical Chemistry B* **2006**, *110*, 22353.
- (213) Ambati, J.; Rankin, S. E. *J. Phys. Chem. A* **2010**, *114*, 12613.
- (214) Lee, K. T.; Sathyagal, A. N.; McCormick, A. V. *Colloid Surface A* **1998**, *144*, 115.
- (215) Kirschhock, C. E. A.; Ravishankar, R.; Verspeurt, F.; Grobet, P. J.; Jacobs, P. A.; Martens, J. A. *J. Phys. Chem. B* **1999**, *103*, 4965.
- (216) Aerts, A.; Follens, L. R. A.; Haouas, M.; Caremans, T. P.; Delsuc, M. A.; Loppinet, B.; Vermant, J.; Goderis, B.; Taulelle, F.; Martens, J. A.; Kirschhock, C. E. A. *Chem. Mater.* **2007**, *19*, 3448.
- (217) Yang, S. Y.; Navrotsky, A. *Chem. Mater.* **2002**, *14*, 2803.
- (218) Yang, S. Y.; Navrotsky, A.; Wesolowski, D. J.; Pople, J. A. *Chem. Mater.* **2004**, *16*, 210.
- (219) Fedeyko, J. M.; Rimer, J. D.; Lobo, R. F.; Vlachos, D. G. *J. Phys. Chem. B* **2004**, *108*, 12271.
- (220) Rimer, J. D.; Fedeyko, J. M.; Vlachos, D. G.; Lobo, R. F. *Chem. Eur. J* **2006**, *12*, 2926.
- (221) Follens, L. R. A.; Aerts, A.; Haouas, M.; Caremans, T. P.; Loppinet, B.; Goderis, B.; Vermant, J.; Taulelle, F.; Martens, J. A.; Kirschhock, C. E. A. *Phys. Chem. Chem. Phys.* **2008**, *10*, 5574.
- (222) Petry, D. P.; Haouas, M.; Wong, S. C. C.; Aerts, A.; Kirschhock, C. E. A.; Martens, J. A.; Gaskell, S. J.; Anderson, M. W.; Taulelle, F. *J. Phys. Chem. C* **2009**, *113*, 20827.
- (223) Cui, X. H.; Mao, S. Z.; Liu, M. L.; Yuan, H. Z.; Du, Y. R. *Langmuir* **2008**, *24*, 10771.
- (224) Mintova, S.; Valtchev, V. *Micropor. Mesopor. Mat.* **2002**, *55*, 171.
- (225) Kragten, D. D.; Fedeyko, J. M.; Sawant, K. R.; Rimer, J. D.; Vlachos, D. G.; Lobo, R. F.; Tzapatsis, M. *J. Phys. Chem. B* **2003**, *107*, 10006.
- (226) Cheng, C. H.; Shantz, D. F. *J. Phys. Chem. B* **2006**, *110*, 313.
- (227) Franquet, A.; Biesemans, M.; Willem, R.; Terryn, H.; Vereecken, J. *J. Adhes. Sci. Technol.* **2004**, *18*, 765.
- (228) Kay, B. D.; Assink, R. A. *Mat. Res. Soc. Symp. Proc.* **1986**, *73*, 157.
- (229) Corriu, R. J. P.; Granier, M.; Lanneau, G. F. *J Organomet. Chem.* **1998**, *562*, 79.
- (230) Dubois, G.; Volksen, W.; Magbitang, T.; Sherwood, M. H.; Miller, R. D.; Gage, D. M.; Dauskardt, R. H. *J. Sol-Gel Sci. Technol.* **2008**, *48*, 187.
- (231) Su, B. L.; Roussel, M.; Vause, K.; Yang, X. Y.; Gilles, F. S.; L.; Leonova, E. E., M.; Zou, X. *Micropor. Mesopor. Mat.* **2007**, *105*, 49.
- (232) Whitnall, W.; Asefa, T.; Ozin, G. A. *Adv. Funct. Mater.* **2005**, *15*, 1696.
- (233) Fang, Y.; Ferrie, A. M.; Hong, Y.; Webb, B. L. *U.S. Pat. Appl. Publ.* **2005**.
- (234) Kreiter, R.; Rietkerk, M. D. A.; Castricum, H. L.; van Veen, H. M.; ten Elshof, J. E.; Vente, J. F. *ChemSusChem* **2009**, *2*, 158.
- (235) Nakata, R.; Yamada, N.; Miyajima, H.; Kojima, A.; Kurosawa, T.; Hayashi, E.; Seo, Y.; Shiota, A.; Yamada, K. *U.S. Pat. Appl. Publ.* **2002**.
- (236) Kuge, H.; Hagiwara, Y.; Shimojima, A.; Kuroda, K. *Chem. Asian J* **2008**, *3*, 600.
- (237) Shea, K. J.; Loy, D. A. *Acc. Chem. Res.* **2001**, *34*, 707.
- (238) Kay, B. D.; Assink, R. A. *J. Non-Cryst. Solids* **1988**, *99*, 359.
- (239) Sugahara, Y.; Okada, S.; Kuroda, K.; Kato, C. *J. Non-Cryst. Solids* **1992**, *139*, 25.

- (240) Sugahara, Y.; Okada, S.; Sato, S.; Kuroda, K.; Kato, C. *J. Non-Cryst. Solids* **1994**, *167*, 21.
- (241) Marsmann, H. *NMR, Basic Principles and Progress*; Springer-Verlag: Berlin, 1981, 65p.
- (242) Kelts, L. W.; Armstrong, N. J. *J Mater. Res.* **1989**, *4*, 423.
- (243) Loy, D. A.; Carpenter, J. P.; Alam, T. M.; Shaltout, R.; Peter K. Dorhout, J. *J. Am. Chem. Soc.* **1999**, *121*, 5413.
- (244) Blinka, T. A.; Helmer, B. J.; West, R. In *Advances in Organometallic Chemistry*; Stone, F. G. A., Robert, W., Eds.; Academic Press: 1984; Vol. Volume 23, p 193.
- (245) Marquardt, D. W. *J Soc. Ind. Appl. Math.* **1963**, *11*, 431.
- (246) Salter, C. *J Chem. Edu.* **2000**, *77*, 1239.
- (247) Azizi, S. N.; Rostami, A. A.; Godarzian, A. *J Phys. Soc. Jpn.* **2005**, *74*, 1609.
- (248) Sanchez, J.; Rankin, S. E.; McCormick, A. V. *Ind. Eng. Chem. Res.* **1996**, *35*, 117.
- (249) Ng, L. V.; McCormick, A. V. *J Phys. Chem.* **1996**, *100*, 12517.
- (250) Sanchez, J.; McCormick, A. V. *J. Non-Cryst. Solids* **1994**, *167*, 289.
- (251) Manzano, M.; Colilla, M.; Vallet-Regi, M. *Stud. Surf. Sci. Catal.* **2008**, *174A*, 13.
- (252) Gomez-Romero, P.; Sanchez, C. *Hybrid materials, functional applications. An introduction* 2004.
- (253) Kuchanov, S.; Slot, H.; Stroeks, A. *Prog. in Polym. Sci.* **2004**, *29*, 563.
- (254) Wen, M.; Scriven, L. E.; McCormick, A. V. *Macromolecules* **2003**, *36*, 4140.
- (255) Yang, X. M.; Wang, L.; He, X. H. *J Polym. Sci. A* **2010**, *48*, 5072.
- (256) Garofalini, S. H.; Martin, G. *J Phys. Chem.* **1994**, *98*, 1311.
- (257) Malani, A.; Auerbach, S. M.; Monson, P. A. *J Phys. Chem. Lett.* **2010**, *1*, 3219.
- (258) Rao, N. Z.; Gelb, L. D. *J. Phys. Chem. B* **2004**, *108*, 12418.
- (259) Tarasevich, K. V.; Kuchanov, S. *J Polym. Sci. B* **2007**, *45*, 3093.
- (260) Schumacher, C.; Gonzalez, J.; Perez-Mendoza, M.; Wright, P. A.; Seaton, N. A. In *Recent Advances in the Science and Technology of Zeolites and Related Materials, Pts a - C*; VanSteen, E., Claeys, M., Callanan, L. H., Eds. 2004; Vol. 154, p 386.
- (261) Schumacher, C.; Gonzalez, J.; Wright, P. A.; Seaton, N. A. *J. Phys. Chem. B* **2006**, *110*, 319.
- (262) Schumacher, C.; Seaton, N. A. *Ads. J Int. Ads. Soc.* **2005**, *11*, 643.
- (263) Sefcik, J.; Rankin, S. E. *J. Phys. Chem. B* **2003**, *107*, 52.
- (264) Li, X.; Rankin, S. E. *AIChE J.* **2010**, *56*, 2946.
- (265) Li, X.; Rankin, S. E. *Chem. Eng. Sci.* **2011**, *66*, 1015.
- (266) Rankin, S. E.; Kasehagen, L. J.; McCormick, A. V.; Macosko, C. W. *Macromolecules* **2000**, *33*, 7639.
- (267) Ng, L. V.; Thompson, P.; Sanchez, J.; Macosko, C. W.; McCormick, A. V. *Macromolecules* **1995**, *28*, 6471.
- (268) Bailey, J. K.; Macosko, C. W.; Mecartney, M. L. *J. Non-Cryst. Solids* **1990**, *125*, 208.
- (269) Kallala, M.; Julien, R.; Cabane, B. *J. Phys. II Fr.* **1992**, *2*, 7.
- (270) Hendrickson, R. C.; Gupta, A. M.; C.W. Macosko *Comput. Polym. Sci.* **1994**, *4*, 53.
- (271) Kasehagen, L. J.; Rankin, S. E.; McCormick, A. V.; Macosko, C. W. *Macromolecules* **1997**, *30*, 3921.
- (272) Li, X. 2008, p 91.
- (273) Eisenberg, P.; Erra-Balsells, R.; Ishikawa, Y.; Lucas, J. C.; Nonami, H.; Williams, R. *J. J. Macromolecules* **2002**, *35*, 1160.
- (274) Kudo, T.; Gordon, M. S. *J Phys. Chem. A* **2002**, *106*, 11347.

- (275) Rankin, S. E.; Sefcik, J.; McCormick, A. V. *Ind. Eng. Chem. Res.* **1999**, *38*, 3191.
- (276) Li, X.; Rankin, S. E. *AIChE J.* **2010**, *56*, 2946.
- (277) Li, X. Dissertation, University of Kentucky, 2008.
- (278) Ambati, J.; Rankin, S. E.; American Chemical Society: 2009, p IEC.
- (279) Flory, P. J. *J. Am. Chem. Soc.* **1941**, *63*, 3083.
- (280) Stockmayer, W. H. *J Chem. Phys.* **1943**, *11*, 12.
- (281) Flory, P. J. *Principles of Polymer Chemistry*; Cornell University Press: Ithaca, NY, 1953.
- (282) Dotson, N. A.; Galvan, R.; Laurence, R. L.; Tirrell, M. T. *Polymerization Process Modeling*; Wiley VCH: New York, 1996.
- (283) Rankin, S. E. Dissertation, University of Minnesota, 1998.
- (284) Vallet-Regí, M.; Ruiz-Gonza´lez, L.; Izquierdo-Barbaa, I.; Gonza´lez-Calbetb, J. M. *J. Mater. Chem.* **2006**, *16*, 26.
- (285) Vallet-Regí, M. *Chem. Eur. J* **2006**, *12*, 5934.
- (286) Vallet-Regí, M.; Balas, F. *Open BioMed. Eng. J* **2008**, *2*, 1.
- (287) Vallet-Regí, M.; Ra´mila, A.; Real, R. P. d.; Pe´rez-Pariente, J. *Chem. Mater.* **2001**, *13*, 308.
- (288) Lopez-Noriega, A.; Acros, D.; Izquierdo-Barba, I.; Sakamoto, Y.; Terasaki, O.; Vallet-Regí, M. *Chem. Mater.* **2006**, *18*, 3137.
- (289) Vallet-Regí, M.; Acros, D. *Curr. Nanosci.* **2006**, *2*, 179.
- (290) Beaux, M. F.; McIlroy, D. N.; Gustin, K. E. *Expert Opin. Drug Deliv.* **2008**, *5*, 725.
- (291) Acros, D.; Greenspan, D. C.; Vallet-Regí, M. *Chem. Mater.* **2002**, *14*, 1515.
- (292) Lai, C. Y.; Trewyn, B. G.; Jeftinija, D. M.; Jeftinija, K.; S. Xu, S. J.; Lin, V. S.-Y. *J. Am. Chem. Soc.* **2003**, *125*, 4451.
- (293) Anderson, J.; J. Rosenholm; Areva, S.; Lindén, M. *Chem. Mater.* **2004**, *16*, 4160.
- (294) Zeng, W.; Qian, X. F.; Zhang, Y. B.; Yin, J.; Zhu, Z. K. *MRS Bull.* **2005**, *40*, 766.
- (295) Vallet-Regí, M.; Doadrio, J. C.; Doadrio, A. L.; Izquierdo-Barba, I.; Pérez-Pariente, J. *Solid State Ionics* **2004**, *172*, 435.
- (296) Trewyn, B. G.; Whitman, C. M.; Lin, V. S.-Y. *Nano Lett.* **2004**, *4*, 2139.
- (297) Doadrio, A. L.; Sousa, E. M. B.; Doadrio, J. C.; Pérez-Pariente, J.; Izquierdo-Barba, I.; Vallet-Regí, M. *J Control. Release* **2004**, *97*, 125.
- (298) Gwinn, M. R.; Vallyathan, V. *Environ. Health Perspect.* **2006**, *114*, 1818.
- (299) Kroll, A.; Pillukat, M. H.; Hahn, D.; Schnekenburger, J. *Eur. J. Pharm. Biopharm.* **2009**, *72*, 370.
- (300) Papp, T.; Schiffmann, D.; Weiss, D.; Castranova, V.; Vallyathan, V.; Rahman, Q. *Nanotoxicology* **2008**, *2*, 9.
- (301) Park, E. J.; Park, K. *Toxicol. Lett.* **2009**, *184*, 18.
- (302) Eom, H. J.; Choi, J. *Toxicol. Vitro* **2009**, *23*, 1326.
- (303) Wang, F.; Gao, F.; Lan, M. B.; Yuan, H. H.; Huang, Y. P.; Liu, J. W. *Toxicol. Vitro* **2009**, *23*, 808.
- (304) Fubini, B.; Hubbard, A. *Free Radic. Biol. Med.* **2003**, *34*, 1507.
- (305) Vallyathan, V.; Leonard, S.; Kuppusamy, P.; Pack, D.; Chzhan, M.; Sanders, S. P.; Zweir, J. L. *Mol. Cell. Biochem.* **1997**, *168*, 125.
- (306) Barrett, E. G.; Johnston, C.; Oberdo¨rster, G. n.; Finkelstein, J. N. *Toxicol. Appl. Pharmacol.* **1999**, *158*, 211.
- (307) Lin, W. S.; Huang, Y. W.; Zhou, X. D.; Ma, Y. F. *Toxicol. Appl. Pharmacol.* **2006**, *217*, 252.



- (308) IARC Working Group on the Evaluation of Carcinogenic Risks to Humans. *Silica, some silicates, coal dust and para-aramid fibrils.*, Monogr. Eval. Carcinog. Risks Hum., Lyon, 15-22 October 1996,1997; Vol. 68.
- (309) Castranova, V.; Vallyathan, V.; Wallace, W. E. *Silica and silica induced lung diseases* Boca Raton, FL, 1996.
- (310) Hellawell, B.; Gutteridge, J. *Free radicals in biology and medicine*; Oxford University Press: Oxford, 1999.
- (311) Liu, S.; Cool, P.; Collart, O.; Voort, P. V. D.; Vansant, E. F.; Lebedev, O. I.; Tendeloo, G. V.; Jiang, M. *J. Phys. Chem. B* **2003**, *107*, 10405.
- (312) Tan, B.; Rankin, S. E. *Langmuir* **2005**, *21*, 8180.
- (313) Xing, R. Dissertation, University of Kentucky, 2007.
- (314) Brunauer, S.; Emmett, P. H.; Teller, E. *J. Am. Chem. Soc.* **1938**, *60*, 309.
- (315) Barrett, E. P.; Joyner, L. G.; Halenda, P. P. *J. Am. Chem. Soc.* **1951**, *73*, 373.
- (316) Dziubla, T. D.; Shuvaev, V. V.; Hong, N. K.; Hawkins, B. J.; Madesh, M.; Takano, H.; Simone, E.; Nakada, M. T.; Fisher, A.; Albelda, S. M.; Muzykantov, V. R. *Biomaterials* **2008**, *29*, 215.
- (317) Papirer, E. *Adsorption on Silica Surfaces* CRC Press, 2000; Vol. 90.
- (318) Yu, J.; Xu, R. *Acc. Chem. Res.* **2010**, *43*, 1195.
- (319) Roque-Malherbe, R.; Marquez-Linares, F.; Del Valle, W.; Thommes, M. *J Nanosci Nanotechnol.* **2008**, *8*, 5993.
- (320) Meynen, V.; Busuioc, A. M.; Beyers, E.; Cool, P.; Vansant, E. F.; Bilba, N.; Mertens, M.; Lebedev, O. I.; Van, T. G. In *American Chemical Society*; Nova Science Publishers, Inc.: 2007, p 63.
- (321) Serna-Guerrero, R.; Sayari, A. *Environ. Sci. & Technol.* **2007**, *41*, 4761.
- (322) Sablon, K. *Nanoscale Res. Lett.* **2008**, *3*, 265.
- (323) Chen, L. F.; Norena, L. E.; Navarrete, J.; Wang, J. A. *Mater. Chem. Phys.* **2006**, *97*, 236.
- (324) Chen, S.-Y.; Jang, L.-Y.; Cheng, S. *Chem. Mater.* **2004**, *16*, 4174.
- (325) Kargol, M.; Zajac, J.; Jones, D. J.; Roziere, J. *Thermochim. Acta* **2005**, *434*, 15.
- (326) Liu, Y.; Murata, K.; Inaba, M.; Mimura, N. *Appl. Catal. A* **2006**, *309*, 91.
- (327) Zhang, W.-H.; Lu, J.; Han, B.; Li, M.; Xiu, J.; Ying, P.; Li, C. *Chem. Mater.* **2002**, *14*, 3413.
- (328) Kargol, M.; Zajac, J.; Jones, D. J.; Roziere, J.; Steriotis, T.; Jimenez-Lopez, A.; Rodriguez-Castellon, E. *Chem. Mater.* **2005**, *17*, 6117.
- (329) Saha, B. B.; Chakraborty, A.; Koyama, S.; Lee, J. B.; He, J.; Ng, K. C. *Philos Mag* **2007**, *87*, 1113.
- (330) Santiago, M. A. N.; Sanchez-Castillo, M. A.; Cortright, R. D.; Dumesic, J. A. *J Catal* **2000**, *193*, 16.
- (331) Pietrogiacomini, D.; Sannino, D.; Magliano, A.; Ciambelli, P.; Tuti, S.; Indovina, V. *Appl. Catal. B: Environ.* **2002**, *36*, 217.
- (332) Kickelbick, G. *Prog. in Polym. Sci.* **2003**, *28*, 83.
- (333) Kiel, J. H. A.; Edelaar, A. C. S.; Prins, W.; van Swaaij, W. P. M. *Appl. Catal. B: Environ.* **1992**, *1*, 41.
- (334) Kiel, J. H. A.; Prins, W.; van Swaaij, W. P. M. *Appl. Catal. B: Environ.* **1992**, *1*, 13.
- (335) Gang, L.; van Grondelle, J.; Anderson, B. G.; van Santen, R. A. *J Catal* **1999**, *186*, 100.
- (336) Pietrogiacomini, D.; Magliano, A.; Ciambelli, P.; Sannino, D.; Campa, M. C.; Indovina, V. *Appl. Catal. B: Environ.* **2009**, *89*, 33.

- (337) Anderson, B. G.; Dang, Z.; Morrow, B. A. *J Phys. Chem.* **1995**, *99*, 14444.
- (338) Centeno, M. A.; Carrizosa, I.; Odriozola, J. A. *J Alloy Compd* **2001**, *323*, 597.
- (339) Desmartin-Chomel, A.; Flores, J. L.; Bourane, A.; Clacens, J. M.; Figueras, F.; Delahay, G.; Fendler, A. G.; Lehaut-Burnouf, C. *J. Phys. Chem. B* **2006**, *110*, 858.
- (340) Szczodrowski, K.; Prelot, B.; Lantenois, S.; Douillard, J.-M.; Zajac, J. *Micropor. Mesopor. Mat.* **2009**, *124*, 84.
- (341) Anstrom, M.; Dumesic, J. A.; Topsoe, N. Y. *Catal Lett* **2002**, *78*, 281.
- (342) Erdogan, R.; Ozbek, O.; Onal, I. *Surf. Sci.* **2010**, *604*, 1029.
- (343) Erdogan, R.; Fellah, M. F.; Onal, I. *Int. J Quantum Chem.* **2011**, *111*, 174.
- (344) Cheng, H. S.; Reiser, D. B.; Mathias, P. M.; Baumert, K.; Dean, S. W. *J Phys. Chem.* **1996**, *100*, 9800.
- (345) Lange, B.; Schmidt, W. G. *Surf. Sci.* **2008**, *602*, 1207.
- (346) Kanougi, T.; Atoguchi, T.; Yao, S. *J Mol. Catal. A: Chem* **2002**, *177*, 289.
- (347) Wallin, M.; Gronbeck, H.; Lloyd, S. A.; Skoglundh, M. *Appl. Surf. Sci.* **2004**, *235*, 487.
- (348) Kravchenko, A. A.; Grebenyuk, A. G.; Lobanov, V. V. *Khim., Fiz. Tekhnol. Poverkhni* **2010**, *1*, 177.
- (349) Tanaka, T.; Nakajima, T.; Yamashita, K. *Thin Solid Films* **2002**, *409*, 51.
- (350) Chashchikhin, V.; Rykova, E.; Bagaturyants, A. *Phys. Chem. Chem. Phys.* **2011**, *13*, 1440.
- (351) Civalleri, B.; Garrone, E.; Ugliengo, P. *Langmuir* **1999**, *15*, 5829.
- (352) Roggero, I.; Civalleri, B.; Ugliengo, P. *Chem. Phys. Lett.* **2001**, *341*, 625.
- (353) Cahnmann, H. J. *Anal. Chem.* **1957**, *29*, 1307.
- (354) Aomura, Y.; Kobayashi, Y.; Miyazawa, Y.; Shimizu, H. *J Chromatogr. A* **2010**, *1217*, 1838.
- (355) Bromley, S. T.; Sankar, G.; Catlow, C. R. A.; Thomas, J. M.; Maschmeyer, T. *Micropor. Mesopor. Mat.* **2001**, *44*, 395.
- (356) Delabie, A.; Pierloot, K.; Groothaert, M. H.; Weckhuysen, B. M.; Schoonheydt, R. A. *Micropor. Mesopor. Mat.* **2000**, *37*, 209.
- (357) Ugliengo, P.; Saunders, V. R.; Garrone, E. *Surf. Sci.* **1989**, *224*, 498.
- (358) Senchenya, I. N.; Civalleri, B.; Ugliengo, P.; Garrone, E. *Surf. Sci.* **1998**, *413*, 141.
- (359) Bruehwiler, D. *Nanoscale* **2010**, *2*, 887.
- (360) Gorogotskaya, L. I.; Bokii, G. B. *J Struct. Chem.* **1972**, *13*, 600.
- (361) Bacon, G. E.; Titterton, D. H. *Z. Kristallogr.* **1975**, *141*, 330.
- (362) Harris, A. D.; Kalbus, L. H. *J Chem. Educ.* **1979**, *56*, 417.
- (363) Rahaman, O.; van Duin, A. C. T.; Bryantsev, V. S.; Mueller, J. E.; Solares, S. D.; Goddard, W. A.; Doren, D. J. *J Phys. Chem. A* **2010**, *114*, 3556.
- (364) Sauer, J.; Hill, J. R. *Chem. Phys. Lett.* **1994**, *218*, 333.
- (365) West, J. K.; Zhu, B. F.; Cheng, Y. C.; Hench, L. L. *J. Non-Cryst. Solids* **1990**, *121*, 51.
- (366) Sauer, J.; Zahradník, R. *Int. J Quantum Chem.* **1984**, *26*, 793.
- (367) Eddaoudi, M.; F. Eubank, J.; Liu, Y.; Ch. Kravtsov, V.; W. Larsen, R.; A. Brant, J. In *Studies in Surface Science and Catalysis*; Ruren Xu, Z. G. J. C., Wenfu, Y., Eds.; Elsevier: 2007; Vol. Volume 170, p 2021.
- (368) Kinrade, S. D.; Donovan, J. C. H.; Schach, A. S.; Knight, C. T. G. *J. Chem. Soc., Dalton Trans.* **2002**, 1250.
- (369) Mellot-Draznieks, C.; Girard, S.; Ferey, G.; Schon, J. C.; Cancarevic, Z.; Jansen, M. *Chemistry* **2002**, *8*, 4102.

- (370) Xiong, G.; Yu, Y.; Feng, Z. c.; Xin, Q.; Xiao, F. S.; Li, C. *Micropor. Mesopor. Mat.* **2001**, *42*, 317.
- (371) Civalleri, B.; Garrone, E.; Ugliengo, P. *Chem. Phys. Lett.* **1999**, *299*, 443.
- (372) Civalleri, B.; Zicovich-Wilson, C. M.; Ugliengo, P.; Saunders, V. R.; Dovesi, R. *Chem. Phys. Lett.* **1998**, *292*, 394.
- (373) Wildner, M.; Giester, G. *Miner. Petrol.* **1988**, *39*, 201.
- (374) Varghese, J. N.; Maslen, E. N. *Acta Crystallogr. B* **1985**, *41*, 184.
- (375) Frisch, M. J. T., G. W.; Schlegel, H. B.; Scuseria, G. E.; Robb, M. A.; Cheeseman, J. R.; Scalmani, G.; Barone, V.; Mennucci, B.; Petersson, G. A.; Nakatsuji, H.; Caricato, M.; Li, X.; Hratchian, H. P.; Izmaylov, A. F.; Bloino, J.; Zheng, G.; Sonnenberg, J. L.; Hada, M.; Ehara, M.; Toyota, K.; Fukuda, R.; Hasegawa, J.; Ishida, M.; Nakajima, T.; Honda, Y.; Kitao, O.; Nakai, H.; Vreven, T.; Montgomery, Jr., J. A.; Peralta, J. E.; Ogliaro, F.; Bearpark, M.; Heyd, J. J.; Brothers, E.; Kudin, K. N.; Staroverov, V. N.; Kobayashi, R.; Normand, J.; Raghavachari, K.; Rendell, A.; Burant, J. C.; Iyengar, S. S.; Tomasi, J.; Cossi, M.; Rega, N.; Millam, N. J.; Klene, M.; Knox, J. E.; Cross, J. B.; Bakken, V.; Adamo, C.; Jaramillo, J.; Gomperts, R.; Stratmann, R. E.; Yazyev, O.; Austin, A. J.; Cammi, R.; Pomelli, C.; Ochterski, J. W.; Martin, R. L.; Morokuma, K.; Zakrzewski, V. G.; Voth, G. A.; Salvador, P.; Dannenberg, J. J.; Dapprich, S.; Daniels, A. D.; Farkas, Ö.; Foresman, J. B.; Ortiz, J. V.; Cioslowski, J.; Fox, D. J. *Gaussian, Inc., Wallingford CT* **2009**.
- (376) Crépeau, G.; Montouillout, V.; Vimont, A.; Mariey, L.; Cseri, T.; Maugé, F. *J Phys. Chem. B* **2006**, *110*, 15172.
- (377) Mayer, I. *J Comput. Chem.* **2007**, *28*, 204.
- (378) Wiberg, K. B. *J. Am. Chem. Soc.* **1968**, *90*, 59.
- (379) Wiberg, K. B. *Tetrahedron* **1968**, *24*, 1083.
- (380) Reed, A. E.; Curtiss, L. A.; Weinhold, F. *Chem. Rev.* **1988**, *88*, 899.
- (381) Gao, B.; Liu, Z. F. *J Chem. Phys.* **2004**, *121*, 8299.
- (382) Adrian-Scotto, M.; Mallet, G.; Vasilescu, D. *J Mol. Struct. Theochem* **2005**, *728*, 231.
- (383) Buzko, V.; Sukhno, I.; Buzko, M. *Int. J Quantum Chem.* **2007**, *107*, 2353.
- (384) Shubina, T. E.; Clark, T. In *High Performance Computing in Science and Engineering, Garching/Munich 2007*; Wagner, S., Steinmetz, M., Bode, A., Brehm, M., Eds.; Springer Berlin Heidelberg: 2009, p 201.
- (385) Chaban, G. M.; Huo, W. M.; Lee, T. J. *J Chem. Phys.* **2002**, *117*, 2532.
- (386) Bersuker, I. B. *Chem. Rev.* **2001**, *101*, 1067.
- (387) Hertl, W.; Hair, M. L. *Nature* **1969**, *223*, 1150.
- (388) Gluszak, T. J.; Chen, D. T.; Sharma, S. B.; Dumesic, J. A.; Root, T. W. *Chem. Phys. Lett.* **1992**, *190*, 36.
- (389) Fubini, B.; Bolis, V.; Cavenago, A.; Garrone, E.; Ugliengo, P. *Langmuir* **1993**, *9*, 2712.

## Vita

**Date of Birth:** 9/4/1980

**Place of Birth:** Nizamabad, Andhra Pradesh, India

**Education:** B.S. Chemical Engineering, *Birla Institute of Technology and Science*, Pilani, Rajasthan, India, June 2002

### Professional Positions Held:

NMR Analyst, *ChemPharma Int'l LLC*, Richmond, KY, July 2005-December 2005

Project Associate, *Indian Institute of Chemical Technology*, Hyderabad, India, July 2002-July 2003

Student Intern, *Indian Institute of Chemical Technology*, Hyderabad, India, January 2002-July 2002

In-plant Student Intern, *Vasant Chemicals Pvt. Ltd.*, Hyderabad, India, May 2000-July 2000

### List of Publications:

1. **Ambati, J.**, Rankin, S.E., "Reaction-Induced Phase Separation of Bis(triethoxysilyl)ethane upon Sol-gel Polymerization in Acidic Conditions", *Journal of Colloid and Interface Science* (2011), in press
2. Rahman, M.S., **Ambati, J.**, Rankin, S.E., "Incorporation of isolated Ti sites into mesoporous silica thin films by sugar surfactant complexation", *Microporous and Mesoporous Materials*, submitted
3. Song, Y., **Ambati, J.**, Parkin, S., Rankin, S.E., Lehmler, H., "Crystal Structure and Density Functional Theory Studies of Quinone Metabolites of Polychlorinated Biphenyls" *Chemosphere*, submitted
4. **Ambati, J.**, Syed., H., Rankin, S.E., "DFT Investigation of NH<sub>3</sub> Physisorption on CuSO<sub>4</sub> Impregnated SiO<sub>2</sub>", *Journal of Physical Chemistry A*, to be submitted
5. **Ambati, J.**, Rankin, S.E., "Determination of <sup>29</sup>Si NMR coupling constants in organoalkoxysilanes with non-trivial scalar coupling patterns", *Journal of Physical Chemistry A* (2010), *114*, 12613-12621
6. **Ambati, J.**, Rankin, S.E., "DFT calculation of indirect <sup>29</sup>Si-<sup>1</sup>H coupling constants in organoalkoxysilanes", *Journal of Physical Chemistry A* (2010), *114*, 5279-5286

7. **Ambati, J.**, Rankin, S.E., “<sup>29</sup>Si NMR investigation of the polymerization kinetics of bis(triethoxysilyl)ethane in acidic alcohol/water solution”, *PMSE preprints* (2006), 94, 610-611 (conference proceedings)
8. Kiranmai, D., **Jyothirmai, A.**, Murty, C.V.S., “Determination of kinetic parameters in fixed film bio-reactors: an inverse problem approach”, *Biochemical Engineering Journal* (2005), 23(1), 73-83

**List of Technical Papers:**

1. **Ambati, J.**, Lopez A., Cochran, D., Wattamwar, P., Bean, K., Dziubla, T., Rankin, S.E., “Controlling Silica-induced Oxidative Stress to Facilitate Therapeutic Applications of Engineered Silica”, *SFB 2011 Annual Meeting*, Orlando, FL, April 13-15, 2011
2. **Ambati, J.**, Saiyed., H., Rankin, S.E., “Quantum Mechanical Investigation of Ammonia Adsorption On Mixed Hydroxylated Copper Sulfate-Silica System”, *AIChE 2010 Annual Meeting*, Salt Lake City, UT, November 7-13, 2010
3. **Ambati, J.**, Lopez A., Cochran, D., Wattamwar, P., Bean, K., Dziubla, T., Rankin, S.E., “Antioxidant Enzyme Loading On Mesoporous Silica to Facilitate Application of Engineered Silica in Therapeutic Drug Delivery”, *AIChE 2010 Annual Meeting*, Salt Lake City, UT, November 7-13, 2010
4. **Ambati, J.**, Rankin, S.E., “Kinetic Investigation of Bridged Organoalkoxysilanes”, *Chemical & Materials Engineering Graduate Student Association Poster Presentation Competition*, University of Kentucky, Lexington, KY, September 17<sup>th</sup> 2010
5. **Ambati, J.**, Rankin, S.E., “<sup>29</sup>Si NMR of bridged organoalkoxysilanes – Challenges and solutions”, *239<sup>th</sup> ACS National Meeting*, San Francisco, CA, March 21-25, 2010
6. **Ambati, J.**, Wattamwar, P., Bean, K., Dziubla, T., Rankin, S.E., “Engineered silica for anti-oxidant enzyme Loading and protection”, *239<sup>th</sup> ACS National Meeting*, San Francisco, CA, March 21-25, 2010 (poster)
7. **Ambati, J.**, Rankin, S.E., “Dynamic Monte Carlo simulation of sol gel polymerization of bridged alkoxy silanes”, *AIChE 2009 Annual Meeting*, Nashville, TN, November 8-13, 2009

8. **Ambati, J.**, Rankin, S.E., “ $^{29}\text{Si}$  NMR of Organoalkoxysilanes – Challenges and solutions”, *Chemical & Materials Engineering Graduate Student Association Poster Presentation Competition*, University of Kentucky, Lexington, KY, October 2<sup>nd</sup> 2009
9. **Ambati, J.**, Rankin, S.E., “Study of the reaction kinetics of bis(triethoxysilyl)ethane and methyltriethoxysilane”, *238<sup>th</sup> ACS National Meeting*, Washington, DC, August 16-20, 2009 (poster)
10. **Ambati, J.**, Rankin, S.E., “ $^{29}\text{Si}$  NMR study of bis(triethoxysilyl)ethane polymerization kinetics”, *Proceedings of the 50<sup>th</sup> Experimental NMR Conference*, Asilomar, CA, March 29-April 3, 2009 (poster)
11. **Ambati, J.**, Rankin, S.E., “Investigation of NMR signal loss during hydrolytic polycondensation of organoalkoxysilanes”, *AIChE 2008 Annual Meeting*, Philadelphia, PA, November 16-21, 2008
12. **Ambati, J.**, Rankin, S.E., “DFT calculation of  $^{29}\text{Si}$ - $^1\text{H}$  coupling constants in organoalkoxysilanes”, *AIChE 2008 Annual Meeting*, Philadelphia, PA, November 16-21, 2008
13. **Ambati, J.**, Rankin, S.E., “Complexity from a small molecule: Unexpected NMR spectral patterns observed from selective bridge  $^1\text{H}$  coupling to  $^{29}\text{Si}$  in bis(trimethoxysilyl)ethane”, *Proceedings of the 49<sup>th</sup> Experimental NMR Conference*, Asilomar, CA, March 9-14, 2008 (poster)
14. **Ambati, J.**, Rankin, S.E., “NMR Investigation of Polymerization-Induced Microphase Separation in Bis(Triethoxysilyl)Ethane”, *AIChE 2006 Annual Meeting*, San Francisco, CA, November 12-17, 2006
15. **Ambati, J.**, Rankin, S.E., “The early time polymerization kinetics in acidic water/alcohol solutions of bis(trialkoxysilyl)alkanes with short bridging chains”, *AIChE 2006 Annual Meeting*, San Francisco, CA, November 12-17, 2006
16. **Ambati, J.**, Rankin, S.E., “ $^{29}\text{Si}$  NMR investigation of the polymerization kinetics of bis(triethoxysilyl)ethane in acidic alcohol/water solution”, *231<sup>st</sup> ACS National Meeting*, Atlanta, GA, March 26-30, 2006 (poster)

17. **Ambati, J.**, Rankin, S.E., "Comparison of the polymerization kinetics of methyltriethoxysilane and bis(triethoxysilyl)ethane", *AIChE 2005 Annual Meeting*, Cincinnati, OH, October 31-November 4, 2005
18. **Ambati, J.**, Murty, C.V.S., "Modeling and simulation of a methanol reformer", *Indian Institute of Chemical Technology*, Hyderabad, India, May 2003

**List of Contributed Papers:**

19. Lopez A., **Ambati, J.**, Cochran, D., Dziubla, T., Rankin, S.E., "Nano-Engineered Silica Based Drug Delivery System", *AIChE 2010 Annual Meeting*, Salt Lake City, UT, November 7-13, 2010
20. Lopez A., **Ambati, J.**, Cochran, D., Dziubla, T., Rankin, S.E., "Nano-Engineered Silica Based Drug Delivery System", *Engineered Bioactive Interfaces and Devices REU Poster Session*, University of Kentucky, Lexington, KY, July 31<sup>st</sup> 2010 (poster)
21. Bean, K., **Ambati, J.**, Wattamwar, P., Dziubla, T., Rankin, S.E., "Enzyme loading and activity in nanoporous metaloxides", *AIChE 2009 Annual Meeting*, Nashville, TN, November 8-13, 2009 (poster)
22. Bean, K., **Ambati, J.**, Wattamwar, P., Dziubla, T., Rankin, S.E., "Enzyme loading and activity in nanoporous metaloxides", *Engineered Bioactive Interfaces and Devices REU Poster Session*, University of Kentucky, Lexington, KY, July 31<sup>st</sup> 2009 (poster)
23. Rankin, S.E., **Ambati, J.**, "Ab initio calculation of  $^1\text{H}$ - $^{29}\text{Si}$  coupling constants in organoalkoxysilanes", *235<sup>th</sup> ACS National Meeting*, New Orleans, LA, April 6-10, 2008 (poster)